Final Report

Bigger is Better Group 12

Version Number: 03
First version: June 25, 2019
Second version: June 29, 2019

by

Bram Asselman	4432029
Daniël Brus	4379179
Hidde Jansen	4551141
Max Knoop	4551826
Reinoud Lampe	4557964
Mathilde Terleth	4497392
Nikki van Luijk	4551842
Sebastiaan van Paasen	4558944
Floyd van Steen	4551001
Mels Wittenberg	4430581

To obtain the degree of Bachelor of Science
at the Delft University of Technology,
July 2, 2019

Project duration: April 23, 2019 – July 4, 2019

Project committee:

Ir. F.J. Abbink,	Clean Sky, client
Ir. J.A. Melkert,	TU Delft, supervisor
S. Sun,	TU Delft, coach
T. Mkhoyan ,	TU Delft, coach
Ir. H. Mulder,	TU Delft, coach

TU Delft

Contents

Nomenclature

List of Symbols

α	Angle of attack	deg
α_{aa}	Atmospheric absorption	dB/m
β	Prandtl-Glauert correction factor	-
δp	Pressure difference	Pa
δ_f	Flap deflection	deg
ΔT	Temperature rise across the fan	K
ΔY	Airfoil sharpness parameter	-
$\dot{F}$	Fuel flow	kg/s
$\dot{m}$	Mass flow rate	kg/s
η	Efficiency	-
Γ	Dihedral/Anhedral angle	deg
Λ	Sweep	deg
λ	Engine bypass ratio	-
λ	taper ratio	-
μ	Dynamic viscosity	kg/ms
$\prod$	Pressure ratio	-
ρ	Density	kg/m^3
σ_z	Stress around axis z	Pa
θ	Climb angle or emission angle	deg
(O)SPL	(Overall) Sound pressure level	dB
A	Area	m^2
A	Aspect ratio	-
a	Acceleration	m/s^2
a	Distance to wing tip	m
b	Span	m
c	Chord length	m
C_{D_0}	Zero lift drag coefficient	-
C_{D_i}	Induced drag coefficient	-
$C_{D_{misc}}$	Miscellaneous drag coefficient	-
C_D	Drag coefficient	-
C_f	Friction coefficient	-
C_{L_α}	Lift curve slope	1/rad
C_{l_α}	Airfoil lift curve slope	1/rad
$C_{L_{mac}}$	Maximum lift coefficient	-
$C_{l_{mac}}$	Airfoil maximum lift coefficient	-
C_L	Lift coefficient	-
C_p	Specific heat	J/K
c_r	Root chord	m
c_T	Thrust specific fuel consumption	kg/Ns
c_t	Tip chord	-
D	Drag force	N
d	Deflection	m
d	Diameter	m
E	Mass emitted of emission	kg
e	Oswald efficiency factor	-
EF	Emission factor	kg/kg
EI	Bending stiffness	Nm^2
f	Frequency	Hz
FF	Form factor	-
g	Gravitational constant	m/s^2
h	Height	m
I_{ij}	Moment of inertia around axis i and j	
IF	Interference factor	-
K	Column effective length factor	-
k	Drag polar factor $1/\pi Ae$	-
k	Heat capacity ratio	-
L	Lift force	N
L/D	Lift over drag ratio	-
L_A	A-weighted sound pressure level	dBA
LHV	Lower heating value	MJ/kg
M	Mach number	-
M_i	Moment around axis i	Nm
n	Load factor	-
N_{eng}	Number of engines	-
p	Pressure	Pa
p_{e0}	Reference sound pressure $2x10^{-5}$	Pa
p_e	Effective sound pressure	Pa
Q	Ground reflectivity coefficient	-
q	Dynamic pressure	kg/m^2s
R	Gas constant	J/kg K
R	Range	m
r	Distance to source	m
RC	Rate of climb	m/s
RD	Rate of descent	m/s

Re	Reynolds number	-
S	Surface area	m^2
s	Horizontal distance	m
S’	Wing area when HLD’s deployed	-
Swf	Area affected by the HLD’s	-
T	Temperature	K
T	Thrust force	N
t	Time	s
t/c	thickness over chord ratio	-
V	Airspeed	m/s
V_i	Shear force of axis i	N
VA	Apparent power	
W	Weight	N
Wh/kg	Specific energy	
Wh/L	Energy density	
x_{trans}	transition point	m

List of Subscripts

∞	Free stream condition
0	Sea level condition
a	Approach
amb	Ambient
cc	Combustion chamber
cr	Cruise
crit	Critical
dd	Drag divergence
exp	exposed
F	Fuel
f	fatigue
fus	fuselage
g	Gas, e.g. mix of fuel and air
h	Horizontal tailplane/horizontal
lam	laminar
LE	Leading edge
LOF	Lift off condition
noz	Nozzle
ref	reference
s	Stall
td	Touchdown
TO	Take-off
tur	turbulent
w	Wing
wet	Wetted

List of Abbreviations

AFRA	Aircraft fleet recycling association
APU	Auxiliary power unit
ATC	Air traffic control
BFL	Balanced field length
DOC	Direct operating costs
FAA	Federal aviation association
FFD	Functional flow diagram
HLD	High lift device
HPC	High pressure compressor
HPT	High pressure turbine
ICAO	International civil aviation organization
IOC	Indirect operating costs
LPC	Low pressure compressor
LPT	Low pressure turbine
LTO	Landing and take-off
LTO	Lift and take-off
MAC	Mean aerodynamic chord
MAI	Manufacturing, assembly and integration
MFW	Maximum fuel weight
MLW	Maximum landing weight
MPW	Maximum payload weight
MTOW	Maximum take-off weight
NC	Non-recurring costs
NMVOC	Non methane volatile organic compounds
NPV	Net present value
OEW	Operational empty weight
OHC	Overhead costs
RF	Radiative forcing
RoI	Return on investment
SAR	Specific Air Range
TRL	Technology readiness level
TS	Thrust setting
UHBP	Ultra-high bypass
WBS	Work breakdown structure

1 Executive overview

The following report covers the detailed design phase of the DSE - Bigger is Better. An overview of the work performed for this report is presented in this chapter. The mission of the project is to design a state of the art, dedicated fixed wing aircraft for 450 passengers on a typical intra-continental mission. This report follows from the conceptual design analyses performed in the Midterm report [1]. An overview of the different analyses performed throughout the project is provided in this chapter.

1.1 Design overview

The EcoHopper 450 is a short range high capacity aircraft. 450 Passengers can be transported in a single class configuration with a design range of 1,400 km. By keeping the maximum range of the aircraft to a minimum, a significant weight reduction was made. This weight reduction directly influenced the fuel consumption in a positive way. To improve further in sustainability the decision was made to fly at a lower altitude and at a lower cruise Mach number. This presented the opportunity to fly with an unswept wing increasing aerodynamic efficiency. Flying at a lower altitude also has the advantage of a reduction in the radiative forcing of aircraft emissions. A strutted design was chosen which supports the wing, this gives the opportunity to increase the slenderness or aspect ratio of the wing, which again contributed to the aerodynamic efficiency. This design shows a decrease in fuel consumption of 14.3% and a decrease in radiative forcing of 21.1% with respect to the highly efficient B737-MAX 8. Next to emissions and fuel consumption the EcoHopper 450 has improved noise emissions with respect to the current state of the art. In Table 1.1 the specifications of the aircraft can be seen, a comparison is made with the B737-MAX 8 and the Boeing 747-8 which are the current standard for short range low capacity flights and long range high capacity flights respectively. In Figure 1.1 an overlay diagram is shown comparing the EcoHopper 450 to the B737-MAX 8, B747-8 and the A380-800.

Table 1.1: Design overview of the EcoHopper 450 in comparison to the B737-MAX 8 and B747-8.

Parameter	EH450	B737-MAX 8	B747-8
Maximum seating [pax]	450	200	605
Length [m]	49.3	39.5	76.3
Height [m]	19.4	12.5	19.4
Wing Span [m]	52.0	35.9	78.4
Aspect ratio [-]	13	10.2	8.5
MTOW [kg]	153,000	82,000	448,000
OEW [kg]	87,000	45,000	220,000
Fuel capacity [kg]	17,400	20,730	190,000
Range [km]	1,400	6,570	14,320
Cruise altitude [m]	9,000	11,000	11,000
Cruise Mach [-]	0.72	0.79	0.85
Cruise speed [m/s]	218	233	259
Take-off Runway Length [m]	2,548	2,500	3,100

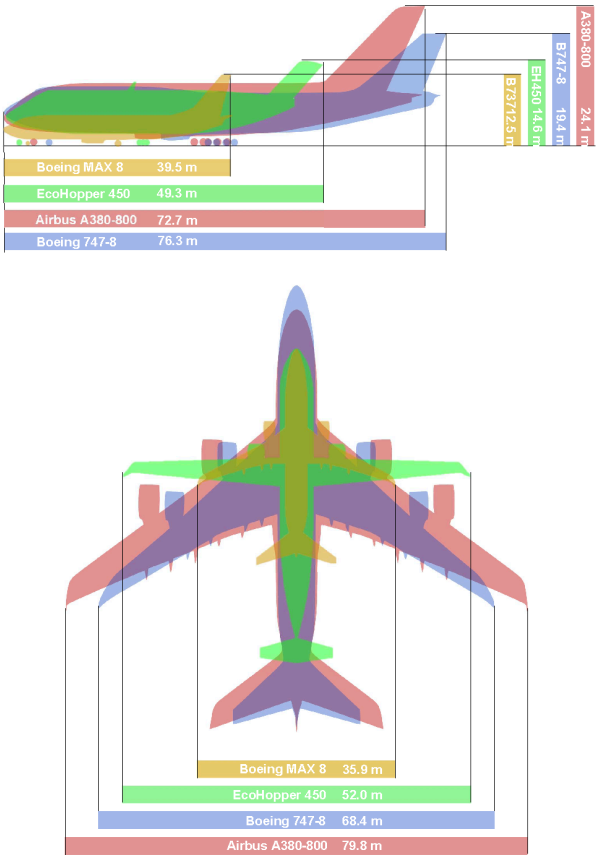

Figure 1.1: Overlay diagram comparing the EcoHopper 450 with existing aircraft models.

1.2 Aircraft systems

In order to reduce the environmental impact of ground operations and to lower fuel burn, the EcoHopper 450 features an electric taxiing system. The design of the electric taxiing system consisted of the following steps. First, the placement of

the electric motors in the landing gear was determined. It was chosen to implement two electric motors in the outboard wheels of the main landing gear, such that tractive forces are sufficiently high, even in wet conditions. Next, the battery pack and electric motors were sized based on the required performance of the system. The technical specifications of one electric motor is shown in Table 1.2. The battery pack capacity needed for the electric taxiing system was found to be equal to 68.53 kWh, resulting in a mass of 227 kg and volume of 99 L.

Table 1.2: Technical specifications electric motor.

Parameter	Value
Continuous Torque [Nm]	1,909
Rotational speed [rpm]	1,300
Mass [kg]	47.74
Continuous Power [kW]	260
Gear ratio [-]	7.56:1
Gearbox torque [kNm]	13

Once the electric taxiing system was sized, its fuel and cost savings were examined. It was found the electric taxing system leads to a fuel weight reduction of 852 kg and an overall fuel consumption reduction of 6.04% compared to state-of-the-art reference aircraft. The negative effect of the increased weight due to the larger battery pack and electric motors was found to be marginal, with a worsening of the fuel consumption reduction of just 0.4%.

Aside from the electric taxiing system, the electrical system, hydraulic system, flight control system, fuel system and environmental control system were analysed and designed according to the requirements. Significant efforts were made to make the EcoHopper 450 a more electric aircraft. The APU was discarded and a no-bleed architecture was chosen, which improved reliability and reduced maintenance costs significantly.

1.3 Propulsion system

In order to select a suitable propulsion system the requirements driving the design were identified. These were found to be the noise generation, fuel consumption and technology readiness level (TRL). Based on these requirements, a trade-off was performed between the open rotor engine and the ultra-high bypass geared turbofan engine. The engines were assessed against criteria considering the fuel efficiency, noise, TRL and placement. This finally resulted in the choice of the ultra-high bypass (15:1) geared turbofan engine. Considering the design point chosen (T/W = 0.26) it was found that the engines should be able to deliver a static sea level thrust of 214.1 kN each. An additional constraint for the engine was found from the sustainability analysis as the NO_x emission highly depends on the combustion chamber inlet temperature. Therefore, it was said that this temperature should be as low as possible. Creating a tool which performs a thermodynamic engine cycle calculation, the engine could be designed using these constraints. This resulted in the engine parameters shown in Table 1.3 and Table 1.4.

Table 1.3: Engine component properties [2].

Parameter	Value	Parameter	Value
η_{inlet}	0.97	$\eta_{gearbox}$	0.995
η_{fan}	0.93	η_{noz}	0.98
η_{LPC}	0.9	$\prod_{intake}$	0.92
η_{HPC}	0.92	$\prod_{fan}$	1.4
η_{LPT}	0.9	$\prod_{LPC}$	6
η_{HPT}	0.89	$\prod_{HPC}$	6.5
η_{cc}	0.99	$\prod_{cc}$	0.96
$\eta_{mechanical}$	0.99	$T_{exit,cc}$ [K]	1,750

Table 1.4: Resulting main engine properties during take-off conditions.

Parameter	Value
Fuel flow [kg/s]	0.581
Air mass flow [kg/s]	450
$T_{inlet,cc}$ [K]	985
Core thrust [kN]	57.5
Fan thrust [kN]	156.8
Total thrust [kN]	214.3

The design of the outer dimensions of the engine was done using the empirical sizing method obtained from Torenbeek [3]. As it was found that the method was not fully valid for an ultra-high bypass engine, statistical data for existing high bypass geared turbofan engines was used in combination with the Torenbeek method. This resulted in a fan case diameter of 3.15 m while the fan itself is 2.87 m, and the length of the nacelle is 5.60 m in total. In order to estimate the mass of the engine, a statistical method was used as no valid empirical method was available. Although a lot of effort was put into reducing the weight of the engine (fan blades alone for example are made out of carbon instead of titanium), it was deemed necessary to include a margin of 500 kg. The mass of the engine was then determined to be 4,760 kg for a thrust level of 214 kN.

1.4 Aerodynamic design and analysis

The aerodynamic sizing consisted of the sizing of the aerodynamic geometry and the analysis of the aerodynamic coefficients and aerodynamic performance. A high aspect ratio of 13 was selected for high aerodynamic performance. The 3D wing was designed to be unswept with a super critical airfoil to prevent Mach drag divergence. A thicker root airfoil was selected to reduce structural weight by increasing the area moment of inertia of the wing cross-section. An overview of the important parameters for the 3D wing geometry is shown in Table 1.5.

Table 1.5: Overview of the 3D wing Geometry.

Parameter	Value
A [-]	13.0
S [m^2]	208
b [m]	52.0
λ [-]	0.357
c_r [m]	5.89
c_t [m]	2.01
MAC [m]	4.30
$(t/c)_r$ [-]	0.20
$(t/c)_t$ [-]	0.12
$(t/c)_{avg}$[-]	0.13
$\Lambda_{0.25}$ [deg]	0.00
Γ [deg]	-1.50

Table 1.6: Overview of the aerodynamic analysis for different conditions.

Parameter	Cruise	Take-off	Landing
C_{L_α} [1/rad]	5.70	6.65	6.80
α_{0L} [deg]	-3.90	-10.39	-13.64
$C_{L_{max}}$ [-]	1.48	2.77	3.05
α_s [deg]	13.57	16.11	14.65
C_L [-]	0.621	1.92	1.80
C_{D_0} [-]	0.0233	0.0318	0.0775
e [-]	0.720	0.765	0.765
C_D [-]	0.0356	0.143	0.175
L/D [-]	17.43	13.44	10.28
$(L/D)_{max}$ [-]	18.32	16.16	10.35

The high lift devices combined with the take-off thrust determine the required take-off length. In order to choose the type of high lift devices, the available area was determined first. The leading edge devices could be placed from 10% to 97% of the half-span, with a 4% interruption for the engine pylon. The trailing edge devices could be placed from 10% to 71% of the half-span uninterruptedly, the rest of the span was used for the fuselage and ailerons. When the available area was set, the leading edge devices were chosen. It was found that three position slotted leading edge flaps have the best ΔC_{Lmax} to weight ratio. As trailing edge device a single slotted fowler flap was chosen, since it also resulted in the best ΔC_{Lmax} to weight ratio. A single slotted flap is also lighter since a simpler link/track end support may be used. The high lift devices combined resulted in a C_{Lmax} of 2.8 during take-off and 3.0 during landing. The stall angles of attack were determined to be 16.1 and 14.7 respectively.

The design of the spoilers was mainly based on reference aircraft since the spoilers have multiple tasks to perform, therefore calculations to meet only one requirement were of no use. The spoilers sizing was mainly based on the B777 and the A320. In the design, three inboard spoilers are used, with as main purpose lift dumping, and 3 outboard spoilerons. Spoilerons provide both roll control and aid with lift dumping. The roll control of spoilerons is needed at high speeds, when aileron reversal might occur.

In the analysis part the lift and drag performance of the aircraft was analysed. The lift curves were constructed using the Raymer method [4]. The drag analysis was split up in two parts; zero lift drag and induced drag. In the induced drag calculation an estimation for the Oswald efficiency was made for the aircraft flying at high Mach numbers. Drag polars were constructed for three conditions, from this the aerodynamic performance in terms of L/D was calculated. In Table 1.6 an overview of the results can be seen for cruise, take-off and landing.

1.5 Stability and control analysis

To ensure stability on the ground, the undercarriage was sized with respect to CS-25 requirements [5]. A tool was written to analyse the lateral and longitudinal landing gear displacements, and the feasibility of such an initial design was investigated. Due to the high wing configuration the centre of gravity was estimated to lie higher than for conventional aircraft, resulting in very tall landing gear struts required to comply with longitudinal tip-over requirements. The tall landing gear contributed to exceptionally wide track requirements of 5 m from the centre line. It was determined that a redesign of the tailcone would decrease the height of the landing gear as the scrape angle would be less limiting, which in turn brought the required main gear track inwards. Only increasing the tailcone length was not enough to make the landing gear feasible. It was determined that the still placing the entire weight of the plane on slanted struts, far out to the sides of the aircraft would be structurally unfeasible. The initial Class I strut sizing was discarded and a third, main strut was added under the fuselage centreline to carry most of the weight of the aircraft when grounded. The side tracks would then be used primarily to limit lateral tip-over, and thus do not have to be designed to carry the full weight of the aircraft.

Controllability during flight is achieved through deflection of primary control surfaces. The three control surfaces most often employed are elevator(s) for pitch control, ailerons for roll control and rudder(s) for yaw control. These three surfaces were sized for the EcoHopper 450 for the design concept data. The control surfaces were sized for their most limiting use cases. The elevator was sized for the MTOW configuration during take-off, whereby the elevator must deliver a large enough negative pitching moment to achieve adequate lift. The ailerons were sized for the time to roll angle requirement during take-off. The rudder was designed for two cases: the crosswind landing and the single engine out scenario. Sizing methods were primarily based on linearised, control surface defined stability derivatives in combination with maximum deflection angles to elicit some dynamic response. Results for all three surfaces are presented in Table 1.7, where subscript c refers to the respective control surface. Note that the deflections are symmetric, so they can deflect the same amount in positive and negative direction.

Table 1.7: Control surface sizing results.

Parameter [unit]	Elevator	Aileron	Rudder
b_c/b [-]	1	0.26	1
c_c/c [-]	0.5	0.3	0.5
$\delta_{c_{max}}$ [deg]	30	25	30

1.6 Structural analysis

Regarding the structural aspect, the EcoHopper 450 should be able to carry the loads defined in the CS-25 requirements. First the flight envelope was developed for the aircraft, after which the critical load cases were evaluated to size the main aircraft components. Note that a shear analysis was not performed as it was determined that this will not be the limited sizing factor for either of the main aircraft components.

The sizing of the strut and main wing were combined as these components are inter-related and formed an indeterminate system. The different strut materials considered were Aluminium 2024, Aluminium 7075 and two types of carbon fibre epoxy composites. One of these materials had unidirectional lay-up while the other was quasi-isotropic. For the wing the Aluminium 2024 was selected, while the strut was made of the unidirectional carbon fibre as this yielded the lightest and smallest strut. Simultaneously, the structure was optimised for the best strut position, which turned out to be at 69% of the half span. Based on deflection compatibility of the strut and the wing, the required strut force was determined. With all the forces known, the shear force and bending moment distributions along the span of the wing were generated. Using this data, the required wing inertia was computed. This way the wing was sized to meet the fatigue stress limits. The final wing design contains two spars placed at 15% and 55% of the chord, such that they have a large contribution to the moment of inertia required to withstand the bending moments around the axis parallel to the chord line. In between the spars five booms were placed on both the upper and lower skin or the airfoil with a size of 11 cm^2 from the root till the strut, after which they are cut off. Some additional values of the wing components are shown in Table 1.8.

Table 1.8: Comparison initial and final wing parameters.

Parameter	Final values
Total strut mass [kg]	3,736
Total boom mass [kg]	1,094
Total spar mass [kg]	10,481
Total skin mass [kg]	1,176
Total wing mass [kg]	16,487
Total wing cost [€]	156,490

Moving on to the fuselage, the loading diagrams were created based on the root forces and moments of the main wing, horizontal tail, fuselage weight and payload weight. Based on the maximum resulting bending moment, the fuselage thickness and the area of the stiffened elements in the fuselage frame were sized. Furthermore, the stresses based on pressurisation were computed. It was found that the required thickness for pressurisation was 1.66 mm. However, the required thickness to withstand the critical bending moments turned out to be limiting. The final design has a thickness of 2 mm with nine booms in the upper right, upper left, lower left and lower right corners.

Finally, the horizontal tail was sized for the load case during take-off. This loading condition was chosen as the elevator has its highest deflection in this flight phase, which is 30 deg. A similar method as the one for the wing analysis was used, however, without strut force, engine and fuel weight.

1.7 Performance analysis

In order to assess the performance of the EcoHopper 450, several performance parameters were chosen to be investigated. These parameters were analysed using tools which were created based on theory obtained from Anderson [6] and Torenbeek [3]. The parameters under consideration were the payload range characteristics of the aircraft, climb performance and runway performance. From the first, it was found that the aircraft could meet its design range of 1,400 km under harmonic conditions (maximum payload). Then the climb performance was analysed to assess the aircraft against CS-25 regulations [5]. After the analysis it turned out that the EcoHopper 450 meets these requirements. However, it meets the requirements with a margin of 14%, this was still deemed acceptable as it serves as a contingency value for the next design phases.
The next performance parameter was the runway performance. This included the computation of the take-off and landing distance as well as the balanced field length (BFL), which is important when an engine failure occurs. This would then lead to the required runway length for the aircraft, which could be found by multiplying the landing distance with 10/6 and the take-off distance with 1.15 [7]. The latter is only valid if the BFL is shorter than the nominal take-off distance. The computed values for these parameters are shown in Table 1.9. According to the requirements specified in the Baseline report [8], the aircraft shall have a required runway length of at most 2,700 m. From the computed values, it can thus be said that this requirement is met.

Table 1.9: Take-off and landing distances for the EcoHopper 450 and the B737-MAX 8.

Parameter	EcoHopper 450
Take-off distance [m]	2,216
Landing distance [m]	1,594
Balanced field length [m]	1,774
Required landing runway length [m]	2,657
Required take-off runway length [m]	2,548

1.8 Sustainability analysis

In order to assess the sustainability aspect of the aircraft, its fuel consumption, emissions, and noise output were assessed. These sustainability aspects are summarised below. The term LTO cycle appears in the following sections, it can be defined as all aircraft operations below an altitude of 3,000 ft, this includes the modes taxiing, take-off, initial climb-out, approach and landing.

Fuel consumption

The fuel consumption for the entire mission was analysed. The fuel consumption during cruise could be found from the Specific Air Range (SAR), see Equation 1.1 [9]. It was chosen to express the cruise fuel consumption in kg/km-pax in order to fairly compare the EcoHopper 450 and the B737-MAX 8. For the first it was found to be 0.00969 kg/km-pax, while for the latter it was 0.0108 kg/km-pax. Then the fuel consumption during the climb, from the LTO cycle (3,000 ft) up to cruise, was computed. This was done by integrating the the rate of climb over the altitude to be climbed. In addition, using the fuel flow for the engine found from the propulsion system analysis, the fuel burnt during the climb could be found. The climb profile considered for this analysis was a maximum continuous thrust case, which resulted in a thrust setting of 90% [10], and a free stream velocity of 60% of the cruise velocity [11]. From the time to climb and rate of climb, the horizontal distance covered could also be found. The last phase considered was the descent. However as it was found that it is mostly performed in idle, the fuel consumption could be neglected. Thus a continuous descent from cruise to the LTO cycle altitude (3,000 ft) was modelled. Subtracting the horizontal distances combined from the design mission range of 1,400 km resulted in the distance covered in cruise mode. Finally combining all the values resulted in Table 1.10. The EcoHopper 450 saves 24.5% fuel per passenger during the mission under consideration.

$$SAR = \frac{V_{cr}}{[C_{D_0} + k(\frac{W_{cr}}{q_{cr}S})^2]q_{cr}SC_T} \tag{1.1}$$

Table 1.10: Resulting trip fuel consumption for the EcoHopper 450 and the B737-MAX 8.

Parameter	LTO cycle [kg]	Climb [kg]	Cruise [kg]	Total [kg]	Total [kg/pax]
EcoHopper 450	288.2	1,643.5	4,539.3	6,471.0	14.4
B737-MAX 8	365.9	1,213.6	2,230.5	3,810.0	19.1

Emissions

The emissions of the aircraft could be found using the fuel flow, time in mode and thrust setting (TS) in mode, in combination with the emission factor. The emission factor indicates the amount of substance emitted per kg of fuel burnt. The emissions considered were H_2O, CO_2, N_2O, NO_x, non methane volatile organic compounds (NMVOC), CO and hydrocarbons (HC). As the EcoHopper 450 possesses an electric taxiing system and no APU, the emissions for the LTO cycle

were significantly reduced compared to the current state of the art (B737-MAX 8). The computed emissions for the LTO cycle and cruise can be found in Table 1.11 and Table 1.12 respectively. The large reduction in NO_x emissions resulted from the fact that the engines of the EcoHopper 450 operate at a low combustion chamber inlet temperature which reduces the amount of NO_x emitted significantly. The reduction in fuel consumption and emissions during cruise is less compared to the LTO cycle. This is because the EcoHopper 450 employed some novel systems during the LTO cycle while during cruise the operation can be compared to the B737-MAX 8.

Table 1.11: Resulting emissions for the nominal LTO cylce.

Aircraft	Fuel	H_2O	CO_2	SO_2	N_2O	NO_x	NMVOC	CO	HC
EcoHopper 450 [kg]	288.22	356.55	907.94	0.29	$2.88x10^{-2}$	3.66	2.14	1.84	$1.15x10^{-2}$
B737-MAX 8 [kg]	365.88	452.59	1,152.54	0.37	$3.65x10^{-2}$	5.07	2.72	2.34	$1.46x10^{-2}$
Reduction	21.2%	21.2%	21.2%	21.2%	21.2%	27.7%	21.2%	21.2%	21.2%

Table 1.12: Resulting emissions for cruise of the EcoHopper 450 and the B737-MAX 8.

Aircraft	H_2O	CO_2	SO_2	N_2O	NO_x	NMVOC	CO	HC
EcoHopper 450[kg/km]	5.39	13.73	$4.36x10^{-3}$	$4.36x10^{-4}$	$3.29x10^{-2}$	$3.05x10^{-3}$	$2.18x10^{-2}$	$1.74x10^{-4}$
Cruise of 1,000 km [kg/pax]	11.98	30.52	$9.69x10^{-3}$	$9.69x10^{-4}$	$7.32x10^{-2}$	$6.78x10^{-3}$	$4.84x10^{-2}$	$3.88x10^{-4}$
B737-MAX 8 [kg/km]	2.67	6.80	$2.16x10^{-3}$	$2.16x10^{-4}$	$2.34x10^{-2}$	$1.51x10^{-3}$	$1.08x10^{-2}$	$8.64x10^{-5}$
Cruise of 1,000 km [kg/pax]	13.36	34.02	$1.08x10^{-2}$	$1.08x10^{-3}$	0.12	$7.56x10^{-3}$	$5.40x10^{-2}$	$4.32x10^{-4}$
Reduction	10.3%	10.3%	10.3%	10.3%	37.5%	10.3%	10.3%	10.3%

Next, the impact of the emissions could be determined using the radiative forcing (RF). RF is a measure for the change in energy the Earth receives from the Sun, and the energy that the Earth radiates back into space [8]. The RF is thus expressed in watts per square meter (W/m^2). The radiative forcing also takes contrails and cirrus clouds into account. Using the cruise altitude of the EcoHopper 450 and the B737-MAX 8, it was found that the RF of the first was 69.2 W/m^2 and 87.7 W/m^2 for the latter. Therefore, it yielded a reduction of 21.1% in the RF for the EcoHopper 450.

Noise

As requirements were imposed on the noise output of the aircraft, it was also analysed. The requirements stated that the cumulative noise of the aircraft at the ICAO measurement points shall be a maximum of 282 dB, and the aircraft shall be one noise class better than current state of the art aircraft, e.g. B737-MAX 8. The ICAO measurement points are listed below:

1. **Approach**: 6.5 km before the runway threshold, 120 m under the flight path (overhead).
2. **Sideline**: the highest noise measurement recorded at any point 450 m from the runway axis during take-off.
3. **Fly-over**: 6.5 km from the brake release point, 1,000 ft (300 m) under the take-off flight path (overhead).

It was chosen to model the aircraft's noise in two ways: first the airframe noise produced by the airflow encountering irregularities on the surface of the aircraft, and secondly the engine noise produced by the fan of the ultra-high bypass engine. The model used to compute the noise is NASA's Aircraft Noise Prediction Program (ANOPP). It is a semi-emperical method based on databases containing measured acoustic data [12]. Only the components which contribute the most to the airframe noise were modelled, these included the clean wing, the horizontal tail, the slats and flaps and the landing gears [12][pg. 189]. It was found that the airframe noise is the highest during approach as the landing gears are extended and the flaps are fully extended. The sound pressure level (SPL) of the airframe during approach can be seen in Figure 1.2, it shows the contribution of the different noise components as well as the total noise output.

To model the engine noise, it was chosen to only model the fan noise as the other components like the turbine and jet required detailed inputs. This was justified by the fact that the main contributors to the engine noise are the fan and the jet exhaust, and as the bypass ratio of the engine is high the fan noise overrules the jet noise [13]. Also for the fan noise NASA's ANOPP model was used. It was however found that there is a cut-off in the fan model for frequencies lower than 1 kHz due to the uncertainty of the empirical data at lower frequencies [11]. Therefore, in order to compute the cumulative noise, the fan noise below 1 kHz was assumed to be equal to the airframe noise instead of the modelled noise. To give an indication of the order of magnitude of the engine noise, the fan noise during approach is visualised in Figure 1.3.

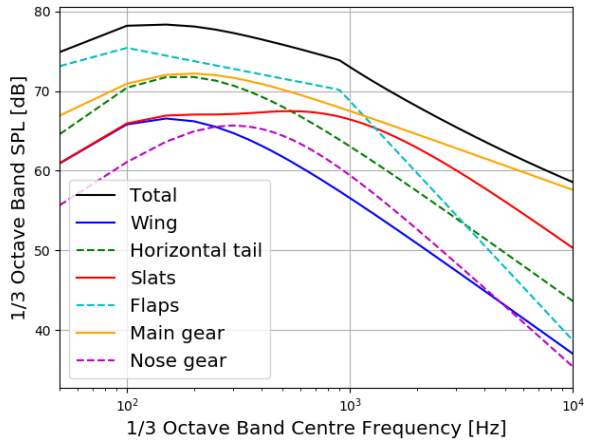

Figure 1.2: Airframe noise at the approach measurement point for the EcoHopper 450.

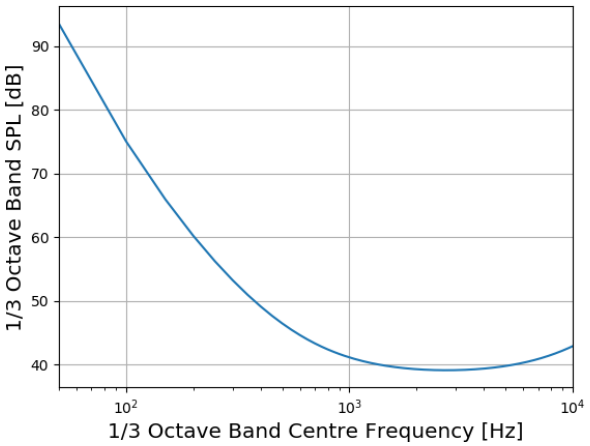

Figure 1.3: Fan noise at the approach measurement point for the EcoHopper 450.

Finally, in order to assess the overall noise output of the aircraft, it was chosen to convert the SPL to the A-weighted SPL. This means that an A-type filter was used to filter the decibel levels. The filter takes into account the loudness and thus the level of annoyance of the noise. The cumulative A-weighted noise was computed for the ICAO measurement points mentioned above for the EcoHopper 450 as well as for the B737-MAX 8. The results are shown in Table 1.13. As can be seen, the aircraft produces significant less noise than the B737-MAX 8 during take-off. This is because the engine is a geared turbofan, the gearbox ensures that the fan spins slower and thus creates less noise. In combination with the acoustic liners in the fan inlet duct, the overall noise reduction of these technologies was estimated to be 5-7 dB [14]. Even though the approach noise is higher than the reference aircraft (since the aircraft has larger gears and flaps), the total noise of the aircraft is lower than the 282 dB specified by the requirement BIB-SYS-FLP-03. The cumulative noise is in total 5.4 dBA less than the B737-MAX 8 and 56% less per passenger.

Table 1.13: Final modelled A-weighted SPL for the EcoHopper 450 and B737-MAX 8 at the measurement points.

Parameter	Approach	Sideline	Fly-over	Total	Total per pax
EcoHopper 450 A-weighted SPL [dBA]	89.6	81.8	85.4	256.8	0.57
B737-MAX 8 A-weighted SPL [dBA]	88.1	87.9	86.2	262.2	1.3

1.9 Operational Analysis

An operational analysis was performed to gain insight into differences in operation with respect to conventional aircraft. Following an analysis of projected turnaround time based on regression to both narrow-body and wide-body aircraft the turnaround times for different scenario's were determined. It was determined that a minimum of three doors must be used during boarding to achieve the turnaround top-level requirement. Following a description of ground handling, a RAMS analysis was performed. The RAMS shows that aircraft operation time and CS-25 requirements are adhered to, even with the unconventional design. The ground operations description primarily focused on the effect of electric taxiing. Taxi speeds and steering methods were laid out, along with the effect of push-back autonomy and engine start-up effects, since the engines are not started until the aircraft arrives on the runway.

1.10 Financial Analysis

The aircraft price has been estimated by combining a bottom-up approach of NASA, an engine cost estimation by Kroo and a non-recurring cost estimation by RAND. Some of formulae of the bottom-up have been changed according to specific design features. The relations to estimate the wing, fuselage, hydraulic system, flight controls, furnishings, electrical system, air-conditioning system and anti-ice system have been adjusted. The resulting cost-breakdown is shown in Table 1.14. The aircraft price of the Ecohopper 450 per passenger is slightly lower than that of the B737-MAX 8, namely 7%. The engine costs are relatively low, while the airframe costs are quite high. Over a time span of 19 years, until 2038, the return on investment has been estimated to be 8.8% per year.

Table 1.14: Costs estimation of the EcoHopper 450 per subsystem in 2019 million dollars.

Aircraft Component	Weight / Costs Estimation Method	Cost Estimation	B737 MAX-8 Cost Estimation
Wing	Class II, NASA	19.14	7.88
Fuselage	Class II, NASA	28.40	10.77
Tail	Class II, NASA	3.05	1.44
Landing Gear	Class II, NASA	4.26	1.55
Nacelle	Class II, NASA	6.45	2.44
Flight Control	NASA, NASA	2.81	1.30
Hydraulics	NASA, NASA	0.45	0.19
Electrical System	NASA, NASA	8.25	3.02
Air-conditioning	NASA, NASA	6.37	2.30
Anti-ice System	NASA, NASA	0.78	0.33
Furniture + Interior	NASA, NASA	24.59	11.74
Engine + fuel Systems	NASA, NASA	1.10	1.45
Avionics	NASA, NASA	1.67	0.90
APU	-, NASA	0	1.42
Pneumatic system	-, NASA	0	0.81
Assembly	NASA, NASA	28.81	13.41
Engine	Class II, Kroo	59.92	34.85
Recurring Costs	-	201.0	100.3
Engineering	RAND	5.37	0.19
Tooling	RAND	3.79	0.01
Flight test	RAND	0.33	0.19
Development Support	RAND	1.28	0.03
Non-Recurring Costs	RAND	10.78	0.42
Profit	-	42.53	20.27
Total	-	254.2	121.6
Total per pax	-	0.565	0.608

The direct operating costs (DOC) are calculated using an approach of the Air Transport Association of America (ATA). The components of the direct operating costs and its values are shown in Table 1.15. The DOC per passenger of the EcoHopper 450 is 14% lower than that of the B737-MAX 8. The costs of the depreciation, insurances, interest are relatively high due to the expensive aircraft and low flight speed. Also the cabin crew is relatively expensive due to the low flight speed. However, the flight crew and navigation and landing fees are relatively cheap due to scaling profits. The maintenance and fuel costs contribute the most to the reduction in costs. The maintenance is cheaper due to the relatively cheap engines and low flight speed, while the fuel costs is low due to the low fuel consumption. The return on investment of an airliner has been estimated to be 23.4 million dollars each year above the interest rate.

Table 1.15: Cost estimation of every component of the direct operating costs, presented in 2019 dollars.

Component	EcoHopper 450 [$]	B737-MAX 8 [$]
Depreciation	5,777	2,288
Insurance	348	133
Interest	3745	1,617
Flight Crew	1855	1,605
Cabin Crew	2321	919
Navigation and Landing Fees	1,556	1,080
Maintenance	8,445	4522
Fuel	9,425	5247
Total	33,473	17,410
Total per Block Hour	14,463	8447
Total per pax	74.4	87.1
Total per pax per Block Hour	32.1	42.2

2 Introduction

Since the beginning of commercial aviation the market has grown exponentially. This growth is expected to continue in the coming decades. Many parties around the world are worried about the ever growing aviation industry. Especially the impact on the climate, air quality and noise generation are controversial. It has been known for a while that it is not possible to continue business operations in the current fashion. In 2005 the mass of CO_2 in the atmosphere was already 800 Mt, this is expected to increase significantly if no further actions are taken [15]. There are several solutions to reduce the net CO_2 emission and thus reduce the environmental impact. For example consider the implementation of available technologies, optimisation of operations, improving the infrastructure, innovative technologies like biofuels, and economic measures [15]. Some measures seem realistic while others are out of reach. Promising technologies can still take up 30-40 years to mature.

It is simply not possible to wait for those technologies to develop since the aviation industry keeps growing in the mean time. Readily available short term solutions might be a welcome first start. One possible solution is to look at what can be improved in the aircraft design to make aircraft more sustainable. From a study performed in 2010 by Zeinali and Rutherford it was found that the average usage of aircraft is far from the available limits of payload-range combinations [15]. Most aircraft used nowadays are designed for a relatively large range, such that the aircraft could be used for many different mission and offers flexibility. However, this means that most aircraft are used well below their optimised design range, so they are overpowered and overweight for the missions they are performing [15]. To optimise the current aircraft design, the aircraft should be designed for the actual operating conditions. This leads to a high capacity short range aircraft. Some new readily available technology could also be implemented in this new state of the art aircraft in order to make the aviation industry more sustainable.

The goal of this project is therefore to design a state of the art high capacity (450 passengers) short range aircraft. This aircraft should comply with some top-level requirements driving the sustainability of the design, like noise and fuel consumption. The top-level requirements provided by the client are listed below. Next to improving the aircraft itself, attention can be placed on the flight procedures to optimise the operations.

- **BIB-SYS-TEC-03**: The aircraft shall accommodate 450 passengers in a single class configuration.
- **BIB-SBS-OPS-04:** The cargo hold of the aircraft shall accommodate cargo containers of standard dimensions.
- **BIB-SYS-MKO-01:** The range of the aircraft shall be between 1,000-2,500 km.
- **BIB-SYS-TEC-02:** The cruise profile of the aircraft shall be optimised for climate optimised flights.
- **BIB-SYS-TEC-06:** The aircraft shall be able to operate from all major European airports.
- **BIB-SYS-TEC-09:** The noise produced by the aircraft shall be at least one noise class better than current state of the art aircraft.
- **BIB-SYS-SDL-01:** The operational costs of the aircraft shall be 10% less than current state of the art aircraft.
- **BIB-SYS-TEC-08:** The aircraft shall have 10% reduced fuel consumption per passenger with respect to current state of the art.
- **BIB-SYS-TEC-01:** The aircraft shall be propelled by either jet or propeller driven propulsion.
- **BIB-SYS-TEC-05:** The aircraft shall have a turnaround time of at most 45 minutes.

This is the final progress report provided by the DSE group Bigger is Better. It contains the detailed design of the design concept chosen in the Midterm report [1]. The analyses performed in that report were expanded to analyse and size the design in more detail. The requirements set out in the Baseline report [8] were used as guidelines for the design choices. Finally, the results of the analyses were used to show compliance with the requirements.

First, an overview of the project logic and sequence is given in chapter 3 in order to gain insight in the project. Then the functional analysis is performed in chapter 4 before moving on to the market analysis in chapter 5. Next, an overview of the design is given in chapter 6. Then the aircraft's propulsion system is described in chapter 7. Next, the detailed analysis of different aspects of the aircraft are shown. The aerodynamic analysis is shown in chapter 8 while the stability and control of the aircraft was assessed in chapter 9. Then the structural design is determined in chapter 10, before moving on the the aircraft systems in chapter 11. After which the aircraft's operations and performance could be assessed in chapter 12 and chapter 13. In order to show compliance with the requirements, sustainability analyses were performed in chapter 14, chapter 15 and chapter 16. Then the financial aspect of the aircraft was investigated to assess the feasibility of the project, see chapter 17. This would then lead to the compliance of the requirements in chapter 20.

3 Project logic

A lot has to be done before the presented design in this report may actually be build. Everything that has to be done before the production phase will start will be described in this chapter. First of all the design is far from finalised and a lot more engineering and other research has to be done, this will be described in section 3.1. When all of the analysis and sizing is performed, the detailed design may start. The detailed design in this context refers to sizing all the 'nuts and bolts' and making a production plan, as described in section 3.2. Once the design is finalised, it has to be tested and certified, as described in section 3.3, before the aircraft will be build and sold as explained in section 3.4. The project Gantt chart is shown in Appendix E.

3.1 Finalising the preliminary design

As the design is for from finalised, a planning of the future design phase has to be made. As described by Anderson [6], the design of an aircraft generally consists of three phases: The conceptual design, the preliminary design and the detailed design. The conceptual design has already been performed in the midterm report [1]. The preliminary design has been started with in the current report. The preliminary design is far from finalised since a lot of parameters of the aircraft may still change and sizing of almost every subsystem is not detailed enough. The tasks that have to be done will be described in this section. The preliminary design ends when the 'frozen' design is made, no changes could be made to the design anymore and all analysis have been performed. The crucial point of the phase is the decision of the manufacturer, to commit or not? If the manufacturer commits to the design, the detailed design could begin.

Further designing analysis is required for the so-called departments. A class III estimation has to be made before even more detailed analysis could start. For the first department, the structures department, more detailed analysis and sizing has to be performed on the structural design of the strut, wing, fuselage, tail and also all other elements that experience loads while operating the aircraft. A general approach on how to produce the aircraft and join certain materials to each other has to be made. For the aerodynamics department, a computational fluid dynamics calculation has to be done for the entire aircraft experiencing different conditions. The aerodynamic performance during take-off, landing and cruise has to be thoroughly analysed for all occurring environmental conditions. Besides, many wind-tunnel test should be performed to measure the practical behaviour of for example the airfoil. The high-lift device and control surface performance should also be thoroughly analysed. The performance department should finalise all of the performance characteristic in detail, for example the fuel consumption, noise runway length etc. A detailed flight envelope should be created for different mission ranges, environmental conditions and cost indexes. The propulsion department should have finalised the engine design and its performance under all possible conditions and already have contact with a possible manufacturer. Finally, all system should be sized in more detail and analyses have to be performed on the actual performance under all possible conditions.

The subsystems designed in this phase should be verified to ensure they meet the requirements they have to fulfil. The verification may be done by means of inspection, analysis, demonstration or testing, depending on the subsystem that has to be verified. All requirements should be checked on their compliance and another risk analysis regarding these requirements should be made.

Besides the further analysis and design of the technical departments, the operational life of the aircraft should be elaborated upon. An approach for the ground handling should be made, including the turnaround procedure, the storage of the aircraft and the maintenance. Since the aircraft differs to other existing commercial aircraft, the operational procedures might differ. The approach should comply with existing airports and the feasibility of the operations should be discussed. When airports have to make adjustments to their infrastructure, the process of it should be discussed too. The costs of these operations should also be finalised.

Communication should also be present with possible customers (airliners) of the aircraft, as the customers may have specific wishes and requirements, which have to be incorporated. The design could be changed slightly at the current stage in order to meet these requirements. Extra features may also be added according to the customer's demands. When contact has been established with with the customers, a better estimation on the batch size can be made. The return on investment may also be revised, and depending on the outcome, the costs of the production has to be either limited or if possible to grow. Lobbying for possible investors of the project should also be done during this stage.

Because the aircraft needs to be certified to be able to fly, research has to be performed on this area and the FAA and EASA, the organisations that decide on these licences, should be involved with the entire design. Due to design innovations such as the two compartment double decker, specific regulations may be set for the EcoHopper 450. The extra regulations has to be known beforehand such that design changes can still be made.

The entire duration of this phase is estimated to be three years and will therefore end in 2022. The class III weight estimation should be made in the first year. Also, communication with the airports, the manufacturers and the customers has to be set in the first year. Once the contacts are established and the class III estimation is performed, the final preliminary design can be made. The design and verification of certain subsystems will probably overlap. However, towards the end, relatively more verification will be performed. The communication with other parties will be maintained throughout the entire design phase.

3.2 Detailed design

In the current report and previous reports [1], [8], the term 'detailed design' has been used for different purposes. However, in this chapter, the detailed design refers to finalising the design so it can be produced by the manufacturer. This definition is also used by Anderson [6]. The end of the preliminary design results in a 'frozen design', meaning that no further changes can be made to the design. During the detailed design the 'nuts and bolts' will be designed. All of the ribs, spars, stiffeners and skin sections will be sized. The number of, size and placement of the fasteners, including rivets, bolts and welding bonds, are determined. The manufacturing tools and jigs are also designed during this phase in order to realise the production of the aircraft. The detailed design results in a finalised production plan. Special attention must be paid to producing the strut of the wing. During the detailed design, a simulation of the actual aircraft is made to verify the analysis made in the preliminary design phase. Orders by customers are set and investments are secured such that the program is financially feasable. The entire duration of the detailed design is assumed to be three years. The detailed design phase will thus end in 2025.

3.3 Testing and licensing

Once the complete production plan is set, the first test aircraft can be build. This aircraft will be tested on various performance parameters and tested for specific capabilities. When the design team, the customer or the airport feels like changes should be made, minor changes on the design can be performed. During this phase, the certification from the FAA should be received such that the production phase can be started. The duration of this phase is assumed to be two years. One year of safety margin is planned for the design and testing phases. So the production phase can start in 2028.

3.4 Production

When the certification is obtained, the production can actually start. The production phase is estimated to start in 2028. From the market analysis performed at this stage, a total of 500 ordered aircraft is estimated. When 50 aircraft can be produced each year, the entire production phase would last for ten years. The production plan is highly focused on sustainability and is described in section 18.2. Once the aircraft have been sold, profit will be made and investors will earn back investments.

4 Functional analysis

This chapter describes the functional analysis performed on the product; the aircraft. Section 4.1 describes the functional flow diagram while section 4.2 elaborates on the functional breakdown structure. The analysis was performed in order to gain insight into the functions that the aircraft subsystems have to perform. This chapter provides an overview of the functions of the entire aircraft while the functions for the different subsystems are discussed in their respective chapters.

4.1 Functional flow

The functional flow diagram (FFD) shows all the functions the aircraft has to perform in a time-sequenced manner. Each block represents a function that will be performed. Actions that are performed in parallel are indicated by an AND gate while optional actions are indicated by an OR gate [15]. In addition, a FFD could also contain higher levels which indicate how the product or aircraft interacts with its environment. The FFD for this system is shown in Appendix B.

The first level of the flow diagram consists of five main blocks. They represent the main steps in the life cycle of an aircraft. It starts of with designing the aircraft, followed by the manufacturing and operating phase. Next, the maintenance of the aircraft has been incorporated into the life cycle and refers back to the operating block since it can be performed throughout the operating life of the aircraft. Finally, once the aircraft has reached its maximum life time the final block referring to the end of life operations is executed. It was chosen to not only show the operating block but also the higher levels of the life cycle since more requirements could be derived from these functional flows. A small description of each main block is given below.

1. **Design the aircraft**: this block simply covers the entire design process described in the previous report the Project Plan [16]. In that report the flow diagram for this main block is presented.
2. **Manufacture the aircraft**: it starts with sublevels representing the manufacturing of main components of the aircraft. Each of these sublevels are again divided in the main tasks needed for manufacturing. All of the manufacturing subtasks can be performed in parallel and are therefore connected through an AND gate. Next, all the components are collected and assembled in an assembly line until the aircraft is ready for certification. Finally the aircraft has to be painted and delivered to the client.
3. **Operate the aircraft**: this main block can be easily divided into the main phases of operating an aircraft from an airport. The sublevels consist of performing pre-flight operations, the mission and post-flight procedures. The operations from loading the aircraft with passengers and cargo until the shutdown procedure after landing are described in the FFD. In addition, the emergency actions regarding an aborted take-off or landing, a go-around and diverting to an alternative airport have also been included to ensure that all critical operational conditions are accounted for.
4. **Perform maintenance**: as explained before, this block can be executed throughout the lifetime of an aircraft. In the FFD this can be seen in the sublevel of this block which references back to the operating block. The maintenance is divided in performing the aircraft maintenance checks and performing unexpected repairs. The first type of maintenance represents the checks done after a certain amount of operating hours. These checks have been established by the FAA. In addition, it has to be checked whether the aircraft reached its maximum lifetime. If so, the aircraft enters the final block of the flow diagram. The latter type of maintenance represents the unexpected repairs needed to keep the aircraft operational. This type of maintenance will lead to delays and possibly the cancellations of flights.
5. **Perform end of life procedure**: this final block of the flow diagram describes what happens to the aircraft after it has reached its maximum life time. In this procedure the aircraft will be set apart from existing operational aircraft. Nowadays, most aircraft which are retired are not used to their full extent being stored at some abandoned place, like the aircraft graveyards in the desert of the US. This aircraft, however, will be used to its full extend to also remain sustainable after it has retired. The components of the aircraft will be reused for maintenance or will be recycled for the production of new aircraft.

4.2 Functional breakdown

The functional breakdown structure (FBS) represents the functions of the system using a hierarchically organised structure. In contrary to the FFD it is not a time-sequenced structure but rather an AND tree. It can be used to have different views on the functions in order to identify which functions rely on eachother [15]. The FBS typically goes one level deeper than the FFD. The breakdown structure has been divided into the main blocks described earlier. The breakdown structure can be found in Appendix C.

5 Market analysis

Currently, the majority of airline routes are flown using aircraft that are vastly overdesigned for the range they are used for. By lowering the design range fuel efficiency can be increased, which in turn lowers operational costs, thus increasing potential profits. On the other hand, lowering the maximum range decreases the operational capability of the aircraft as the aircraft isn't capable of performing certain missions. In order to reach a compromise regarding this matter, a market analysis was performed and previously presented in the Baseline Report [8], and will be shortly summarised here.

5.1 Current market

Following the market analysis performed in the baseline report a design range of 1400 km was chosen. This range was based on the cumulative daily return flights for a given maximum range, based on the amount of passengers travelling a certain distance between two airports as presented in Figure 5.1. It was determined a cumulative passenger serviceability of around 70% would be sufficient, especially when considering that the aircraft will become overdesigned when designing for a longer range than that of the broadest part of the market: around 1000 km. A decrease in the cumulative passengers to design range slope is noted at around the 1400 km point, further decreasing the value of designing beyond this range.

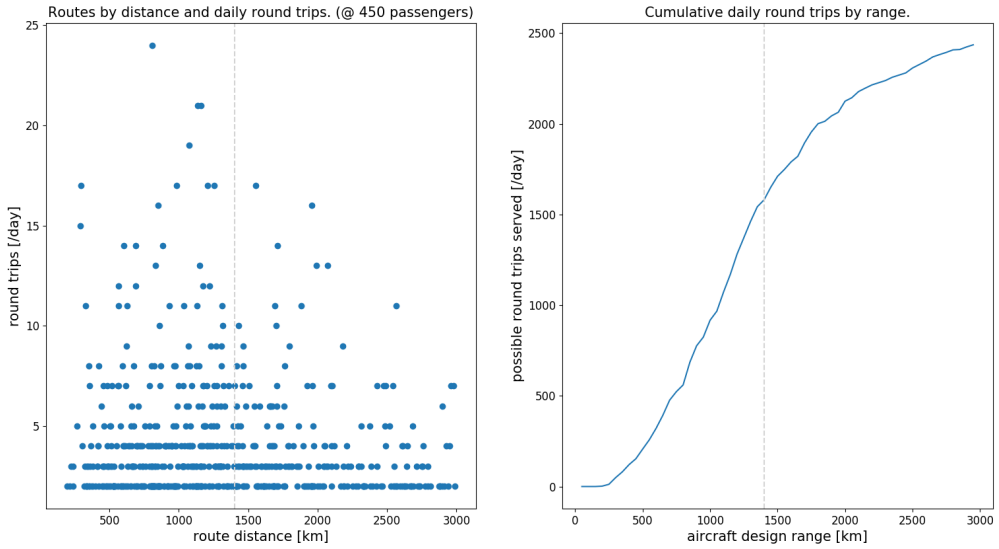

Figure 5.1: Daily Asian commercial aviation market. (retrieved 05/05/19 and 06/05/19)

From this analysis an estimate of the total market for the EcoHopper 450 follows. Below the chosen design range of 1400 km, a total of around 1500 daily return flights are performed. Assuming a market penetration of 50% and a daily operation of three return flights per aircraft, an estimate of around 250 potentially marketable aircraft is obtained. A market penetration of 50% is determined to be a reasonable estimate given the per passenger cost reduction to be presented in chapter 17. It is left up to the airline to employ the aircraft properly and attain a high aircraft operating time.

5.2 Future market

As noted in the baseline report [8], a growth in the commercial aviation sector has been noted to lie, conservatively, in the 6% range for the past decades and can be expected to keep growing as such in the future due to emerging markets and a growth of the middle-class in industrialising countries. Furthermore, as the analysis has primarily been performed for the Asian market, sustained growth could make the aircraft viable in other markets in coming decades. Especially the European market, which currently features too few high-volume routes to support the aircraft adequately, could become a secondary market in the future due to its small geographic scale, similar to that of (Southeast) Asia. Assuming a competitive service life of around 27 years, a future market at least as large as the current market is expected. Another 250 aircraft can reasonably be expected to be sold in the future, bringing the total expected aircraft market over the entire service life of the aircraft to lie around the 500 mark. This is further supported by annual orders and deliveries reports by Boeing and Airbus, showing a sustained interest in designed aircraft up to two decennia after the initial introduction date.[1]

[1]Boeing. Orders & Deliveries. Retrieved June 24, 2019, http://www.boeing.com/commercial/#/orders-deliveries

6 Design Overview

The EcoHopper 450 is a short range high capacity aircraft. 450 passengers can be transported in a single class configuration with a design range of 1,400 km. The goal of this design was to supply in areas of high demand for short range flights with sustainability and cutting down emissions in mind. By keeping the maximum range of the aircraft to a minimum a significant weight reduction was made. This weight reduction directly influenced the fuel consumption in a positive way. To improve further in sustainability the decision was made to fly at a lower altitude and at lower Mach numbers. This presented the opportunity to fly with an unswept wing increasing aerodynamic efficiency. Flying at a lower altitude also has the advantage of a reduction in the radiative forcing of aircraft emissions. A strutted design is presented which supports the wing, this gives the opportunity to increase the slenderness or aspect ratio of the wing, which again contributed to the aerodynamic efficiency. This design shows a decrease in fuel consumption of 14.3% and a decrease in radiative forcing of 21.1% with respect to the highly efficient B737-MAX 8. Next to emissions and fuel consumption the EcoHopper 450 has improved noise emissions with respect to the current state of the art. In Table 6.1 the specifications of the aircraft can be seen, a comparison is made with the B737-MAX 8 and the B747-8 which are the current standard for short range low capacity flights and long range high capacity flights respectively. In Figure 6.1 an overlay diagram of the comparing the EcoHopper to B737-MAX 8, B747-8 and to the A380-800. A top front and side view is shown in Figure 6.2.

The overall layout of the aircraft is further explained in this chapter. First, the design process is described in section 6.1. Then the weight breakdown resulting from this design process is explained in section 6.2. Next, the designs of the main components of the aircraft are explained. The fuselage design is elaborated on in section 6.3.

Table 6.1: Design overview of the EcoHopper 450 in comparison to the B737-MAX 8 and B747-8.

Parameter	EH450	B737-MAX 8	B747-8
Maximum seating [pax]	450	200	605
Length [m]	49.3	39.5	76.3
Height [m]	19.4	12.5	19.4
Wing Span [m]	52.0	35.9	78.4
Aspect ratio [-]	13	10.2	8.5
MTOW [kg]	152,600	82,000	448,000
OEW [kg]	87,000	45,000	220,000
Fuel capacity [kg]	17,400	20,730	190,000
Range [km]	1,400	6,570	14,320
Cruise altitude [m]	9,000	11,000	11,000
Cruise Mach [-]	0.72	0.79	0.85
Cruise speed [m/s]	218	233	259
Take-off Runway Length [m]	2,548	2,500	3,100

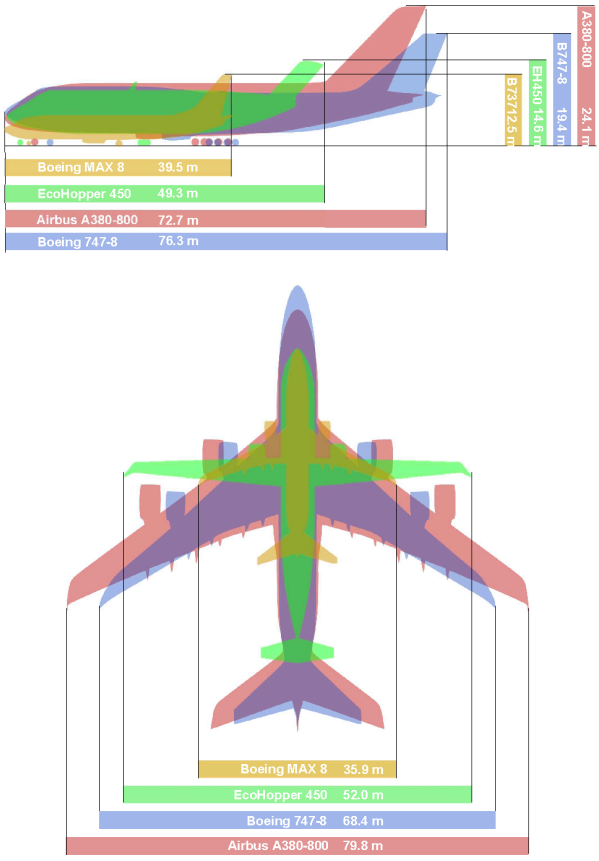

Figure 6.1: Overlay diagram comparing the EcoHopper 450 with existing aircraft models.

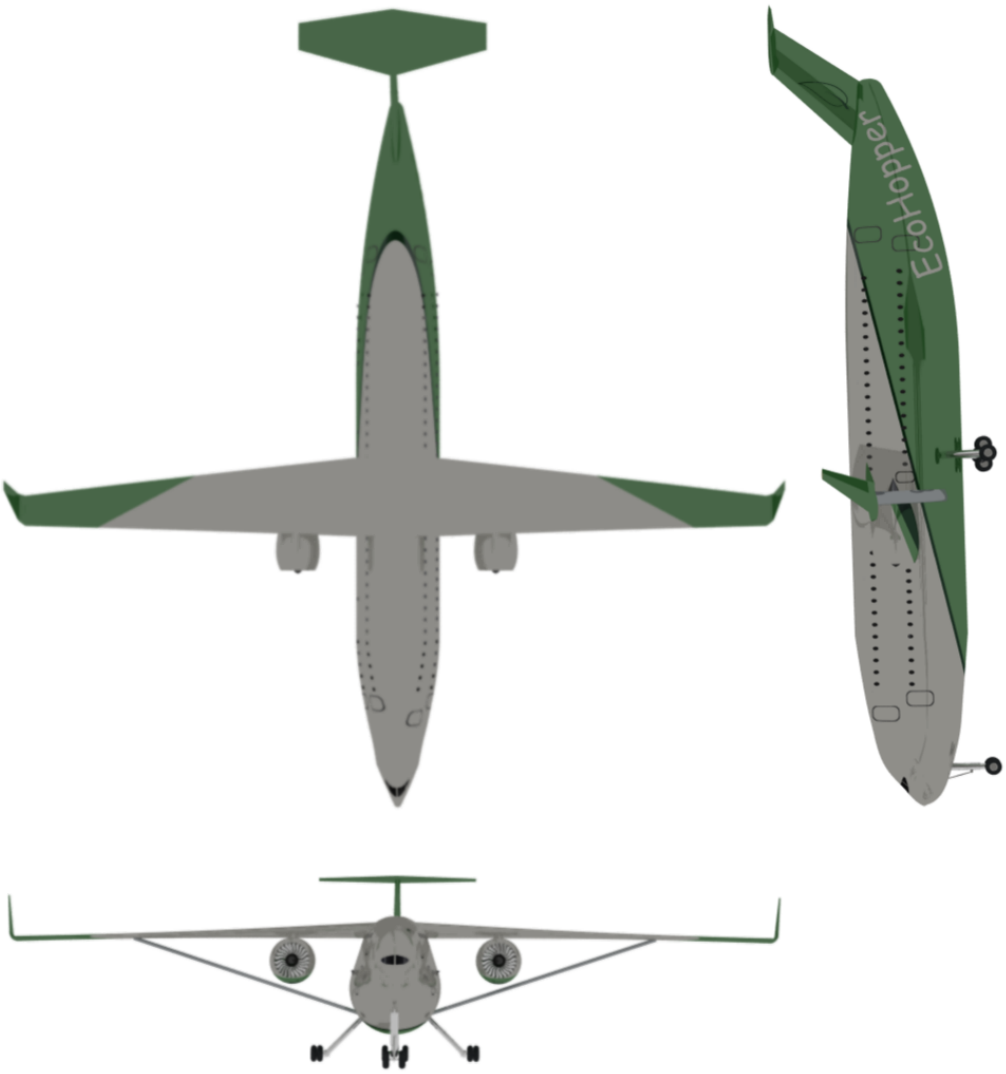

Figure 6.2: A top, front and side view of the EcoHopper 450.

6.1 Design process

Multiple tools were created to come up with the detailed design of the EcoHopper 450. The initial sizing of of the aircraft was done through Class I and II weight estimations methods proposed by Roskam [17]. It consisted of an iterative process between the two weight estimations. This iterative process is shortly discussed below, details on this process can be found in the Midterm report [1].

The first step in the iterative process was to conduct a Class I weight estimation. This analysis provided the initial take-off, payload, fuel and empty weight of the aircraft based on initial estimates from reference aircraft. Next, based on these weights and other data from theory a thrust loading versus wing loading diagram was made in order to determine feasible design points. Chosen design points were then used together with the weights computed in the Class I weight estimation to come up with an initial sizing of the major components of the aircraft such as the wing, fuselage and empennage. Next, the aerodynamic sizing was performed to compute the initial aerodynamic coefficients like the induced drag and zero-lift drag. This was done using the aerodynamic analysis program AVL. The major inputs to the AVL program were obtained from the initial sizing of the aircraft's components. Afterwards, the results from the initial component sizing and the aerodynamic analysis served as inputs to the Class II weight estimation. The Class II weight estimation determines the weight of the main aircraft components. This was used to determine a better estimate of the aircraft's empty weight.

The goal was to obtain a difference of less than 1% between the empty weights estimated by the Class I and Class II weight estimation methods. If the empty weights differ less, the approximation of the fuel weight will be more accurate as well since it is based on the final empty weight of the aircraft. Whenever this requirement was satisfied, the program was said to be converged to the most accurate design values. The final block, cruise condition optimisation, used the values of the last iteration as input to determine the optimal cruise altitude and speed to comply with requirements on fuel consumption, costs and sustainability.

Once the values were obtained from the iterative process, they were used as base inputs for the further detailed design tools. The detailed design tools included a propulsion system analysis, an aerodynamic analysis, a structural analysis and finally a control & stability analysis. The values from the iterative process were then updated according to the results from the detailed analyses. This finally resulted in the design presented in this chapter. The different detailed design analyses are explained in the following chapters: the propulsion analysis in chapter 7, the aerodynamic analysis in chapter 8, structural analysis in chapter 10, and control & stability analysis in chapter 9. The aircraft systems used in the design of the EcoHoppr 450 were analysed as well, which is explained in chapter 11. The resulting design of these analyses was then assessed for its performance (chapter 13), operations (chapter 12), emissions (chapter 15) and noise (chapter 16). The overall design layout of the EcoHopper 450 is summarised in this chapter.

6.2 Weight breakdown

Using the iterative process described in section 6.1 a Class II weight was performed. A weight estimation per component or component group is made based on the aircraft geometry. A detailed description of the Class II weight estimation can be found in the mid term report [1]. Table 6.2 shows an overview of all weight components of the EcoHopper 450 and Figure 6.3 shows the percentual division of the total weight.

Table 6.2: Weight breakdown of the EcoHopper 450.

Weight	Value
W_{TO} [N]	1,497,151.2
W_F [N]	170,548.2
W_{PL} [N]	472,485.2
W_E [N]	854,117.8
W_{fus} [N]	261,471.0
W_{emp} [N]	17,175.5
W_{wing} [N]	139,715.8
W_{nac} [N]	25,479.8
W_{lg} [N]	37,408.5
$W_{prop,sys}$ [N]	76,512.3
$W_{fix,ep}$ [N]	291,003.0

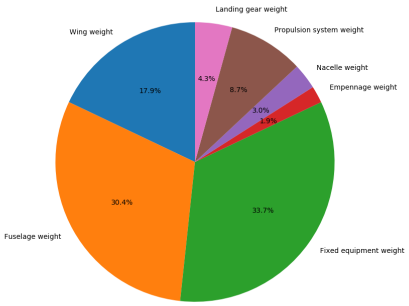

Figure 6.3: Weight breakdown of the EcoHopper 450.

6.3 Fuselage Design

The following section goes over the fuselage layout, how this was designed and presents the selected layout. During the fuselage design process four different fuselages were considered:

- Single floor fuselage
- Double decker fuselage
- Semi double decker fuselage
- Double decker with two upper floor compartments.

The main considerations for the fuselage design were the length and wetted area relating to aerodynamic performance. The length of the fuselage had influence on the tail sizing, a longer fuselage meant a longer tail arm and in turn a smaller tail. The other consideration is the wetted area which is mainly determined by the cross sectional area and the fuselage length. Here a shorter length and tightly packed fuselage is ideal, since these result in a low wetted area leading to low zero lift drag and thus increasing aerodynamic performance. From the analysis tool developed in the mid-term phase each of the fuselages was checked, it turned out that the double floor concepts performed significantly better although the empennage weight would be heavier than for the single floor concept. It turned out that the aerodynamic performance was driving in the fuselage design process. Based on this the double decker with two upper floor compartments was selected. This design allows the wingbox to pass trough the upper floor compartment, in turn not adding a fairing on top of the fuselage thus keeping the zero lift drag to a minimum while still having a two floor design to keep the fuselage length to a a minimum. Due to the high aspect ratio of the wing, the root chord is relatively small, keeping the space lost by the wingbox to a minimum. In Table 6.3 an overview of the important fuselage parameters can be seen. In the following sections the sizing and design of the cross-section and fuselage layout will be elaborated on.

Table 6.3: Important outputs from the fuselage design.

Parameter	Value
w_{Fus} [m]	5.95
h_{Fus} [m]	7.64
$w_{floor,1}$ [m]	5.55
$w_{floor,2}$ [m]	4.01
$w_{floor,cargo}$ [m]	3.50
$l_{fuselage}$ [m]	48.62
l_{cabin} [m]	35.12
$l_{tailcone}$ [m]	7.75
$l_{nosecone}$ [m]	13.80

6.3.1 Fuselage cross section

The fuselage cross section was selected to be a double bubble fuselage. This to save space and optimise for the wetted area. The connection between the two bubbles is made on the upper floor, stresses will be present at the intersection between the bubbles, the floor serves as loadpath for this and will be loaded in tension. In Table 6.5 a drawing of the fuselage cross section can be seen.

The seating configuration selected for the lower floor is 2-4-2 and for the upper floor it was set to be 3-3. This configuration is the most space efficient based on the double bubble concept. In designing the fuselage clearances and safety margins were taken into account to make sure customers would be comfortable during flight. In Table 6.4 the the clearances and measurements for the fuselage are summarised. The cargo hold was sized to take Unit loading devices, in this case an LD1 was selected to fit in the cargo hold. The LD1 has a cargo volume of $5m^3$. For each of the containers 10cm clearance was taken in the cargo hold.

6.3.2 Floor plan

Designing the fuselage layout is dependant on multiple factors, below a list of considerations for the design can be seen. In Figure 6.4 a graphical overview of the floor plan can be seen.

- One lavatory required for 50 people
- Big galleys can be used for 100 people
- Small galleys can be used for 75 people
- The cabin starts at 4 meter from the nose
- The cockpit is positioned and accessed from the lower floor
- Type A exits are used for boarding the aircraft
- Type C exits are used on the lower floor as emergency exits
- Two spiral stair cases are used to connect the upper floors to the lower floor

Table 6.4: Input parameters for the fuselage cross section design.

Parameter	Value
$h_{shoulder}$ [m]	1.10
$h_{headroom}$ [m]	1.65
h_{aisle} [m]	1.95
w_{aisle} [m]	0.381
w_{seat} [m]	0.508
$w_{arm-rest}$ [m]	0.051
$s_{clearance}$ [m]	0.02
$h_{overhead}$ [m]	0.2
S_{cargo} [m]	0.1

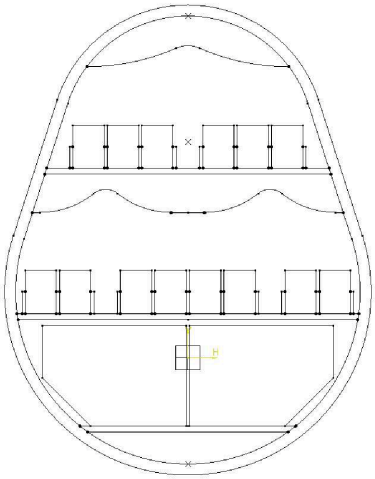

Table 6.5: Fuselage cross section

Based on these guidelines the floor plan was made. On the lower floor 268 passengers are located in a single class configuration. The front of the lower floor consists of two small galleys, two lavatory's, and staircase to the upper floor. The exits used in this area are type A exits, the capacity for this door type is 110. This area is also designated with crew seats for use during take-off and landing. The middle section of this floor is equipped with a small galley together with two lavatory's, and two type C emergency exits with an exit capacity of 55. In back area again two lavatory's are present, a slightly bigger galley and a staircase to the second upper deck. In the back type A exits are used as emergency exits and for loading. With this the exit limit of one side of the aircraft is 275 passengers therefore complying with CS-25 regulations. In the back there are folding chairs for the crew. Note that in the last two rows the seating configuration is altered, this is to allow people to sit at the beginning of the tailcone and optimise the spacing of the people.

In the first compartment of the upper floor 102 people are seated. Two lavatories were positioned in the front of the compartment and a big galley is placed in the same area. Two type A exits are positioned to allow for possible loading though a boarding bridge and to comply with CS25 on the emergency exits. The crew can be seated at the start of this compartment on folding chairs.
The second compartment has 80 people seated. A decision was made to place a small galley to service this floor, when extra supplies are needed the can be found on the floor below. Two lavatory's are set to be sufficient, again crew seating is possible in the back area. Two Type A doors were put in to allow loading to this floor directly and as emergency exits. The last two rows are smaller to allow people to sit in the tailcone. Seating for crew is available in the form of folding chairs at the end end of this compartment.

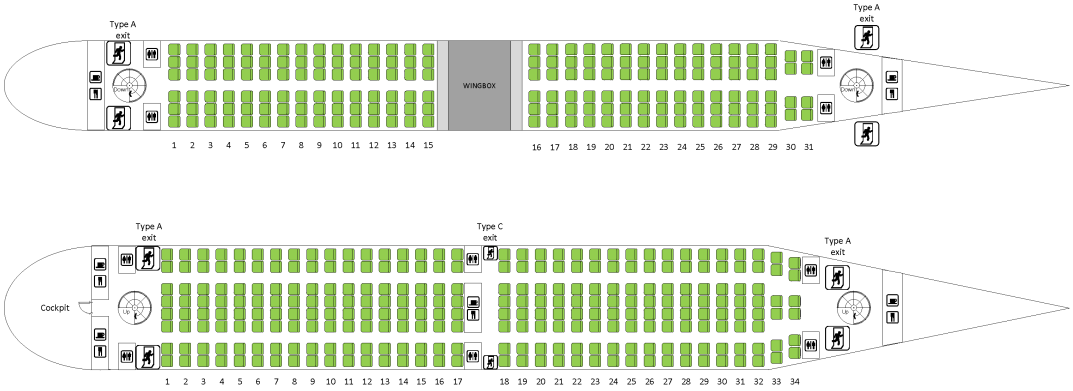

Figure 6.4: Floor plan.

7 Propulsion

Once the general layout of the design was established, it was time to investigate the options for the propulsion system. It was important to size the propulsion system before further analysis of the design was conducted as the propulsion system highly influences certain aspects of the design, i.e. the structural design. The type of propulsion system selected for the aircraft was discussed in the Midterm report [1]. However, a short recap is given in section 7.1 in order to clearly establish the type of propulsion system chosen. Then the engine is preliminary sized in section 7.2 using thermodynamic cycle calculations and sizing relations.

7.1 Propulsion system selection

In order to give the reader a thorough insight in the propulsion system selection process, decisions taken and reasoning behind them are described. First the functions of the engine were shortly summarised before identifying the requirements affecting the propulsion system selection, see subsection 7.1.1. Finally, the trade-off performed to select a propulsion system is shown in subsection 7.1.2.

7.1.1 Requirement analysis

The propulsion system has multiple functions, not only to provide thrust. These are first listed before the requirements flowing from the functions and risks are discussed.

Functional analysis

The functions of the aircraft engine are listed below:

1. Provide enough thrust to be able to take-off and climb to cruise altitude
2. Provide safe operations
3. Provide power to the aircraft's systems through generators
4. Provide breaking power for landing

Risks

As the engine is delivered by the engine manufacturer, most technical risks were identified and mitigated by them. For example, requirement BIB-SYS-PRP-02 states that the engines shall be fully FAA certified. This certification procedure is performed by the engine manufacturer and not the aircraft manufacturer. Therefore, all the technical engine risks were not included in this risk analysis. Merely the risks the engines have on the entire design and operation of the aircraft are addressed below:

- **Engine failure:** during an engine failure, more power is required from the remaining engine. The available thrust of the engine should be fully known under each aircraft configuration to be able to determine whether the engine is capable of handling the situation. If it provides too little thrust, the engine manufacturer must iterate the design or provide a similar engine which does meet these requirements.
- **Engine fire:** the engines should be equipped with a fire extinguisher system as required by the FAA regulations. However, sometimes the fire is too extensive and cannot be put out by the system. Therefore, the aircraft itself must provide a fire protection shield around the engine preventing the fire to reach crucial systems in the wing, e.g. fuel tanks and control surface actuators.
- **Engine late to market:** as the engine is not yet existing and still in the development phase, it is possible that the engine might be late to the market compared to the time planning of the aircraft's development. This can cause delays in the production of the EcoHopper 450. In order to minimise this risk, an engine was chosen with a TRL of at least six and geared turbofan engines with a lower bypass ratio are already available which meet the thrust requirement. However, they might not meet the requirements imposed on the noise and fuel consumption. This should be then further investigated.
- **Engine sub-optimal operation:** in case that the engine is operated far from its design point, it can consume too much fuel or produce too much noise. Therefore, operations of the aircraft outside the design range for the engine should be kept to a minimum. This can be done by requesting certain flight routes at air traffic control (ATC).
- **Engine exceeds design weight:** in the case that the actual engine and nacelle exceed the budgeted mass, the structures of the wing might have to be adjusted to account for the increase in weight. This can be mitigated by employing sufficient contingency values on the engine weight.

Requirements
The (driving) requirements associated with the selection of the propulsion system are listed below. They include additional requirements following from the functional analysis, these are indicated by PRP. The values for those requirements were obtained from either the iterative process described in chapter 6 or from the analyses performed in chapter 11.

- **BIB-SYS-TEC-01:** The aircraft shall be propelled by either jet or propeller driven propulsion.
- **BIB-SBS-PRO-03:** The propulsion system shall comply with CS25.901 - CS25.1207.
- **BIB-SYS-TEC-09:** The noise produced by the aircraft shall be at least one noise class better than current state of the art aircraft.
- **BIB-SBS-FLP-03:** The accumulated noise generated by the aircraft shall be below 282 dB at the ICAO measurement points.
- **BIB-SYS-SDL-03:** The aircraft design phase shall be finished by 2025.
- **BIB-SYS-TEC-08:** The aircraft shall have 10% reduced fuel consumption per passenger-kilometer with respect to current state of the art aircraft.
- **BIB-SYS-PRP-01:** The engines shall provide a static thrust at sea level of 214 kN each.
- **BIB-SYS-PRP-02:** The engines shall be FAA certified.

7.1.2 Trade-off
As the requirements set by the client were considered to be challenging, it was deemed necessary and beneficial to look into advanced propulsion systems that could outperform current state-of-the-art systems. Eventually, a trade-off was performed for the open rotor engine and the ultra-high bypass geared turbofan engine. The trade-off criteria were determined to be engine placement, technology readiness level, noise and fuel efficiency. The open rotor engine scored well on fuel efficiency while the ultra-high bypass ratio turbofan got a high score on noise and technology readiness level, as can be seen in Table 7.1. Eventually, the lower noise emissions of the ultra-high bypass turbofan, mainly due to the nacelle covering the fans and core of the engine, together with its higher technology readiness level were decisive. The trade-off scoring was set-up using a scale from one to three, one being the lowest score. The geared high-bypass ratio turbofan turned out to perform best overall.

Table 7.1: Engine selection trade-off

	Fuel Efficieny	Noise	TRL	Placement
Open Rotor	green 3	red 1	red 1	yellow 2
Geared UHBP Turbofan	yellow 2	green 3	yellow 2	green 3

Besides the ultra-high bypass ratio of 15:1, new technologies were included in the design like a reduction gear system between the low pressure spool and fan. This allows the fan to spin slower hence lowering noise, and increase the low pressure spool rotational speed which increases fuel efficiency. Further noise reduction is obtained by placing acoustic liners in the fan inlet duct. In combination with the geared turbofan this can reduce the noise by 5-7 dB. Furthermore, the fan has a variable fan pitch. After touchdown the fan pitch can be varied such that the necessity for thrust reversers is eliminated, reducing the nacelle weight. Moreover, the fan is made out of composite, also reducing the dry weight of the engine. As the thrust-to-weight ratio of 0.26 was selected, the take-off thrust was determined to be 389,259 N. Using a contingency value of 10%, the maximum thrust per engine was found to be 214.1 kN. According to Anderson [6], thrust at a certain altitude is related to thrust at sea level with Equation 7.1 where m was found from Anderson [6] and Ruijgrok [18]. The value of m was said to be 1.3 according to Anderson and 1/0.75 according to Ruijgrok, so a rounded off value of 1.3 was used. This yielded a maximum cruise thrust per engine of 61.6 kN resulting in a thrust setting of 70%. This thrust setting is below the maximum continuous thrust of modern high bypass ratio turbofans so it was deemed a feasible value.

$$T_h = T_0 \cdot \left(\frac{\rho_h}{\rho_0}\right)^m \tag{7.1}$$

7.2 Initial sizing
Once the type of propulsion system was selected, the engine could be sized. As there was chosen to opt for an ultra high bypass geared turbofan with a bypass ratio of 15, no reference engine data was available as they do not exist yet. Therefore, there was chosen to base most of the sizing calculations on an empirical method proposed by [3, 19]. However, first the initial thermodynamic properties of the engine had to be found, this is described in subsection 7.2.1. Next, the outer dimensions are determined using the proposed method, which is discussed in subsection 7.2.2. Finally, the engine

mass was determined using statistical data on high bypass engines since this was the only way to make an educated guess for the mass as no empirical relations were available, see subsection 7.2.3. Note that the engine will be manufactured outside the aircraft company. They will be delivered to the aircraft from external clients.

7.2.1 Cycle calculation

The initial thermodynamic properties of the engine had to be found to assess the sustainability of the aircraft, see the emissions and noise analyses in chapter 15 and chapter 16. The pressures and temperatures over the fan, compressor, combustion chamber and turbine were evaluated, as well as the air properties of the bypass airflow. This resulted in the thrust the engine could deliver. The pressures and temperatures were determined using the equations shown in Table 7.2 [2] in combination with Equation 7.2 and Equation 7.3. Which determine the work done, e.g. by a compressor stage, and the fuel mass flow respectively. Finally, the nozzle area, for both the core flow as well as the bypass flow could be determined using Equation 7.4, which could be used to determine the thrust output given by Equation 7.5. Where V_{jet} is determined using $\sqrt{TRk_g}$ [2].

Table 7.2: Engine cycle calculation equations used to compute the total pressure and temperature, and these parameters after compression or expansion [2].

Parameter	Temperature	Pressure
Totals	$T_0 = T(1 + \frac{k-1}{2}M^2)$	$p_0 = p(\frac{T_0}{T})^{\frac{k}{k-1}}$
Compression	$\frac{T_2}{T_1} = 1 + \frac{1}{\eta}[(\frac{p_2}{p_1})^{\frac{k-1}{k}} - 1]$	$\frac{p_2}{p_1} = [\eta(\frac{T_2}{T_1} - 1) + 1]^{\frac{k}{k-1}}$
Expansion	$\frac{T_2}{T_1} = 1 - \eta[1 - (\frac{p_2}{p_1})^{\frac{k-1}{k}}]$	$\frac{p_2}{p_1} = [1 - \frac{1}{\eta}(1 - \frac{T_2}{T_1})]^{\frac{k}{k-1}}$
Chocked/unchocked nozzle	-	$\frac{p_1}{p_{crit}} = [(1 - \frac{1}{\eta}\frac{k_g-1}{k_g+1})^{\frac{k_g}{k_g-1}}]^{-1}$

$$W = \dot{m}C_p\Delta T \quad (7.2)$$

$$\dot{m}_f = \frac{\dot{m_{air}}C_{p_g}\Delta T}{LHV\eta_c} \quad (7.3)$$

$$A_{noz} = \frac{\dot{m}}{\rho V_{jet}} \quad (7.4)$$

$$T = \dot{m}(V_{jet} - V_{inlet}) + A_{noz}(p_{jet} - p_{amb}) \quad (7.5)$$

Design sizing

As the total static thrust of both engines was determined to be 428.19 kN, engine parameters like the air mass flow, could be adjusted such that the engines could deliver the required thrust in take-off conditions. Thus the engines were designed to each deliver a static thrust of 214.1 kN at sea level. Moreover, it was found that the combustion chamber inlet temperature had to be as low as possible to reduce the NO_x emissions, this is further discussed in chapter 15. So, the engine parameters had to be adjusted such that the engine could deliver 214.1 kN of thrust while maintaining the lowest possible combustion chamber inlet temperature. The initial values regarding the internal components of the engine had to be assumed. These concerned the pressure ratios of the low and (high) pressure compressor and turbine stages, as well as efficiencies of the different components. These initial values were based on data of turbofan engines retrieved from AE2230-II [2]. Then, it was decided to vary the pressure ratio of the high pressure compressor, the outlet temperature of the combustion chamber, and the air mass flow rate, as they have the largest influence on the combustion chamber inlet temperature and the thrust output respectively. However, it turned out that the engine could not meet all constraints with the assumed values for the efficiencies and pressure ratios. Therefore, it was decided to also adjust these values to obtain an engine which could meet all requirements. The values for the pressure ratios, e.g. the fan pressure ratio, were checked against theory for feasibility [20]. This finally resulted in the values shown in Table 7.3 and Table 7.4, these values are based on take-off conditions.

Table 7.3: Engine component properties [2].

Parameter	Value	Parameter	Value
η_{inlet}	0.97	$\eta_{gearbox}$	0.995
η_{fan}	0.93	η_{noz}	0.98
η_{LPC}	0.9	$\prod_{intake}$	0.92
η_{HPC}	0.92	$\prod_{fan}$	1.4
η_{LPT}	0.9	$\prod_{LPC}$	6
η_{HPT}	0.89	$\prod_{HPC}$	6.5
η_{cc}	0.99	$\prod_{cc}$	0.96
$\eta_{mechanical}$	0.99	$T_{exit,cc}$ [K]	1,750

Table 7.4: Resulting main engine properties during take-off conditions.

Parameter	Value	Parameter	Value
Fuel flow [kg/s]	0.581	Core thrust [kN]	57.5
Air mass flow [kg/s]	450	Fan thrust [kN]	156.8
$T_{inlet,cc}$ [K]	984.7	Total thrust [kN]	214.3

Verification & validation

In order to verify the tool the calculation was done by hand and the order of magnitude of the outputs and of the intermediate results were compared to cycle calculations provided in [2]. It was determined that the model yielded realistic results and could thus be used for further analyses. In addition, the tool was run for inputs provided on the Olympus 593 engine of the Concorde. The inputs were obtained from [2], it also provided the results of all intermediate calculation steps. It was found that the tool was implemented correctly as the same outputs were found from the tool and the source [2]. However, it was not know how realistic these input values were, therefore they could not be used for validation. As engine manufacturers do not provide details on the thermodynamic properties of their engines, the tool could not be fully validated using verified input data. However, as the tool computed the correct outputs for the engine cycle example calculations provided by [2], it was said that the tool could still be used for an initial internal design of the engine.

7.2.2 Outer dimensions

Once the initial internal design of the engine was determined, the outer dimensions of the engine could be computed. The outer dimensions are needed to perform further analysis on the design as the engines should have enough clearance. The empirical method used for the sizing was obtained from Torenbeek [3]. The dimensions that could be determined using this method are shown in Figure 7.1. The following dimensions are indicated, the equation to compute them is also mentioned [2, 3]:

1. D_h fan case diameter, $D_h = D_i$
2. D_i inlet/fan diameter, Equation 7.6
3. D_s/D_i spinner to inlet diameter, Equation 7.7
4. l_n nacelle length, Equation 7.8[1]
5. l_f fan cowl length, $l_f = \phi l_n$, see [1]
6. D_n maximum cowl diameter, $D_n = D_\mathrm{i} + 0.06\phi l_n + 0.03$
7. D_{ef} exit fan diameter, $D_{ef} = D_n(1 - \frac{1}{3}\phi^2)$
8. l_g exposed length of gas generator, $l_g = (1 - \phi)l_n$
9. D_g gas generator cowling diameter at the fan exit, Equation 7.9
10. D_{eg} gas generator cowling diameter at the has generator exit, $D_{eg} = 0.55D_g$

$$D_i = 1.65\sqrt{\frac{\frac{\dot{m}}{\rho_0 c_0} + 0.0050}{1 - (D_s/D_i)}})^2 \qquad (7.6)$$

$$\frac{D_s}{D_i} = 0.05[1 + 0.1\frac{\rho_0 c_0}{\dot{m}} + \frac{3\lambda}{1+\lambda}] \qquad (7.7)$$

[1]Where c_n and Δl are constants depending on the nacelle type determined by the value of ϕ. Torenbeek suggest to assume ϕ = 0.75 which results in a type C nacelle, where the gas generator sticks out of the nacelle. This gives c_n = 7.8 and Δl = 0.10.

$$l_n = c_n[\sqrt{\frac{\dot{m}}{\rho_0 c_0}\frac{1+0.2\lambda}{1+\lambda}} + \Delta l] \quad (7.8)$$

$$D_g = D_{ef}(\frac{0.089\frac{\dot{m}}{\rho_0 c_0}\lambda + 4.5}{0.067\frac{\dot{m}}{\rho_0 c_0}\lambda + 5.8})^2 \quad (7.9)$$

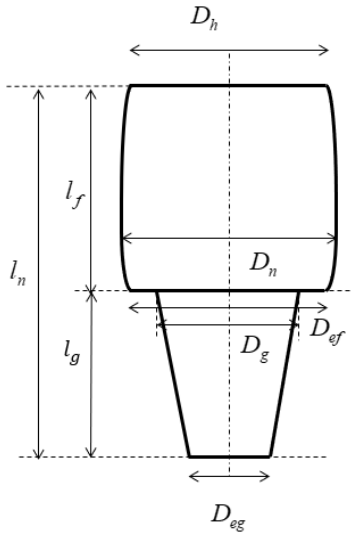

Figure 7.1: Engine dimensions according to the empirical method proposed by Torenbeek. [2, 3].

Design sizing

The resulting dimensions of the engine and nacelle are shown in Table 7.5. It should be noted that these values were not entirely based on the equations provided by Torenbeek. They are merely a combination of the results provided by Torenbeek, statistical data and correction factors. This is further explained in the following section on verification and validation.

Table 7.5: Resulting engine properties during take-off conditions.

Parameter	Value	Parameter	Value
D_h (fan case) [m]	3.15	D_i (fan) [m]	2.87
D_n [m]	3.16	l_f [m]	4.20
D_{ef} [m]	2.56	l_g [m]	1.40
D_g [m]	1.65	l_n [m]	5.60
D_{eg} [m]	0.91		

Verification & validation

The calculations could be verified by computing the dimensions by hand and checking the order of magnitude of the results. Furthermore, the tool was validated by running it for different existing engines, such as the CFM LEAP family [2], and the geared turbofan family of Pratt & Whitney (The PW1000G Family) [3]. It was found that the tool overestimated the nacelle length significantly, on average by 30.9% while the fan diameter was underestimated by 21.6%. As it was initially assumed that the fan case diameter is the same diameter as the fan itself, some errors where introduced too. Based on the validation engines, it was found that $D_h = 1.097\ D_i$. It could thus be said that the method proposed by Torenbeek is not fully applicable to high bypass engines. However, in order to get a rough estimation of the engine dimensions the found correction factors were applied, and the results were combined with statistical data for high bypass engines [2] [3]. Combining these two sources provided more confidence in the validity of the results which are shown in Table 7.5.

7.2.3 Mass estimation

To determine the mass of the engine, it was chosen to opt for a statistical method as no empirical method was available. The statistical data used to construct Figure 7.2 was retrieved from technical specifications of modern high bypass engines

[2] A technological LEAP forward. Retrieved June, 18 2019, from https://www.safran-aircraft-engines.com/commercial-engines/single-aisle-commercial-jets/leap/leap-1b

[3] GTF Engine Family. Retrieved June, 18 2019, from https://www.mtu.de/engines/commercial-aircraft-engines/narrowbody-and-regional-jets/gtf-engine-family/

(8:1 to 12:1) rather than ultra high bypass engines (12:1 to 15:1). Although a lot of effort is put into reducing the weight of the engine (fan blades alone for example are made out of carbon instead of titanium), it was deemed necessary to include a margin of 500 kg. Subsequently, the linear equation relating the engine thrust to the engine mass was determined.

$$M_{eng} = 16.05 \cdot T_{eng} + 790.6 \tag{7.10}$$

The mass of the engine was then determined to be 4,760 kg for a thrust level of 214 kN.

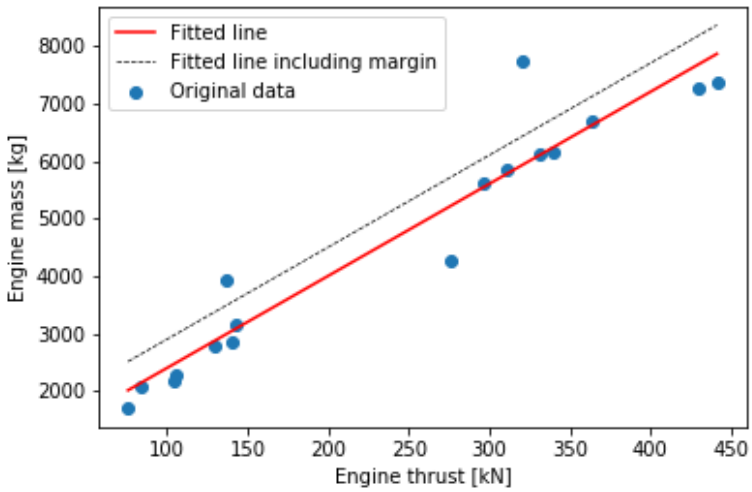

Figure 7.2: Engine mass estimation based on data of modern high-bypass turbofan engines.

8 Aerodynamic design and analysis

The goal of the aerodynamic analysis is to create a wing geometry with optimal aerodynamic performance, meaning a high lift over drag ratio and low drag. Optimising these parameters can be achieved by tweaking parameters like the aspect ratio and sweep. However, it turned out that the weight influenced the aerodynamic parameters the most. Three flight phases were considered in the aerodynamic analysis, these were; cruise, take-off and landing. But first the requirements on the subsystem had to be identified, see section 8.1. After this the 3D wing geometry and the lift and drag analyses were performed in section 8.2, section 8.3 and section 8.4 respectively. In section 8.5 a sensitivity analysis is performed on the strut and winglets to investigate their effect on the design. The aerodynamic verification is done in section 8.6 and finally the high lift devices are selected and sized in section 8.7. The spoilers will be sized in section 8.8.

8.1 Requirement analysis

The requirements regarding the aerodynamic characteristics of the EcoHopper 450 are discussed here, these flow down from the functional and risk analyses.

8.1.1 Functional analysis

The main function of the aerodynamics is to provide sufficient lift such that is able to stay in the air, so one wants to maximise the lift while keeping the drag as low as possible. To prevent a high induced drag a low cruise angle of attack is required, for the EcoHopper 450 the maximum cruise angle of attack was set to 3 degrees. Furthermore to ensure aerodynamic performance a L/D ratio of at least 15 shall be achieved.

8.1.2 Risk analysis

One of the risks that involves aerodynamics is stalling. During flight one wants to prevent that from happening, so there should be enough margin between the stalling angle of attack and the cruise angle of attack. Another risk that might occur is a high increase of drag due to drag divergence. So the Mach number for drag divergence should lie above the cruising Mach number. These risks can be prevented when designing the wing with enough margin with respect to these risks.

8.1.3 Requirements

The functions and risks from the previous sections are formulated in the following requirements:

- **BIB-SBS-AED-02**: The maximum cruise angle of attack shall at least be lower than 3 degrees.
- **BIB-SBS-AED-03**: The L/D ratio in cruise conditions shall be at least 15.
- **BIB-SBS-AED-04**: There shall be at least a 5 degree margin between the cruise and stall angles of attack.
- **BIB-SBS-AED-05**: The Mach number at which drag divergence occurs should be above the cruising Mach number for the biggest part of the wing.

8.2 3D wing geometry

The wing geometry significantly influences the aerodynamic properties of the aircraft. The parameters considered for the wing geometry design are: the aspect ratio, sweep, taper ratio, thickness over chord ratio and dihedral/anhedral. These parameters were based on the surface area and cruise conditions. Where the surface area was based on the take-off weight and the cruise conditions were selected in an earlier stage of the project. The required surface area was determined to be 208 m^2.

8.2.1 Method

In the concept analysis performed in the Midterm report [1], several aspect ratios were tested for the different design concepts. For the concept chosen, it turned out that an aspect ratio of 13 was the most optimal. This aspect ratio is significantly higher compared to state of the art aircraft like the Boeing777x and Boeing 737-MAX 8 which have aspect ratios of around 10 [1] [2]. Due to the high aspect ratio the aerodynamic performance will improve as the lift induced drag decreases according to Equation 8.1. Returning to the T/W-W/S diagram from the class-I weight estimation, there the aspect ratio has influence on the horizontal lines of the T/W as the aspect ratio determines how much thrust is needed and thus how much drag is produced. Increasing the aspect ratio from 10 to 13 has a Δ T/W of 0.0183, which amounts to an decrease of 6.5% in the required thrust, this justifies the use of higher aspect ratio wings. However, high aspect ratio wings carry a weight penalty the reason being that the wing becomes slender and the root chord becomes relatively small.

[1] Detailed Technical Datasheet. Retrieved May, 21 2019, from http://www.b737.org.uk/techspecsdetailed.htm
[2] Boeing 777X. Retrieved June, 23 2019, from https://en.wikipedia.org/wiki/Boeing_777X

Therefore, more material must be added to obtain the required moment of inertia. The strutted wing design was chosen to reduce the root moment and thus the structural wing weight.

$$C_{D_i} = \frac{C_L^2}{\pi A e} \tag{8.1}$$

The sweep and thickness over chord ratio of the wing are both of significant influence on the drag divergence (M_{dd}) of the wing. Low sweep and high thickness over chord ratios let the M_{dd} decrease as dictated by Equation 8.2 [4]. When flying at Mach numbers above M_{dd} the unfavourable induced drag increases significantly. Since the cruise Mach number of 0.72 means that drag divergence does not have to occur, the wing was designed without sweep. This brings two big advantages; first the wing weight is reduced since torsional stresses are lower, secondly the design is aerodynamically more efficient as the flow speed seen by the wing will be lower. When zero sweep is selected Equation 8.3 was used to check for Mach drag divergence. Here k_a is a technology factor for the airfoil, t/c is the maximum thickness over chord, and C_L is the cruise lift coefficient of the 3D wing.

$$M_{dd} = \frac{k_a}{cos\Lambda} - \frac{t/c}{cos^2\Lambda} - \frac{C_L}{10cos^3\Lambda} \tag{8.2}$$

$$M_{dd} = k_a - t/c - \frac{C_L}{10} \tag{8.3}$$

8.2.2 Results

The resulting 3D geometry is presented in this section. To achieve a M_{dd} above the cruise Mach number a supercritical airfoil was selected. These airfoils have a high k_a since this is favourable for increasing the M_{dd}. The technology factor of supercritical airfoils was found to be 0.935 [21]. Although the wing is strutted, the root of the wing will still see the highest bending moments. To design for this bending moment, a certain moment of inertia (MOI) is required. Increasing the thickness of the wing increases the moment inertia based on the increased distance with respect to the neutral line. Due to this phenomena an airfoil with t/c of 0.20 was selected at the root. This linearly decreases to a t/c of 0.12 at 25% of the semi span. From 25% onward the airfoil stays constant until the wing tip.

The supercritical airfoils selected are the NACA SC(2)-0612 and NACA SC(2)-0620 as seen in Figure 8.1, These airfoils have a design lift coefficient of 0.6 which is close to $C_{L_{Cruise}}$ of the design of 0.621. With these airfoils the M_{dd} values become 0.71 and 0.75 respectively. This means a slight increase in drag is experienced at the wing root. However, when the t/c has decreased spanwise to 0.15 the cruise Mach number is already below the drag divergence value. This is thus selected for structural reasons.

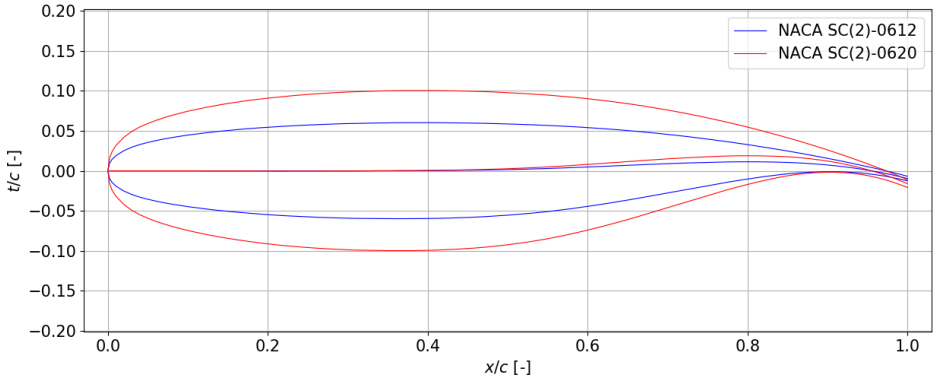

Figure 8.1: Root and tip airfoils with its respective camber lines.

Next, an anhedral angle of 1.5 degrees was selected based on the roll stability of the aircraft. The taper ratio of the wing was selected to be 0.357, this was based on the ideal taper ratio approximating an elliptical lift distribution as described by Hoerner [22]. In Table 8.1 an overview of the 3D wing parameters can be seen. The winglets were sized to be similar to current state of the art aircraft due to the time constraint of this project [3]. The resulting geometric properties of the winglet are shown in Table 8.2. The variable that will be investigated is the winglet angle with the vertical plane, but that will be elaborated upon in section 8.5. The effective aspect ratio due to the addition of the winglets will be 13.82, which is explained in section 8.4. In Figure 8.2 the resulting wing geometry is shown in a top view.

[3]B737 winglets. Retrieved June, 5, 2019, from http://www.b737.org.uk/winglets.htm

Table 8.1: Overview of the 3D wing Geometry.

Parameter	Value
A [-]	13.0
S [m^2]	208
b [m]	52.0
λ [-]	0.357
c_r [m]	5.89
c_t [m]	2.01
MAC [m]	4.30
$(t/c)_r$ [-]	0.20
$(t/c)_t$ [-]	0.12
$(t/c)_{avg}$[-]	0.13
$\Lambda_{0.25}$ [deg]	0.00
Γ [deg]	-1.50

Table 8.2: Geometric properties of the winglet.

Parameter	Value
A [-]	2.5
λ [-]	0.3
Λ_{LE} [deg]	30
Root chord [m]	1.95
Tip chord [m]	0.59

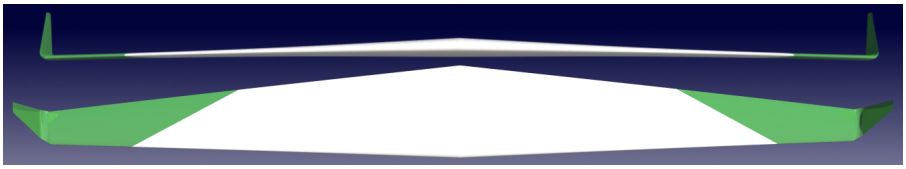

Figure 8.2: Top and front view of the wing.

8.3 Lift analysis

The lift analysis will focus on the lifting performance of the aircraft during three stages of the mission; cruise, take-off and landing. For each of these phases a lift curve slope was generated and analysed. From this the lift coefficients were selected for take-off and landing conditions. The cruise lift coefficient was based on the cruise conditions and weight in cruise. In order to construct the lift curve slope, a number of data points is needed; C_{L_α} and α_{0L} are needed to construct the linear part of the curve, while $C_{L_{max}}$ and α_s are needed to construct the stalling part of the curve.

8.3.1 Method

This section contains the methods to calculate the lift characteristics in cruise, take-off and landing.

Cruise analysis method

Information about the lift curve slope for the airfoil was obtained from Xfoil and a preliminary sizing method found in Raymer [4]. As α_{0L} is the same for an airfoil as well as for a 3D wing, an analysis using Xfoil was made to determine the lift curve slope of the different airfoils used. Both the root and tip airfoils were analysed as well as an interpolation between the two airfoils with an average t/c which was assumed to be the wing average airfoil. A Reynolds number of 30,000,000 was selected based on cruise conditions and the mean aerodynamic chord (MAC). To calculate C_{L_α}, Equation 8.4 from Raymer [4] was used, this equation takes the effects of compressibility, airfoil efficiency and 3D wing geometry into account. Here β is the compressibility factor (Equation 8.5) and η is an airfoil efficiency factor described by Equation 8.6.

$$C_{L_\alpha} = \frac{2\pi A}{2 + \sqrt{4 + \left(\frac{A\beta}{\eta}\right)^2 \left(1 + \frac{\tan^2 \Lambda_{max,t}}{\beta^2}\right)}} \tag{8.4}$$

$$\beta = \sqrt{1 - M^2} \tag{8.5}$$

$$\eta = \frac{C_{l_\alpha}}{2\pi/\beta} \tag{8.6}$$

Finding $C_{L_{max}}$ in the conceptual design phase was rather difficult and to make a good estimation, a wind tunnel or flight test is required [19]. However, an approximation is made using the Raymer method[4]. In Equation 8.7 the approximation for high aspect ratio wings can be found. Here $\frac{C_{L_{max}}}{C_{l_{max}}}$ is a scaling factor and can be found for the wing based on the leading edge sweep and the airfoil sharpness parameter, ΔY. This parameter is defined as the slope of the upper part of the airfoil between 0.0015c and 0.06c. For the NACA SC(2)-0612 and NACA SC(2)-0620 airfoils ΔY was found to be 3.09% and 4.12% of the chord respectively. In Figure 8.3 the approximation for $\frac{C_{L_{max}}}{C_{l_{max}}}$ can be seen, note that this is for an untwisted

wing with constant airfoil cross-section. However, for a ΔY above 2.5 the same value is given so the changing airfoil would not be of influence. The leading edge sweep is close to 0 degrees so from this, $\frac{C_{L_{max}}}{C_{l_{max}}}$ was determined to be 0.9.

$$C_{L_{max}} = \left[\frac{C_{L_{max}}}{C_{l_{max}}}\right] C_{l_{max}} + \Delta C_{L_{max}} \tag{8.7}$$

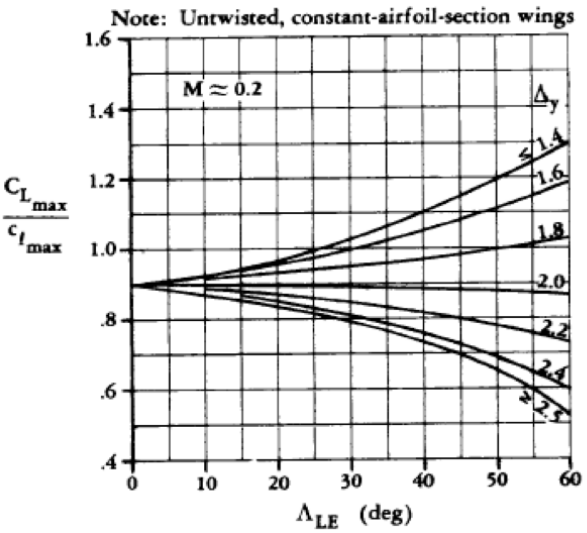

Figure 8.3: Estimation of the scaling factor for $C_{L_{max}}$ [4].

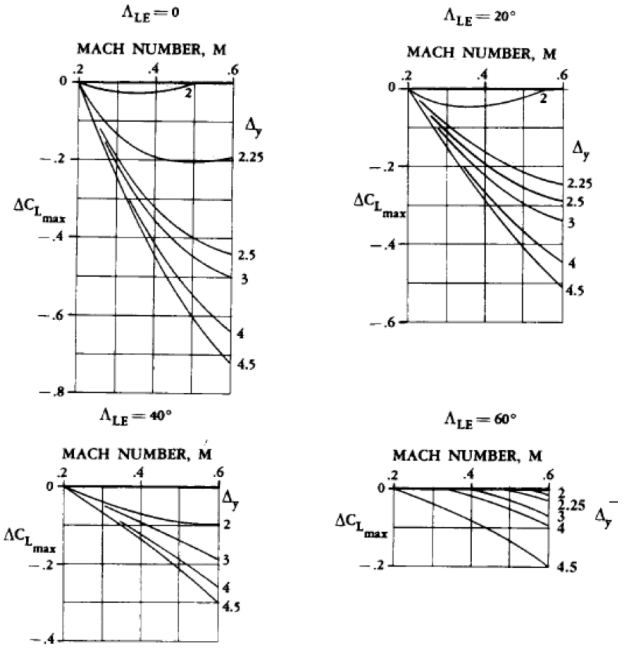

Figure 8.4: Estimation for $\Delta C_{L_{max}}$ [4].

In Equation 8.7, $\Delta C_{L_{max}}$ takes into account the compressibility. In Figure 8.4 the figures from Raymer can be seen for approximating $\Delta C_{L_{max}}$. It can be seen that $\Delta C_{L_{max}}$ depends on Λ_{LE}, ΔY and the M. The leading edge sweep is close to zero and ΔY ranges from 3.09% - 4.12%. From this an educated guess was made setting $\Delta C_{L_{max}}$ at -0.5, while $C_{l_{max}}$ for the airfoil was set to be 2.2 in cruise. From the Xfoil analysis the airfoil, maximum lift coefficient turned out to be too high. Xfoil overestimates $C_{l_{max}}$ at high Reynolds numbers since separation is delayed due to the high energy flow. Xfoil gives more accurate results at lower Reynolds numbers. The $C_{l_{max}}$ was found based on wind tunnel tests for the NACA supercritical airfoils at high Reynolds numbers [23, 24].

Then the stall angle of attack, α_s, was estimated using Equation 8.8, where $\Delta\alpha_{C_{L_{max}}}$ was estimated using Figure 8.5 and selected to be 2.6 degrees. During cruise, the lift coefficient is determined by its weight and cruise conditions. The cruise weight was approximated using Equation 8.9 [25], then the cruise lift coefficient was obtained by Equation 8.10.

$$\alpha_s = \frac{C_{L_{max}}}{C_{L_\alpha}} + \alpha_{0L} + \Delta\alpha_{C_{L_{max}}} \tag{8.8}$$

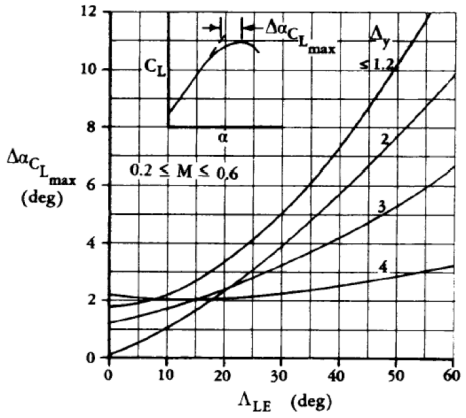

Figure 8.5: Estimation for $\Delta\alpha_{C_{L_{max}}}$ [4].

$$W_{cruise} = W_{MTOW} - 0.4W_F \quad (8.9)$$

$$C_{L_{Cruise}} = \frac{W_{cruise}}{\frac{1}{2}\rho V^2 S} \quad (8.10)$$

Take-off and landing analyses method

The first step in analysing the take-off and landing was creating a new clean C_{l_α} curve for the 3D wing. This is because speeds are significantly lower so a lower Reynolds number had to be used. An assumption was made that the Mach number equals 0.2 so compressibility effects could be neglected. A new Reynolds number was computed based on a speed of 70 m/s which was a first order approximation for the take-off speed. Together with sea level conditions the Reynolds number turned out to be approximately 17,000,000. As in the previous section, a new C_{l_α} curve was constructed for the wing averaged airfoil using Xfoil.

For take-off and landing, the stall speeds could be determined using Equation 8.11. These stall speeds were then used to calculate the take-off and landing speeds which are in turn used to find the respective lift coefficient. The take-off speed and approach speeds were estimated by $V_{LOF} = 1.2V_{s,TO}$ and $V_{land} = 1.3V_{s,land}$ respectively, see chapter 13. The take-off weight was set at the MTOW. For landing weight a crude estimation was made: $W_{Land} = W_{TO} - 0.8W_F$. Making the assumption that 80% of the fuel weight is lost during flight. Subsequently the corresponding lift coefficient was calculated with Equation 8.12.

$$V_s = \sqrt{\frac{W}{\frac{1}{2}\rho C_{L_{max}} S}} \quad (8.11)$$

$$C_L = \frac{W}{\frac{1}{2}\rho V^2 S} \quad (8.12)$$

8.3.2 Results

In Table 8.3 an overview of the most important values are given for the different conditions. In Figure 8.6 the lift curve slopes obtained for the three airfoils can be seen. The average wing airfoil was set to be the one used in further analysis. From this α_{0L} was found to be -3.9 degrees. Based on the cruise Mach number, β is 0.693 and C_{l_α} was found to be 6.71 /rad from Figure 8.6. This led to a value of 0.741 for η. The maximum thickness over chord sweep, $\Lambda_{max,t}$ was found to be -0.86 degrees. Using Equation 8.4 a C_{L_α} of 5.70 /rad was found.$C_{l_{max}}$ was set at 2.2 based on the research on super critical airfoils. Next, equation 8.7 led to a $C_{L_{max}}$ of 1.48 and from Equation 8.8 α_s was calculated to be 12.8 degrees. Taking all of these data points, the lift curve slope for cruise was drawn and can be seen in Figure 8.6. Using Equation 8.9 in combination with Equation 8.10 and the cruise conditions, resulted in a cruise lift coefficient of 0.621. From Figure 8.6 it can be seen that the cruise angle of attack would then be around 2 degrees.

Table 8.3: Overview of the lift characteristics in cruise, take-off and landing conditions.

Parameter	Cruise	Take-off	Landing
C_{L_α} [1/rad]	5.70	6.65	6.80
α_{0L} [deg]	-3.90	-10.39	-13.64
$C_{L_{max}}$ [-]	1.48	2.77	3.05
α_s [deg]	13.57	16.06	14.65

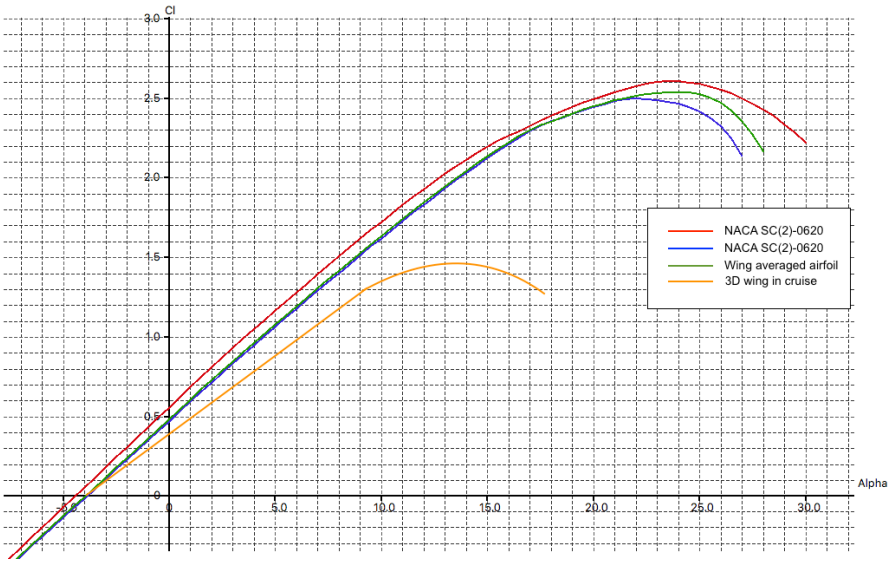

Figure 8.6: $C_L - \alpha$ curves for cruise conditions at Re = 30,000,000 and the 3D wing in cruise.

For take-off and landing, the clean curve $C_{l_{max}}$ was found to be 2.0 based on the same research on supercritical airfoils [24]. From Figure 8.7, C_{l_α} was found to be 6.66/rad. With β is 0.98 and η is 1.04. From this the C_{L_α} at sea level becomes 5.68/rad. Recalculating $C_{L_{max}}$ for sea level conditions without compressibility yielded a value of 1.8 and α_s became 16.8 degrees. With this, the new clean lift curve slope was made. The flapped lift curve slopes could be made using the values calculated in section 8.7. The clean and flapped curves can be seen in Figure 8.7. The take-off speed was found to be 78.9 m/s and the landing speed was found to be 76.9 m/s. From this the lift coefficient could be calculated using Equation 8.12. This yielded a take off C_L of 1.92 and landing C_L of 1.80.

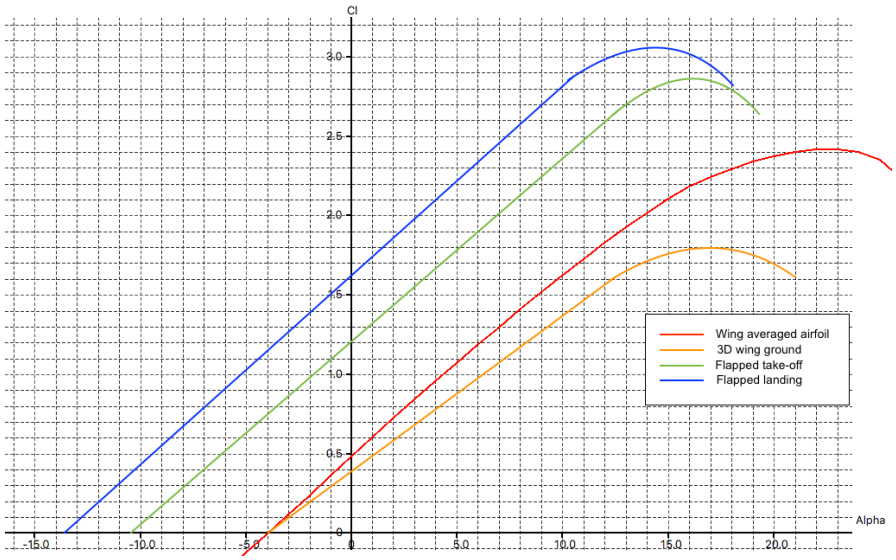

Figure 8.7: $C_L - \alpha$ curves for the wing averaged airfoil at Re = 17,000,000 and 3D wing in clean, take-off and landing conditions.

8.4 Drag analysis

This section covers the drag estimation of the aircraft for cruise, take-off and landing conditions respectively.

8.4.1 Method

First, the zero lift drag was calculated using the drag component build-up method. Secondly the Oswald efficiency factor was estimated. With this and the corresponding lift coefficients of each condition calculated in the previous , the drag polars and aerodynamic performance parameters were calculated in the final part of this section.

Zero lift drag estimation

The zero lift drag or profile drag is created by a body being present in a flow. This drag is mainly due to the frictional interaction of the flow with the body. The zero lift drag coefficient C_{D_0} can be estimated using Equation 8.13. In this

equation, the component drag coefficient is multiplied with the component wetted area. All these values are summed and normalised with respect to S_{ref} which is the wing surface area. C_{fc} is the skin friction coefficient which is multiplied by a form factor FF_c and an interference factor IF_c, these together with the wetted area of the component form the component drag coefficient. $C_{D_{misc}}$ is added for miscellaneous drag components like the landing gears and flaps during take off and landing.

$$C_{D_0} = \frac{1}{S_{ref}} \sum_c C_{fc} \times FF_c \times IF_c \times S_{wet,c} + C_{D_{misc}} \tag{8.13}$$

The components considered in the zero lift drag build up were: the wing, the fuselage, the horizontal and vertical tail, the wing strut, engine nacelles and the landing gear fairings. The C_f is based on a laminar and a turbulent friction coefficient, Equation 8.14 and Equation 8.15 respectively. The ratio of the laminar and turbulent friction coefficients is based on the transition point. The transition point is the percentage of the transition location over the total length and gives the friction coefficient as in Equation 8.16.

$$C_{f_{lam}} = \frac{1.328}{\sqrt{Re}} \tag{8.14}$$

$$C_{f_{tur}} = \frac{0.455}{(log_{10}Re)^{2.58}(1 + 0.144M^2)^{0.65}} \tag{8.15}$$

$$C_f = \frac{x_{trans}}{l} C_{f_{lam}} + \left(1 - \frac{x_{trans}}{l}\right) C_{f_{tur}} \tag{8.16}$$

The Reynolds number used during these calculations could either be the normal Reynolds number or a cut off Reynolds number. For subsonic flow, the Reynolds number is defined as in Equation 8.17. Where l is the characteristic length for the wing or in this case the mean aerodynamic chord and k is the surface roughness coefficient which was selected to be $0.634 \text{x} 10^{-5}$ m for smoothly painted aircraft.

$$Re = min(\frac{\rho V l}{\mu}, 38.21(l/k)^{1.053}) \tag{8.17}$$

For the different components, different types of form factors apply. The form factor for the wing, empennage and other airfoil shaped components like the strut can be seen in Equation 8.18. Where $(x/c)_m$ is the maximum thickness over chord location as fraction of chord, and Λ_m is the sweep of the maximum thickness location. For fuselages and smooth canopy the form factor is defined as in Equation 8.19, for the nacelles and external storage it is defined as in Equation 8.20. In both equations, f is the slenderness ratio as defined in Equation 8.21.

$$FF = \left[1 + \frac{0.6}{(x/c)_m}\left(\frac{t}{c}\right) + 100\left(\frac{t}{c}\right)^4\right][1.34M^{0.18}(cos\Lambda_m)^{0.28}] \tag{8.18}$$

$$FF = 1 + \frac{60}{f^3} + \frac{f}{400} \tag{8.19}$$

$$FF = 1 + \frac{0.35}{f} \tag{8.20}$$

$$f = \frac{l}{d} = \frac{l}{\sqrt{(\pi/4)A_{max}}} \tag{8.21}$$

The interference factor is based on the interference between two components. Locally the velocity is increased between these components resulting in a higher dynamic pressure and thus a local increase in drag. The interference factors are in this case selected from literature and are shown in the next section [21]. The wetted area of the wing could be approximated by Equation 8.22. The exposed area is the surface area without the wing area that is located in the fuselage. For the empennage the wetted area for both surfaces could be found using Equation 8.23. For the fuselage the approximation in Equation 8.24 could be used. This assumes a circular fuselage cross-section, however the design uses a double bubble fuselage. To come up with an effective diameter the same approximation as in the denominator in Equation 8.21 was used with the cross sectional area of the fuselage. $L1$, $L2$ and $L3$ are the nosecone, midsection and tailcone lengths respectively.

$$S_{w_{wet}} = 1.07 \times 2 \times S_{w_{exp}} \tag{8.22}$$

$$S_{t_{wet}} = 1.05 \times 2 \times S_{t_{exp}} \tag{8.23}$$

$$S_{f_{wet}} = \frac{\pi d}{4}\left(\frac{1}{3L_1^2}\left[\left(4L_1^2 + \frac{d^2}{4}\right)^{1.5} - \frac{d^3}{8}\right] - d + 4L_2 + 2\sqrt{L_3^2 + \frac{d^2}{4}}\right) \tag{8.24}$$

$$S_{s_{wet}} = 2.17 * 2 * C_s * l_s \tag{8.25}$$

For the strut to be aerodynamically efficient, it was designed to be enclosed by an airfoil. The airfoil considered for the strut is a NACA 0030 airfoil and its angle of attack in cruise is set to zero such that it does not produce any lift. Since a high thickness airfoil was chosen Equation 8.22 cannot be used to approximate the wetted area. The airfoil was analysed in Xfoil and from here the circumference over chord ratio turned out to be 2.17. From this a wetted area estimation of the strut was defined (Equation 8.25). For the take-off and landing a drag increase due to the flap deflection was calculated by Equation 8.26 [4]. For slotted flaps F_{flap} is 0.0074, the formula is only valid for flap deflections above 10 degrees which is the case for this design.

$$\Delta C_{D_{flap}} = F_{Flap}\left(\frac{c_f}{c}\right)\left(\frac{S_{flapped}}{S}\right)(\delta_{flap} - 10) \tag{8.26}$$

Oswald efficiency factor estimation

The Oswald efficiency factor was estimated using a method proposed by M. Nita and D. Scholz [26]. The method is described by Equation 8.27. Where e_{theo} is the theoretical Oswald efficiency factor, and $k_{e,f}$ is a factor taking into account the effect of the fuselage. The fuselage would slightly decrease the optimal lift distribution so this factor would be below one. Then k_{e,D_0} is the influence of the zero lift drag on the efficiency. From statistics, this value was estimated to be 0.804. The last factor $k_{e,M}$ takes into account the effect of compressibility, especially at high mach numbers the compressibility significantly reduces the e. A sharp drop in $k_{e,M}$ is experienced between Mach numbers 0.7 and 0.8 which was validated with data from the Airbus A320 [26].

$$e = e_{theo} \cdot k_{e,f} \cdot k_{e,D_0} \cdot k_{e,M} \tag{8.27}$$

The theoretical Oswald efficiency factor was calculated using Equation 8.28. Where $f(\lambda)$ is the Hoerner's theoretical Oswald efficiency line based on the taper ratio [22]. This was approximated by a fourth order polynomial Equation 8.29. Since the wing has no sweep no correction for sweep had to be made. In theory $k_{e,f}$ is calculated by Equation 8.30. This equation is based on a mass conservation analysis of the flow around the fuselage. However in reality the drag losses are bigger thus Equation 8.31 is to be used. Finally, $k_{e,M}$ could be estimated by Equation 8.32, this formula is a better approximation for compressibility effects on e compared to the Prandtl-Glauert correction. From this, the Oswald efficiency factor was estimated to be 0.720 and 0.765 for cruise and ground conditions respectively.

$$e_{theo} = \frac{1}{1 + f(\lambda)A} \tag{8.28}$$

$$f(\lambda) = 0.0524\lambda^4 - 0.15\lambda^3 + 0.1659\lambda^2 - 0.0706\lambda + 0.0119 \tag{8.29}$$

$$k_{e,f} = 1 - \left(\frac{d_f}{b}\right)^2 \tag{8.30}$$

$$k_{e,f} = 1 - 2\left(\frac{d_f}{b}\right)^2 \tag{8.31}$$

$$k_{e,M} = 1 - 0.00152\left(\frac{M}{0.3} - 1\right)^{10.82} \tag{8.32}$$

Drag polars

The following section describes the drag polars which can be constructed with the information from the previous sections. The drag polar is defined as Equation 8.33. The Oswald efficiency factor was calculated in the previous section. Since winglets are used, the effective aspect ratio should be used in the lift over drag polar. From M. Nita and D. Scholz the effective aspect ratio could be approximated by Equation 8.34. Here h is the wing tip height and k_{WL} is a correction factor based on geometry. The designed winglets are similar to the winglets on the Boeing 737-800 which has a k_{WL} of 3.08 [26]. With a winglet height of 2 meter the effective aspect ratio becomes 13.82.

$$C_D = C_{D_0} + \frac{C_L^2}{\pi A_{eff} e} \tag{8.33}$$

$$A_{eff} = A\left(1 + \frac{2}{k_{WL}}\frac{h}{b}\right)^2 \tag{8.34}$$

8.4.2 Results

The following section covers the drag estimation results for the design. The drag coefficient was finally approximated using Equation 8.35.

$$C_D = C_{D_0} = \frac{C_L^2}{\pi A e} \tag{8.35}$$

In Table 8.4 and Table 8.5 the drag breakdown can be seen for each component considered. Since the landing gear storage was not designed in detail, an approximation of 5% of the Clean C_{D_0} is added to the total. Two tables were considered to both consider cruise conditions and ground conditions because the atmospheric properties influence the drag. Summing the values for cruise gives a $C_{D_{0,cruise}}$ of 0.0233. For ground condition the clean C_{D_0} is 0.0226, adding the flaps results in a $C_{D_{0,TO}}$ of 0.0318 and a $C_{D_{0,LA}}$ of 0.0775. From Figure 8.8 it can be seen that the strutted wing adds about 11% to the zero lift drag. The fuselage and wing also have large contribution since these are large components of the aircraft. An 11% zero lift drag penalty is significant but this is justified by the highly efficient wing. A consideration for later design stages is to reduce this percentage by means of techniques like boundary layer suction. The value of C_{D_0} is comparable to the drag coefficients of the Boeing 737 and Airbus A320 which are approximated to be 0.024 and 0.023 by an stochastic hierarchical model [27].

Table 8.4: Zero lift drag breakdown per component for cruise conditions.

Component	C_f [-]	FF [-]	IF [-]	S_{wet} [m^2]	C_{D_0} [-]	%
Fuselage	0.00172	1.169	1.0	693.5	0.00647	29.2
Wing	0.00221	1.565	1.1	425.04	0.00749	33.8
Horizontal tail	0.00229	1.506	1.05	85.60	0.00144	6.5
Vertical tail	0.00221	1.421	1.05	56.97	0.000684	3.9
Naccelle	0.00233	1.197	1.1	87.28	0.00124	5.6
Strut	0.00302	2.021	1.1	78.03	0.00243	11.0
Fairings and pylons					0.00117	5.0
Leakages					0.00117	5.0
Total in cruise					0.0233	100

Table 8.5: Zero lift drag breakdown per component for take-off and landing conditions.

Component	C_f[-]	FF [-]	IF[-]	S_{wet} [m^2]	C_{D_0}[-]	% TO	% Land
Fuselage	0.00180	1.189	1.0	693.5	0.00711	23.3	9.3
Wing	0.00245	1.242	1.1	425.04	0.00660	21.6	8.6
Horizontal tail	0.00254	1.196	1.05	85.60	0.00127	4.1	1.7
Vertical tail	0.00245	1.122	1.05	56.97	0.000760	2.5	1.0
Naccelle	0.00258	1.197	1.1	87.28	0.00137	4.5	1.8
Strut	0.00338	1.605	1.1	78.03	0.00216	7.1	2.8
Fairings and pylons					0.00107	3.5	1.4
Leakages					0.00107	3.5	1.4
Flaps due to landing					0.0633	-	71.9
Flap due to take-off					0.0105	29.9	-
Total in take-off					0.0318	100	-
Total in landing					0.0775	-	100

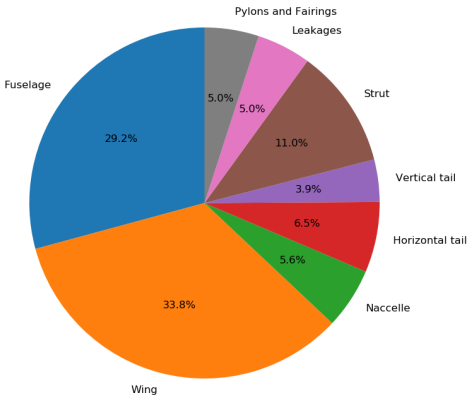

Figure 8.8: Zero lift drag breakdown per component in cruise conditions.

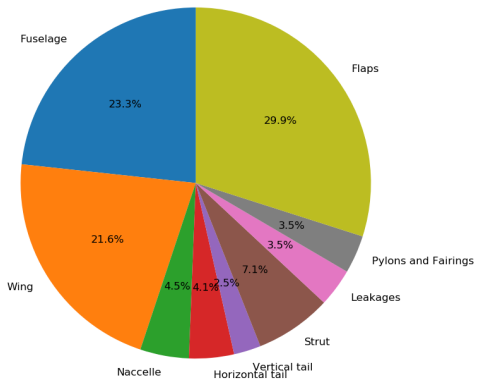

Figure 8.9: Zero lift drag breakdown per component in take-off conditions.

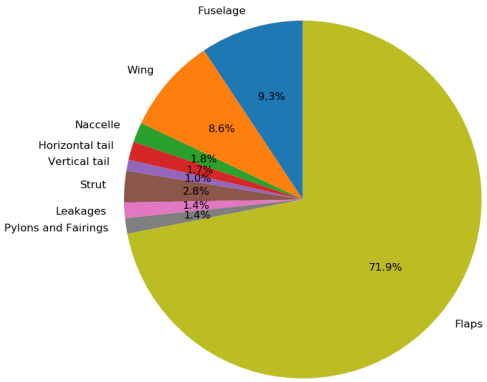

Figure 8.10: Zero lift drag breakdown per component in landing conditions.

For cruise, take-off and landing the drag polars were constructed which can be seen in Figure 8.11, Figure 8.12 and Figure 8.13. From the drag polars C_D was calculated for the specific conditions based on their corresponding C_L calculated in section 8.3, from this the L/D ratio was also calculated. The maximum L/D coefficient was approximated by the line tangent to the curve and crossing the origin. This point is also calculated by Equation 8.36 [4], based on the fact that the optimum C_D is located at $2C_{D_0}$. In Table 8.6 an overview of the values obtained from the drag polar can be seen.

$$\left(\frac{L}{D}\right)_{max} = \frac{1}{2}\sqrt{\frac{\pi A_{eff} e}{C_{D_0}}} \tag{8.36}$$

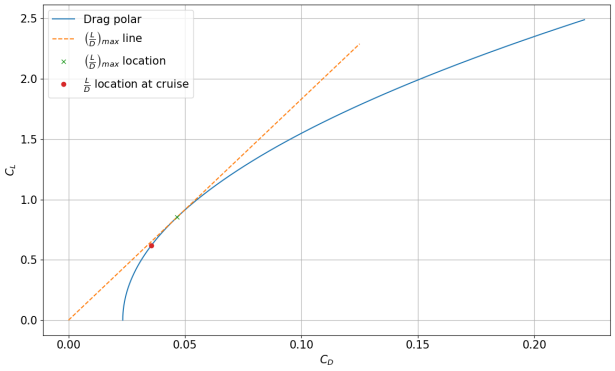

Figure 8.11: Drag polar in cruise

Table 8.6: Overview of the drag characteristics obtained from the drag polar, in cruise, take-off and landing conditions

Parameter	Cruise	Take-off	Landing
C_D [-]	0.0356	0.143	0.175
L/D [-]	17.43	13.44	10.28
$(L/D)_{max}$ [-]	18.32	16.16	10.35

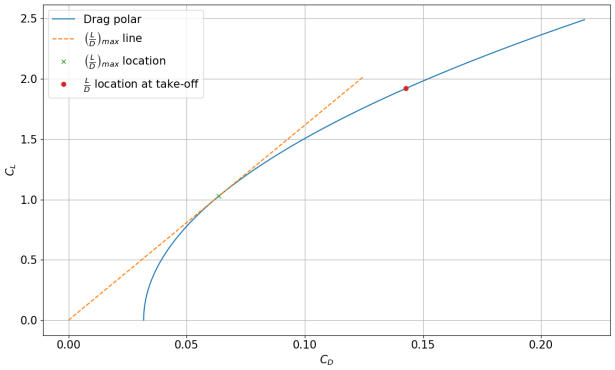

Figure 8.12: Drag polar during take-off

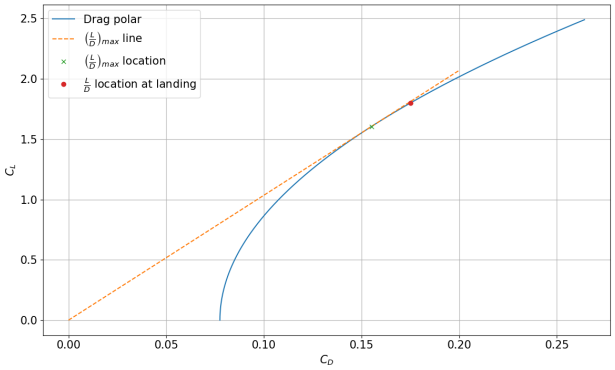

Figure 8.13: Drag polar during landing

8.5 AVL sensitivity analysis

in adition to the method described above, also the Athena Vortex Latice (AVL) method was used to analyse the aerodynamics of the aircraft, in particular the influence of the strut and the winglets. AVL models the surfaces and its trailing wakes as a single vortex sheet, which is discretised in horseshoe vortex filaments. AVL also takes into account compressibility effects by applying a Prandtl-Glauert transformation while assuming irrotationality and linearisation of the freestream. Then applying the Kutta-Joukowski theorem to each vortex the forces are computed.[4]

For the aircraft model the following components are included: wing, winglets, horizontal stabiliser, vertical fin, fuselage, engine nacelles and the strut supporting the wing. Viscous effects are not taken into account in AVL, so the zero lift drag estimation of subsection 8.4.1 is used as input. Allowing AVL to compute the induced drag and subsequently summing this with the inputted zero lift drag.

The wing, horizontal stabiliser, vertical fin, winglets and strut are modelled by defining leading edge locations and the corresponding chord length of at least 2 sections of each wing. AVL then computes the geometry by interpolating linearly between each section. For the main wing, the airfoil can be specified and its corresponding cross sectional drag polar, by specifying three points on the drag polar which AVL then quadratically interpolates on the intermediate points. The fuselage was modelled as a circular cross section where the radius were determined by the actual cross sectional area of the fuselage. Then a horizontal and a vertical surface in the shape of the fuselage were specified to account for the contribution of lift the fuselage generates when the incidence angle of the fuselage is nonzero. The engine nacelles were defined in a

[4]AVL. Retrieved May 20, 2019, http://web.mit.edu/drela/Public/web/avl/

similar way with round flat surfaces, to account for their respective drag and lift contributions. The resulting geometry is shown in Figure 8.14 and Figure 8.15.

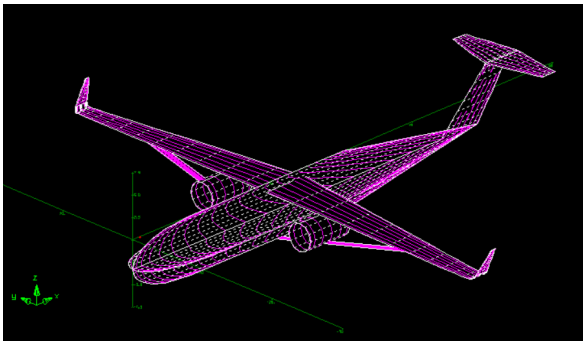

Figure 8.14: The resulting geometry as described in AVL.

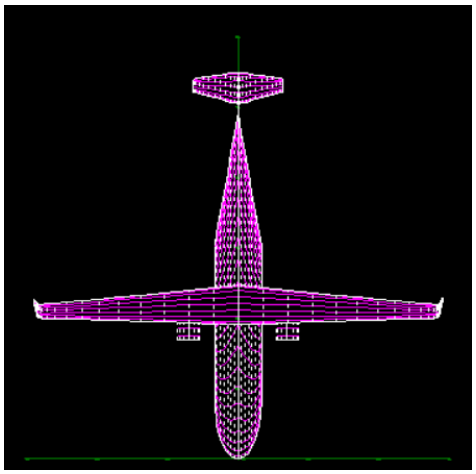

Figure 8.15: Top view of the resulting AVL geometry.

Strut sensitivity

In order to see the influence of the strut on the aerodynamics of the aircraft. AVL analysis were performed with and without the strutted wing at the same cruise conditions. As described before the angle of incidence of the strut was set such that the strut does not provide any lift during cruise. The results of the avl analysis is shown in Table 8.7 it can be seen that the angle of attack changes slightly for the strutted design, resulting in a slightly higher induced drag. The difference in the cruise drag coefficient can be attributed to the increase in zero lift drag 0.00243 and the difference in induced drag 0.00019. The L/D ratio is 18.66 for the strutted wing, which is similar to the L/D ratios found in subsection 8.4.2. However, for the non strutted wing a L/D ratio of 29.09 was found which is quite high. This can be attributed to the fact that AVL overestimates the Oswald efficiency factor considerably, which increases the eccentricity of the drag polar. Nonetheless it can be seen that for a strutted wing the L/D is reduced, so for an high aspect ratio wing does not lead to an increase of L/D in this case. This is due to the added drag of the strut and the strut itself does not produce any lift in cruise.

Furthermore, it can be seen that the drag polar is not symmetrical as in Figure 8.11 this is because that method did not take into account the non symmetry of the airfoil and therefore underestimates the drag coefficient slightly. The drag polar resulting from the AVL analysis is shown in Figure 8.16. It shows the drag penalty for a strutted wing, this decreases as the angle of attack increases, due to the added lift of the airfoil around the strut.

Table 8.7: AVL results of strutted and non strutted wing in cruise conditions.

Parameter	With strut	without strut
α [-]	1.86	1.79
$C_{D_{tot}}$ [-]	0.0315	0.0289
C_{D_i} [-]	0.00955	0.00934
ΔC_D w.r.t. strut [-]	0	0.026

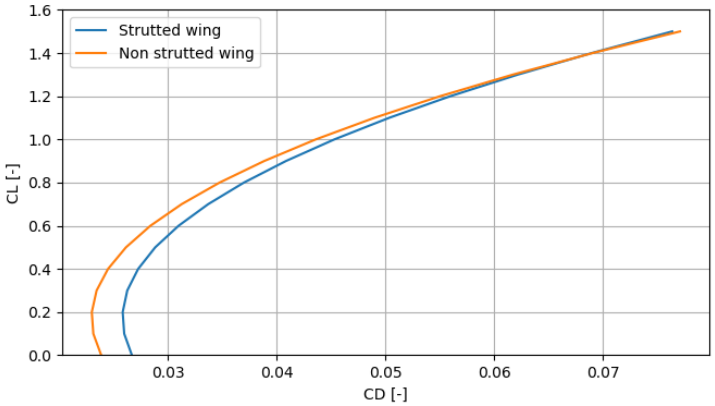

Figure 8.16: Drag polars resulting from AVL.

Winglet sensitivity

In addition to the strut analysis, also the winglets have been analysed. The winglets reduce the tip vortices that arise due to the pressure difference between the top and bottom of the wing, and thereby increase the efficiency of the wing allowing for a reduced angle of attack and induced drag.

Due to the limited time available, the decision was made to size the winglets to similar winglets on current aircraft. This resulted in the values shown in Table 8.2. The analysis then focused on finding the ideal angle the winglet has with its local vertical. Or in other words, how far does the wing bend up. In AVL a model of only the wing with winglets was created. Subsequently various winglet angles have been inputted from 0 to 40 degrees with steps of 10 degrees, and the

induced drag of each angle has been computed. The results of this analysis are shown in Figure 8.17. The figure clearly indicates that the induced drag is minimised for the lowest winglet angle. But when considering the production of the winglets, it could create some problems to have a zero degree angle at the wingtip. Therefore, the winglet angle was set to 10 degrees.
To investigate the added value of the winglets, also an AVL computation has been performed on the aircraft model with and without the winglets. First, the added zero lift drag has been computed using the method explained in subsection 8.4.1, where the form factor and friction coefficient have been assumed to be equal to that of the wing. This resulted in $C_{D_{0,winglets}}$ = 0.000619. The results of both AVL computations are shown in Table 8.8. this shows that the decrease in induced drag is bigger than the increase in zero lift drag and the overall reduction in drag amounts to 1.02%, justifying the additions of the winglets. Although the effects on the structure of the wing are not taken into account here.

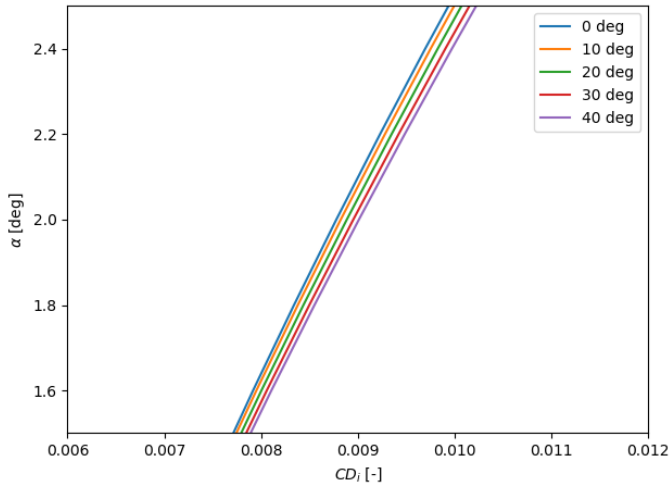

Figure 8.17: Induced drag computed in AVL using various winglet angles.

Table 8.8: AVL analysis on aircraft with and without winglets.

Parameter	Without winglet	With winglet
α_{cruise} [deg]	2.045	1.948
C_{D_i} [-]	0.00828	0.00744
ΔC_{D_i} w.r.t. without winglet	0	-0.00084

8.6 Verification

In order to verify the results, the theoretical drag polar is compared with the drag polar that is outputted from AVL. The results is shown in Figure 8.18. Again it shows that the theoretical drag polar does not take into account asymmetry of the airfoil, next to that there might be some offset in the way AVL interpolates the drag polar of the airfoil as only three points on the drag polar are inputted. Finally as the strut has an incidence angle, it was expected that the drag at zero lift would be higher as then the angle of attack is nonzero which produces induced drag. Next to this also the lift curve slope C_{L_α} was compared from Table 8.3 this turned out to be 5.70 1/rad while from avl it resulted in 6.27 1/rad, this again is attributed to the incidence angle of the strut. In a later design phase a more detailed analysis has to be performed, such that these values are closer, but for stage in the design this is deemed valid. The L/D ratio is also quite different, but as explained before AVL overestimates the Oswald efficiency factor making the drag polar more eccentric.

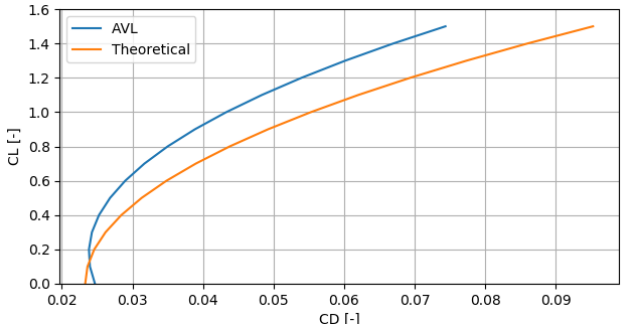

Figure 8.18: Drag polars from AVL and from theory.

Now focussing on the requirements specified earlier in this chapter. The cruise angle of attack was found to be around 2 degrees and the stall angle of attack was found to be 13.67 degrees. Satisfying requirements BIB-SBS-AED-02 and BIB-SBS-AED-04. The L/D ratio was found to be 17.43 so the design is above the ratio of 15 specified in requirement BIB-SBS-AED-03. The drag divergence Mach number was found to be above the cruise Mach number for a t/c of 0.15 so only a small part of the wing experiences an increase of drag, satisfying requirement BIB-SBS-AED-05.

8.7 High lift devices

High lift devices (HLD) are devices, usually flaps that are placed on the leading and trailing edge of the wing. In the fuctional analysis the function and risks of the high lift devices are discussed. The requirements that follow from these functions and risks are also mentioned.

8.7.1 Functional analysis

The HLDs will be used to provide extra lift during take-off and landing. They will be deployed before the take-off or landing to the desired position. Actuators that will be chosen in this section, will ensure that the HLDs are able to move to this desired position. HLDs are used because an increase of the lift coefficient results in a lower flight speed needed to fly, which is favourable for take-off and landing conditions. The function of the HLDs during take-off is to provide an increase in lift, optimised for the optimal rate of climb. This means that the possible increase in drag is limited. During landing, the HLDs have an extra function. Besides increasing the lift of the wing, the HLDs should cause drag in order to slow the aircraft down. The maximum lift coefficient caused by the HLDs in combination with the engine take-off thrust combined determine the required take-off length. The HLDs combined with the brakes of the aircraft determine the required runway length for landing.

Risk analysis

The HLD's are used during take-off and landing to ensure a safe flight speed of the aircraft. Risks that come up during the design of the HLDs are listed below.

- **HLD actuator fails:** the actuator that deploys the HLDs to a desired position may fail either due to a failure of the actuator itself or due to failure of the hydraulic system. The risk of the hydraulic system is mitigated in section 11.4. In order minimise the severity of one actuator failing, the size of the HLDs should be limited.
- **Angle of attack during take-off and landing is too large:** the angle of attack should be limited in order to avoid tip-over, ensure comfortable conditions and allow for enough vision of the pilots.
- **The wing stalls during take-off or landing:** wing stall during take-off or landing results in an uncontrollable aircraft, which leads to dangerous situations. The difference between the stall and the actual lift coefficient shall be high enough.

Requirements

The requirements that influence the design of the HLDs are listed below.

- **BIB-SBS-FLP-01:** The aircraft shall be able to take-off from a runway of 2,700 m at sea-level at MTOW.
- **BIB-SBS-FLP-02:** The aircraft shall be able to land on a runway of 2,700 m at sea-level at MLW.
- **BIB-SBS-HLD-01:** The HLD's shall provide an increase in lift coefficient during take-off optimised for the rate of climb
- **BIB-SBS-HLD-02:** The HLD's shall provide an increase in both lift and drag during landing
- **BIB-SBS-HLD-03:** The HLD's shall be able to be deployed in three positions.
- **BIB-SBS-HLD-04:** The HLD's shall be redundant.
- **BIB-SBS-HLD-05:** The angle of attack during take-off and landing shall be below 14 degrees.
- **BIB-SBS-HLD-06:** The HLD's shall fit in the wing structure.

8.7.2 Method

Multiple types of HLD's exist for both the leading edge and trailing edge. In general more complex HLD's are able to increase the maximum lift coefficient by an even higher amount. Existing HLD's described in a NASA report [28] were analysed and their performance was compared with respect to each other. When designing the HLD's, a comparison has to be made between an increase in lift coefficient versus an increase in complexity and thus weight and costs. When the maximum lift coefficient is lower, the required thrust during take-off will be higher. This causes that the design of the HLD's is integrated with the engine design in order fulfil the requirements BIB-SYS-TEC-06 and BIB-SBS-FLP-01. Since The six-step approach of F. Oliviero is used to design the HLDs [21]. The available area for the HLD's will be determined first in the next paragraph, then the leading edge devices will be sized and the trailing edge devices thereafter.

In order to determine which HLDs are suitable for the EcoHopper 450, the available area of the wing for HLDs has to analysed first. When the available area increases, the increase in lift will also increase. It has been determined that the aileron takes up space until 71% of the trailing edge span as described in section 9.3 and that the fuselage takes up roughly 7% of the wing span. So the trailing edge flaps could be placed from 10% to 71% of the wing span. Starting at 10% should leave enough space between the fuselage and the flaps. Using no discontinuities increases the performance of the flaps. The leading edge HLDs could be placed from 10% to 97% of the wing span, while keeping space for the engine pylon of approximately 4%. The leading edge HLDs should leave space on the leading edge for the engine pylon. The spars of the wing are placed at 10% and 55% of the chord, and so the leading edge HLDs may use 8% of the chord and the trailing edge 38% of the chord in order to ensure enough space for the actuators. Oliviero suggest sizes in this range for the HDLs.

Leading edge high lift devices

Leading edge HLDs extend the lift curve such that a higher maximum lift coefficient may be reached at a higher angle of attack by delaying stall behaviour. Many kinds of leading edge HLDs exist [21], however not all of them are used on commercial aircraft [28]. The most used leading edge HLDs are: nose flaps, Krueger flaps, Krueger VC flaps and three position slotted leading edge flaps (slats). According to F. Oliviero, slats provide the highest increase of C_{Lmax} [21]. The increase in C_{Lmax} of the slats is approximately 0.4 compared to 0.3, what the other devices provide. Slats also have the benefit that they increase the wing surface area slightly, which causes a lower angle of attack needed at C_{Lmax}. The effect of an increase in surface area on the lift curve slope is shown Equation 8.37, where S represents the surface area when the HLDs are deployed. The weight of the slats is approximately 29 kg/m^2 compared to 25 kg/m^2 of Krueger flaps according to NASA [28]. The increase in C_{Lmax} is higher than the increase in weight, so slats have been chosen as leading edge HLDs. The three position slats refers to the slat having positions for cruise, take-off and landing. Typically aircraft have three to six slats [28], the amount of slats of the EcoHopper 450 has been set to five, which ensures that the slats are not too large. Their width is now 4.65 m. Five slats ensure a high enough redundancy too. The slats are actuated by one circular arc track per slat. The slat lay-out is shown in Figure 8.19.

$$C_{L\alpha flapped} = \frac{S'}{S} C_{Laclean} \tag{8.37}$$

Trailing edge high lift devices

Again, many types of trailing edge HLDs exist, the most HLDs on commercial aircraft are; single, double (fixed vane, articulating vane and main/aft), and triple slotted fowler flaps. Fowler flaps do have the benefit that they provide a relatively large increase in C_{Lmax} and that they increase the surface area of the wing. Fowler flaps are relatively complex too, however, their increase in performance is desired. According to NASA manufactures Boeing and Airbus strive for more simplicity in the trailing edge HLDs while keeping the required increase in C_{Lmax} [28]. A relatively high priority is put into the design of single slotted fowler flaps [29]. Using single slotted flaps, a simpler actuation mechanism is possible, which will lower the weight significantly. In order to select the trailing edge HLDs for the EcoHopper 450, a comparison of the increase in C_{Lmax} of suitable flaps is compared to the weight of the flaps. The results are shown in Table 8.9. The ΔC_{Lmax} is calculated using Equation 8.38 from F. Oliviero, ΔC_{lmax} represents the increase in lift coefficient due to flaps on an airfoil and Swf the wing area affected by the flaps. The deflections of the flaps for take-off and landing has been set to 15% and 40% for the single slotted flap and to 20% and 40% for the others. Visible in the table is that the weight of the flaps increases rapidly compared to the ΔC_{Lmax}, the weight increase is present due to the increase of flaps, and more complex actuating mechanisms. At first sight, the single slotted flaps result in an acceptable performance, while keeping the weight low. However, does the provided C_{Lmax} has to be checked together with the engines in order to determine the runway length. The analysis performed resulted an runway length required of 2548 m for take-off and 2657 m for landing, which fulfils the requirements. An higher C_{Lmax} would result in a weight reduction of the engines, or a better runway length performance. The weight increase of the flaps is too much and so the benefits can not compensate for this.

$$\Delta C_{Lmax} = 0.9 \Delta C_{lmax} \frac{Swf}{S} cos\Lambda_{hingeline} \tag{8.38}$$

A remarkable result of the weights shown in Table 8.9, is that the weight of the single slotted flaps differs heavily between using a Boeing, the hooked track mechanism, and an Airbus, the link/track end support. The differences occur due to the relatively simple mechanism used by Airbus. The airbus mechanism consists of a pair of straight tracks on fixed structure for the front attachment of the flap and an upright link as the aft attachment. The flap is deployed by means of a roller carriage. The mechanism is designed to optimise fowler deflection while keeping the weight low [29]. The forward link of the Boeing mechanism is hinged to a fitting underneath the wing box and the aft link penetrates the aft cove and is hinged off a fitting on the rear spar. The flap connects to the lower ends of the links through a very long flap fitting. The actual reason why Boeing uses heavier mechanism is not certain. It could be because Boeing has used relatively many double or triple slotted flaps in the past [28], while Airbus mostly uses single slotted flaps. More research of Airbus results in more optimal mechanisms. The final selected trailing edge HLDs will be single slotted fowler flap, using a link/track end support. Three separate flaps are used for each wing, because the total span used for flaps is relatively high. When two flaps would be used, their width would be approximately 8.5 m. Due to the slenderness of the wing and so the HLDs is this width too handle if one actuator fails. The flap width is now 5.7 m. Each flap has two fairing underneath it to carry the actuators, their location is at 25% and 75% of the flap span. The drag influence of the fairings during cruise has not been included in the aerodynamic analysis yet, and should be added in the next design phase.

Table 8.9: Trailing edge high lift devices results.

High Lift Device	ΔC_{Lmax} over full wing (TO/LA)	Weight of flaps [kg]
Single slotted fowler flap, Boeing mechanism	0.72 / 0.93	2328
Double slotted flap	0.86 / 1.15	3673
Triple Slotted Flap	1.03 / 1.36	4184
Single slotted flap, Airbus mechanism	0.72 / 0.93	1647

8.7.3 Results

The total weight of the slats have been calculated to be is 509 kg, while the weight of the trailing edge flaps is 1647 kg. Their combined weight is 2156 kg. The C_{Lmax} of the entire wing including all HLDs have found to be 2.8 for the take-off configuration and 3.0 for the landing configuration. Using Equation 8.39 and Equation 8.37, the angle of attack at C_{Lmax} could be determined. An extra $\Delta\alpha_{C_{Lmax}}$ is added too, as will be described in Figure 8.3.1. As result, the stall angle of attacks are 16.1 degrees and 14.7 degrees during take-off and landing respectively. During take-off and landing, the actual angle of attack will be lower, namely 11.3 degrees and 12.3 degrees. The angle of attack during take-off and landing is based on the C_L 10% lower than the C_{Lmax}. These angles of attack do not result in difficulties with the control and stability of the aircraft. The lay-out of the HLDs is shown in Figure 8.19

$$\Delta\alpha_{0L} = \Delta(\alpha_{0l})_{airfoil}\frac{Swf}{S}cos\Lambda_{hingeline} \tag{8.39}$$

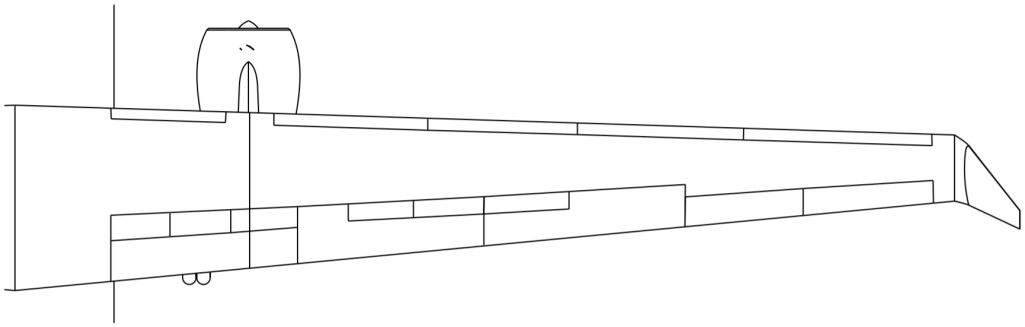

Figure 8.19: Top view of the wing.

8.7.4 Verification

The method used by F. Oliviero [21] is also used by Raymer [4]. The method uses assumptions on the performance of the HLDs. Since the values of the method are used on statistical data, the values are assumed to be valid. Noticeable is that the method assumes that all of the same type of HLDs provide the same increase in lift. Probably the performance of single slotted flaps of Boeing and Airbus differ in reality. This effect is not taken in consideration, so the Airbus mechanism might be chosen on wrong information. However, since Airbus always uses single slotted flaps, it could be assumed that more research is put into these flaps. This causes the actuation mechanisms to be lighter, while keeping the same performance. The actual provided $\Delta\alpha_{C_{Lmax}}$ will thus probably differ from the currently estimated one. However, since statisitcal data shows relatively consistent results on the performance of HLDs, a confidence bound of 5% could be used. The weight is purely based on statistical data too, and so might differ in reality.

8.8 Spoiler design

Spoilers are placed on top of the wing in front of the trailing edge HLD's. They function as primary and as secondary flight control. Although the spoilers may be referred to as control surfaces, spoilers mainly influence the lift of the aircraft and are therefore described in this chapter.

8.8.1 Requirement analysis

This section covers the requirements that apply to the spoilers are discussed.

Functional analysis

The spoilers have multiple functions. The spoilers will be deflected upwards with use of actuators such that one of the functions will be fulfilled. The upwards deflected spoiler causes flow separation, which in return causes a decrease in lift and increase in drag. The first function is aiding with roll control. When spoilers are used for roll control they are referred to as spoilerons. Spoilerons are quite beneficial to the design of the EcoHopper 450 since when ailerons, which are located close to the the wing tips, are used for roll control at high speeds, the wing twist introduced might be too large. The wing twist may affect the performance of the ailerons which might cause undesired control reversal. When spoilerons which are located closer to the wing root, are used, will the implied wing twist be reduced.

The spoilers also act as lift dumpers and brakes. The pilot of the aircraft may want to dump lift in order to descent quicker, or to provide more normal force on the wheels to assist with braking. Bouncing during landing is also prevented when lift is dumped. The aircraft needs to reduce speed when landing and the spoilers aid to the braking by increasing the drag.

Risk analysis

The only risk of the spoiler is the risk of an actuator failing. This shall be mitigated by providing enough redundancy.

Requirements

No hard values on the requirements of the spoilers could be set, since they mostly aid another system with their function. The requirements that have an influence on the spoilers are listed below.

- **BIB-SBS-FLP-02:** The aircraft shall be able to land on a runway of 2,700 m at sea-level at MLW.
- **BIB-SBS-STC-04:** The aircraft shall be controllable during all flight phases.
- **BIB-SBS-SPL-01:** The spoilers shall fit behind the aft spar and before the trailing edge flaps.
- **BIB-SBS-SPL-01:** The spoilers shall be able to rotate 60% upwards.

8.8.2 Method

Since the spoilers mostly aid other systems with their function, no clear sizing method of the spoilers is present. Due to time limitations will there be no design based on calculations. The spoilers will be sized based on reference aircraft. The size and number of the spoilers will be determined first and the placement of them thereafter. The B777, which has a larger surface area, but roughly the same span, uses seven spoilers: two inboard and five outboard, and their area is 5.5% of the total wing area [30]. Their chord length is 12% of the wing chord. The A320, which has a much smaller wing area and wing span, uses five spoilers: one inboard and four outboard. The total spoiler area is 7.1% of the wing area and their chord is approximately 18% of the chord [31]. The data results in the fact that spoiler size and number is dependent on the wing size.

8.8.3 Results

In order to meet roll control requirements at different speeds, spoilers are placed at different locations on the wing span. Some will be placed near the middle of the wing to provide roll control while the may be used as lift dumpers, while others are placed near the fuselage and mainly act as lift dumpers. At lower speed are the ailerons used for roll control, since the location makes them the most efficient.

Based on the reference aircraft, there will be used six spoilers in the design of the EcoHopper 450. Three inboard spoilers will be present, being 16% of the chord length long. These spoilers will act purely as lift dumpers. Three spoilers are used instead of two, since the chord of the EcoHopper 450 is relatively small. This causes that the chord of the spoilers are small as well, and so, a higher number of spoilers needs to be placed next to each other to ensure a high enough surface area of the spoilers. The three inboard spoilers will be equal in width and placed before the inboard flap as shown in Figure 8.19. Three outboard spoilers will be used, with a length of 12% of the chord. These will provide enough roll control at high speeds. Two of the spoilers are placed in front of the middle flap and one of them in front of the outboard flap. The total spoiler area has to be determined to be 6.5% of the wing area.

9 Stability and control analysis

In order to have a stable and controllable aircraft during all phases of the mission, a detailed stability and control analysis will be provided in this chapter. First of all, the undercarriage will be designed in section 9.1 by determining the centre of gravity range and the constraints regarding tip-over and clearances during ground handling. Subsequently aircraft properties regarding pitch, roll and yaw will be analysed by sizing the elevator, aileron and rudder in section 9.2, section 9.3 and section 9.4 respectively.

9.1 Landing gear

Though primarily designed for aeronautical operations, controllability and stability when on the ground offers a significant challenge. The positioning and sizing of the landing gear should take both these factors into account. In this section the landing gear sizing is presented. The sizing is based on requirements following from the intended functions of the undercarriage. Preliminary results are presented, after which a sensitivity analysis is performed to better understand the results. In the final subsection the requirements are verified.

9.1.1 Requirements analysis

Functional analysis

The undercarriage of an aircraft has five main functions, as per Lecture 7 of the ADSEE-I course [19].

1. Absorb landing and taxiing shocks.
2. Provide ground maneuvering ability.
3. Provide braking capability.
4. Allow for aircraft towing.
5. Protect the ground surface.

From these functions certain requirements follow. The identified requirements for each function are summarised below.

Absorb landing and taxiing shocks: The undercarriage should decrease the vertical velocity of the aircraft to zero. Furthermore, as runways and other airport surfaces are not perfectly smooth some shocks during taxiing are expected. All these loads should be adequately absorbed by the undercarriage. It is presumed the vertical loads presented by touchdown are limiting. During crabbed landing large shear loads are also encountered, which should also be adequately absorbed by the undercarriage.

Provide ground maneuvering ability: Aircraft generally steer with the nose gear. This is only possible when adequate friction force is supplied by the nose gear. Thus, a large enough part of the weight of the aicraft should be carried by the nose gear to supply adequate normal force in order to generate enough friction force.

Provide braking capability: The aircraft should be able to brake within an acceptable distance. This braking force introduces shear forces into the undercarriage which it should be able to withstand.

Allow for aircraft towing: Aircraft pushback introduces more shear loads into the undercarriage which it should withstand. Furthermore points of application for the towing vehicles should be present.

Protect the ground surface: The ground surface of a runway should not be damaged by the aircraft, this imposes requirements on the pressure the aircraft may exert on the ground surface.

Risk analysis

The (placing of) the landing gear carries some risks with it. These risks will be taken into account in designing and placing the landing gear. The most important risk is the event of a flat tire, which shall be mitigated by absorbing the load by the remaining tires.

Requirements

In the Baseline Report certain requirements influencing the undercarriage were identified, listed below [8]. The additional requirements following from the functional and risk analyses are added to this list under the identifier UND.

- **BIB-SBS-STC-03** The aircraft shall possess static stability at every moment.

- **BIB-SBS-OPS-05** The aircraft shall not tip-over during loading on ground.
- **BIB-SBS-UND-01** The undercarriage shall absorb all vertical loads encountered.
- **BIB-SBS-UND-02** The undercarriage shall absorb all shear loads encountered.
- **BIB-SBS-UND-03** The undercarriage shall provide adequate steering authority to taxi at all servicable airports identified in the market analysis.
- **BIB-SBS-UND-04** The aircraft shall be rated to land on the runway with the lower Load Classification Number of all servicable airports identified in the market analysis.

9.1.2 Method

Component sizing

A Class I sizing is performed for the undercarriage. The method relates the MTOW to the amount of nose and main wheels based on statistics. Based on the amount of wheels the number of struts is determined. For large transport aircraft the number of main gear wheels is determined by Equation 9.1, rounded to the nearest multiple of four. The number of struts is then determined using Equation 9.2.

$$N_{mw} = \frac{W_{TO}}{210,000} \tag{9.1}$$

$$\begin{aligned} N_{mw} &\leq 12 : 2 \text{ struts} \\ N_{mw} &> 12 : 3 \text{ or } 4 \text{ struts} \end{aligned} \tag{9.2}$$

Each runway is rated using a Load Classification Number (LCN), a measure of runway strength. After obtaining the lowest LCN of the runways the aircraft should be able to land on, Equation 9.3 can be used to determine the tire pressure.

$$p_{tire} = 430 * \ln(LCN) - 180 \tag{9.3}$$

Tires are selected based on tire pressure and static load per tire. The equivalent single wheel loads for the nose and main gear are calculated using Equation 9.4. It should be noted that $P_{mw} * N_{mw} + P_{nw} * N_{nw}$, or the sum of the forces carried by all tires, is equal to W_{TO}. The scalars in the equations (0.08 and 0.92) signify the nose gear carries 8% of the load, ensuring adequate ground steering authority. Some examples of possible tire options are provided in Figure 9.1.

$$\begin{aligned} P_{mw} &= \frac{0.92 * W_{TO}}{N_{mw}} \\ P_{nw} &= \frac{0.08 * W_{TO}}{N_{nw}} \end{aligned} \tag{9.4}$$

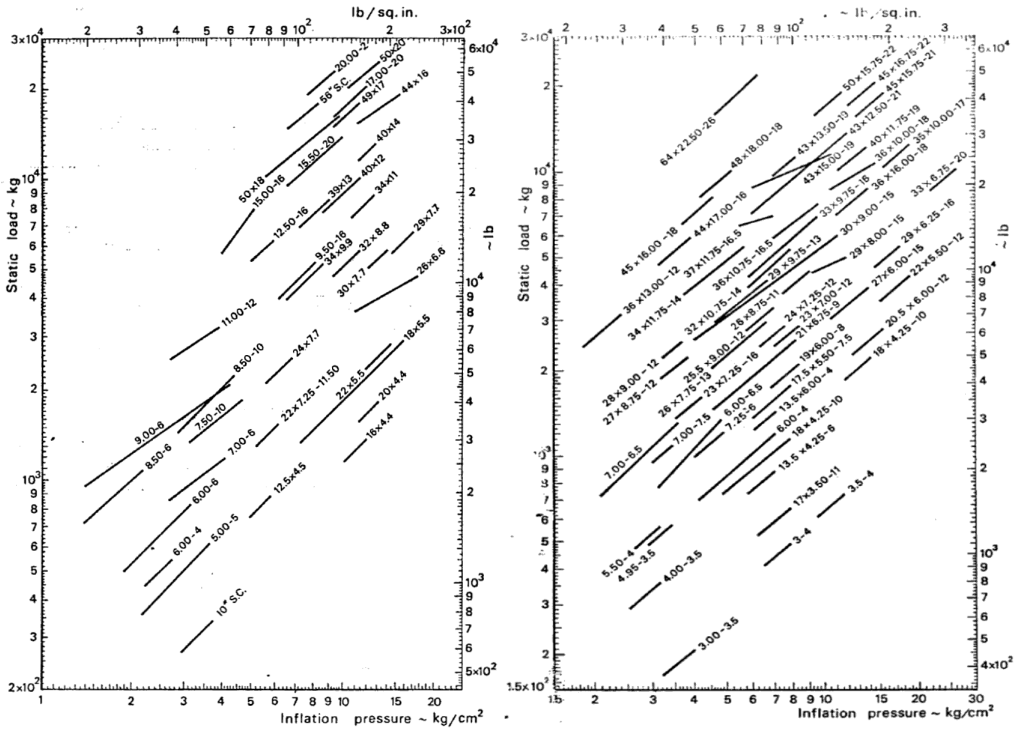

Figure 9.1: Selection of American and British aircraft tires [3].

Centre of gravity range

In order to establish the longitudinal and lateral disposition of the undercarriage, the centre of gravity (cg) range for the aircraft had to be determined. The cg range along the longitudinal x-axis of the aircraft was constructed by generating a loading diagram for the aircraft and subsequently the z-location of the cg was established by evaluating the cg's of the fuselage and wing group. The y-location of the cg was assumed to be on the centre line of the fuselage, as the aircraft is symmetric along this axis.

The loading diagram for the cg range along the x-axis was developed by loading the empty aircraft with cargo, passengers in the window seats, aisle seats, middle seats and fuel respectively. The result, depicted in Figure 9.2, shows a cg range of 0.53% of the mean aerodynamic chord (MAC). The wing position corresponding to the minimum tail size was placed at $X_{LEMAC} = 19.48$ m, which followed from the scissor plots explained in further detail in the Mid-term Report [1]. Since the wing is located slightly to the front of the aircraft, the aircraft operational empty weight (OEW) cg location is located slightly more to the left in the loading diagram (0.34% MAC) compared to the other weight components. Furthermore it can be seen that the aisle seats have a larger contribution to the cg excursion than the window and middle seats, due to the seating abreast configuration that was established in subsection 6.3.1.

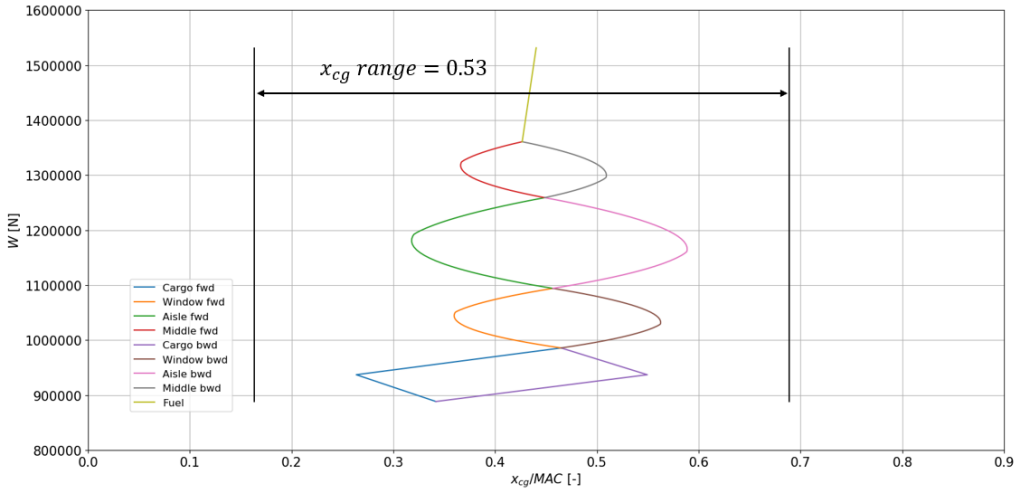

Figure 9.2: Loading diagram for the final design with the corresponding centre of gravity range.

For the vertical position of the centre of gravity a simplified model of the aircraft was made by dividing it into the fuselage and the wing group. All weight components, including payload and fuel, were taken into account in Equation 9.5 that relates the weights and cg's of the individual groups to the overall cg of the aircraft on the z-axis. By drawing the components that belong to the aforementioned groups, the cg locations were obtained resulting in the wing and fuselage group cg locations of $z_{cg_{WG}} = 6.37$ m and $z_{cg_{FG}} = 3.73$ m respectively, measured from the bottom of the fuselage. The total cg of the aircraft was found to be $z_{cg} = 4.48$ m.

$$z_{cg} = \frac{z_{cg_{WG}} W_{WG} + z_{cg_{FG}} W_{FG}}{W_{WG} + W_{FG}} \tag{9.5}$$

It should be noted however, that this cg location is only valid at the maximum take-off weight (MTOW). During a typical mission the aircraft will burn most of the fuel, shifting the cg location on the z-axis to the bottom of the aircraft. This was not taken into account for the landing gear dispositioning, since the highest cg location was found to be critical for the lateral tip-over constraint.

Longitudinal disposition

The longitudinal position of the gear is affected by a number of parameters. First of all, the aircraft should be statically stable on the ground for the entire cg range. Therefore, the most aft cg location of the previously determined range should be taken into account. A tip back angle θ of 15 deg is imposed to prevent longitudinal tip-over. The aircraft must tip back during takeoff, so an adequate scrape angle must be ensured. A scrape angle of 15 deg is initially assumed. This scrape angle requirement increases the height of the landing gear. In turn, an increased cg height increases the longitudinal distance from the cg to the main gear due to the longitudinal tip-over requirement.

Having determined the distance from the most aft cg to the main gear, the longitudinal location of the nose gear can easily be derived using a sum of forces and sum of moments static analysis. As previously mentioned, to ensure adequate steering capability 8% of the total weight will be carried by the nose gear. Requiring the sum of moments about the cg to equal zero leads to a relation for the nose gear location:

$$x_{nw} = \frac{P_{mw}}{P_{nw}} * x_{mw} \tag{9.6}$$

Which is solvable by requiring $P_{mw} = 0.92 * W_{TO}$ and $P_{nw} = 0.08 * W_{TO}$.

Lateral disposition

Lateral disposition of the undercarriage is driven by three key requirements: tip clearance, engine clearance and lateral tip over. The governing equations for these requirements are provided in Equation 9.7a, Equation 9.7b and Equation 9.7c, for $\phi > 5$ deg and $\psi < 55$ deg, defined in Figure 9.3, with span b, lateral engine placement y_e and tip, engine and cg heights z_t, z_n and z_{cg}, respectively.

$$y_{MLG} > \frac{b}{2} - \frac{z_t}{\tan(\phi))} \tag{9.7a}$$

$$y_{MLG} > y_e - \frac{z_n}{\tan(\phi)} \tag{9.7b}$$

$$y_{MLG} > \frac{l_n + l_m}{\sqrt{\frac{l_n^2 \tan^2(\psi)}{z_{cg}^2} - 1}} \tag{9.7c}$$

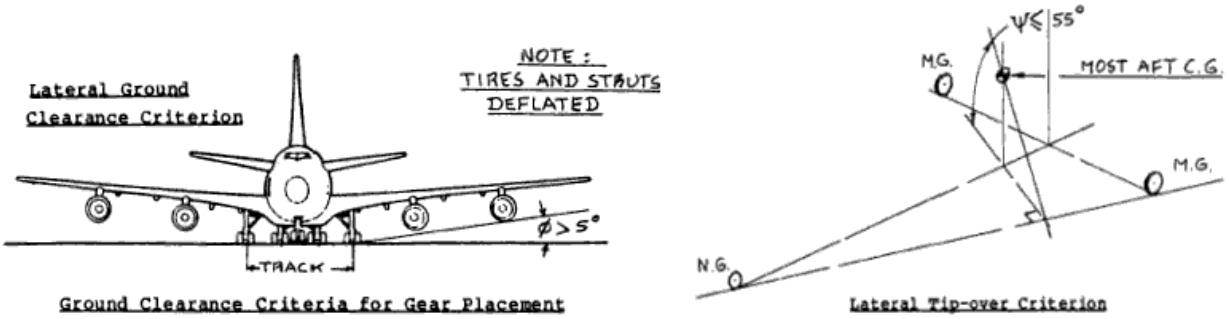

Figure 9.3: Lateral tip-over angle definitions [3].

Due to the high-wing configuration the engines and wing-tips are shifted up compared to conventional aircraft significantly. The cg is also shifted up somewhat. For these reasons it is expected the lateral tip-over criterion will be critical.

9.1.3 Results

Initial results

Results of the Class I component sizing are presented in Table 9.1. In order to be competitive with similar aircraft, a tire pressure of 160 psi or 1.1 MPa was selected, leading to a minimal LCN rating of 80. Initial tire sizing results are also presented.

Table 9.1: Initial strut and tire sizing.

Parameter	Output
N_{mw} [-]	8
N_{nw} [-]	2
N_{struts} [-]	2
p_{tire} [MPa]	1.1
$D_m \times b_m$ [m × m]	1.14 x 0.40
$D_n \times b_n$ [m × m]	0.81 x 0.23

Now that the method for the landing gear disposition had been established as well, the computations were performed with an initial value for the tip-over and scrape angle of $\theta = 15$ deg and the tailcone length computed in section 6.3 of $l_{tailcone} = 14.74$ m. These inputs yielded an initial undercarriage placement which is shown in Table 9.2. Note that for the analysis, a shock absorber stroke length of 0.5 m was used as a preliminary estimate. Later mechanical analysis will more precisely size the shock absorber. Furthermore, the x-locations are measured from the nose, the y-location from the fuselage centreline and the z-locations from the bottom of the fuselage. The most remarkable result is that the nose

landing gear is in front of the nose of the fuselage. Therefore, it could be concluded that the landing gear positioning with the initial inputs was not feasible.

Table 9.2: Initial nose and main landing gear locations

Parameter	Output
x_{nlg} [m]	-1.26
x_{mlw} [m]	24.24
y_{mlg} [m]	5.95
z_{nlg} [m]	3.27
z_{mlg} [m]	3.27

Sensitivity analysis

To be able to reach a feasible landing gear design, a sensitivity analysis on the tip-over angle θ and the length of the tailcone was performed. The reasoning behind choosing these parameters for the sensitivity analysis was that they had the largest impact on the longitudinal positioning of the undercarriage and thus would might change the nose landing gear such that it would fit under the fuselage. The tip-over angle was changed to 13 and 11 deg and the tailcone length was elongated with 5 and 10 m. The sensitivity on the landing gear was purely evaluated when varying one single parameter at the time, because then the effect would become more directly visible.

From the results of sensitivity analysis presented in Table 9.3, it can be concluded that both the tip-over angle and the tailcone length significantly influence longitudinal position of the undercarriage. Moreover, an elongated tailcone is beneficial for the lateral position. Since a reduced tip-over angle increases the probability of the aircraft actually tipping over, reducing the angle should be avoided when possible. Furthermore, through visual analysis of the fuselage it was found that elongating the tailcone with more than 5 m, the passenger would not fit in the cabin anymore and possible problems with engine clearance under the fuselage could arise due to the reduced z-location of the landing gear.

Table 9.3: Sensitivity of the landing gear positioning to changes in the longitudinal tip-over criterion and tailcone length

Parameter	No adjustments	$\theta = 13$ deg	$\theta = 11$ deg	$l_{tailcone} + 5$ m	$l_{tailcone} + 10$ m
x_{nlg} [m]	-1.26	2.78	6.58	2.59	6.44
x_{mlw} [m]	24.24	23.89	23.56	23.91	23.57
y_{mlg} [m]	5.95	5.77	5.60	4.97	4.00
z_{nlg} [m]	3.27	2.96	2.64	2.02	0.77
z_{mlg} [m]	3.27	2.96	2.64	2.02	0.77

Final results

To conclude, it was found that elongating the tailcone with 5 m would yield the best result without changing the design of the aircraft too much. The only problem that arose was that the y-location of the main landing gear was relatively far from the fuselage, which is a problem that is frequently encountered in the design of high wing aircraft [19]. The solution for this problem was the placement of an additional strut with a stiff shock absorber under the centre of the fuselage and two struts with less stiff shock absorbers on the y-location specified in Table 9.3. This is done so a larger part of the aircraft weight load is carried by the vertical centre strut. With this configuration the aircraft would comply with the lateral tip-over requirement without using excessively complex and heavy structures for the main landing gear. A render of the layout is presented in Figure 9.4.

9.1.4 Verification

Since the method for sizing the undercarriage was rather straightforward, the verification of the process was done by calculating the expected output by hand. Minor differences were found due to rounding errors, but these were not significant. Additionally, the landing gear was designed such that all the aforementioned requirements were met. By incorporating these requirements, the EcoHopper 450 will be statically stable on the ground and will not experience tip-over at any moment on the ground. The undercarriage will be sized to absorb all vertical and shear loads encountered during landing, take-off and taxiing after a more in-depth structural sizing at a later point in the design phase. Even in the event of a flat tire, the pressure in the remaining tires is still acceptable and thereby the risk is mitigated.

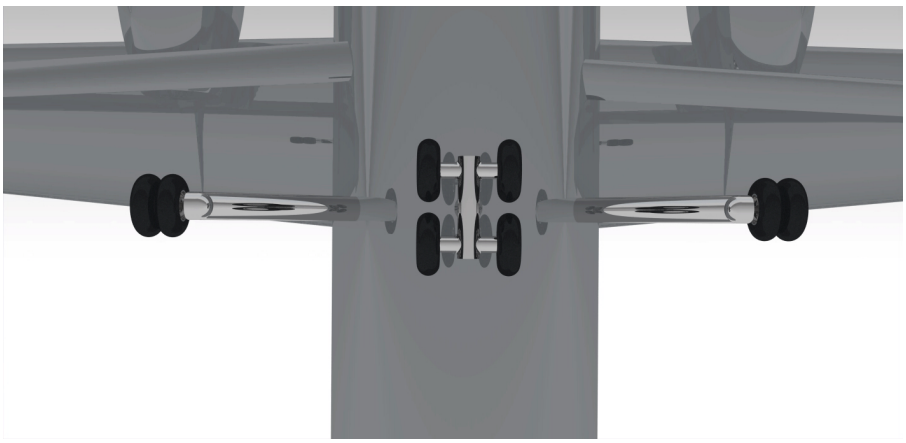

Figure 9.4: Landing gear design overview.

9.2 Elevator

The elevator is the control surface mounted on the horizontal tail of an aircraft that is used to induce pitching motion. The control surface is used to control the aircraft at all stages of its mission and is considered as a primary control surface. A more in depth functional analysis will first be provided, in which the requirements for the elevator will be outlined. Subsequently the sizing method will be explained after which the results and a sensitivity analysis are provided. Finally, the method will be verified and the compliance with requirements will be presented.

9.2.1 Requirements analysis

Functional analysis

The main function of the elevator is to control the aircraft along the longitudinal axis, that is pitching the aircraft up and down by means of positive and negative deflection of the elevator respectively. When the elevator is deflected, the camber of the horizontal tail increases which results in the production of additional lift and thus an increased moment around the centre of gravity, causing the aircraft to pitch either up or down depending on the direction of the deflection. Hereby the pilot is able to control the pitch angle of the aircraft.

During cruise, elevator deflections are rather small since the elevator is commonly designed to have zero deflection in this flight phase to minimise trim drag. During take-off and landing on the other hand, the elevator experiences large deflections, since the airspeed is lower than in cruise and more extreme pitch attitudes are required.

The most critical condition for the elevator is experienced during take-off, since the aircraft needs to be capable of reaching a certain rotational acceleration to comply with the take-off requirements. Additionally the aircraft has the maximum weight during take-off, causing a larger nose-down pitching moment. The sizing method of the elevator for this aircraft will thus be based on the take-off condition [32].

Risk analysis

The risks most commonly associated with elevators are the occurrence of horizontal tail stall and occurrence of the control surface jamming.

Requirements

From the functional and risk analyses of the elevator the requirements could be derived. For large passenger aircraft, an angular acceleration during take-off of 6 deg/s^2 is commonly used [32]. The following requirements for the elevator apply:

- **BIB-SBS-STC-04** The aircraft shall be controllable during all flight phases.
- **BIB-SBS-STC-05** The stability and control subsystems shall comply with CS-25.143 - CS-25.255.
- **BIB-SBS-ELV-01** The horizontal tail shall not stall in case the elevator is deflected to its maximum extent.
- **BIB-SBS-ELV-02** The angular acceleration of the aircraft during take-off shall be at least 6 deg/s^2.

9.2.2 Method

Take-off analysis

During take-off the aircraft experiences a horizontal acceleration, and subsequently an angular acceleration of the centre of gravity about the main landing gear. The required lift that the entire horizontal tail needs to produce at this instant is found by moment equilibrium as shown in Equation 9.8. Since the aircraft needs to rotate around the main landing gear, the moment equilibrium was taken around that point. Furthermore the most forward centre of gravity location was used, as this caused a larger moment of the weight around the main landing gear to be counteracted by the elevator. The

moments caused by the weight M_W, thrust M_T, horizontal acceleration M_{acc} and resulting angular acceleration $I_{yy_{mg}}\ddot{\theta}$ all have a negative contribution to the required horizontal tail lift L_h, whereas the moments from the lift of the fuselage and wing $M_{L_{wf}}$, the aerodynamic centre $M_{ac_{wf}}$ and the drag M_D have a positive contribution. Note that it is expected that the horizontal acceleration would cause a moment with a positive sign, but since it is a resultant acceleration it has a negative sign.

$$L_h = \frac{M_{ac_{wf}} + M_{L_{wf}} - M_W + M_D - M_T - M_{acc} - I_{yy_{mg}}\ddot{\theta}}{x_{h-mg}} \tag{9.8}$$

Now that the required horizontal tail lift has been established for take-off, the lift coefficient C_{L_h}, could be computed by using the take-off velocity of $V_t = 1.3V_s$. This lift coefficient was used as requirement for the sizing of the elevator geometry using Equation 9.9

$$\tau_e = \frac{\alpha_h + C_{L_h}/C_{L_{\alpha_h}}}{\delta_{E_{max}}} \tag{9.9}$$

In this formula τ_e is the elevator effectiveness which is related to the elevator chord over horizontal tail chord ratio (C_e/C_h) [32]. So by selecting an initial value for the maximum elevator deflection, the required C_e/C_h could be computed to reach the required horizontal tail lift coefficient. Furthermore, the horizontal tail angle of attack α_h is related by $\alpha_h = \alpha + i_h - \epsilon$, hence the inclination of the horizontal tail i_h is also a variable that could be adjusted.

Lifting line theory

To check whether the required lift coefficient can actually be attained by the elevator design, the lifting line theory was used. The method calculates the spanwise lift distribution and uses the geometry of the horizontal tail as input. The zero lift angle of attack following from the maximum negative elevator deflection was approximated with Equation 9.10 [32]. If the required lift coefficient was larger than the lift coefficient computed with the lifting line theory, the elevator design variable needed to be iterated in order to satisfy this requirement.

$$\alpha_0 = -1.15\frac{C_e}{C_h}\delta_E \tag{9.10}$$

Horizontal tail stall analysis

To comply with the requirement that the horizontal tail shall not stall when the elevator is deflected to its maximum extent, a horizontal tail stall analysis was performed. The angle of attack at stall is related by Equation 9.11, where the stall angle of attack with no elevator deflection ($\alpha_{h_{s,\delta_E=0}}$) is based on the aerodynamic analysis of the horizontal tail airfoil explained in chapter 8 and the change in stall angle due to the elevator deflection $\Delta\alpha_{h_E}$ is obtained from statistics [32].

$$\alpha_{h_s} = \alpha_{h_{s,\delta_E=0}} - \Delta\alpha_{h_E} \tag{9.11}$$

This angle was then compared to the actual angle of attack of the horizontal tail during take-off, $\alpha_{h_{TO}}$, which is calculated based on the angle of attack of the wing during take-off α_{TO}, the downwash effect and the inclination of the horizontal tail as shown in Equation 9.12. In case $\alpha_{h_s} < \alpha_{h_{TO}}$ the geometry of the elevator had to be adjusted to comply with the tail stall requirement.

$$\alpha_{h_{TO}} = \alpha_{TO}\left(1 - \frac{d\epsilon}{d\alpha}\right) + i_h - \epsilon_0 \tag{9.12}$$

Elevator trim curve

In order to know at which elevator deflection at a certain airspeed the pilot has to fly, elevator trim curves were constructed. These curves were constructed for the most forward and aft centre of gravity locations and follow from Equation 9.13 [32]. In this equation the elevator deflection is determined based on moment equilibrium.

$$\delta_E = \frac{\left(\frac{T \cdot z_T}{\bar{q} \cdot S \cdot \bar{C}} + C_{m_0}\right) C_{L_\alpha} + \left(C_{L_1} - C_{L_0}\right) C_{m_\alpha}}{C_{L_\alpha} C_{m_{\delta_E}} - C_{m_\alpha} C_{L_{\delta_E}}} \tag{9.13}$$

It should be noted that the moments in this equation were made dimensionless and the moment arm of the thrust was taken from z-location of the centre of the engines to the centre of gravity. Furthermore C_{L_1} is the lift coefficient for the specific flight condition and C_{L_0} is the lift coefficient at $\alpha = 0$. The longitudinal stability derivatives follow from Equation 9.14a,

Equation 9.14b, Equation 9.14c and Equation 9.14d. These equations are based on the geometry of the horizontal tail and elevator, the lift curve slopes for the tail and wing combined with the fuselage, downwash and tail airfoil efficiency η_h.

$$C_{m_\alpha} = C_{L_{\alpha_{wf}}}(\overline{x}_{cg} - \overline{x}_{ac}) - C_{L_{\alpha_h}}\eta_h \frac{S_h}{S}\left(\frac{l_h}{\overline{C}}\right)\left(1 - \frac{d\varepsilon}{d\alpha}\right) \tag{9.14a}$$

$$C_{m_{\delta_E}} = -C_{L_{\alpha_h}}\eta_h \overline{V}_h \frac{b_e}{b_h}\tau_e \tag{9.14b}$$

$$C_{L_{\delta_E}} = C_{L_{\alpha_h}}\eta_h \frac{S_h}{S}\frac{b_e}{b_h}\tau_e \tag{9.14c}$$

$$C_{L_{h_{\delta_E}}} = C_{L_{\alpha_h}}\tau_e \tag{9.14d}$$

9.2.3 Results

Initial results

As an initial estimate, the changeable horizontal tail and elevator parameters were set to $i_h = 0$ deg, $b_e/b_h = 1$ and $\delta_E = 30$ deg. Table 9.4 shows the required horizontal tail lift coefficient $C_{L_{h_{req}}}$ and the lift coefficient that follows from the lifting line theory $C_{L_{h_{LL}}}$. Furthermore it shows the difference between the angle of attack at take-off and stall angle of the horizontal tail with deflected elevator, which were explained in subsection 9.2.2. Although it can be concluded that the horizontal tail does not stall with this geometry and thus complies with the stall requirement, the required lift coefficient is not reached. Therefore, this elevator design is not feasible and a sensitivity analysis is required to get to a more reasonable design.

Table 9.4: Lift and stall characteristics for the horizontal tail at take-off.

Parameter	Output
$C_{L_{h_{req}}}$ [-]	-1.25
$C_{L_{h_{LL}}}$ [-]	-0.66
$\alpha_{h_{TO}}$ [deg]	0.04
α_{h_s} [deg]	1.90

Sensitivity analysis

To get a design that complies with all elevator requirements, a sensitivity analysis was performed. Since the maximum elevator deflection and span ratio were already at or near their maximum, the only parameter that was left to adjust was the inclination of the horizontal tail i_h. A more negative inclination will create a larger downforce, which is favorable for pitching the aircraft up during take-off. To see the actual effect of adjusting the inclination of the horizontal tail, the required and lifting line theory lift coefficients are depicted in Figure 9.5. It could be seen that from an inclination of approximately -3 deg and more negative values, yield a C_{L_h} that is negative enough.

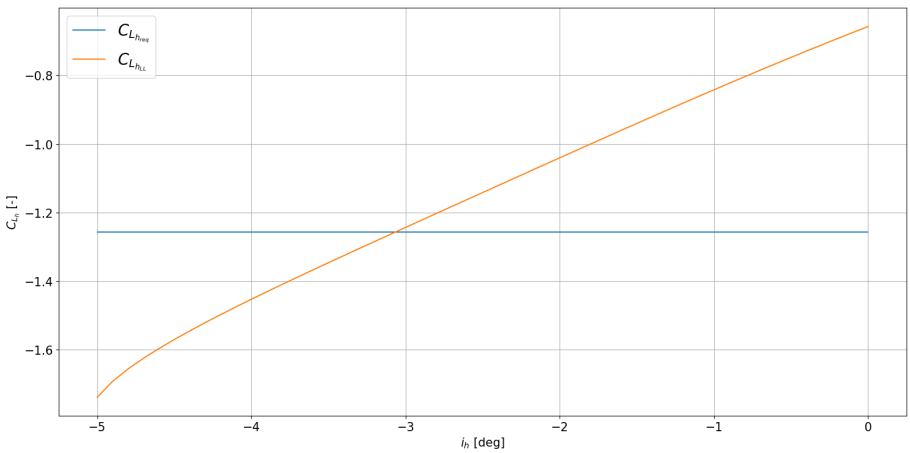

Figure 9.5: Horizontal tail inclination versus required and lifting line theory lift coefficients.

Final results

To allow for a safety margin, an inclination of -4 deg is selected for the final design of the horizontal tail and the maximum elevator deflection and span ratio are kept the same. To reduce drag during cruise, the inclination should be adjusted back

to 0 deg during this flight phase, and therefore and adjustable horizontal tail is selected. Furthermore, the horizontal tail stall will not be encountered, as $\alpha_{h_s} = 1.90$ deg and $\alpha_{h_{TO}} = -3.95$ deg. An overview of the elevator and horizontal tail geometry is given in Table 9.5. For the elevator trim curve, it should be noted this is given in the case the adjustable horizontal tail inclination is reverted to the zero degree setting. This is done after adequate pitch authority without inclination is granted by use of only the elevator, which is calculated to above 100 m/s, signified by the vertical dashed line. The horizontal dashed line shows the maximum elevator deflection angle.

Table 9.5: Finalised elevator sizing results.

Parameter	Output
b_e/b_h [-]	1
c_e/c_h [-]	0.5
i_h [deg]	-4
$\delta_{e_{max}}$ [deg]	30.0

The lift distribution of the final design of the horizontal tail during take-off is shown in Figure 9.6. Furthermore, the elevator trim curves for the most aft and forward cg locations is shown in Figure 9.7. It is noted that at the cruise condition very little elevator deflection is required, which has a positive effect on the trim drag of the aircraft.

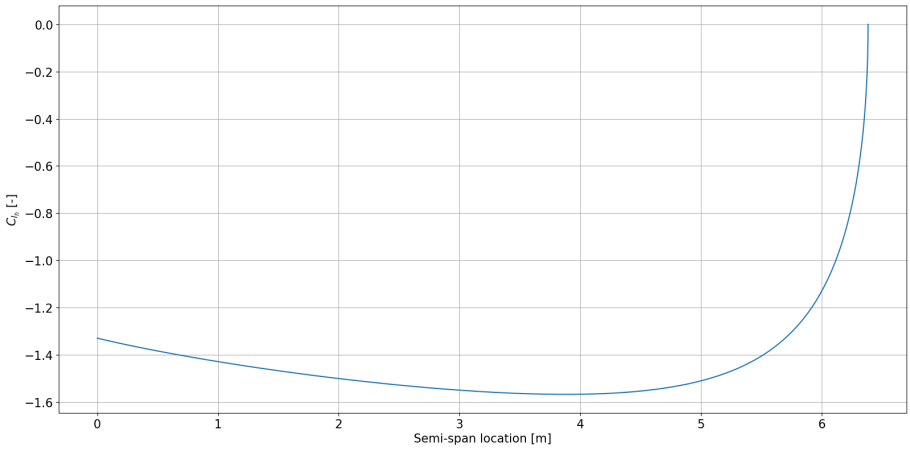

Figure 9.6: Horizontal tail lift distribution for the final elevator design at maximum negative deflection.

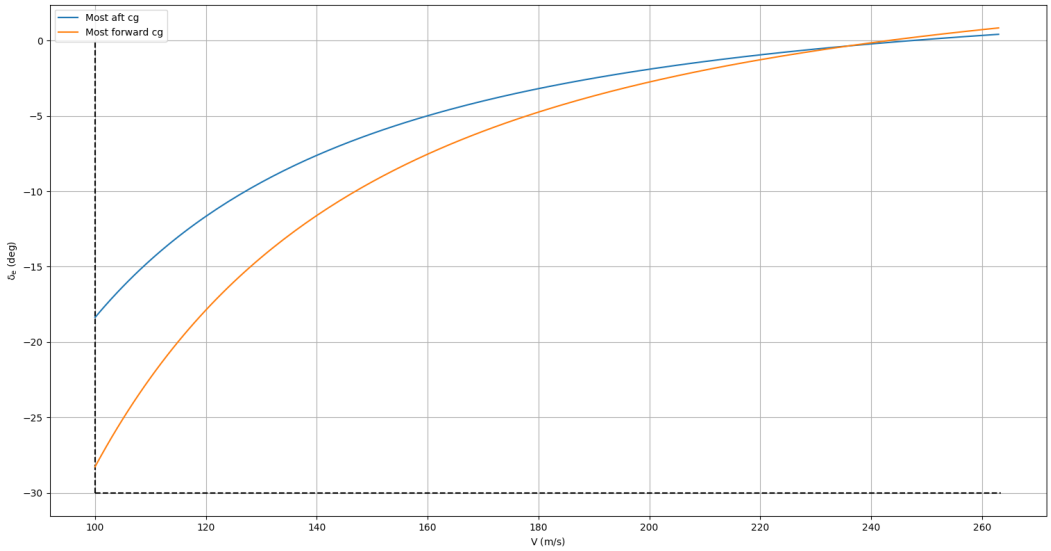

Figure 9.7: Elevator deflection to trim the aircraft versus airspeed for the most forward and aft cg.

9.2.4 Verification

The computer program that was build to size the elevator was verified with a similar model based on the same method [33]. The outputs were nearly the same, but as the verification model rounded some values, minor differences occurred.

Regarding the requirements that apply to the elevator, it can be concluded that all of them are met. The aircraft is controllable during all flight phases, since the elevator is large enough to control the most critical flight phase, which is take-off. Furthermore, it complies with the angular acceleration following from CS-25 and the tail does not stall when the elevator is deflected to its maximum extend [5]. Furthermore, to account for the possibility of an actuator jamming the elevator will be driven by two actuators for redundancy purposes.

9.3 Aileron

Ailerons are - for conventional aircraft - control surfaces on the wings placed far away from the centre line, deflected in opposite directions in order to roll the aircraft. Roll control is of importance as a banked turn is the most common way aircraft perform a turn in flight. Furthermore, disturbances may deviate the aircraft from its symmetric attitude, requiring a counteracting motion. The following section will detail the sizing of the ailerons, following the same layout as the previous section.

9.3.1 Requirements analysis

Functional analysis

The aileron generally serves only one purpose: inducing a rolling motion. Based on the aircraft class a rolling requirement follows from CS-25 [5]. The aircraft being designed falls under Class 3, leading to a roll performance requirement of 30 deg in 1.5 seconds.

Risk analysis

Besides the possibility of an actuator jamming, the aileron poses a unique risk: the occurrence of aileron reversal. As per usual, redundancy and stall must also be accounted for.

Requirements

In addition to the previously derived requirement, two requirements first identified in the baseline report are of importance. The requirements are repeated below for ease of reference.

- **BIB-SBS-STC-04** The aircraft shall be controllable during all flight phases.
- **BIB-SBS-STC-05** The stability and control subsystems shall comply with CS-25.143 - CS-25.255.
- **BIB-SBS-AIL-01** The aircraft shall be able to roll 30 deg in 1.5 seconds.
- **BIB-SBS-AIL-02** The aircraft shall not suffer from aileron reversal under any condition.

9.3.2 Method

Aileron design is an iterative process, whereby roll performance for some initial design is analysed. The design is subsequently changed in order to meet requirements or further optimise. A complete aileron design consists of an elevator span, location and an elevator chord to wing chord ratio.

Roll rate performance is determined by aileron control and roll damping derivatives $C_{l_{\delta a}}$ and C_{l_p}. These parameters relate to roll rate according to Equation 9.15, where V is the airspeed and b is the wing span.

$$P = -\frac{C_{l_{\delta a}}}{C_{l_p}} \delta a_{max} \left(\frac{2V}{b}\right) \tag{9.15}$$

The most limiting case is the case for which V is lowest. Thus, the rotation speed V_r is used. If the requirement is met in this regime then all flight phases have been accounted for. The derivation of the formulae for $C_{l_{\delta a}}$ and C_{l_p} is outside of the scope of this report, and are presented as is in Equation 9.16a and Equation 9.16b. The variable y signifies span-wise location, such that $c(y)$ signifies the chord length at a spanwise location y, and b_i and b_o signify most inboard and most outboard aileron spanwise location, respectively. All other variables including the control surface effectiveness, τ, have been previously defined.

$$C_{l_{\delta a}} = \frac{2C_{l_\alpha}\tau}{S_{ref}b} \int_{b_i}^{b_o} c(y) y dy \tag{9.16a}$$

$$C_{l_p} = -\frac{4(C_{l_\alpha} + C_{d_0})}{S_{ref}b^2} \int_0^b c(y) y^2 dy \tag{9.16b}$$

Inspecting Equation 9.15 and Equation 9.16a a few observations can be made. An increased aileron control derivative increases the roll speed, thus this should be made to be as large as possible. It is observed this is possible by placing the ailerons far away from the fuselage, thereby increasing y, with which C_{l_α} scales nearly quadratically. Intuitively, this makes sense. Assuming a constant increasing and decreasing lift differential due to aileron deflection, a longer lever arm vector will increase the induced force couple about the fuselage centreline. Another option is increasing τ, the control surface effectiveness, which scales positively with increasing control chord to wing chord ratio as previously presented, or increasing δa_{max} the maximum aileron deflection. It should be noted high deflection angles will lead to local stall.

The formula for the roll damping derivative makes it clear its value has been fully fixed, and the aileron design has no influence on its value. From the roll rate P the time to achieve some change in roll orientation, $\Delta\phi$, is easily calculated using Equation 9.17.

$$\Delta t = \frac{\Delta\phi}{P} \tag{9.17}$$

9.3.3 Results

Initial results

Taking into account wing stall, high-lift devices and other factors, the design was optimised and finalised as presented in Table 9.6. The results are inline with those of historical aircraft [3].

Table 9.6: Aileron sizing results.

Parameter	Output
b_i [% b/2]	72
b_o [% b/2]	98
b_a [m]	7.3
c_a/c [-]	0.3
$\delta_{a_{max}}$ [deg]	25

9.3.4 Sensitivity analysis

Little sensitivity analysis was performed. As the possible aileron location range was primarily determined by the high-lift devices placement, the only remaining design variables were the maximum deflection angle and the chord ratio. A $\delta_{a_{max}}$ of 25 deg was set so as to prevent tip stall. This leaves only the chord ratio as variable to meet the roll performance requirements, which was subsequently found to be 0.3.

9.3.5 Verification

To verify the computer software used to analyse the roll performance the aileron data of the Boeing 777-200 (B772) was used as verification data. Aileron data of the B772 as provided by Torenbeek is presented in Table 9.7 [3]. Though aileron reversal has not been taken into account explicitly during the design, the inclusion of spoilerons as presented in chapter 8 will allow the aircraft to rely less on the ailerons, thus decreasing the possibility of aileron reversal.

Table 9.7: Boeing 777-200 aileron data.

Parameter	Output
b [m]	60.9
c_a/c [-]	0.22
$b_i/(b/2)$ [-]	0.32
$b_o/(b/2)$ [-]	0.76
$\delta_{a_{max,up}}$ [deg]	30
$\delta_{a_{max,down}}$ [deg]	10

Analysing the roll performance for the given aileron data results in a time to turn 30 deg of 1.25 seconds, well under the requirement of 1.5 seconds. No source on actual roll performance in the most adverse conditions of the B772 has been found. However, the software indicates that the roll duration lies below the roll time requirement in the most adverse condition by quite a large margin, so it is deduced the aileron sizing is accurate. Future in depth aerodynamic analysis will size the ailerons even more accurately, taking into account differential aileron deflection angles, as seen in the B772 aileron data.

The requirements as stipulated in the functional analysis subsection have all been complied with, in as far as they have influence on the aileron design. The most adverse, limiting conditions for the roll angle time requirement have been taken

into account, such that all flight phases are accounted for.

9.4 Rudder

The rudder is a control surface conventionally found on the vertical stabiliser. It is generally used as a restoring force and is not used as the primary means of turning an aircraft. Causes of the need to restore aircraft orientation might be the occurrence of adverse yaw, crosswind, or a thrust differential.

9.4.1 Requirements analysis

Functional analysis

As previously mentioned the rudder is used as a directional restoring force due to some disturbance. According to Torenbeek, the most limiting cases for large commercial aircraft are performing a landing with crosswind and when keeping the aircraft straight during a One Engine Out situation [3]. In order to ensure market competitiveness a maximum crosswind requirement of 40 kts will be upheld. The rudder will be sized for these limiting cases, ensuring controllability in other, non-limiting cases.

Risk analysis

Similar to the other control surfaces, the risk of rudder stall applies as well. This risk shall be mitigated during all phases of the mission. Furthermore, the risk of a jamming actuator applies as well.

Requirements

Requirements noted to have an effect on rudder design will be repeated once more, along with the newly derived requirement following from the functional and risk analyses.

- **BIB-SBS-STC-04** The aircraft shall be controllable during all flight phases.
- **BIB-SBS-STC-05** The stability and control subsystems shall comply with CS-25.143 - CS-25.255.
- **BIB-SBS-RUD-01** The aircraft shall be able to land safely in a One Engine Out situation.
- **BIB-SBS-RUD-02** The aircraft shall be able to land safely in 40kts crosswind.
- **BIB-SBS-RUD-03** The rudder shall not stall when maximally deflected.

9.4.2 Method

The rudder will be sized for both limiting conditions. A complete rudder design designates the maximum rudder deflection, $\delta_{r_{max}}$, the rudder to vertical stabiliser span, and the rudder chord length, defined as a rudder to vertical stabiliser chord fraction. These parameters fully define the maximum achievable rudder force, and in turn, through aircraft geometry, the maximum achievable rudder moment.

The total vertical stabiliser force is defined as in Equation 9.18a, further related tot the yawing moment through Equation 9.18b.

$$L_v = qS_vC_{l_v} \tag{9.18a}$$

$$N_a = l_vL_v \tag{9.18b}$$

Lateral forces are defined as being in the Y direction, such that the stability derivative of the lateral lifting force is defined as in Equation 9.19.

$$C_y = C_{y_0} + C_{y_\beta}(\beta - \sigma) + C_{y_{\delta_r}}\delta_r \tag{9.19}$$

C_{y_0} is zero for symmetric airfoils. C_{y_β} is the force stability derivative caused by the lifting force of the vertical stabiliser. It scales with the sideslip angle, defined in this analysis as the angle between the angle from the runway to the true airspeed, β, minus the angle between the runway and the aircraft centreline, σ. The rudder deflection force coefficient is determined through Equation 9.20.

$$C_{y_{\delta_r}} = C_{l_{\alpha_v}}\eta_v\tau_r\frac{b_rS_v}{b_vS} \tag{9.20}$$

Defining N_a as a sum of products of a derivative coefficients and control variables, a rudder deflection moment coefficient arises:

$$C_n = C_{n_0} + C_{n_\beta}\beta + C_{n_{\delta_r}}\delta_r + C_{n_{\delta_a}}\delta_a \tag{9.21}$$

As for the previous zero-angle coefficient, C_{n_0} will be equal to zero for symmetric vertical stabiliser airfoils, which is generally the case. The derivative C_{n_β} is then identified as the weathervane stability. This derivative has an effect of turning the aircraft towards the direction of the true airspeed. The value of the weathervane stability derivative coefficient is determined by aircraft geometry, further defined in the crosswind landing subsection. $C_{n_{\delta r}}$, the rudder deflection moment coefficient, is determined through Equation 9.22 as a function of the curve slope coefficient of the vertical tail lift, $C_{l_{\alpha_v}}$, the volume coefficient of the vertical tail, V_v, the previously defined control surface efficiency, and the rudder to vertical stabiliser span ratio. In the limiting case the ailerons are assumed to not be deflected, thus the value of $C_{n_{\delta a}}$ will not be of importance for further analysis.

$$C_{n_{\delta r}} = -C_{l_{\alpha_v}} V_v \eta_v \tau_r \frac{b_r}{b_v} \tag{9.22}$$

The previously mentioned design parameters are all noted here, with τ_r relating to the chord ratio parameter.

For the limiting cases, the stability coefficient representation can be used to analyse requirement compliance for each of the limiting cases, as will be presented hereafter.

Differential thrust

In the case of a engine inoperative condition, a moment summation relation is used to determine the required rudder induced moment to keep a required ground heading angle. For the designed two-engine aircraft, a single engine out occurrence will cause a yawing moment defined by Equation 9.23, for a thrust T_L and lateral engine placement y_T.

$$N_a = -T_L y_T \tag{9.23}$$

The total moment summation must be equal to zero, therefore Equation 9.24a must hold:

$$N_a = \overline{q}_c S b (C_{n_\beta} \beta + C_{n_{\delta r}} \delta_r) \tag{9.24a}$$

$$\overline{q}_c = \frac{1}{2} \rho_0 (0.8 V_s)^2 \tag{9.24b}$$

The minimum controllable speed is required to be 0.8 times the stall speed, such that $\overline{q}_c$ is defined to be as in Equation 9.24b. Imposing a zero sideslip requirement, this leads to a maximum required rudder deflection angle for a given rudder-design defined $C_{n_{\delta_r}}$:

$$\delta_r = \frac{T_L y_T}{-\overline{q} S b C_{n_{\delta r}}} \tag{9.25}$$

Crosswind Landing

During a crosswind landing the rudder is used to trim the aircraft against crosswind, v_w, induced aerodynamic loads. Keeping the heading of the aircraft oriented towards the runway (crab angle σ), the sideslip with respect to the true airspeed vector (β, defined in Equation 9.26a) causes a control force as defined in Equation 9.26b.

$$\beta = \arctan\left(\frac{v_w}{v_f}\right) \tag{9.26a}$$

$$F_{a_y} = \overline{q} S (C_{y_\beta} (\beta - \sigma) + C_{y_{\delta_r}} \delta_r) \tag{9.26b}$$

Furthermore, for a aircraft side area S_s and drag coefficient C_{d_y} the aerodynamic force caused by the crosswind is defined as:

$$F_w = \frac{1}{2} \rho v_w^2 S_s C_{dy} \tag{9.27}$$

In a trimmed condition the crosswind induced force must be equal to the control force, leading to the first equation of the system to be solved:

$$\frac{1}{2}\rho v_w^2 S_s C_{dy} = \overline{q} S(C_{y_\beta}(\beta - \sigma) + C_{y_{\delta_r}}\delta_r) \tag{9.28}$$

Taking the moment equilibrium about the centre of gravity, the aircraft control yawing force must alleviate the moment induced by the crosswind force, acting at a distance d_c:

$$N_a + F_w d_c \cos\sigma = 0 \tag{9.29}$$

N_a has been previously defined in Equation 9.24a. The remaining stability derivative, the weathervane stability, is given in Equation 9.30. K_{f2} is a measure of fuselage contribution to the stability derivative, typically lying between 1.3 and 1.4. The slope $\frac{d\sigma}{d\beta}$ is the sidewash gradient of the vertical tail.

$$C_{n_\beta} = K_{f2} C_{l_{\alpha_v}} \left(1 - \frac{d\sigma}{d\beta}\right) \eta_v \frac{l_v S_v}{bS} \tag{9.30}$$

Expanding Equation 9.29, the second equation of the system to be solved arises:

$$\frac{1}{2}\rho v_t^2 Sb \left(C_{n_o} + C_{n_\beta}(\beta - \sigma) + C_{n_{\delta r}}\delta_r\right) = -F_w d_c \cos\sigma \tag{9.31}$$

Solving Equation 9.28 and Equation 9.31 simultaneously results in a required rudder deflection angle δ_r, for a given rudder-design defined $C_{n_{\delta_r}}$.

9.4.3 Results

Initial results

The method as described above was performed using detailed design concept data. For both limiting cases, the results for maximum deflection angles are presented in Table 9.8, with subscript t signifying the differential thrust setting, and subscript c signifying the crosswind landing thrust setting. The engine spanwise location has previously been set following structural analysis at 7m from the centreline. Due to the doubledecker configuration of the aircraft, the tail arm from the centre of gravity to the rudder force application force is shorter than in conventional aircraft. Therefore, an initial rudder span is taken to be over the entire span of the vertical tailplane. An initial chord ratio of 0.3 is chosen.

Table 9.8: Preliminary rudder sizing results.

Parameter	Output
b_r/b_v [-]	1
c_r/c_v [-]	0.3
y_T [m]	7.0
$\delta_{r_{max,t}}$ [deg]	37.8
$\delta_{r_{max,c}}$ [deg]	-9.8

Sensitivity analysis

It is noted the thrust differential case seems to be limiting. It is hypothesised that due to the shorter fuselage not only are the required rudder deflection angles larger than usual, the moment arm from the crosswind aerodynamic centre to the centre of gravity is also shorter, resulting in decreased crosswind angle requirements. It should be noted that for such large deflection angles rudder stall might occur, so a sensitivity analysis is performed to gain insight into behaviour of the system, aiming to decrease the required deflection angles.

As the span ratio is already maximised and engine spanwise location has already been optimised following the structural analysis, the only remaining design variable is the chord ratio, c_r/c_v. The effect of the chord ratio on the required deflection angles is presented in Figure 9.8.

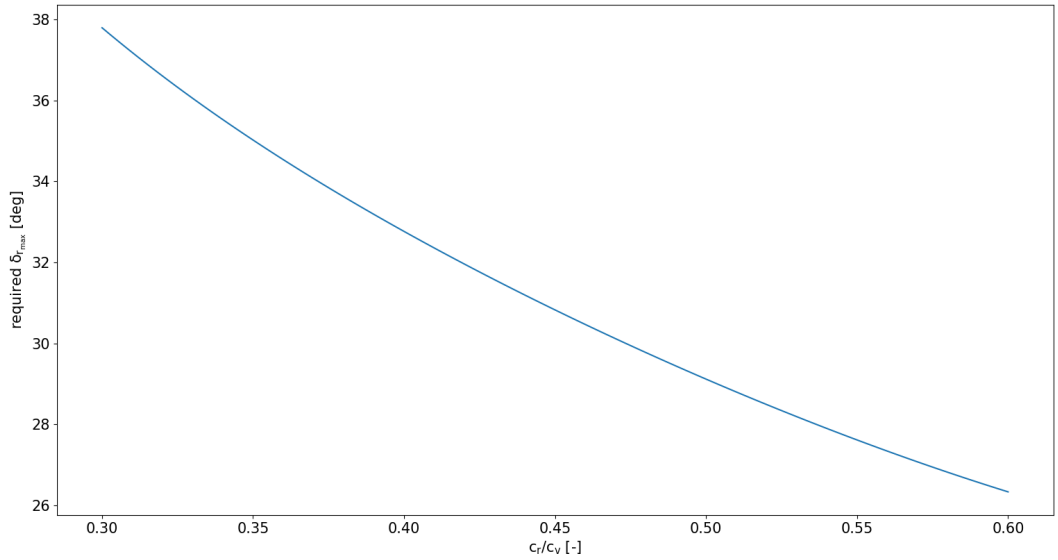

Figure 9.8: Required deflection angles versus rudder chord span for the one engine out case.

Final results

In order to prevent rudder stall a conservative value of $30°$maximum deflection is chosen. As seen in Figure 9.8, the required chord ratio lies around 0.45, which is not immediately determined to be unfeasible. To account for a contingency factor, a chord ratio of 0.5 is selected. The increased chord length requirement for the rudder is similar to that of the elevator, and has to do with the same factors - primarily the shortened fuselage. Due to similar increases with respect to conventional aircraft as the elevator sizing, using completely different methods of analysis, more confidence is gained in the design. The final results are presented in Table 9.9.

Table 9.9: Final rudder sizing results.

Parameter	Output
b_r/b_v [-]	1
c_r/c_v [-]	0.5
y_T [m]	7.0
$\delta_{r_{max,t}}$ [deg]	29.1
$\delta_{r_{max,c}}$ [deg]	-7.5

9.4.4 Verification

The software written for the design of the rudder was verified in the same way as the elevator [34]. Again, the outputs were similar, but as the verification model rounded some values, some marginal differences occurred.

The requirements that were outlined for the rudder were all met, since the design of the rudder was based on them. It complies with the One Engine Out and crosswind criteria set by CS-25 and it does not stall when maximally deflected [5]. Furthermore, it ensures the controllability of the aircraft, regarding yaw, at all phases of the mission. Additionally, the rudder is split into two separate surfaces for redundancy, to account for the jamming of an actuator.

10 Structural analysis and design

This chapter describes the feasibility of the structure. It elaborates on the design of the wing-strut configuration, fuselage and empennage for different load cases. It should be mentioned that other structural aspects, such as the winglets, connection of the strut to the fuselage and landing gear connections have not been investigated. Also no shear flow analysis was performed, as it was determined that this would not be the limiting sizing factor for either of the main aircraft components. Before analysing each of these structural components, first the materials that were considered will be investigated in section 10.1. Then the wing, empennage and fuselage will be analysed in section 10.2, section 10.3 and section 10.4 respectively. Each section will start with an functional analysis, followed by the sizing method that was used. Then, if applicable, a performed trade-off will be discussed. Subsequently, the result, sensitivity and verification are presented.

10.1 Material selection

Materials determine if a structure can handle certain loads and moments. Aluminium alloys are primarily used in wing and fuselage structures, however, nowadays composites are also being used more often. This section will elaborate upon the functional analysis of materials, the sizing method, in which materials for the different structural components are selected and a fatigue analysis was performed. The section will end with showing the important material characteristics.

10.1.1 Requirements analysis

The requirements related to the materials that are used are investigated by means of functional and risk analyses in this section.

Functional analysis

There are several functions that the materials of the EcoHopper 450 have. First of all, the materials should be resistant against the environment. Furthermore, the materials should be strong enough to handle the loads that are applied on the structure. Finally, the materials that are used for the structural components should be processable.

Risk analysis

All different materials have different characteristics. Some are beneficial to have while others are not. A trade-off between these characteristics was made to select the best material for each component. However, as explained they will introduce certain risks to the structure. These risks are listed below.

- **Fatigue life:** A special analysis has to be performed for aluminium alloys. These alloys are extremely vulnerable for fatigue. Therefore, they should be evaluated for a lower tensile strength and should be inspected repeatedly.
- **Crack initiation and propagation:** Cracks are difficult to detect in carbon fibre composites when compared to aluminium alloys. Special inspections with special equipment should be scheduled for analysing carbon composites components of the aircraft.

Requirements

The following requirements were identified, from the functional analysis. Most requirements were based on the structural requirements that were identified in the baseline report [8].

- **BIB-SBS-MAT-01** The material shall be processable for its specific structural component.
- **BIB-SBS-MAT-02** The material shall not corrode due to changing humidity levels.
- **BIB-SBS-MAT-03** The material shall not lose its properties due to thermal expansion in cruise.

10.1.2 Method

This section elaborates on the material selection and the fatigue analysis of these selected materials. Fatigue plays a critical role in aircraft structures as the aircraft will experience cyclic loads. Therefore, first the proposed materials for the wing, fuselage and empennage are discussed, after which the method to analyse fatigue is explained.

Material selection

Two different aluminium alloys were considered for the wing of the EcoHopper 450. These were an aluminium alloy out of the 2xxx series and one alloy out of the 7xxx series. The difference between these two materials is that the 2xxx series perform better under fatigue. Combining both materials in the wing is also possible. A common approach is to use an aluminium alloy from the 7xxx series for the upper skin and one out of the 2xxx series for the lower skin of the wing, as the lower skin generally experiences most of the fatigue stresses during the aircraft's life time. For now, only one material will be used in the analysis. The two proposed materials for the wing were aluminium 7075 and aluminium 2024.

The EcoHopper 450 will make use of a strut to relief the bending moment at the root of the wing. Different materials were proposed to construct the strut. The aluminium alloys that were considered for the wing could be used for the strut as well. However, the strut will mainly experience tensile or compressive forces. Therefore, carbon fibre composites could be used as well. Due to their higher tensile strength and lower density it could reduce the weight significantly. However, carbon fibre composites are more brittle and do not yield plastically under high stresses. It should be taken into account that new techniques are necessary for checking the structure for crack initiation and propagation. Two different carbon fibre epoxy composites were proposed for the strutted wing. One with a quasi isotropic lay-up and one with a unidirectional lay-up.

The structure of the fuselage is constantly pressurised during its operational lifetime. Therefore, Aluminium 2024 is proposed as the main material in the fuselage of the EcoHopper 450. Aluminium 7075 was not considered for this structure due to the importance of fatigue strength. Furthermore, carbon fibre composites were also disregarded as main material for the fuselage due to the fact that they have poorly perceptible crack initiation.

Fatigue analysis

To analyse the fatigue strength, a tool was developed that plots the ultimate stress against the number of cycles. Aiming for an aircraft lifetime of 27 years with six flights a day resulted in a total of 59,130 flights. To come up with a total amount of cycles a safety factor of eight was multiplied with the total amount of flights. The reason behind this safety factor is that one flight can not be compared with one cycle due to the small amplitude of taxiing and turbulence during one flight. Therefore, the fatigue strength was analysed for a number of cycles equal to 473,040. Another important factor in the S-N diagrams is the stress amplitude for which the fatigue strength is analysed, illustrated below in Figure 10.1.

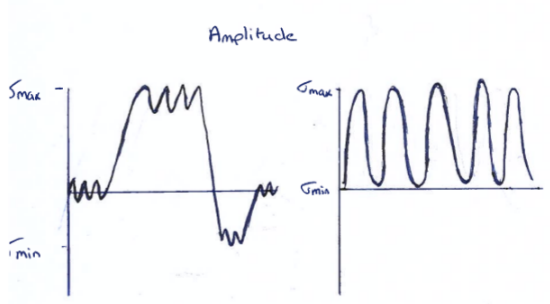

Figure 10.1: Amplitude of the wing on the left and fuselage on the right.

$$S_a = \frac{\sigma_{max} - \sigma_{min}}{2} \tag{10.1}$$

The stress amplitude could be calculated by using Figure 10.1 and Equation 10.1. This stress amplitude was used in order to define the tensile strength at zero cycles. Since the fuselage is either pressurised or not, a stress amplitude of -0.5 was used. Determining the stress amplitude for the wing is more complicated. It was assumed that the lower surface of the wing will always be in tension during the flight and only in compression during landing. Furthermore, it is assumed that the minimum stress, represented by the part under the horizontal axis in the left diagram in Figure 10.1, is equal to $1/3$ times the maximum stress. This resulted in an amplitude of -0.667.

10.1.3 Results

An overview of the different proposed materials for the different components is provided below in Table 10.1. All the important material characteristics that were used are stated in the table. Most of the material characteristics were taken from an aerospace material database called CES Edupack [35]. The value for the fatigue strength was calculated by making use of the method explained in subsection 10.1.2. A fatigue strength of 135 MPa was used when analysing landing procedures, while a fatigue strength of 114 MPa was used during cruise. The reason for this is that the landing condition only occurs once per flight, thus the safety factor of eight is not used. For the fuselage, the fatigue strength of 114 MPa was used as the circumferential limit stress, as it is only pressurised once per flight. The fatigue strength of 105 MPa was used for all other cases. However, it must be noted that this can only be tested on full scale. The S-N curve for both, the wing and fuselage, is illustrated below in Figure 10.2.

Table 10.1: Proposed materials with their specifications for different aircraft components.

Designed for	Amplitude ratio	Material	E-modulus [GPa]	Tensile Strength [MPa]	Fatigue stress [MPa]	Density [kg/m^3]	Cost [€/kg]
Wing	-0.667	Aluminium 2024	75.0	485	114	2780	1.96
		Aluminium 7075	72.0	485	114	2810	3.70
Strut	-0.667	Aluminium 2024	75.0	485	114 / 135	2780	1.96
		Aluminium 7075	72.0	485	114 / 135	2810	3.70
		Carbon fibre QI lay-up	60.1	671	140	1580	35.20
		Carbon fibre UD lay-up	130	1400	1400	1580	35.20
Fuselage	-0.5	Aluminium 2024	75.0	485	105 / 114	2780	1.96

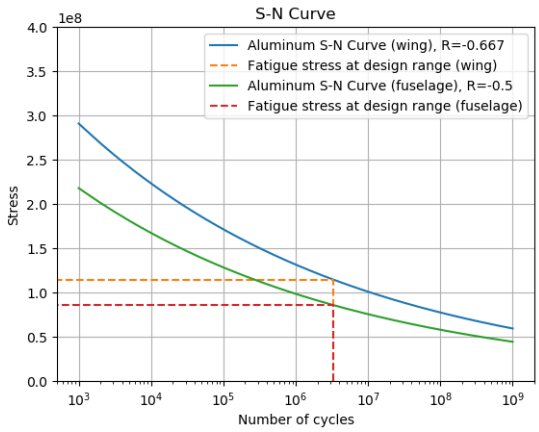

Figure 10.2: Fatigue analysis of aluminium alloys.

10.2 Wing and strut

In this section the wing and strut sizing is presented. The sizing is based on requirements following from the functional analysis, which will be discussed first. Next, the sizing method, material trade-off and and preliminary results are presented. Based on the preliminary results, a sensitivity analysis was performed to better understand the results and come to a final design. In the final subsection the requirements are verified.

10.2.1 Requirements analysis

Functional analysis

The wing has several important functions from a structural point of view. First of all, it should allow for fuel storage inside the wing box. Therefore, the wing box should be large enough to accommodate all the fuel. Furthermore, the wing should provide stiffness to carry the loads acting on it.

Requirements follow from all functions listed above. Note that for the third function, the requirements are obtained from the flight envelope. Therefore, this plot is shown first, after which all the requirements will be listed for the wing.

Flight envelope

In CS-25 it is stated that the aircraft should be able to carry the load under nominal conditions multiplied with an ultimate load factor [5]. The conditions and accompanying load factor follow from the flight envelope. Note that to obtain the ultimate load factor, the load factor from the flight envelope should be multiplied with 1.5. This envelope consists of the manoeuvring envelope and the gust envelope. Both have been generated using the method described in Roskam V [17][page 35 - 38]. Below, in Figure 10.3, the flight envelope of the EcoHopper 450 is shown.

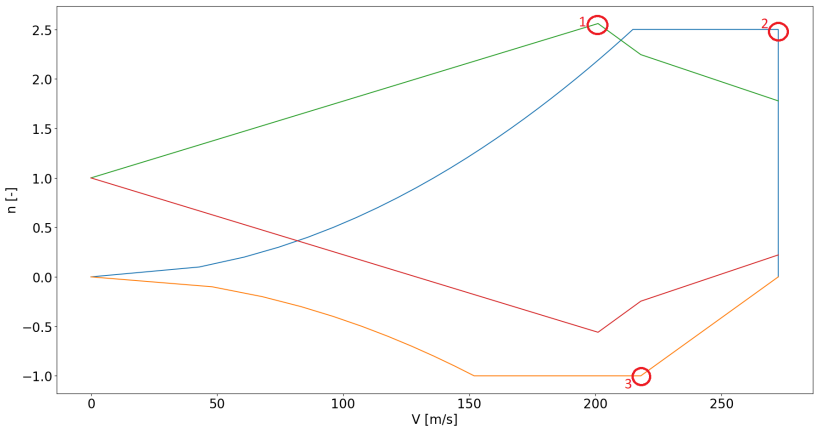

Figure 10.3: The flight envelope constructed for the EcoHopper 450.

It was chosen to evaluate the three different points highlighted in Figure 10.3 in order to find the most critical case. Case 1 is chosen as it contains the highest load factor value, while case 2 was chosen as it contains the highest speed the aircraft will fly at (e.g. the dive speed). For this case, it was assumed that the aircraft would go to maximum thrust setting at cruise altitude and then make a straight vertical dive. Using Equation 10.2 the altitude was calculated at which the dive speed of

272.5 m/s was reached. This resulted in the altitude of 7,637 m. Case 3 was chosen as it contains the lowest load factor and the highest speed at which this load factor could occur.

$$a \int ds = \int V dV \tag{10.2}$$

In addition, the landing condition was evaluated because the strut will take up a compression load during landing, which might be higher than the negative load case selected from the flight envelope. In order to determine the load factor during landing, Equation 10.2 was used. In order to satisfy the CS-25 requirements, the limit vertical speed V of 3.05 m/s was used [5]. Finally, the acceleration was computed as being -9.303 m/s^2, using the Δ s_{stoke} of 0.5 m obtained from the landing gear characteristics [36].

With all the possible critical load cases known, an overview can be made of the load cases for which the aircraft needed to be evaluated. This is shown below in Table 10.2.

Table 10.2: The different load cases that were evaluated for the wing.

Load case	Load factor [-]	Speed [m/s]	Altitude [m]
1	n_1 = 2.56	201	9000
2	n_2 = 2.50	272.5	7637
3	n_3 = -1.00	218	9000
4	$n_{landing}$ = -0.949	65	sea level

Risk analysis

There are different risk associated with the wing structure.

- **Strutted wing difficulties:** A strut was placed to relief the bending moment at the root chord of the wing. This has big advantages in the weight and structural design of the wing. However, due to the strut, flutter might occur which could make the whole wing vulnerable.
- **Location of the fuel tanks:** Placing the fuel tanks near the tip of the wing reliefs the bending moment at the root again. However, it could be possible that during ground operations the wing tip crashes with an obstacle, such as scratching the tip from the aircraft to a side wall of an hangar or another aircraft. Depending on the position that the wing would break, the fuel tank might be damaged, resulting in fuel leakage. Also, in case of an engine fire fuel closely stored to the engine might cause an explosion.
- **Wrong strut positioning:** Not only the lateral position of the strut, but also the position of the strut chordwise is crucial. If this is not placed as supposed to, the forces will induce different moments into the structure, which could result in unexpected failure.
- **Strut disconnection:** Disconnection of the strut to either the fuselage or the wing results in loads that the wing is not able to carry, which in the worst case can cause wing failure.

Requirements

From the functional analysis and the baseline report the following requirements were identified [8]. Note that the new requirements can be found under the identifier SNR. Behind the new requirements the number of the function is listed from which the requirement followed.

- **BIB-SBS-STR-03**: The wings of the aircraft shall be able to carry all limit loads obtained out of the flight envelope.
- **BIB-SBS-STR-05**: The structure shall not fail below ultimate load level.
- **BIB-SBS-STR-06**: The structure shall withstand fatigue during its whole operational life.
- **BIB-SBS-STR-09**: The structure subsystem shall comply with CS-25.300 - CS-25.899.
- **BIB-SBS-SNR-01**: The wing box shall have enough volume to store all the fuel.
- **BIB-SBS-SNR-02**: The structure shall be able to withstand the limit vertical landing speed of 3.05 m/s.

10.2.2 Sizing method

This section starts of with establishing the reference systems for the wing-strut configuration. After that, the approach that was used to calculate the wing and strut dimensions based on the given requirements and aircraft characteristics is discussed.

Reference frames

Figure 10.4, Figure 10.5 and Figure 10.6 show the reference frames that were used for the wing analysis. The arrows indicate the positive force and bending moment directions. Furthermore, it should be noted that in case of an angle of attack α, the reference frame rotates with the airfoil, such that the z-axis is always parallel to the chord line. This reference frame change is indicated in blue in Figure 10.7.

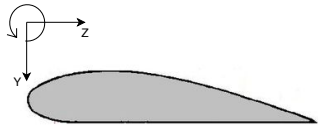

Figure 10.4: Cross-sectional view reference frame of the wing.

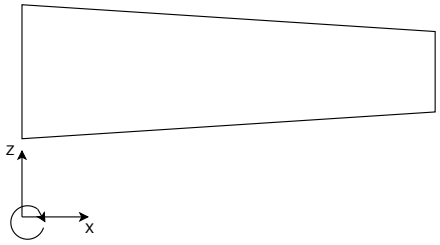

Figure 10.5: Top view reference frame of the wing.

Figure 10.6: Front view reference frame of the wing.

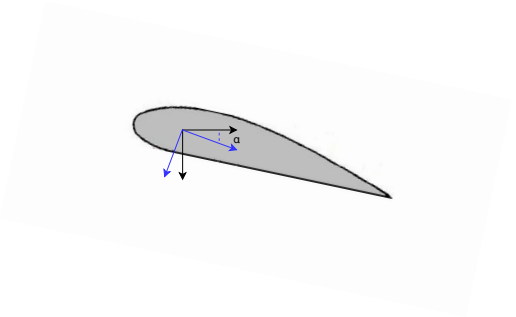

Figure 10.7: Rotation of the reference frame.

Design approach and method

As the sizing of the wing and the strut depend on the material characteristics of both structures, the wing-strut configuration was analysed for several strut materials. A tool was created that is able to analyse the different critical load cases, as described in subsection 10.2.1, for different strut positions. This made it possible to compare the required boom and strut masses, together with the corresponding cost, for the different strut positions. From these values, the lightest strut position for each type of strut material was determined. Below, the iterative process used in order to determine these parameters is described, which is applicable for each material that was analysed.

To start off the strut analysis, a 2-D model of the wing-strut configuration was used as shown in Figure 10.8. The strut is assumed to be hinged to the wing and the connection of the strut to the fuselage is considered to be a ball and socket joint [37]. Furthermore, the force in z-direction due to the generated drag of the strut was not calculated and is assumed to only cause a reaction force at the strut-fuselage connection. Finally, it should be mentioned that for this analysis the strut is assumed to be connected to the quarter chord. Due to this the component of the strut force in x-directions contributes both to the moment around the y- and z-axis.

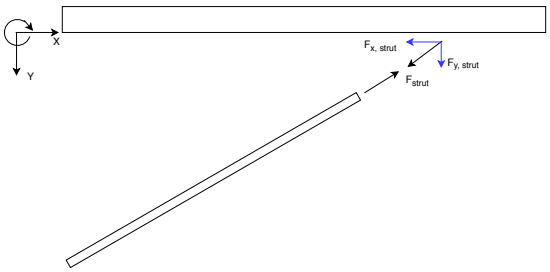

Figure 10.8: 2D view of the wing-strut analysis.

Determining the required strut force for a certain load factor and strut position is an iterative process. It requires a moment of inertia of the wing, and thus wing geometry, while the required moment of inertia in turn depends on the moments that the wing will experience due to the forces that act on it. This iterative process is shown in Figure 10.9. To start off, spar and boom areas and positions were estimated. This allowed for determining the centroid of the wing, which was necessary

to compute the required I_{zz} based on an initial bending moment. The required moment of inertia was determined using the simplified formula $I_{zz} = \frac{M_z y}{\sigma_f}$. This inertia was then used to determine the maximum required new boom area. After updating all these parameters again, the actual cross-sectional I_{zz}, I_{yy} and I_{yz} were computed. This allowed to determine the strut force, obtain shear force and bending moment distributions and to update the required I_{zz} and thus required boom area. If the difference in boom area between the iterations varied more than 0.1 cm^2 the entire iteration process started again. Else, the process was finished by computing the deflection of the wing for the specific strut position that was evaluated. This whole process resulted in the required boom area and based on the computed strut force, the required strut area was determined. For negative load cases, the required area to prevent buckling was used as shown in Equation 10.3 and Equation 10.4 [38]. In Equation 10.3 a value of one was used for K, based on the connections between the strut and the wing and the strut and the fuselage as explained by Duan L. and Chen W.F. [38]. For the positive load cases, on the other hand, the required strut area was computed using Equation 10.5. Note that for these calculations the strut force in the direction of the strut should be used, which can be computed using the angle between the strut and the wing.

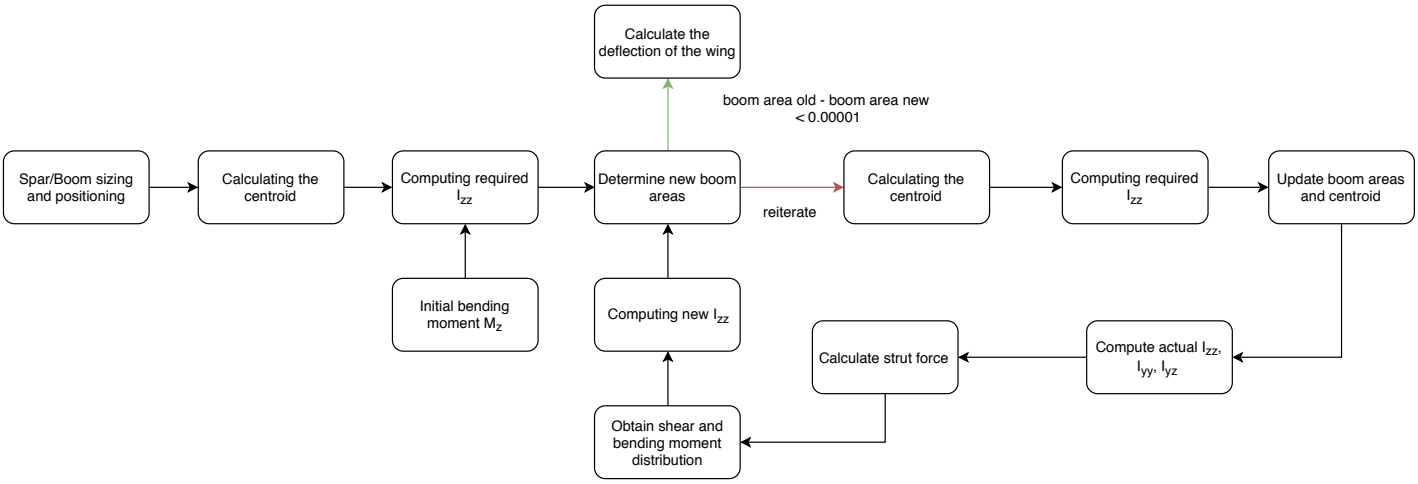

Figure 10.9: The iterative process for analysing the structure of the wing.

$$I_{strut} = F_{strut}\frac{(KL_{strut})^2}{\pi^2 E_{strut}} \quad (10.3) \qquad R_{strut} = \left(\frac{4I_{strut}}{\pi}\right)^{\frac{1}{4}} \quad (10.4) \qquad A_{strut} = \frac{F_{strut}}{\sigma_{f_{strut}}} \quad (10.5)$$

Now the method to calculate the strut force will be explained. As the wing-strut configurations resulted in an indeterminate system, a seventh compatibility equation was needed next to the six equations that were obtained from the sum of moments and forces in all directions. The compatibility condition used is that the vertical deflection of the strut needs to be equal to the deflection of the wing at the position of the strut. In order to determine the maximum allowed deflection of the strut Equation 10.6 was used, in which σ_f was taken to be the first fatigue strength value of the material of the strut, shown in Table 10.1.

$$d_{strut} = \frac{sin(\alpha)\sigma_{f_{strut}} L_{strut}}{E_{strut}} \quad (10.6)$$

Then the deflection of the wing due to the different loads that act on the wing was computed. The principle of superposition was used to superimpose all the loads using equations from Roark [39]. This was possible as all materials are linearly elastic. The considered loads acting in the y-direction are the lift, wing weight, engine weight and fuel weight, which are shown in Figure 10.11. The formula used to compute the deflection at a certain point i along the span of the wing is shown in Equation 10.7, in which W is the force, EI the bending stiffness of the wing, a the distance from the tip at which the force acts, and l the half span length of the wing. Based on the deflection of the wing and the maximum allowed deflection of the strut, the required strut force could be computed using Equation 10.8.

$$\text{Deflection} = y_i = y_a + \theta_a x_i = \frac{-W}{6EI}(2l^3 - 3l^2 a + a^3) + \frac{W(l-a)^2}{2EI}x_i \quad (10.7)$$

$$F_{strut} = \frac{d_{strut_{req}}}{y_a + \theta_a} \quad (10.8)$$

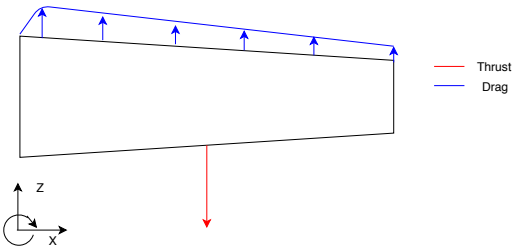

Figure 10.10: Forces acting in the Z-direction on the wing.

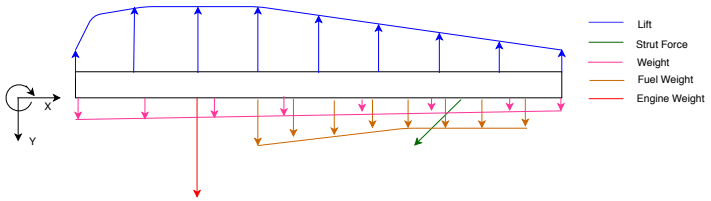

Figure 10.11: Forces acting in the Y-direction on the wing.

In order to evaluate the contribution of each of these forces, the magnitude and position of these forces had to be determined. It should be mentioned that for the different load cases a different velocity and altitude were used. Therefore, the C_L and angle of attack differed per load case as well, which were obtained using AVL. All forces were transformed to the coordinate system shown in Figure 10.7 using the corresponding angle of attack. This rotation was needed as the deflection formula is only valid for the rotated frame. Furthermore, the half span of the wing was separated in N sections. The lift of each section was then computed using the dynamic pressure and the corresponding chord length. The sectional weight was computed using the specific wing weight, which value was calculated by dividing the total wing weight of the class II weight estimation method by the wing volume, again obtained from AVL.

In addition, the position of the fuel tank and the engine needed to be determined. From a structural point of view, placing the engine and the fuel tank towards the tip is favourable, as it allows for bending relief. However, there are also limits on the positioning of these components. First of all, the fuel tank cannot be positioned in the wing at the position of the engine. Secondly, there is a restriction on the lateral position of the engine for the stability and control of the aircraft in case of single engine failure. Also, as there is an emergency exit under the wing, the engine shall not be placed too close to the fuselage. Finally, the wing tip is more prone to damage and is unfavourable to be fuelled in order to avoid leakage. Taking all of this into account resulted in the engine being placed at 6.35 m from the root chord. For the fuel tank, the following was taken into account. Firstly, 0.02 % of the fuel tank volume was reserved for the surge tank. Secondly, the fuel will be loaded between the spars of the wing box, which are located at $0.15\bar{c}$ and $0.55\bar{c}$ respectively. These locations were chosen as at these positions the airfoil is still relatively thick, such that the contribution of the spars to the moment of inertia I_{zz} is large. Finally, an optimisation to create the most bending relief with the fuel was performed as shown in Figure 10.12. This resulted in the fuel tank starting at 7.28 m from the root and ending 1 m before the end of the tip.

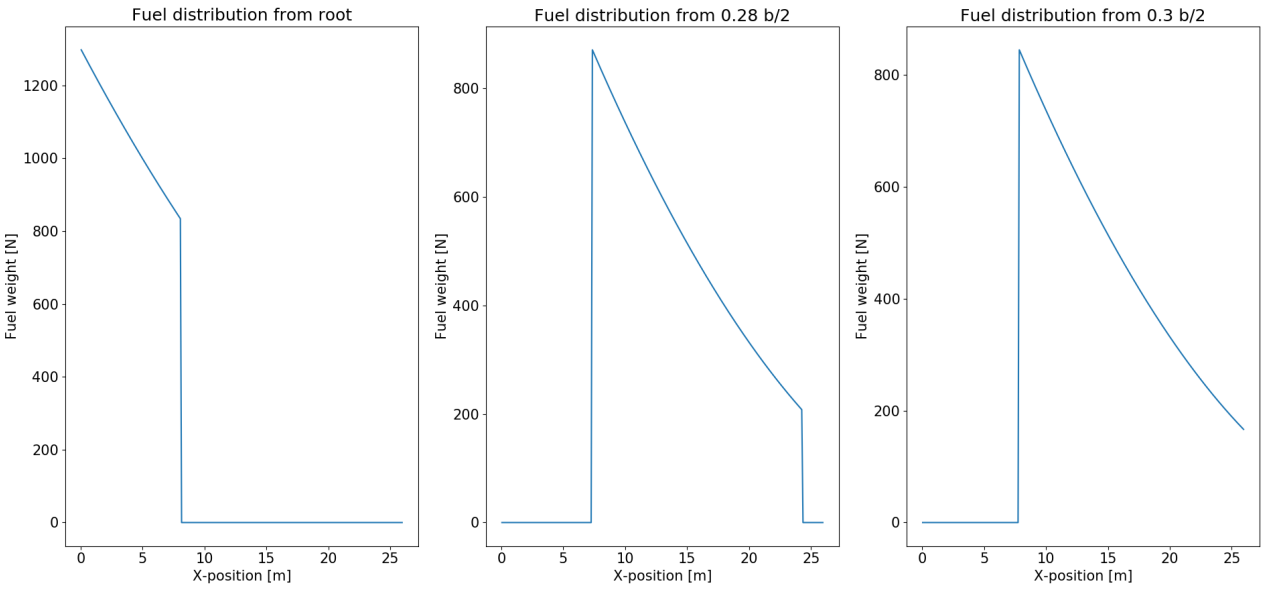

Figure 10.12: Effect of fuel tank position of the fuel weight distribution in the wing.

For the final wing-strut configuration, a more detailed stress analysis will be performed. The previous method only considered a single moment around the z-axis. In order to perform the more detailed analysis also the bending moment around the y-direction was determined based on the thrust and drag forces working on the wing. The assumed directions that these forces act are shown in Figure 10.10. Then, using Equation 10.9, the stress at n positions in the wing's cross-section for all N spanwise positions was computed. Note that for the stress analysis, a positive bending moment is seen as a moment that creates positive stress in the positive quadrant. Finally, the moment of inertia was updated based in order to ensure

that the maximum allowable stress of the material was not exceeded. When this criteria was met for all loading cases, the design of the wing was considered finalised.

$$\sigma_z = \frac{M_y I_{zz} - M_z I_{yz}}{I_{zz} I_{yy} - I_{yz}^2} z + \frac{M_z I_{yy} - M_y I_{yz}}{I_{zz} I_{yy} - I_{yz}^2} y \tag{10.9}$$

10.2.3 Trade-off

As explained in the previous section, there are various materials that were considered for the strut. Some important characteristics of the materials under consideration were shown in Table 10.1. This section will investigate the best material option by analysing the structural feasibility and weight of the wing. In order to do so, the radius of the strut was compared together with the required boom area. In order to determine the required area of the strut and the booms, one positive and one negative load case was considered separately. As the required area to satisfy the buckling requirement turned out to be significantly larger, the negative load case was used for comparing strut sizes. For the sizing of the booms, the positive load case was used, as this resulted in higher bending moments at the root and thus higher required moments of inertia. It should be noted that the required boom area represents the maximum boom area that is required somewhere throughout the span of the wing.

To be able to compare the different materials, it was decided to evaluate all the three materials at strut positions between 9 and 21 meter with respect to the root. This range was chosen as placing the strut closer to the fuselage results into difficulty with the placement of the engine, while placing the strut further away makes the angle between the strut and wing smaller, decreasing its effectiveness. Table 10.4 shows the results for the different materials. The strut force presented in this table represents the compressive strut force for the sizing of the strut. In order to determine the required boom areas for the different positions and materials under consideration, the spar areas and skin thickness remained the same for all computations. Table 10.3 shows the initial spar and skin parameters which were used for determining the required boom areas based on the required moment of inertia. These values will be used up until the final sizing of the booms in the last section of subsection 10.2.4. Furthermore, it should be noted that the presented boom mass is calculated assuming that the maximum required boom area would be used for 20 booms throughout the entire span of the wing. This is of course a large overestimation of the boom mass and only suffices as a method to compare the different materials.

Table 10.3: Assumed dimensions of initial wing structural components.

Parameter	Initial value
Horizontal spar thickness [cm]	2
Horizontal spar length [cm]	30
Vertical spar thickness [cm]	3
Skin thickness [mm]	5
Number of booms	20

Due to the different $\frac{\sigma_{f_{strut}}}{E_{strut}}$ ratios of the different materials, the strut force per material was different for each strut position. Looking at Equation 10.6 and Equation 10.8 it was expected that the allowed deflection of the strut was highest for the unidirectional carbon fibre and lowest for the aluminium. Therefore, the required deflection of the wing due to the strut force was the lowest, resulting in the lowest strut force. However, the differences between the materials are not that large. The main difference in strut radius came from the different Young's moduli which were used in Equation 10.4. As the required strut radius for buckling reduces for increasing Young's modulus and decreasing strut force, the unidirectional carbon fibre turned out the have the smallest strut radius and thus smallest strut mass. As already mentioned in subsection 10.1.3, the only downside of this material is that it can not take up forces in other directions and is expensive.

When looking at the required boom areas, it is observed that the boom areas barely differ between the materials. Although the strut forces and thus bending moments at the root differ a bit, the required difference in boom area is not that large. However, it could still be observed that unidirectional carbon fibre is favoured over the other materials. Based on these results it was chosen to go for the unidirectional carbon fibre strut, as this will yield the lightest total structure of wing and strut together. The cost of the strut will however increase, as the cost of UD carbon fibre composite is 35.2 €/kg compared to the cost of aluminium of 1.96 €/kg. Nonetheless, the weight decrease was considered decisive, as a cost increase of maximum € 130,000 on a total aircraft cost of approximately 200 million is negligible.

Table 10.4: Material trade-off table.

	Aluminium 2024				QI Carbon fibre				UD Carbon fibre			
Strut position [m]	F_{strut} [MN]	R_{strut} [cm]	A_{booms} [cm^2]	Total mass [kg]	F_{strut} [N]	R_{strut} [cm]	A_{booms} [cm^2]	Total mass [kg]	F_{strut} [N]	R_{strut} [cm]	A_{booms} [cm^2]	Total mass [kg]
21	-1,765,872	18.3	46.8	24,865	-1,767,186	19.4	46.7	20,714	-1,757,364	16.0	46.1	18,201
19	-1,870,932	17.7	32.9	18,977	-1,872,499	18.7	32.8	15,500	-1,860,672	15.4	32.0	13,319
17	-1,987,184	16.9	26.1	15,304	-1,988,925	17.9	26.1	12,472	-1,974,894	14.7	31.1	12,331
15	-2,115,743	16.1	47.4	19,933	-2,123,094	17.1	47.4	17,670.9	-2,088,052	14.0	47.4	16,379
13	-2,262,842	15.3	72.8	25,905	-2,282,763	16.2	72.8	24,148	-2,202,482	13.2	72.8	23,115
11	-2,440,389	14.4	101.9	33,150	-2,428,925	15.3	101.9	31,827	-2,309,394	12.4	101.9	31,006
9	-2,676,784	13.6	134.7	41,677	-2,650,848	14.5	134.7	40,713	-2,380,424	11.5	134.6	40,043

10.2.4 Results

This section will discuss the results of the wing-strut configuration. First the positive and negative critical load case will be determined. Based on initial results, a final strut position will be decided upon. Then a sensitivity study was performed to determine what parameters should be changed to get to the optimal, lightest final wing-strut configuration.

Critical load cases

In subsection 10.2.3 it was already mentioned that the positive load cases were sizing for the boom areas, while the negative load cases determined the size of the strut. However, as there are two positive and two negative cases, the critical case among each was evaluated. Table 10.5 shows the parameters that were compared for the different load cases. From this table it can be concluded that it depends on the position of the strut whether Case 1 or Case 2 was sizing. A similar conclusion can be made for the negative cases 3 and 4. Therefore, at this stage, without the final strut position known, non of the cases can be neglected as non-critical.

Table 10.5: Boom area and strut radius comparison for the different load cases.

Strut position [m]	A_{boom} Case 1 [cm^2]	A_{boom} Case 2 [cm^2]	R_{strut} Case 3 [cm]	R_{strut} Case 4 [cm]
21.0	46.4	43.1	16.0	15.6
19.0	32.0	27.4	15.4	15.1
17.0	31.1	35.2	14.7	14.4
15.0	47.9	59.3	14.0	13.8
13.0	73.4	87.0	13.2	13.1
11.0	102.6	118.0	12.4	12.5
9.0	135.5	152.0	11.5	11.9

As these values are based on the strut force and bending moments along the wing span, Figure 10.13 and Figure 10.14 show the shear force and bending moment diagrams for the maximum load factor (Case 1) and the minimum load factor (Case 3) respectively. These diagrams show the results for the same strut positions considered in Table 10.5.

In the V_y distribution in Figure 10.13 and Figure 10.14 it is observed that the strut force in y-direction decreases when moving towards the tip of the wing. First of all, it should be noted that the actual strut force in the direction was determined using the angle between the strut and the wing. Although this angle decreases when moving towards the tip, positioning the strut further away from the root resulted in lower tensile strut forces. This behaviour was not expected as the deflection of the wing without strut is larger at a position further from the root. Therefore, the required strut force in order to meet the maximum allowed deflection was expected to be higher.

However, by performing some additional sensitivity analysis, this behaviour could be explained. Indeed the required deflection due to the strut force decreased when positioning the strut towards the root. Nevertheless, seen in Equation 10.8, the decrease of y_a and θ_a combined is larger than the decrease in required deflection, causing the strut force to be higher. More specifically, moving from 19 m to 18 m from the tip decreased the required deflection with 27% while the denominator decreased with 32%. This result also makes sense as intuitively more force is required to deflect the wing almost the same amount at a position closer to the root.

Furthermore, the step in the V_z diagram represents the thrust force and the small step in the V_y plot, before the strut force, indicates the engine weight. Finally, it could be seen that the strut force position furthest from the root resulted in the highest bending moment at the root. This could be explained by the fact that the decrease in strut force was relatively less than the increase in distance from the root .

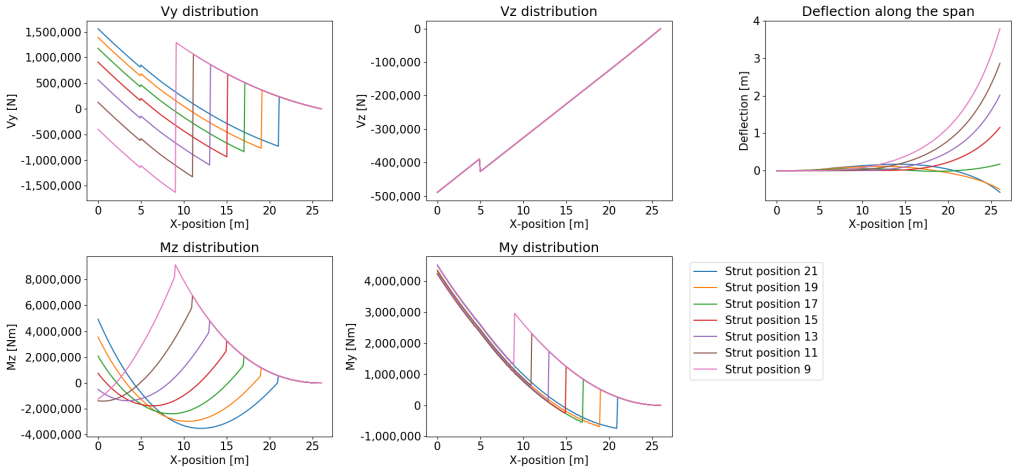

Figure 10.13: The forces, moments and deflection for the UD carbon fibre composite at varying strut positions for loading case 1.

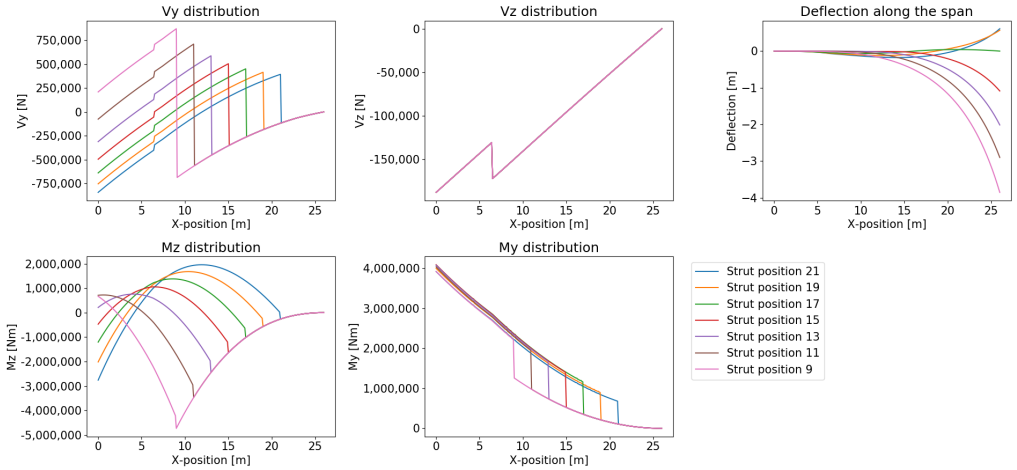

Figure 10.14: The forces, moments and deflection for the UD carbon fibre composite at varying strut positions for loading case 3.

Sensitivity: strut positioning

Varying the strut position along the semi-span influences the force and moment distributions. This in turn affects the required moment of inertia and strut area. Therefore, the change of root moment around the z-axis and the change in root force in y-direction have been investigated, as shown below in Table 10.6. This has been done for different strut positions, where the value indicates the percentage change with respect to the previous strut position. It should be mentioned that the values shown in Table 10.6 were obtained for the maximum load case, Case 1.

Table 10.6: Sensitivity of different strut positions on the root moment and root force of interest.

Strut position [m]	Change in M_{root_z} [%]	Change in F_{root_y} [%]
23	-10.5	-7.4
21	-25.8	-12.5
19	-34.3	-17.6
17	-51.8	-26.9
15	-126.2	-50.7
13	-586.5	-148.6

Determining strut position

In subsection 10.2.3 it was already mentioned that the material selection criteria was weight. Looking at the different strut positions it could be observed that the radius of the strut decreases when moving closer to the root, while the required boom area increases. Although it is favourable to have a smaller strut with respect to the aerodynamics of the aircraft, the weight of the wing is also very important. Finally, it was chosen to search the lowest wing-strut weight combination with a somewhat reasonable strut size. When looking in Table 10.4, for UD carbon fibre composite, it was observed in which range of strut positions the weight would be the least. Therefore, a more narrow range around the optimum of 17 m - 19 m was analysed. The data for these narrowed down strut positions is presented in Table 10.7.

Table 10.7: Parameters of the narrowed UD carbon fibre composite range.

X_{strut} [m]	A_{boom} [cm^2] Case 1	A_{boom} [cm^2] Case 2	R_{strut} [cm] Case 3	R_{strut} [cm] Case 4	Strut mass [kg]	Boom mass [kg]	Total mass [kg]
19.0	32.0	26.1	15.4	15.1	4,102.9	9,149	13,319
18.5	28.2	22.5	15.3	14.9	3,912.3	8,142	12,054
18.0	24.7	24.1	15.1	14.8	3,725.7	7,155	10,881
17.5	21.9	28.9	14.9	14.6	3,543.3	8,369	11,912

Looking at Table 10.7, it was chosen to position the strut at 18 m from the root, as the goal is to design a wing that is as light as possible while still meeting the required loads. Note that the skin and spar mass are not shown here, as these masses remained the same for all strut positions and are not included in the total cost. Furthermore, the boom mass was calculated in a similar way as for Table 10.4.

Sizing for stress

With the final strut position and strut material known, a more detailed stress analysis and boom sizing was performed as described in subsection 10.2.2. Using the moments of inertia that came out of the tool, together with the obtained bending moment distributions around the z- and y-axis, the maximum stresses that occur at each position in the wing's cross-section were computed and are shown in Figure 10.15. This stress plot represents load case 1, which was determined to be sizing for the booms. The assumed initial sizes of the spars and booms were already shown in Table 10.3.

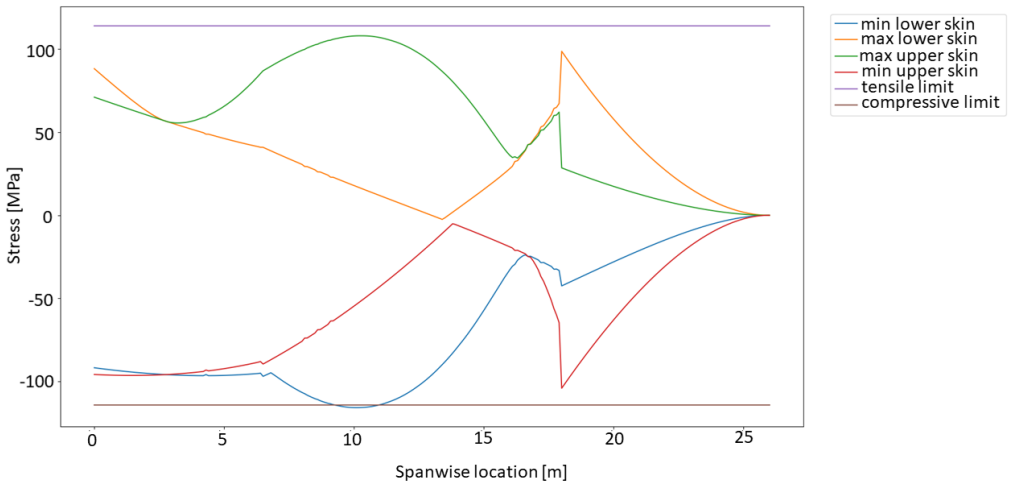

Figure 10.15: Initial wing stresses.

In Figure 10.15 it could be seen that, initially, the stress exceeded the allowed fatigue stress of 114 MPa at only one position in the wing. However, at other positions the stress requirement was easily met, meaning that locally the moments of inertia could be lowered. This directly indicated that the weight could be reduced by optimising the geometry of the wing. So, in order to change the magnitude of the stresses, the moments of inertia needed to change. To determine which areas (spars, boom or thickness of the airfoil) was most favourable to be increased or decreased, in order to have the lightest structure while meeting the stress requirement along the entire span, a sensitivity analysis was performed. This sensitivity analysis will be discussed next.

Sensitivity: moments of inertia

In Table 10.8 it is observed that especially increasing the thickness and length of the horizontal parts of the spars resulted in the largest stress decrease. Increasing the thickness of the vertical parts of the spar has the smallest influence on the mass of the wing, while still reducing the stress level to a large extend relative to the other parameters. Increasing the boom area is evenly effective in reducing the stress level as increasing the vertical spar thickness, however, yielding a mass increase which is four times as large. Finally, increasing the airfoil thickness seems to be the least favourable option to achieve the allowed stress level.

Table 10.8: Sensitivity of changing different areas on the stress in and mass of the wing

Parameter	Parameter change	Mass change	Stress change
Horizontal spar thickness	1%	0.74%	-0.34%
Horizontal spar length	1%	0.75%	-0.49%
Vertical spar thickness	1%	0.25%	-0.25%
Boom area	1%	1%	-0.25%
Skin thickness	1%	1%	-0.02%

Final wing-strut sizing

Keeping the effects of the sensitivity analysis in mind, the different parameters in Table 10.8 were changed such that the stress was closest to the allowed stress level at every position within the wing's cross-section for the entire span of the wing. In this way the lowest wing weight could be achieved. Figure 10.15 showed that especially the moments of inertia from the position of the strut till the tip could be significantly reduced. In addition, from the root till 10 m the moments of inertia could also be lowered. From the sensitivity analysis it was concluded that increasing the vertical and horizontal parts of the spars was most effective. It was also concluded that cutting in boom area would reduce the mass more than when reducing the spar area. Combining this knowledge resulted in linearly increasing and decreasing spars. Furthermore, the number of booms was reduced and were cut off after the strut at 18 m. Table 10.9 shows the final dimensions of the spars, booms and skin of the wing. Two values separated by a dashed sign indicates the linear decrease or increase between the values.

Table 10.9: Final wing geometry.

Parameter	x = 0 - 18 [m]	x = 18 - 22.5 [m]	x = 22.5 - 26 [m]
Horizontal spar thickness [cm]	3.8	3.8 - 1	1
Horizontal spar length [cm]	22 - 40	40 - 5	5
Vertical spar thickness [cm]	4	4 - 1	1
Boom area [cm^2]	11	0	0
Skin thickness [mm]	1	1	1

In Table 10.10 the total wing mass, cost and strut radius are given. The final total wing mass turned out to be 11% of the MTOW. In addition, it was computed what the wing mass would be in case of a wing without strut. It was computed that the wing would then have a mass of 27163 kg. This is 64.7% more than the current mass of the wing. Though this difference is larger than expected, it can be explained when looking at the wing geometry. As the wing is very slender, the wingspan is rather large relative to the surface area. Therefore, the moment generated by the forces at the tip becomes larger than for aircraft with less slender wings. A larger moment directly results in more inertia being required in order to keep the stress in the wings cross-section below the fatigue limit, which results in a heavier wing. Finally, in Figure 10.16 a visual representation of the wing's cross-section up until the position of the strut is shown. This wing geometry satisfied the stress requirement for all loading cases considered, which will be further elaborated on in subsection 10.2.5.

Table 10.10: Final wing parameters.

Total wing mass [kg]	16,487
Total wing cost [€]	156,485
Final strut radius [cm]	15.1

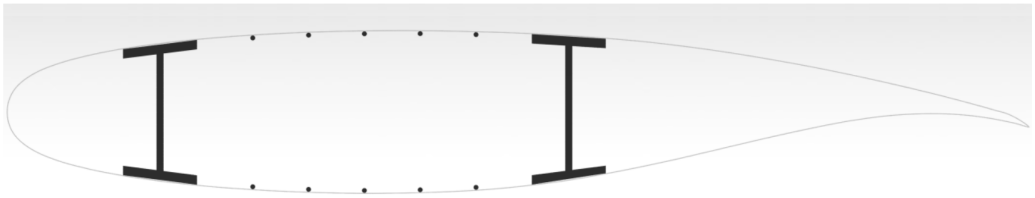

Figure 10.16: An illustration of the wing cross-section.

10.2.5 Verification and validation

In this subsection the verification and validation of the wing analysis method will be discussed. Furthermore, the requirement compliance and risk mitigation will be elaborated upon as well.

Simplified excel model

Before the deflection calculations described in subsection 10.2.2 were implemented in python, a simplified excel model was used to verify the correctness of the equations used and the inputs given. The model was build up step by step in order to check whether the results were and kept being as expected. At first, the model consisted of a rectangular beam with a constant cross-section being clamped on one side, while the other end was kept free. Then, using equations from

Roark, the deflection along the length of the beam was computed based on the loading conditions the beam was subjected to. In order to verify the deflection of each loading component, the different components were plotted to see the effect. This is shown below in Figure 10.17. As can be seen, each component goes as expected, downward acting forces and distributions create a downward deflection, while upward acting forces and distributions yield an upward deflection.

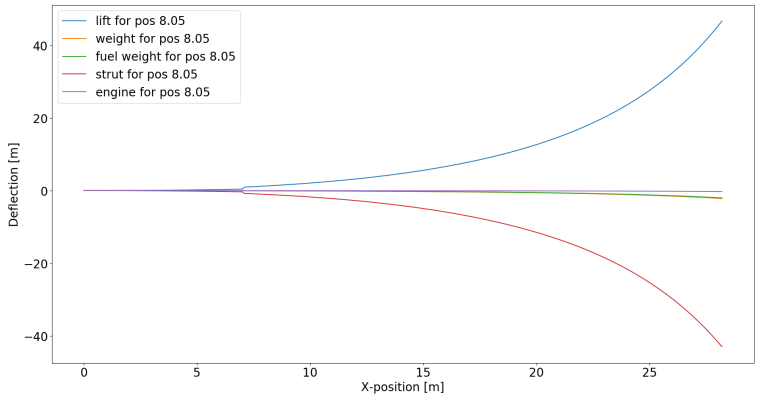

Figure 10.17: The verification for different load components

Derivative calculations

Moving on, the deflection over the semi-span keeps decreasing from the location of the semi-span onward. However, as the lift force is higher than the weight, the derivative or second derivative should increase again from the position of the strut onward. Therefore, a plot was created of the first and second derivative of the shown. This was evaluated for the different loading components as well, which yielded the result shown in Figure 10.18. Note that this graph is for a strut position of 23 m with respect to the root. As can be seen, the deflection itself becomes almost linear behind the position of the strut as the first derivative of the deflection becomes almost constant. This makes sense as the lift behind the strut position is larger then the fuel weight and structural weight together. However, as the strut force is very large, it compensates for an increase in deflection again. For the second derivative, it can be seen that it crosses zero again at the strut position. After the strut, it is in a declining rise until the end. This makes sense taking into account the argument for the first derivative as well. Therefore, the deflection tool is deemed verified.

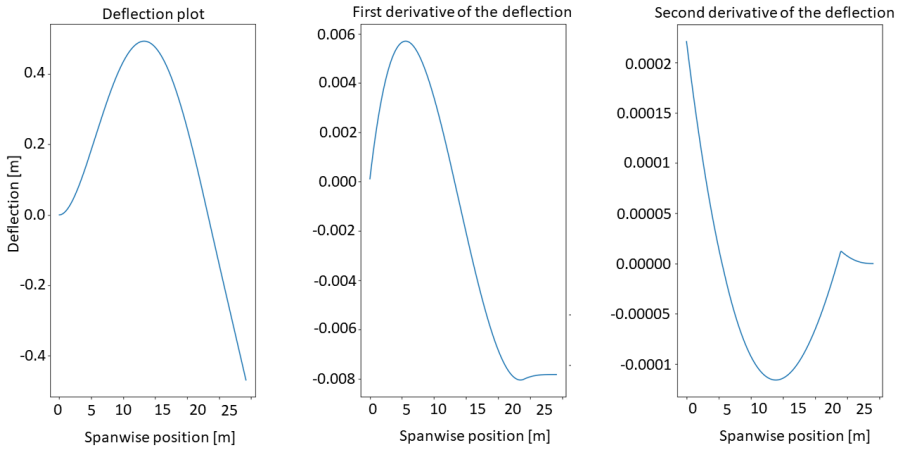

Figure 10.18: The derivatives of the deflection for a single load case.

Wing mass validation

During the initial design phase, a class II weight estimation was made as an indication of the wing weight [17]. This resulted in a wing mass of 14,242 kg. Comparing this with the wing mass of 16,487 kg that resulted from the structural analysis tool, there remains a difference of 2,245 kg, equal to 13.6%. Though this difference is still significant, it can be explained by breaking the wing mass down, as these values both include the mass of the strut. Roskam states that the strut is approximately 10% of the wing mass resulting from the class II weight estimation, which equals a strut mass of 1,424 kg [17]. However, the strut of the EcoHopper 450 weighs 3,736 kg, which is 22.6% of the wing weight. The reason for the strut mass being so large can be explained by the strut positioning. The strut is placed at 18 m from the root (0.69 $\frac{b}{2}$), making it very long. Furthermore, it is 30.2 cm in diameter, making it very thick as well. If the wing masses are compared when the strut mass is subtracted, the residual wing masses are 12,818 kg and 12,752 kg for the class II estimation and the

structural analysis tool respectively. This difference is only 66 kg, equal to 0.52%. Thus, it can be concluded that the wing masses themselves are very close. Therefore, the wing mass resulting from the structural analysis tool is deemed valid.

Requirement compliance

In order to show compliance with the requirements for the final wing geometry, the maximum stress distribution was plotted for all four load cases in Figure 10.19 till Figure 10.22. It can be seen that the maximum load case is indeed the limiting case and that the wing can cope with all load cases. Therefore, the requirements BIB-SBS-STR-03, BIB-SBS-STR-05, BIB-SBS-STR-06, BIB-SBS-STR-09 and BIB-SBS-SNR-02, regarding the load on the structure of the wing, have been met. Furthermore, as all the fuel fits in the wing box, BIB-SBS-SNR-01; is satisfied as well.

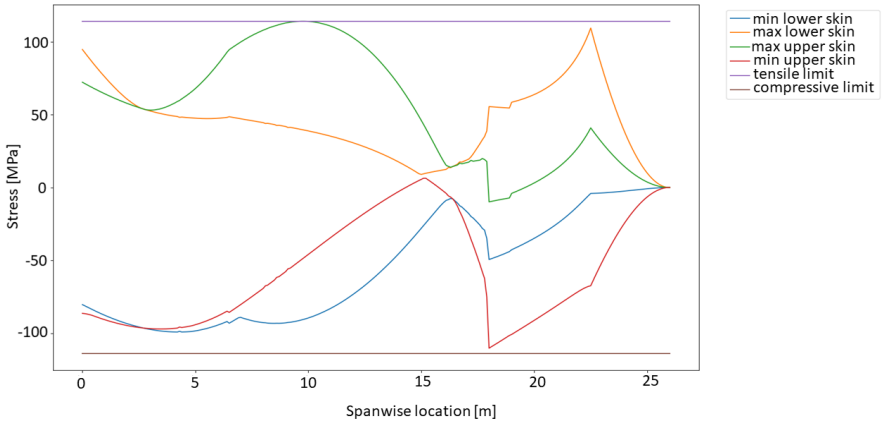

Figure 10.19: Maximum and minimum stress distributions for the entire half span of the wing (Case 1).

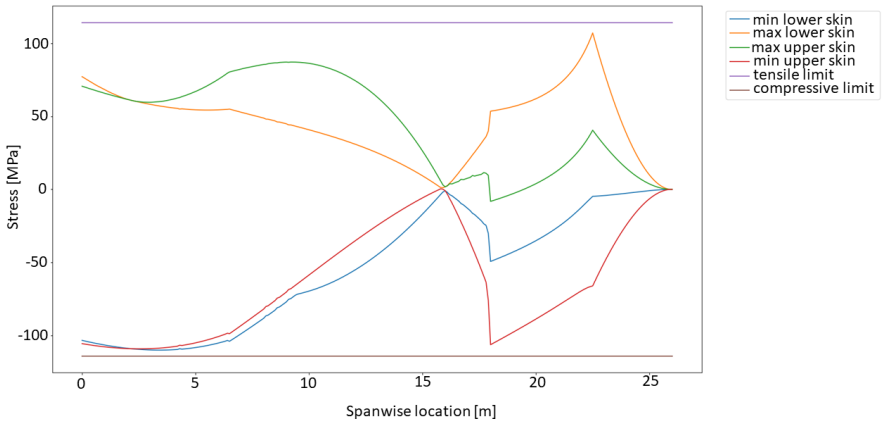

Figure 10.20: Maximum and minimum stress distributions for the entire half span of the wing (Case 2).

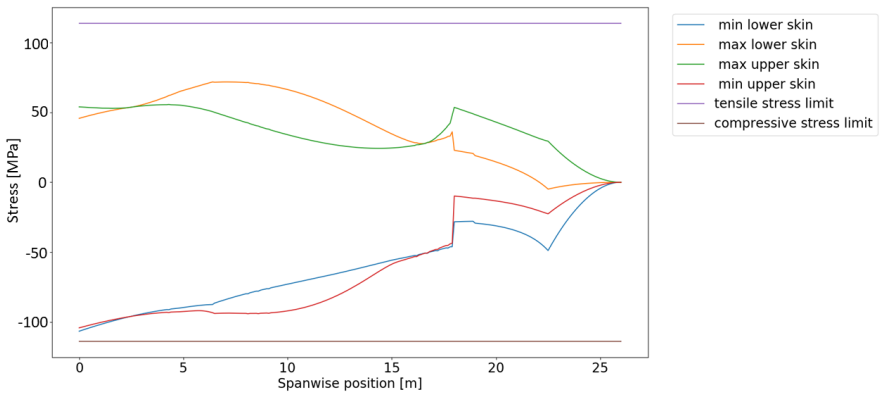

Figure 10.21: Maximum and minimum stress distributions for the entire half span of the wing (Case 3).

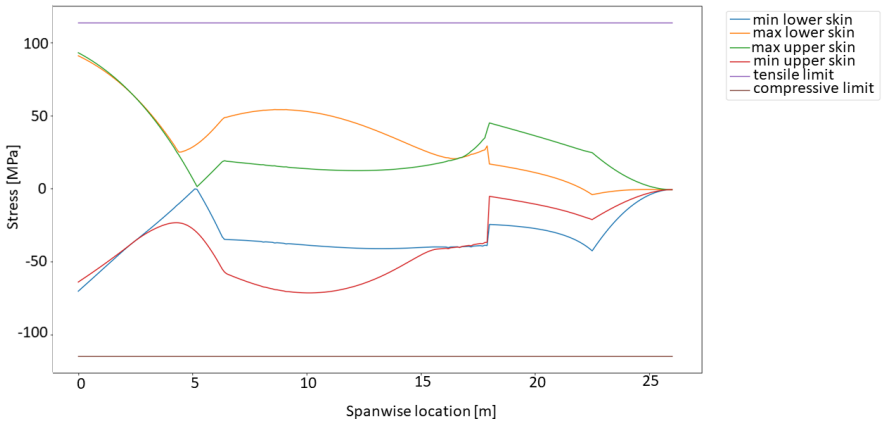

Figure 10.22: Maximum and minimum stress distributions for the entire half span of the wing (Case 4).

Risk mitigation

Damage on the outside of the wing can be mitigated by inspection. The connection of the control and high lift devices can be checked as well. These checks can be performed before and after each flight. Noticing damage, like crack initiation, of the strut is however difficult. Therefore, different non-destructive testing methods should be used regularly. Also, the strut should be sized with sufficient safety margin in order to ensure that the first inspection would only be required after a certain number of flights. When any type of damage is detected, the wing component should be replaced if possible.

10.3 Empennage

The empennage is primarily used for the stability and control of the aircraft. Therefore, the structure needs to be sufficiently strong to cope with the critical load cases encountered. In this section the empennage is analysed.

10.3.1 Requirements analysis

In this subsection the requirements that follow from the functional and risk analysis will be presented.

Functional analysis

The empennage is an important structural component as it stabilises the aircraft. The main function of the structure of the empennage is that it should be designed to handle all the loads that are applied on the horizontal tail to stabilise and control the aircraft.

Risk analysis

The risks that apply on the wing are also applicable for the empennage. However, another risk is introduced due to deflection of the elevator:

Extreme weather conditions: The hinges that support the elevator of the horizontal tail are vulnerable during extreme cold weather conditions. It can happen that the hinges freeze during these weather conditions.

Requirements

From the functional analysis and risk, several requirements can be set up. Requirements **BIB-SBS-STR-06**, **BIB-SBS-STR-09**, **BIB-SNR-03** that can be found in section 10.2 are also applicable for the empennage. The following requirement can be added to the list based on the functional analysis.

- **BIB-SBS-SNR-04:** The horizontal tail shall be able to withstand the loads during a maximum elevator deflection of 30 deg.

10.3.2 Method

First of all, it should be mentioned that for the empennage analysis the same reference frame as for the wing was used. For now, only the horizontal tail was analysed due to the fact that this component of the empennage will experience more critical loads during its lifetime than the vertical tail. To obtain the shear force and bending moment diagrams, the same tool was used as the one for the wing. The only differences were that no engines were placed on the tail, no strut force was acting on the tail and no fuel tanks were located inside the cross-section of the horizontal tail. Furthermore, the horizontal tail was analysed during a different flight condition than the wing due to the fact that the horizontal tail will experience most of its critical forces during take-off when the elevator has its maximum deflection of 30 deg.

10.3.3 Results

This subsection will explain the results that came out of the analysis of the horizontal tail. The shear force en bending moment diagrams during the critical landing condition are shown in Figure 10.23. A similar plot was constructed for the cruise condition, the difference only being the magnitude of the forces and bending moments.
Figure 10.23, evaluates the forces and moments around the root chord of the horizontal tail. The blue line in graph shows the moment and force distributions when the elevator has a maximum negative deflection. This would be the case during take-off. During this procedure the horizontal tail should withstand these distributions. It can be seen that the lift distribution and weight distribution of the horizontal tail works in the same negative y-direction and would create a slightly higher moment and shear force compared to the orange line, which represents the moment and force distribution when the elevator has its maximum positive deflection. This scenario could happen during an emergency situation in flight. However, the graphs also show that the magnitude of the moment and forces are almost the same. The only difference is the direction (sign) of the forces, where for the orange line the lift is working in a different direction than the weight, while for the blue line they are working in the same direction. The horizontal tail should be sized to handle both load cases.

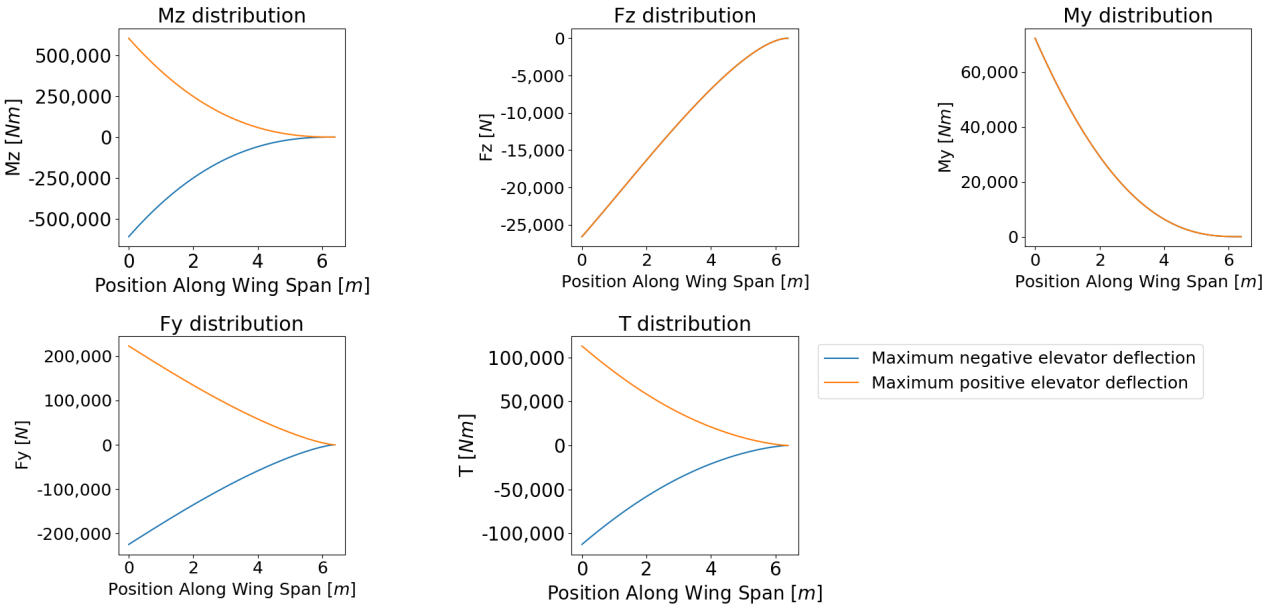

Figure 10.23: The forces and moments of the horizontal tail during its critical load case.

During cruise conditions, the aircraft is trimmed. The horizontal tail generates zero lift during this configuration due to an elevator deflection of 0 deg. Only the weight of the horizontal tail contributes to the forces and moments. Therefore, the forces and bending moments working on the empennage during this condition are significantly smaller and thus not critical. The maximum reaction forces and bending moments at the root chord of the horizontal tail are listed in Table 10.11.

Table 10.11: Results of the horizontal tail analysis.

Load case	V_y [N]	V_z [N]	M_y [Nm]	M_z [Nm]
Maximum elevator deflection	-224,888	-26,606	72,243	-609,611
Cruise	-912	-252	690	-2,493

10.3.4 Verification and validation

As for the empennage the same model as for the wing analysis has been used, no further verification and validation procedures were performed for the analysis method. However, this section will elaborate upon the requirement compliance and risk mitigation.

Requirement compliance

The structure of the empennage has not been sized for bending yet. So, strictly speaking, there is no compliance with the requirements. However, as the magnitude of the bending moments at the root are not that large and decrease quickly when moving towards the tip, sufficiently thickening the skin at the root or placing a few stiffeners would be sufficient.

Risk mitigation

Similar ways of risk mitigation as described previously for the wing apply. This mainly includes inspection for damage before and after flights. If a part of the empennage is damaged, such as the elevator, this should be replaced. Differently from the wing, the empennage has no strut which risks need to be mitigated.

10.4 Fuselage

This section contains the complete analysis that has been performed for the fuselage of the EcoHopper 450. First, a requirements analysis will be presented in subsection 10.4.1, after which the method used to analyse the fuselage is shown in subsection 10.4.2. Finally, the results are shown in subsection 10.4.3 and verification and validation is performed in subsection 10.4.4.

10.4.1 Requirements analysis

Functional analysis

The fuselage has a number of functions. First of all, it should protect the payload from the harsh outside environment. Moving on, it should withstand the loading of pressurisation and carry all the loads acting on it. Finally, it should provide a view to the passengers of the outside world.

Risk analysis

When looking at the functions of the fuselage a risk can be identified:

External object collision: The fuselage can be hit by, for example, a bird while in flight or a refuelling car while on the ground. This might damage the fuselage, resulting in a lower strength of the structure.

Requirements

From the functions and the risk that have been identified for the fuselage, several requirements can be set up. Note that the requirements **BIB-SBS-STR-05**, **BIB-SBS-STR-06** and **BIB-SBS-STR-09** mentioned in section 10.2 are requirements for the fuselage as well. Additionally, remaining requirements are shown based on the functional analysis.

- **BIB-SBS-SNR-04**: The fuselage structure shall be able to withstand the pressurisation loading during its lifetime.
- **BIB-SBS-STR-02**: The aircraft shall contain windows for passengers to view the outside world.

10.4.2 Method

This subsection will elaborate upon the sizing of the fuselage for the EcoHopper 450. First, the reference frames that were used will be discussed, after which the fuselage analysis method will be presented.

Reference frames

The reference system used for the fuselage sizing is shown in Figure 10.24. In this figure, the axes with subscript 1 were used to evaluate the bending moments and thickness distribution of the fuselage, which will be discussed in subsection 10.4.2. The axis with subscript 2 indicate the tilted axis system in case of an bank angle. Furthermore, α_{fus} indicates the angle between the positive x-axis (X_1) and the evaluated point in the fuselage and θ_{fus} is the bank angle of the aircraft which was used for the fuselage sizing.

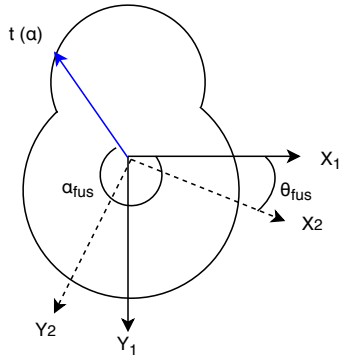

Figure 10.24: Fuselage cross-sectional view with reference frame.

Fuselage analysis

The fuselage should be designed to handle pressurisation and critical moments during take-off, cruise, landing and in case of emergency situations. For example, when there is an engine failure. Therefore, the required fuselage thickness was calculated to handle the pressurisation as well as to cope with the critical bending moments during operation.

To determine the lower boundary for the skin thickness due to pressurisation, Equation 10.10 and Equation 10.11 were used. The pressure difference Δp is the internal pressure minus the pressure at maximum cruise altitude. For passenger comfort, the internal pressure level was taken to be equal to a pressure altitude of 7,000 ft. This inflation of the fuselage is assumed to occur only once per flight, causing circumferential stresses in the fuselage. Therefore, the fatigue stress of aluminium of 114 MPa, as shown in Table 10.1, was used. For the longitudinal stress the fatigue stress of 105 MPa was used, as it is assumed that the fuselage is loaded in tension multiple times per flight. The difference in the fatigue stress values used between the wing and the fuselage was described in section 10.1.

$$t_{min_{hoop}} = \frac{\Delta p R}{\sigma_f} \quad (10.10)$$

$$t_{min_{long}} = \frac{\Delta p R}{2\sigma_f} \quad (10.11)$$

Next, the fuselage should be sized in order to withstand the critical moments that could occur during flight. Therefore, first the critical loading conditions should be determined. A simple 2D drawing was made for the two critical load cases that were considered.

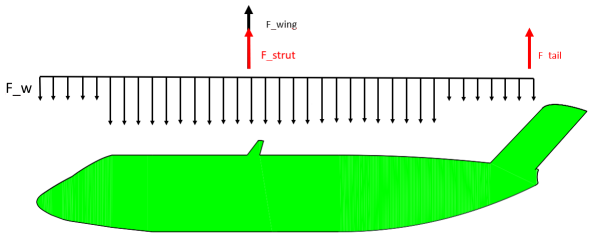

Figure 10.25: The forces and moments of the horizontal tail during cruise.

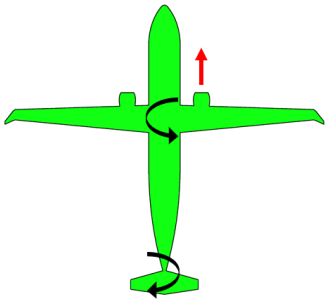

Figure 10.26: The forces and moments of the horizontal tail with one engine inoperative.

Figure 10.25 shows all the different loads that act on the EcoHopper 450 when considering the first load case (Case 1). It can be seen that the payload weight is uniformly distributed over the cabin, without taking the weight of the cockpit and empennage into account. These weights are separately distributed over their own length. The reaction forces of the wing, strut and horizontal tail that came out of the previous analyses, described in subsection 10.2.4 and subsection 10.3.3, were used as point forces in this analysis. Furthermore, this method assumed that the fuselage does not generate any lift, which in practise is not true. However, the generated lift by the fuselage would decrease the force and moment distributions, causing the maximum shear force and moments to become less critical. Therefore, it must be noted that this is a conservative approach. Solving all these forces for force and moment equilibrium resulted in the loading diagrams illustrated in subsection 10.4.3.

Another critical load case that the fuselage can experience during flight is an engine failure, illustrated in Figure 10.26. Such an engine failure will introduce a yawing moment on the fuselage. A reaction to this yawing moment would be to create a counteracting moment using the rudder in the vertical tail. This will in turn result in a bending moment around the y-axis of the fuselage.

Based on the maximum moments around the x- and y-axis of the fuselage, the required thickness of the fuselage was calculated in the following way. The first iteration considered that the fuselage had a simplified variable thickness, since the bending stress is not constant around the fuselage. For this iteration a simplified model of the fuselage was used, in which the cross-section was assumed to be circular. This allowed to rearrange Equation 10.9 into Equation 10.12, in which $I_{xx} = I_{yy} = \pi R^3 t$ could be used. Furthermore, M_x and M_y are the critical bending moments previously discussed. The angle θ_{fus} represents the bank angle that could occur during flight. This angle was used to decompose the moments to the principal axis, indicated with subscript 1 in Figure 10.24. Finally, α_{fus} was the angle between the evaluated point within the fuselage cross-section and the principal x-axis.

$$t_{min_i} = \frac{(-M_x cos(\theta_{fus}) + M_y sin(\theta_{fus}))sin(\alpha_{fus}) + (M_y cos(\theta_{fus}) + M_x sin(\theta_{fus}))cos(\alpha_{fus})}{\pi R^2 \sigma_f} \tag{10.12}$$

The output of this first iteration, which was the minimum required thickness at a specific point based on the different considered bank angles, was used in a second iteration process. This procedure used the thickness distribution from the first iteration to update the moments of inertia using Equation 10.13 and Equation 10.14. In order to do so, the fuselage was discretised into small segments which could all be approximated as flat plates. Then, the normalised stresses at the centroid of each segment were computed for each bank angle using Equation 10.15. The normalised stresses are an indication of the structural efficiency and should be as close to one as possible. The stress ratio of a segment was then used to update the thickness of a segment. Ideally, this reiteration process should continue until the normalised stresses converge to one everywhere. A sufficient amount of iterations resulted in a more specific thickness distribution of the fuselage cross-section. Based on this new thickness distribution the placement of the stringers was determined. Similarly as for the wing analysis method, these stiffened elements were represented as booms.

$$I_{x_1 x_1} = \sum_{i=1}^{n} \frac{t_i a_i^3 \sin^2(\alpha_{fus} + 90^\circ)}{12} + t_i a_i R^2 \sin^2 \alpha_{fus} \tag{10.13}$$

$$I_{y_1 y_1} = \sum_{i=1}^{n} \frac{t_i a_i^3 \cos^2(\alpha_{fus} + 90^\circ)}{12} + t_i a_i R^2 \cos^2 \alpha_{fus} \tag{10.14}$$

$$t_{new} = t_{old}\left(\frac{\sigma_z}{\sigma_f}\right)_i = \left(\frac{-M_x cos(\theta_{fus}) + M_y sin(\theta_{fus}) y}{I_{x_1 x_1}} + \frac{M_y cos(\theta_{fus}) + M_x sin(\theta_{fus}) x}{I_{y_1 y_1}}\right)_i / \sigma_f \tag{10.15}$$

In order to determine the area of the booms, first of all the required thicknesses were multiplied with their corresponding segment length. Based on these required areas, the boom areas were sized such that the fuselage cross-section remained symmetric with respect to the y-axis. Then, using the position and area of the booms, the centroid of the fuselage frame could be determined. The centroid was in turn used to update the moments of inertia. Next, the actual stress distribution was computed for each bank angle and the boom areas were updated until the maximum stress was below the fatigue stress of 105 MPa.

10.4.3 Results

This subsection will present the results that followed from the analysis of the fuselage. The loading diagrams will be presented first, after which the thickness distribution is determined for both pressurisation and the bending moment in the fuselage. Finally, based on the thickness distribution, the placement of the stiffened elements in the fuselage was determined.

Loading diagrams

The loading and moment diagrams for the fuselage during cruise, with an ultimate load factor of 3.84, are illustrated below in Figure 10.27. For a visualisation of the required thickness for a certain position within the fuselage, see Figure 10.24.

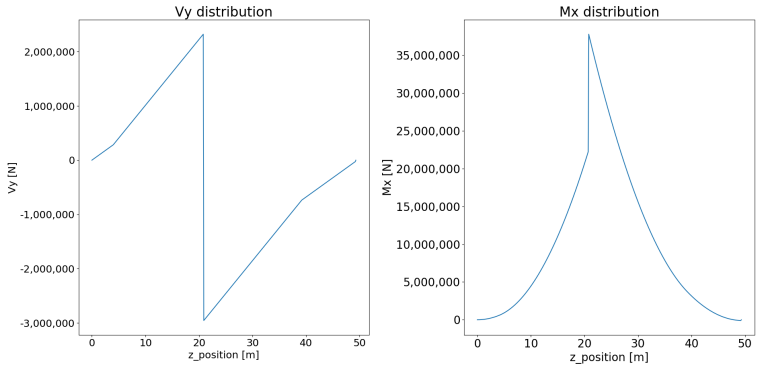

Figure 10.27: The loading and moment diagrams of the fuselage during cruise when experiencing a load factor of 3.84.

According to Figure 10.27, both distributions start with a force/moment equal to zero at the nose of the aircraft. For both, their maximum is at the attachment point of the wing due to an introduction of the wing reaction forces. These maxima are equal to 37,799,412 Nm for the moment and -2,956,635 N for the shear force. Finally, note that both the shear force and the moment return to zero at the end of the fuselage, as this is also required for equilibrium. Note that the small drop at the end of the shear force diagram represents the reaction force of the horizontal tail. Furthermore, the maximum M_y due to the single engine failure, visualised in Figure 10.26, was equal to 1,500,000 Nm.

Stress distribution

As already mentioned, the fuselage thickness requirements were analysed for both the pressurisation and the critical bending moments of the fuselage. Due to the pressurisation, the highest required thickness resulting from either the longitudinal or circumferential (hoop) stress requirement shall be considered. The minimum required thicknesses were computed to be 0.9 mm and 1.66 mm respectively. Next, the minimum thickness due to the maximum bending moments will be discussed.

Following the method as described in subsection 10.4.2, the first iteration yielded a thickness distribution as shown in Figure 10.28 for the combined loading of the maximum moments discussed above. Bank angles ranging from -30 deg until 30 deg were analysed, as a bank angle of 30 deg to turn to the right or the left was considered to be the maximum bank angle that the aircraft could experience during flight. Already in this iteration, certain peaks could be observed. Note that the absolute value of the stress is plotted. At the position of the peaks, the fuselage thickness requirement is the largest, indicating that the stress will be the highest there as well. The shape and varying magnitude of the graph can be explained by the fact that this iteration process assumes a circular cross-section. However, as an input, the tool uses the varying radius of the fuselage. This, for example, causes the radius of the most upper segment of the fuselage to be lower than 2 segments to the left of it.

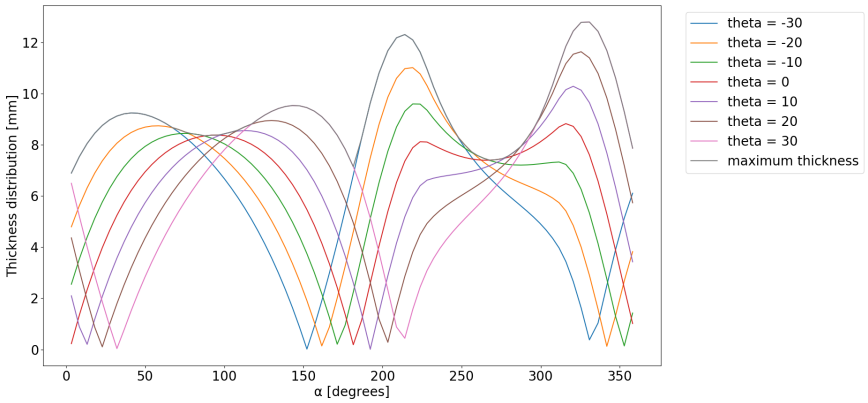

Figure 10.28: Minimum thickness distribution of the fuselage

Using the minimum required thicknesses of the first iteration as an input for the second iteration process, made it possible to update the thicknesses profile using the stress ratios per segment. The iteration criteria for updating the thicknesses were determined to be: if the stress ratio of a segment was between 0.9 and 0.99 or if the thickness of a segment was 0, the thickness of a corresponding segment remained the same. In any other case the thickness was updated using Equation 10.15. Figure 10.29 shows the results of this process for bank angles of -30 deg, 0 deg and 30 deg after performing 50 iterations. It could be observed that the thickness at the previously observed peaks in Figure 10.28 increased while the thickness of the other segments went towards zero with an increased number of iterations. Therefore, 50 iterations seemed

to be sufficient in order to determine where the stiffened elements should be placed. It was also observed that the largest peaks occur at 50 deg, 140 deg, 240 deg and between 280 deg till 300 deg. These peaks are primarily related to the stress in the fuselage generated by the moments in case of the bank angles of 30 deg and -30 deg. This is due to the combined effects of decomposing the moments and the shape of the fuselage mentioned earlier.

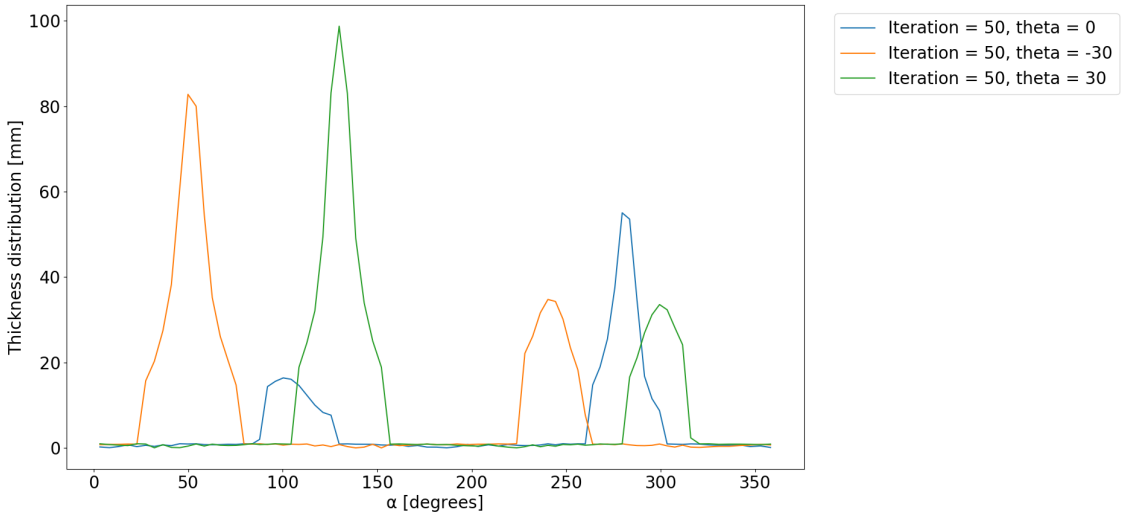

Figure 10.29: Thickness distribution after second iteration process.

Based on the outcome of the second iteration process, the positions of the booms were determined. As already mentioned, it was chosen to position the booms symmetric with respect to the y-axis to simplify calculation. Given certain boom areas, the stress distribution was evaluated for each segment to make sure it was below the 105 MPa. If needed the boom areas were adapted such that the stress requirement was met for the lowest possible fuselage weight. Finally, it was chosen that in case the required boom area was smaller than 10 cm^2 the boom area was set to the length of a segment times 2 mm. In such a case, the boom represents the skin of the fuselage of 2 mm. If the required boom area was larger than 10 cm^2 it was set to 50 cm^2. This resulted in the fuselage geometry shown in Figure 10.30 and a stress distributions shown in Figure 10.31. Assuming that these stiffened elements run through the entire fuselage, the mass of the fuselage frame was estimated to be 28,264 kg costing € 55,397. Assuming that the stringers would run through the entire fuselage would result in an overestimation of the fuselage weight, as normally the amount and size of the stringers will differ per fuselage section. However, other fuselage parts that were not considered, such as the structure of the floor, will increase the weight again. Therefore, this weight estimation is more conservative by assuming that the stringers run through the entire fuselage length.

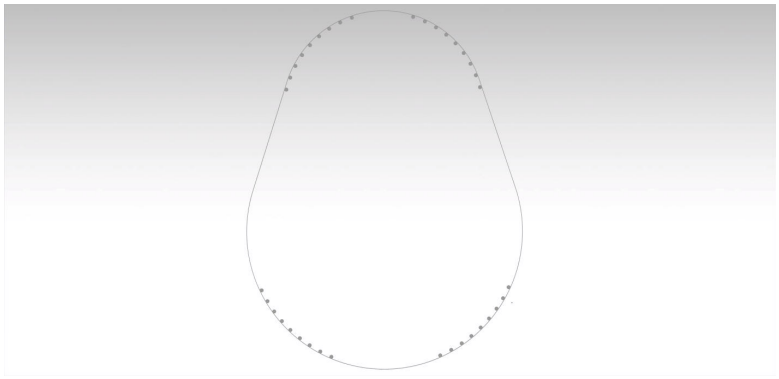

Figure 10.30: Geometry of the stiffened elements in the fuselage cross section.

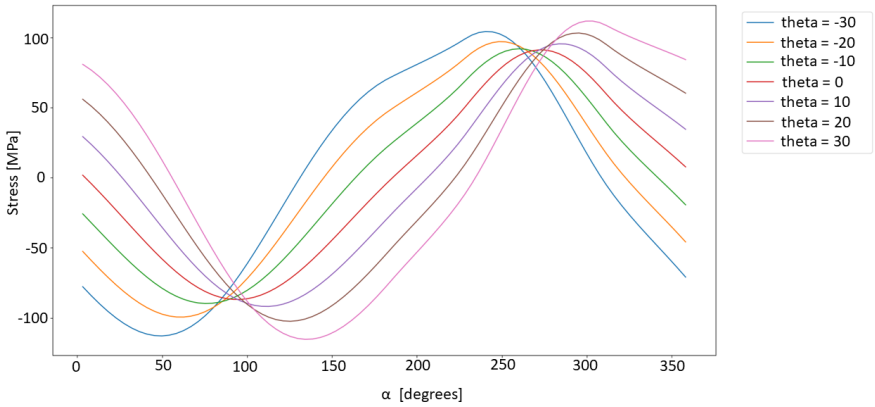

Figure 10.31: Maximum stress in the fuselage.

10.4.4 Verification and validation

First the verification and validation of the fuselage analysis method will be presented. Afterwards, the requirement compliance and risk mitigation will be provided.

Thickness model verification and validation

The distribution of the thickness was checked for either a moment around the y- or x-axis for 0 deg bank angle. This resulted in Figure 10.32 and Figure 10.33.

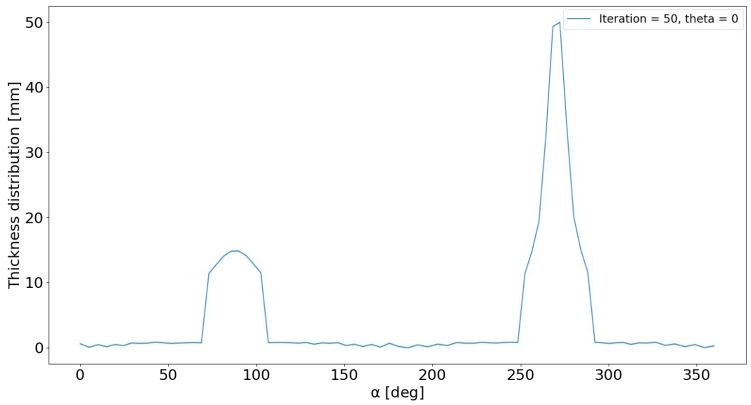

Figure 10.32: Thickness distribution for zero bank angle just a moment around x

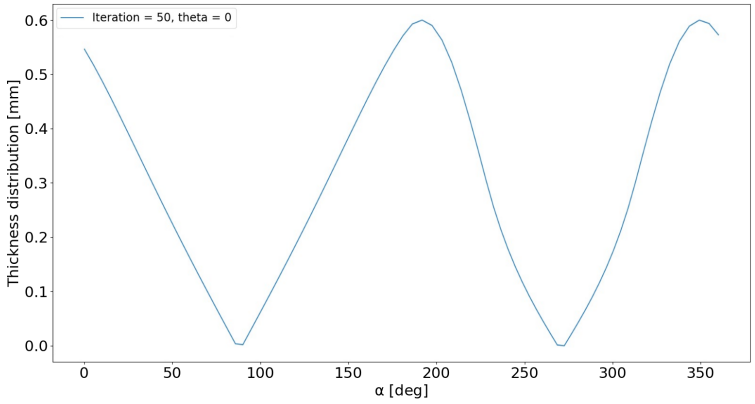

Figure 10.33: Thickness distribution for zero bank angle just a moment around y

As already expected, just considering the M_x moment resulted in large stresses and thus thickness requirements on the top and bottom of the fuselage cross-section. The M_y distribution also had the expected shape, in which the maximum stresses and thus thickness requirements were at the right and left side of the fuselage. Then, only a bank angle of 30 and -30 were plotted as well. It was expected that the shape of the plots remained the same but were shifted to either the right or the left. Figure 10.29 showed that this was indeed the case but that the magnitude changed as well. This change in magnitude is due to the shape of the fuselage. A fuselage segment at an angle of 90 deg with respect to the rotated moment of 30 deg instead of 0 deg has larger or smaller y and x coordinates, resulting in a different stress.

Moving on, the validation of the fuselage analysis method will be presented. The method used in subsection 10.4.2 is based on an analysis presented in the course structural analysis and design [40]. Implementing the values used in the lecture to calculate the required thickness yielded the same plots and required thickness as can be seen below in Figure 10.34 and Figure 10.35. Therefore, it was deemed that the thickness model was validated. It should be mentioned that the different colours in Figure 10.34 appeared due to the different maximum bank angles being plotted separately instead of combined, such as in Figure 10.35.

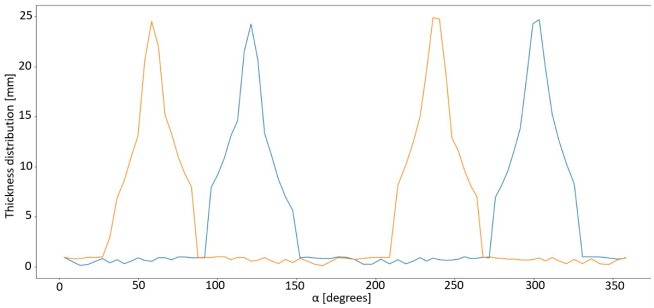

Figure 10.34: The resulting thickness distribution resulting from the model developed to analyse the fuselage.

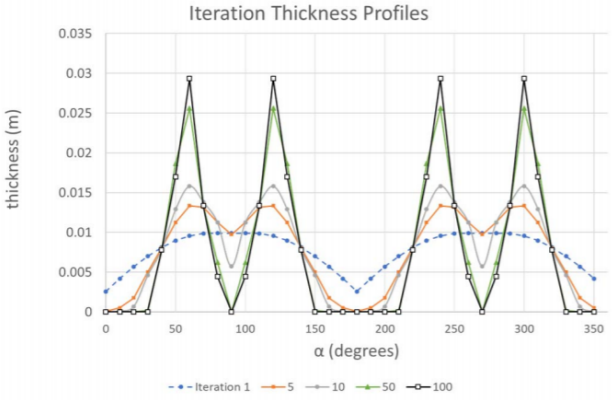

Figure 10.35: The resulting thickness distribution shown for the model from the slides of structural analysis [40].

Fuselage mass validation

For the fuselage the same can be done as for the wing, which is comparing the result of the class II weight estimation with the result of the structural analysis tool. The class II yielded a fuselage mass of 26,654 kg, while the structural analysis tool computed a value of 28,264 kg. This is a difference of 1,610 kg, equal to 6.0%. This increase is probably due to the overestimation of the total stringer weight mentioned before. However, as this difference is quite small, the result of the structural analysis tool is deemed valid.

Requirement compliance

Reflecting on the requirements that were stated at the beginning of this section, it can be concluded that all requirements have been met. **BIB-SBS-SNR-04** has been met as the required thickness for pressurisation is lower than due to the moments. Furthermore, as the fuselage has been sized for the ultimate load case, **BIB-SBS-STR-05**, **BIB-SBS-STR-06** and **BIB-SBS-STR-09** have been met as well.

Risk mitigation

The risk for the fuselage can only be mitigated by inspection of the fuselage, which can be done before and after a flight. This reduces the chance that damage to the fuselage remains unnoticed. When damage is found, the fuselage will have to be repaired in order to restore its load carrying capabilities.

11 Systems

The following chapter contains a description of the main aircraft systems and includes their initial design. First it will be explained why this aircraft does not possess an auxiliary power unit and pneumatic system, see section 11.1 and section 11.2. Next, the electrical system is elaborated upon in section 11.3, including an electric power budget for the main contributors of the aircraft. Thirdly, the hydraulic system is explained and sized according to its regulations, see section 11.4. The systems that the hydraulic system will drive are part of the flight control system. Their interaction and overlap is explained in section 11.5. Furthermore, the fuel system is discussed and its components are identified in section 11.6. Moving on, to ensure the comfort of passengers and crew, an environmental control system was investigated as well. This is explained in section 11.7. Finally, the most novel system in this aircraft, the electric taxiing system, is evaluated and sized in section 11.8. Its performance and main advantages are discussed as well.

11.1 Auxiliary Power Unit

Most current large passenger aircraft are equipped with an auxiliary power unit (APU). It is capable of providing required power when the engines are inoperative, i.e. before taxiing and after landing. Even a more electric aircraft like the B787 still features an APU, though they generally only provide electrical power. By incorporating a larger battery pack that facilitates electric taxiing and has enough capacity to provide the required power for engine starting procedures and the environmental control system, the necessity for an APU is diminished. Discarding the APU from the aircraft design has a positive effect on the direct operative costs as maintenance cost and the operational empty weight are reduced. Finally, this design decision leads to an even more electric aircraft.

11.2 Pneumatic System

In accordance with striving towards a more sustainable and electric aircraft, the aircraft was equipped with a bleedless architecture. Apart from the engine de-icing system and internal cooling of the turbofan engine, no other systems rely on bleed air from the aircraft engines. Boeing claims the no-bleed architecture in the B787 extracts 35% less power from the engines than in an architecture with bleed air systems, mainly due to the fact that the thermodynamic cycle of the engine is not affected when using electrical power instead of engine-generated pneumatic power [41]. This makes the energy extraction more efficient which in turn improves fuel consumption. Additionally, the bleedless architecture has a better reliability as there less parts than in more conventional systems and reduced maintenance costs. Furthermore, eliminating the bleed system greatly reduces maintenance costs, contributing to lower direct operating costs [41].

11.3 Electrical System

One of the most important systems in any aircraft is the electrical system. By implementing an on-board electric taxiing system in a bleedless aircraft without APU, this system becomes even more critical since the battery pack needs to be sized according to the required amount of electrical power during the taxiing process. First the functional analysis is described, followed by the risk analysis. Finally the results are described and the electrical block diagram is presented.

11.3.1 Functional analysis

In order to construct the electrical power budget, the most power demanding systems were considered. These are listed in Table 11.1. The environmental control system can be divided into pressurisation and air-conditioning [42]. The required power for the environmental control system was approximated to be 500 kVA. This was the value found for the B787, one of the only aircraft that could serve as a reference for the electrical power budget due to its bleedless architecture [42]. Although it is a rough estimate, it was also used for this design as the 787 cabin volume is 22% larger than the cabin volume of the EcoHopper 450, which means that a large margin is included. The required air-conditioning power for this aircraft is estimated to be 180 kVA after comparison with data for jumbo, wide and narrow body aircraft[1]. Additionally, 320 kVA is required for pressurisation during flight. Moving on to the wing de-icing system, which consists of electro-thermal panels that melt ice located on the wings by delivering a pulse of high power electricity[2]. Using a load of around 100 kVA, this system requires less power and is thus more efficient than conventional wing de-icing systems. Moving on to the hydraulic system, four electric motor pumps are installed to generate the required hydraulic pressure. The pumps together need a total power of 400 kVA. The value for the electric taxiing system is elaborated upon in section 11.8. Finally, due to the bleedless nature of this aircraft, the engine start-up process is performed by the starters/generators which require around 180 kVA [42].

[1] Purdue University. Air-Conditioning of Parked Aircraft by Ground Based Equipment. Retrieved June 3, 2019, https://docs.lib.purdue.edu/cgi/viewcontent.cgi?article=2085&context=iracc

[2] Isidoro Martinez. Aircraft Environmental Control. Retrieved June 4, 2019, http://webserver.dmt.upm.es/~isidoro/tc3/Aircraft%20ECS.pdf

Table 11.1: Systems requiring electrical power.

System	Maximum load [kVA]
Environmental control system	500
Wing de-icing system	100
Electric taxiing system	397
Hydraulic system	400
Engine starting system	180

Before taxiing away from the gate, the aircraft is connected to ground power. Once ground power is disconnected and the aircraft commences taxi procedures, the electric taxiing system is engaged. At this moment power is needed for the environmental control system, mostly for air-conditioning, and of course electric taxiing. Steering on ground is performed by differential use of the electric motors. This enables the aircraft to perform tight turns. A small turning circle also benefits backtrack operations as less space is needed to perform a 180 degrees turn. Assuming a power factor of 0.8 the total maximum required load during taxiing is 599 kVA, which is visualised in Figure 11.1.

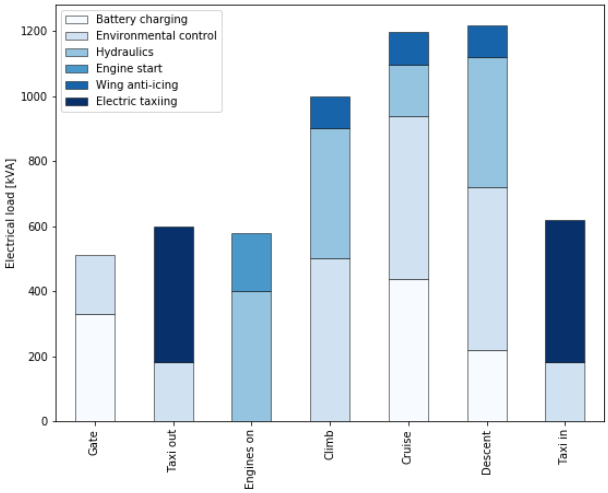

Figure 11.1: Electrical power required for different flight phases.

Two minutes before take-off, the power required for the environmental control system is reduced as the air-conditioning is switched off momentarily. This means around 180 kVA becomes available, which is used to power the starters/converters and generators and eventually start the two engines (which requires around 180 kVA) [42] . Once the engines are started, the electric taxiing system is switched off and the generators connected to the engines provide power to the aircraft systems. Thus, from this moment onward, the batteries are not discharging anymore.

Once cruise altitude is reached, the thrust setting of the engines is reduced. At this stage, besides providing power for the environmental control system and hydraulic system, the generators connected to the engines are used to generate power to recharge the battery pack. The charging power equals 438 kW and the process takes approximately 25 minutes. The systems drawing power from the generators during cruise and descent are the environmental control (air-conditioning and pressurisation), wing de-icing, the hydraulics and the charging of the battery pack. Summing this requires a total power load of 1200 kVA as visualised in Figure 11.1. It was determined that one electric motor pump is needed during cruise, reducing the required hydraulic power for cruise by 60%. During descent, the hydraulic system requires more power as the aircraft has to perform more manoeuvres, for which the control surfaces are used, compared to the cruise phase.

After landing, the main engines are shut down when they are sufficiently cooled-down and the electric taxiing system is engaged. Once arrived at the gate, ground power takes care of fast-charging the battery pack in less than 30 minutes, which is within the turn-around time. Current major airports feature power supplies of more than 360 kVA [43]. Although the maximum power of power supplies is expected to increase in the following years, it may be advantageous or even necessary to implement a second ground power connection point in the aircraft in order to be able to transfer the required power at the gate.

11.3.2 Risk analysis

The generators provide the required power for all systems. Although chances both engines fail are extremely small, one has to design back-up systems for redundancy purposes. It is of highest importance the aircraft remains controllable in this event. Therefore, a ram air turbine, delivering 80 kVA can be deployed when necessary. Together with the remaining battery capacity after taxiing (or even fully charged batteries if this event occurs past 25 min in cruise), the ram air turbine

provides the electric motor pumps with electrical power such that the most important control surfaces, especially elevators and ailerons, can be operated properly and chances of a safe landing are increased significantly.

11.3.3 Design sizing

Energy provided by the battery pack is used to power the electric motors. This design choice omits the necessity for an auxiliary power unit, as the battery pack also serves as energy source for the environmental control system and engine starting process on the ground. The total required battery pack capacity is the summation of the required capacity for electric taxiing and environmental control on ground as shown in Table 11.2. The battery pack is placed underneath the wingbox near the centre of gravity location. The generators are sized according to this maximum required load. Two variable frequency starter/generators are connected to each turbofan engine, generating 310 kVA each. Assuming a power-to-weight ratio of 5 kW/kg, this means each generator will have a mass of 62 kg.

Table 11.2: Battery pack sizing

Parameter	Value
Electric taxiing battery capacity [kWh]	68.53
Environmental control battery capacity [kWh]	60
Total battery capacity [kWh]	128.54
Total battery mass [kg]	383.69
Total battery volume [L]	185.48

11.3.4 Electrical block diagram

Based on previous sections, the electrical block diagram was constructed. The major electrical links in the electrical system architecture are shown in Figure 11.2.

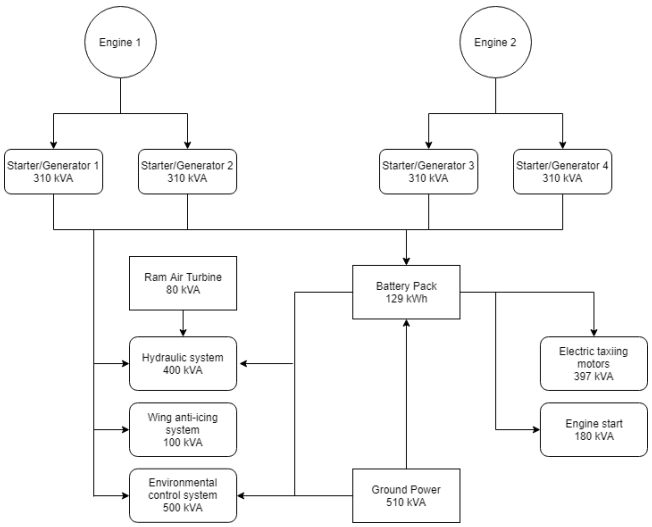

Figure 11.2: Electrical block diagram.

11.4 Hydraulic System

The hydraulic system provides power to both the primary and secondary flight controls, undercarriage, anti-skid systems and cargo doors. The system provides power by means of a pressurised hydraulic fluid, which will be distributed to the desired location using pipes. The pressurised fluid will power actuators so that the actuators can perform the desired movement. Since the hydraulic system provides power to critical components, it is crucial that the entire hydraulic system is designed for redundancy and also for emergency usage. The hydraulic systems consists of the hydraulic pump and other subsystems. The hydraulic system needs a source of energy, a hydraulic fluid, a reservoir to store this fluid, filters to clean the fluid, a system to distribute the fluid and pumps and actuators to provide work. Accumulators are also used to store energy. Throughout the system, temperature and pressure sensors are used to measure and maintain the temperature and pressure of the fluid as much as possible.

In order to provide energy, engine driven pumps (EDP), electrical motor pumps (EMP) and a Ram Air Turbine (RAT) are used. Air Driven Pumps (ADP), which are present in many aircraft designs, are not used in as the design is bleedless. EDP's are directly powered by the engine with the use of a gearbox. Because to EDP's are directly linked to the engines, a relatively high efficiency is achieved. EMP's require electrical power produced by generators in order to pressurise the hydraulic fluid. The RAT is a turbine that deploys from the aircraft into the ambient upon emergency situations. The air velocity powers the turbine, which in return powers the hydraulic system.

As hydraulic fluid, the Exxon Type V HJ5MP will be used. This fluid is used in most commercial aircraft [42]. Note, special attention must be payed to the design of this system as this fluid is not fire-proof. The hydraulic pressure is set at 5000 psi, which is more than what is used in most current state of the art aircraft. However, it has already been used in the B787 [41]. A higher hydraulic pressure results in less fluid needed and also less power needed. However, titanium reservoirs have to be used to withstand the pressure.

The hydraulic system of the EcoHopper 450 consists of three hydraulic systems which are able to operate independently, namely the left, right and centre system. Three independent systems are used to account for redundancy. If one of the systems fails, all desired controls shall still be operative. The left and right system contain an EDP capable of delivering 38 gallons per minute (Gpm) as primary power source. Furthermore, a secondary EMP, powered by the electrical system and capable of delivering 6 Gpm will be used in case of peak demands. To achieve an even higher redundancy, the left and right system are connected to each other. In case the pressure of one of the systems becomes too low, the pilot may choose to distribute the available pressure over the two systems. Moving on, the centre system contains two EMP's, powered by the generator of the electrical system, capable of delivering 30 Gpm each. Only one EMP operates during cruise and the second EMP is used during take-off and landing in order to meet the peak demands. An emergency RAT, capable of delivering 12 Gpm, is also present in the centre system. It is deployed in case the EMP's are not able to provide enough power. All three systems do have their own reservoir. The architecture of the hydraulic system is shown in Figure 11.3. The power required by the pumps is derived from reference aircraft described in [42]. The reference aircraft do have a higher empty weight, which would lead to less power needed in the EcoHopper 450. However, since more advanced high lift devices are used, a higher peak power is present. The pumps are designed such that they are able to deliver the peak power. This usually is when high lift devices or the lading gears are deployed in combination of using the primary flight controls.

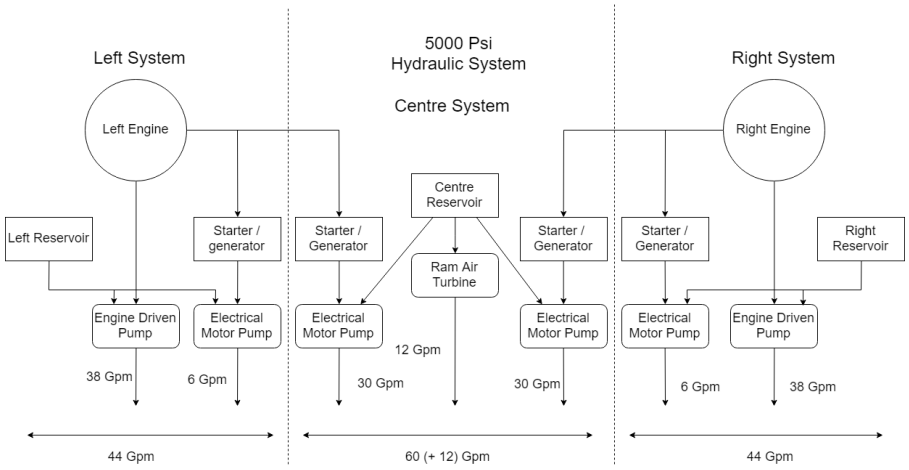

Figure 11.3: Hydraulic system

Research was conducted on regenerative braking. The idea consists of high power converter(s) located in the main landing gear that 'catch' the energy that dissipates during braking if a conventional braking system is used. Assuming a landing speed of 140 knots and a maximum landing mass of 134,275 kg, the kinetic energy was found to be 348 MJ. As the roll-out was assumed to take 25 seconds, the preliminary calculation yielded a load of 13.93 MW the generator(s) should be sized for. Modern lightweight starter/generators achieve a power to weight ratio of up to 5 kW/kg[3]. This would result in a mass for the generator(s) of over 2780 kg. Even neglecting all practical issues this design would yield, the high mass makes it less efficient than charging batteries in-flight using the generators connected to the engines. This technology was deemed unfeasible within the time frame of 2025.

Instead of the above technology, it was chosen to implement a novel integrated self-powered brake system. As the aircraft lands, mechanical energy of the rotating wheel is converted into hydraulic energy. This hydraulic energy is then either used by the brake actuators or stored by a separate storage system. However, during taxiing and while slowing down, the pump is unable to generate sufficient hydraulic power. In this case, the energy storage device is used to provide the required hydraulic power [44]. The concept of this self-powered brake system is visualised in Figure 11.4. The entire system, including the accumulator, weighs 6.5 kg. It is therefore feasible to install this system on every wheel of the main landing gear in order to maximise braking performance. According to research conducted on this concept, the optimum slip ratio of around 0.15, almost equal to the maximum braking capacity, can be obtained by the self-powered brake system which means that a large passenger aircraft having touchdown at 288 km/h would be slowing down to 18 km/h in less than

[3]Experimental aircraft info. Electric aircraft motors. Retrieved June 5, 2019, `https://www.experimentalaircraft.info/homebuilt-aircraft/electric-aircraft-engines.php`

30 seconds [44]. During slow taxiing, at speeds below 20 km/h, the rotational energy is too low for the energy conversion device to provide enough hydraulic energy to the brake actuators. In that case, the accumulator is used to keep the brake flow at the required value.

One of the advantages of the self-powered brake system is the fact that complex hydraulic pipelines to the main wheels can be eliminated. This results in improved economy and reliability and reduces the weight of the aircraft. Furthermore, as said system is installed on every wheel of the main landing gear, due to its low mass, this increases redundancy compared to a conventional braking system [44].

In order to further increase redundancy and mitigate the increased risk of insufficient braking force during slow taxiing (less than 20 km/h), a backup system can be incorporated. A small electro-mechanical actuator in two of the main landing gear wheels powered by the battery pack could provide braking power if the self-powered brake system (partly) fails to do so during slow taxiing. Although this system can be light due to the low required brake flow at speeds below 20 km/h, one should note that this backup system will increase the weight of the aircraft [45]. However, implementing such system in the design greatly decreases the likelihood of having insufficient braking power during slow taxiing.

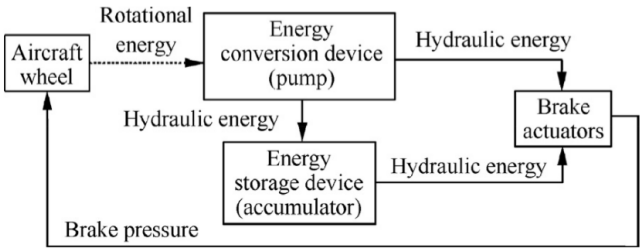

Figure 11.4: Concept of self-powered brake system [44].

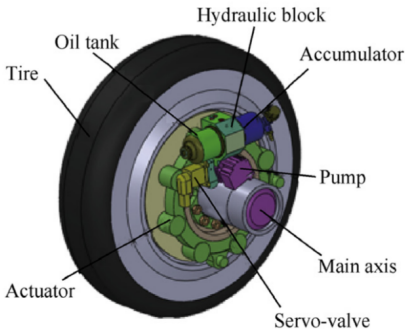

Figure 11.5: Visualisation integrated self-powered brake system [44].

11.5 Flight Control System

The flight control system ensures that the control surfaces of the aircraft are able to be operated properly. In general, the flight control system may be split up in two parts; the primary and secondary flight control system. The primary control system consists of the ailerons, rudder, elevators and spoilers. The secondary flight control system consists of the flaps and slats. The entire flight control system is controlled by means of a fly by wire system. Using this system, inputs from the pilot for the flight controls are transmitted by wires as electronic signals. Flight control computers process incoming data of the flight controls and determine how to move the actuators of each flight control to the desired location and maintain stability. The use of a fly by wire system leads to a reduction of weight compared to a manual flight control system, as electrical wires are lighter than mechanical connections [42].

Multiple flight control computers are needed to handle and analyse the data from the flight controls. The flight control system of the EcoHopper 450 has a total of 10 computers. Three Flight Control Primary Computers, three Flight Control Secondary Computers, two Flight Control Data Concentrators and two Flap/Slat Control Computers. The number of computers is similar to reference aircraft using a fly by wire system [42]. Actuators, of which multiple types exist, are needed as well. The primary flight controls are actuated by means of electrically signalled hydraulic actuators. In order to ensure a fault-tolerant system, two or three levels of redundancy are introduced. The level of redundancy depends on the criticality and size of the component. The secondary flight controls uses conventional screwjack actuators. Electric powered actuators are not used in EcoHopper 450 since the hydraulic system powers all actuators. This is because no bleed air is used, and because the full hydraulic system ensures a high enough redundancy.

The architecture of all the flight control system is shown in Figure 11.6. The letters L, R and C stand for the left, right and centre hydraulic system, respectively. The flaps require three actuators since they have a large width and the rudder requires three actuators since it is a critical component. The spoilers and slats only need one actuator since there are many of them, which already makes it redundant. The ailerons and elevators require two actuators since they are critical, but they do not require three actuators since there are more than one of them.

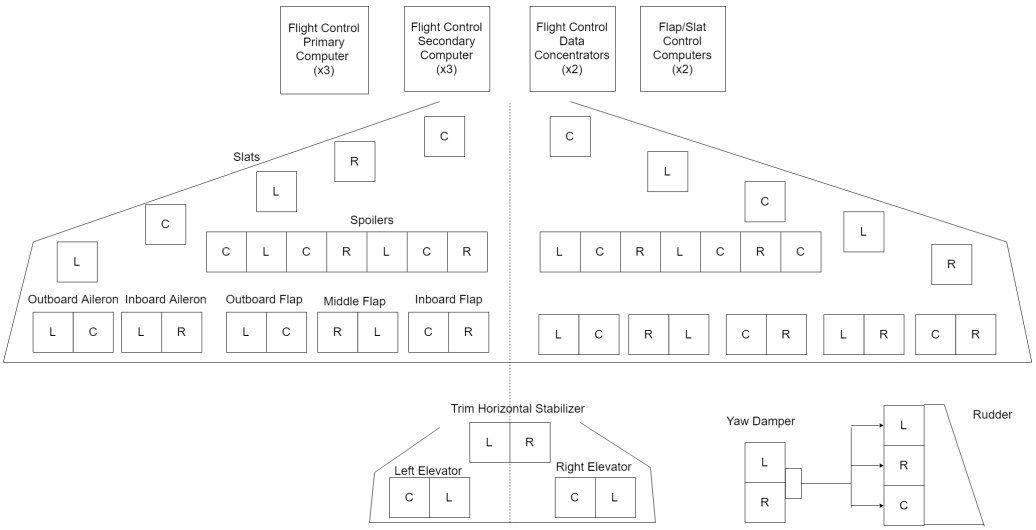

Figure 11.6: Flight control architecture

11.6 Fuel System

The fuel system consists of the fuel tanks and multiple subsystems which in turn rely on different components. The fuel system should be able to store the fuel, vent the system, allow for re- and defuelling, fuel jettison, distribution of the fuel and feeding fuel to the engines.

The fuel can be stored in the wing, fuselage and/or horizontal tail depending on the required volume. As it was found that the wing volume allows for the storage of all the fuel, it was chosen to use wing integrated fuel tanks as this is the solution with the lowest weight penalty. The fuel tank namely makes use of the structure already present in the aircraft, like spars and ribs. A part of the fuel tank is the surge tank, its function belongs to the venting subsystem. This subsystem ensures that the fuel tanks will not implode during flight. When fuel is sucked out of the tank, it has to be replaced by air to keep a constant pressure in the tank, otherwise a very low pressure can occur inside the tank [46][pg. 40]. This can finally result in an imploding fuel tank. To eliminate this risk, an open vent system is employed. It connects the ullage in the tank to the outside air with vent lines, which let the tank ”breath” when climbing and descending. The surge tank itself is only of importance during refuelling. As fuel is not allowed to enter the vent lines due to safety reasons, the overflow of fuel is captured by the surge tank which has a volume equal to 2% of the fuel tank volume [46][pg. 45]. The surge tank is located outboard, which in this aircraft means that it is at the lowest point of the wing due to the anhedral. So, to transfer the captured fuel back into the fuel tanks, scavenge pumps are employed.

The next subsystem is the re- and defuelling system. Refuelling usually occurs before every flight whereas defuelling only occurs before maintenance. The aircraft makes use of pressure refuelling which is provided by the airport’s ground fuel system. It should be provided at a rate of 6.4 kg/s in order to meet BIB-SBS-OPS-06, (the aircraft shall be refuelled within 45 minutes), this was obtained from the fuel weight estimation. As a back-up system the aircraft can also be refuelled by gravity refuelling. The fuel flow rates of gravity refuelling are significantly lower compared to pressure refuelling, therefore it was chosen that it was suitable as a back-up system and not as the main system [46][pg. 54]. The latter aspect of this subsystem, defuelling, can be done by applying suction on the refuelling adapter. Whenever this is not available at the airport, the pumps of the fuel system could also be used to off-load the fuel. A special type of defuelling is fuel jettison, which is only executed in case of an emergency. The worst case fuel jettison requirement is the difference between MTOW and MLW as this yields the maximum amount of fuel that needs to be ejected. To be able to meet the fuel flow requirements for this case, separate jettison pumps are needed. The backup system is provided by the transfer pumps which are part of the fuel distribution subsystem described next. These pumps cannot be used as the main jettison system as the flow capacity of transfer pumps is generally not sufficient [46][pg. 75].

Another aspect of the fuel system is the fuel distribution. This subsystem transfers fuel from one tank to another to make sure the fuel burn sequence is complied with, and to account for the centre of gravity variations that occur due to fuel burn. Inter-tank fuel transfer is done by employing motive flow (or jet) pumps and tank selector valves [47]. These type of pumps rely on the Venturi effect to create suction. The electrically driven pumps provide the flow in the fuel line, which causes a low-pressure area in the line. This in turn creates suction which pulls the fuel out of the fuel tank. The valves then control which tank is used to feed the engine. The fuel distribution system also consists of the cross-feed system. In the case of an engine failure, the cross-feed system can transfer fuel from one wing to another such that the fuel can still be used, and to balance the aircraft [46][pg. 70]. Centrifugal boost pumps are used for the cross-feed operation in combination with cross-feed valves. The pumps are electrically powered and serve as a backup for the engine driven

pumps (feed pumps) and can provide positive pressure to these pumps to avoid cavitation [4][47]. The valves close off the cross-feed line when it is not needed. The motive flow and centrifugal pumps are called transfer pumps which serve as a backup for the jettison system.

Finally, the last subsystem considered is the feeding system which ensures that the fuel is delivered to the engines at the correct rate and pressure. Engine driven feed pumps are used to pump the fuel through the feed lines to the engines. As a back-up system, ejector pumps are installed in parallel. An ejector pump is a simple pump with no moving parts, which increases its reliability, however the fuel pressure it can deliver is lower than desired during nominal operation [46][pg. 60]. To ensure a constant fuel flow towards the engines, a collector cell is present in the main fuel tank. When the aircraft turns or encounters negative g loads, the fuel can slosh such that the pumps will not pump fuel for a certain amount of time. The collector cell can in this case be separated from the main tank by closing baffle check valves [46][pg. 65]. Check valves restrict the flow from one direction to the other. In case of an emergency, firewall shut-off valves (or spar valves) are present which shut-off the fuel flow towards the engine, e.g. in case of an engine fire. An overview of the main components of the fuel system can be seen in Figure 11.7, note that the system can be mirrored.

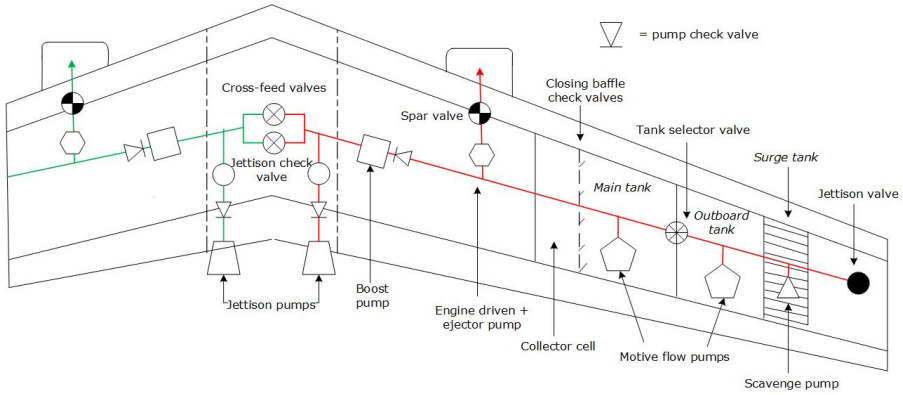

Figure 11.7: Simplified fuel system diagram.

11.7 Environmental Control System

The environmental control system (ECS) ensures comfortable conditions for the crew and passengers of the aircraft. The ECS must cope with widely differing temperature conditions, must extract moisture and provide air with optimum humidity, and must ensure that the air in the aircraft always contains a sufficient concentration of oxygen and that it is safe to breathe. The system also includes the provision of suitable conditions for the avionic, fuel and hydraulic systems by allowing heat loads to be transferred from one medium to another. In addition to these essentially comfort related tasks, environmental control systems provide de-misting, de-icing, anti-g and rain dispersal services [42].

The environmental control system of the cabin ensures comfort conditions by letting clean air flow into the cabin. The clean air is produced by air generation packs (AGP) which pressurise, cool and dehumidify incoming air. The pack consists of two compressors, which pressurise the incoming air. During this pressurisation process, the air heats up. Therefore it flows through a heat exchanger using the ram air as heat sink in order to keep the air cool. Afterwards, the air will be dehumidified by a water extractor. Before the air flows toward the cabin, the air may be optionally cooled even more by means of a turbine. The AGP architecture is shown in Figure 11.8. The AGP makes sure the out-flowing air has enough pressure, oxygen and humidity. The AGP designed differs from AGP's used in aircraft using bleed air because of the second compressor. Since ambient air has to be pressurised more than already pressurised bleed air from the engines, a second compressor is needed in a bleedless design [48].

Once the air from outside the aircraft has been conditioned in the AGP, the air will flow to the mixer unit. This mixer unit mixes cooled cabin air with the new air. The new mixed air will flow into the cabin from overhead intakes. These intakes are present in both floors of the aircraft. The AGP may also deliver hot air as output. This air will be stored in the hot air manifold and, whenever the air coming from the mixer unit is too cold, or the cabin has to be heated, hot air will be mixed with the cold air to get the desired temperature. The out-flowing air from the cabin will be filtered such that no particles are present in the in-flowing air. The cooling system cools the out-flowing air before the air is recirculated in the mixer unit. When the AGP's fail to deliver enough air to the mixer unit, there is the possibility to directly flow ram air into the mixer unit. The ECS architecture is shown in Figure 11.9

[4]The pump creates a low-pressure area as the fuel is accelerated, causing air pockets to form on the suction side of the pump, which can cause cavitation. If the fuel pressure becomes too low, it will vaporise, which can damage the pumps.

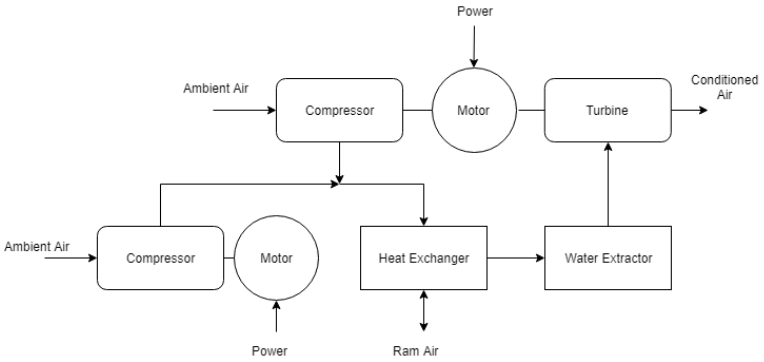

Figure 11.8: Air Generation Pack

The cooling system is used to cool different components of the aircraft and uses cooling liquids and ram air to remove heat from components. The power electronics are cooled by air that has a relatively high temperature, as these typically require a temperature of 70 deg C, which causes a special hot loop for the power electronics [48]. Besides the power electronics, also avionics, galley's and the re-circulation air has to be cooled, as these require a temperature of roughly 5 - 40 deg C.

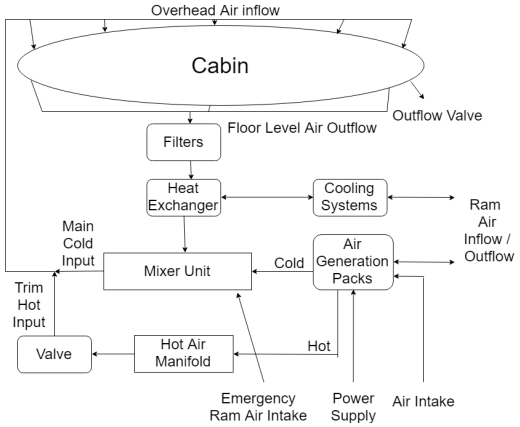

Figure 11.9: Environmental Controls System Architecture

The wing ice protection system is different from aircraft's using bleed air. Aircraft's using bleed air normally use hot bleed air to heat up the wing's leading edge to prevent ice crystals from forming [48]. The wing ice protection system from the EcoHopper 450 is more modern and innovative. The system uses electro-thermal heat blankets inside the leading edge of the wing, which heat up the wing. The use of heat blankets allows for controlled power delivery to the wing's leading edge, which will be just enough to prevent ice crystals from forming. According to the European Commission, the heat blankets use halve the amount of power from that of the bleed air using systems [48].

11.8 Electric Taxiing

In order to reduce the environmental impact of ground operations and to lower fuel burn, the design features an electric taxiing system. In this section, the electric taxiing system is designed based on requirements that follow from the functional analysis presented in subsection 11.8.1. Furthermore, a sensitivity analysis is performed in subsection 11.8.2 and the results are presented in subsection 11.8.3.

11.8.1 Requirements analysis

Functional analysis

The electric taxiing system will be used twice during one flight. First to taxi from the gate to the point where the aircraft is approaching the runway around 2 minutes before takeoff and right after landing when the engines are shut down. In contrast to most developed electric taxiing systems, the auxiliary power unit is not the power source for this system. Instead, a large battery pack consisting of lithium-ion cells is installed providing the required power. In order for the electric taxiing system to be fully operative on every airport in the world, research of taxi distances to gates on major airports was conducted. The longest taxi distance was found to be 6900 m on Schiphol airport, more specifically to runway 18R-36L, also known as the 'Polderbaan' [5]. Incorporating a safety factor, the maximum taxi distance was determined to be 8000 m. Furthermore, a taxi speed of 20 knots was assumed as research shows taxiing at this speed does not cause significant delays [49]. The

[5] Tix. De grootste afstanden op het vliegveld. Retrieved June 4, 2019, https://blog.tix.nl/onderzoeken/grootste-afstanden-vliegveld-gate-landingsbaan/

electric motors powering the aircraft during taxi operations are located on the main landing gear. The main landing gear was chosen since it carries around 90% of the aircraft weight, thus traction will be higher. This allows the electric taxiing system to be operative even in wet conditions. More specifically, two electric motors will be used in the two outboard wheels. The outboard wheels were selected in order to effectively make use of the electric motors during on ground steering. Each of the two motors will drive the respective outer wheel as to ensure sufficient spacing in the main landing gear.

Risk analysis

The electric taxiing system is more electric and advanced compared to the electric taxiing systems produced thus far; more electric because the taxiing is fully electric, i.e. the energy to drive the electric motors is delivered by the battery pack instead of the auxiliary power unit. Implementing these new technologies instead of applying current proven systems comes with increased risk. The two most prominent risks were identified and risk mitigation was performed.

- **Long taxi distance:** The electric taxiing system is designed for a taxi distance of 8000 m. While this distance is way above the maximum distance currently seen in normal airport operations, one should include a proper strategy for extreme cases that may occur. If the required taxi-out distance turns out to be longer than 8000 m and the battery capacity reaches a low value, the pilot should consider to start both main engines. Especially since the engines are started using electricity from the battery pack. After having started both engines, correct functioning of the aircraft on-board systems is assured as the starter/generators then power the aircraft systems.
- **Insufficient ground power:** The battery pack needs to be re-charged with an apparent power of more than 300 kVA. This means that one ground power unit may not be sufficient to provide a load high enough in order to have the battery pack charged within turnaround time. Therefore, the amount of ground power unit connection points on the aircraft can be increased to ensure a sufficient electrical load while standing at the gate which drastically decreases the likelihood of this event.

Requirements

Certain requirements from the Baseline Report that affect the electric taxiing system were included [8]. In addition, requirements following from the functional and risk analysis are added under the identifier TAX.

- **BIB-SBS-OPS-01** The aircraft shall be able to start on its own.
- **BIB-SBS-TAX-01** The aircraft shall be able to accelerate from standstill to 10 knots in less than 20 seconds.
- **BIB-SBS-TAX-02** The aircraft shall be able to taxi continuously at 20 knots.
- **BIB-SBS-TAX-03** The aircraft shall be able to taxi for at least 8000 m.
- **BIB-SBS-TAX-04** The aircraft shall be able to taxi in wet conditions.

11.8.2 Method

In order to determine the required power and torque of the electric motor and to size the battery pack, a tool was created. The inputs are listed in Table 11.3. Finally, the value for the battery specific energy was determined to be 335 Wh/kg by observation of current top-notch lithium-ion batteries and taking into account a yearly advancement in specific energy of 4% [6]. Similarly, the battery energy was found to be 693 Wh/L.

Next, the electric motors were sized. The inputs are shown in Table 11.4. The tire radius was determined in the under-carriage sizing. Furthermore, a gearbox efficiency of 0.9 was assumed. Finally the required acceleration was determined to be constant at 0.3 m/s^2 according to the EGTS acceleration requirements [7]. From these parameters, the roll resistance force and air resistance force were calculated. The total force is then multiplied with the distance to be travelled, resulting in the energy required. This translates into the required battery capacity for the electric taxiing system. Dividing the total energy by the taxi speed, the required taxi power was obtained.

Table 11.3: Input parameters electric taxiing

Parameter	Value
Takeoff weight [kN]	1,522
Roll resistance coefficient [-]	0.02
Taxi distance [m]	8,000
Taxi speed [km/h]	37.04
Battery efficiency [-]	0.9
Battery energy density [Wh/kg]	335
Wing area [m^2]	211
Drag coefficient [-]	0.03

Table 11.4: Electric motor sizing input

Parameter	Value
Taxi power required [kW]	317.33
Gearbox efficiency [-]	0.9
Tire radius [m]	0.572
Required acceleration [m/s^2]	0.3

[6] Vox. Electric batteries aircraft climate change, Retrieved May 16, 2019, https://www.vox.com/2019/3/1/18241489/electric-batteries-aircraft-climate-change

[7] Messier-Bugatti-Dowty and Honeywell. Electric Green Taxiing System. Retrieved June 5, 2019, https://www.arts-et-metiers.asso.fr/manifestationcr/678compterendu.pdf

11.8.3 Results

Performing the calculations yielded a battery capacity of 68.53 kWh which resulted in a mass of 227 kg and a volume of 99 L required to provide power for the electric taxiing system. The outputs are listed in Table 11.5. The required continuous torque to be delivered by the motors equals 17.63 kNm, while the torque necessary for proper acceleration is 43.98 kNm. Therefore, assuming the continuous power equals half of the peak power, it was determined 2 electric motors each having a continuous gearbox torque of 13 kNm deliver sufficient torque. The peak torque can be maintained for more than 45 seconds which safely covers the time at maximum required acceleration.

Table 11.5: Electric taxiing required performance values

Parameter	Value
Tire angular velocity [rpm]	171.92
Required continuous torque [kNm]	17.63
Required torque for acceleration [kNm]	43.98

Table 11.6: Technical specifications electric motor

Parameter	Value
Continuous Torque [Nm]	1,909
Rotational speed [rpm]	1,300
Mass [kg]	47.74
Continuous Power [kW]	260
Gear ratio [-]	7.56:1
Gearbox torque [kNm]	13

The specifications of the electric motor and gearbox are shown in Table 11.6 [8]. Current advanced electric motors feature a torque to mass ratio of over 30 Nm/kg. As development in this sector is going at a fast pace (50% increase in torque to mass ratio was observed over the scope of two years), a torque to mass ratio of 40 Nm/kg was deemed realistic within the time frame of 2025. This yields a total mass of the electric motor with the above specifications of 47.7 kg. In order to reduce the rotations per minute and acquire the desired wheel rotational velocity, a gearbox weighing around 50 kg with a ratio of 7.56:1 was installed between the motor and wheel. It was concluded the weight increase for each of the two wheels equipped with an electric motor including the gearbox and air cooling components equals around 92 kg, bringing the total mass of the electric taxiing system without batteries to 200 kg.

11.8.4 Fuel and cost savings

The short-range aspect of this missions makes it possible to enlarge the benefits provided by the electric taxiing system, as the taxiing phase makes up a large portion of the entire flight. Although the extra weight caused by the battery pack needs to be carried throughout the entire flight, the cruise phase of the flight is shorter in comparison with current aircraft with a similar maximum takeoff weight. This reduces the negative effects of the added weight. It was found the implementation of this electric taxiing system on itself leads to an overall fuel consumption reduction of 1.55%. This value was retrieved from chapter 15. Due to the autonomous nature of the electric taxiing system, the push back time is reduced by 60% which also results in lower operating costs. Another benefit of the autonomous push back is the increased safety of ground personnel and reduced chances of damage caused by ingestion of materials [50].

[8] Siemens. Electrifying propulsion. Retrieved June 8, 2019, https://avinor.no/contentassets/c29b7a7ec1164e5d8f7500f8fef810cc/olafottosiemensoslo22march2018withoutvideo.pdf

12 Operational analysis

This chapter aims to provide an overview of the operations encountered during the life time of the aircraft. An important aspect of the operating hours per day is the turnaround time of the aircraft. An analysis about the ramp activities and taxiing time, which are the main components of the turnaround time will be provided in section 12.1. Other important aspects are the maintenance and novelties encountered during the ground handling, which will be discussed in section 12.2 and section 12.3 respectively. The reliability, availability, maintainability and safety (RAMS) will be analysed in section 12.4. A data handling block diagram is constructed in section 12.5. Finally, the risks of the operational analysis are described in section 12.6.

12.1 Turnaround Time

To determine the availability of the aircraft, a turnaround time analysis was performed. In the Baseline Report a computer program was created that calculates the turnaround time for the aircraft based on multiple variables [8]. Since all input parameters like the amount of fuel, cargo and boarding doors have been either calculated or determined, the turnaround time could be easily computed. To recall, the following assumptions were made with respect to all the loading rates:

- Passenger boarding and deplaning rates are the same as comparable wide body aircraft.
- Cargo loading and unloading rates are the same as comparable wide body aircraft.
- The fuelling rate is the same as comparable wide body aircraft, assuming two hoses are available.
- Services like cleaning and catering are done at same rate as narrow body aircraft, since the mission range is short and thus it is assumed that less catering and cleaning is required.
- Positioning of loading gear is assumed to take a constant amount of time.

As the aircraft has enough doors for passenger boarding, the available boarding bridges at the airport determine the time it takes to load the passengers. Moreover, the passenger loading and unloading was found to be the critical path for the time at the gate of the aircraft. A brief sensitivity analysis was performed on the amount of boarding bridges available, of which the results are presented in Table 12.1. It could be concluded that applying more than three boarding bridges will not affect the ramp time, as the passenger boarding and deplaning rates are not part of the critical path anymore. Furthermore, other ramp activities like cleaning and catering, which are part of the critical path are hard to reduce in time.

Table 12.1: Turnaround time versus the number of boarding bridges available at the airport

Number of boarding bridges	Turnaround time [min]
1	72
2	48
3	45
4	45

Assuming that at most major airports, two boarding bridges are available for passenger boarding the total ramp time was set to 48 minutes. Furthermore, the total taxiing time was found to be in the range of 22 to 32 minutes based on statistics [8]. So the total turnaround time range was determined to be 70 to 80 minutes. The average turnaround time of 75 minutes will be used for the availability of the aircraft.

12.2 Maintenance

This section elaborates on maintenance that should be performed during the lifetime of the EcoHopper 450. Different components of the EcoHopper 450 that would require regularly maintenance checks are described n this section.

Materials should be regularly checked for crack initiation and propagation. Due to fact that they are critical for the structure and determine if it fails or not. Carbon fibre composites are difficult as they require special maintenance checks due to the poorly visibility of cracks. However, the characteristics of carbon fibre composites should result in fewer maintenance checks compared to the aluminium alloys. The inspection techniques that are used for carbon fibre composites are time consuming and require special equipment, as they should be tested for delamination and fibre irregularities. Common inspection techniques for carbon fibre composites are tap tasting, borescoping, ultrasonic testing, radiography and penetrant inspections, while metal materials can simply be checked by visual inspections. Due to the novelty of the engines a specific maintenance plan will be implemented as provided by the manufacturer.
[1].

[1] https://www.mro-network.com/aerospace-materials/cost-maintaining-composites-can-offset-performance-gains

12.3 Ground Handling

This section elaborates on the novelties included in the design of the EcoHopper 450 and how they affect ground operations. A simulation of the EcoHopper 450 arriving at an arbitrary airport and departing from the parallel runway is visualised in Figure 12.1, summarising some of the novelties included in the design of the EcoHopper 450. Several changes with respect to ground operations of more conventional large passenger aircraft are listed below.

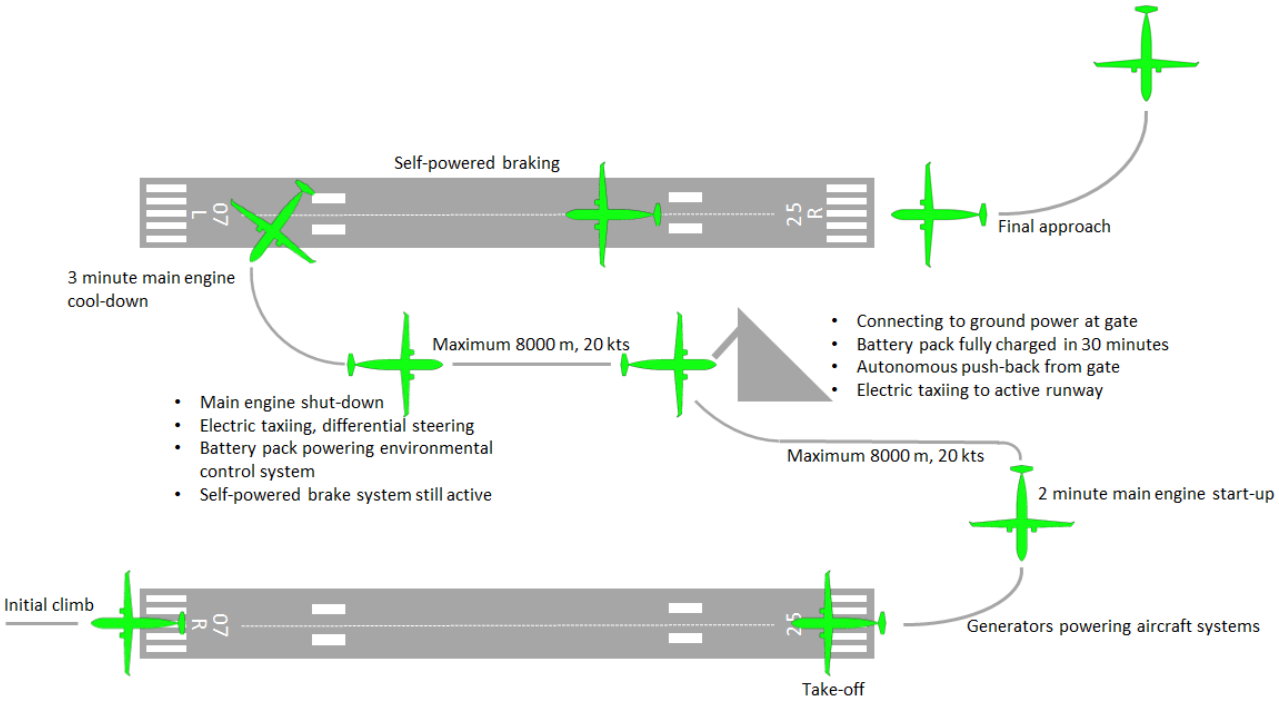

Figure 12.1: Simulation of ground operations on a major airport.

- **Taxiing speed:** the maximum constant speed of the electric taxiing system is set to be 20 knots. For taxiing on long straights, for example back-tracking on the runway, this is around 10 knots less than the maximum allowed taxi speed for most large passenger aircraft [2]. Although the effect of slower taxiing is found to be marginal [49], pilots and airlines should take this difference into account.
- **Differential steering:** on ground steering is performed with differential use of the electric motors. For very tight turns (or even quasi-stationary turns), it is possible to have one wheel powered forward and one backward. This steering system is controlled with the rudder pedals. The throttle levers can be used by the pilot to control the forward motion during electric taxiing.
- **Autonomous push-back**: an autonomous system part of the electric taxiing system takes care of the push-back from the gate to the taxiway. The pilot activates the system and selects the direction (left or right) of the push-back. Subsequently the system, equipped with plenty of sensors and cameras, fully autonomously performs the manoeuvre.
- **Engine start-up**: for most current aircraft, the main engines are started during push-back. The main engines of the EcoHopper 450 on the other hand are only started two to three minutes before departure. This means the pilots will face a higher workload right before take-off. Also, the hydraulics will only be powered when the main engines are started. As full control surface deflections are then part of the before take-off checklist, the workload inside the cockpit is further increased. It is evident that pilots need to be trained in order to properly perform said actions.

12.4 RAMS

The following section covers the reliability, availability, maintainability and safetey (RAMS) of the EcoHopper 450. The goal of the EcoHopper 450 is to fly a short range mission with carrying 450 passengers in a single class configuration. To make sure the operational aspect of the EcoHopper can be preformed as optimal as possible, it is important to have an overview of the four RAMS aspects. This way the operational planning can be adapted and executed in the best way possible.

[2] 737ng. Flight Crew Training Manual. Retrieved June 15, 2019, http://www.737ng.co.uk/B737%20Flight%20Crew%20Training%20Manual%20-%20All.pdf

12.4.1 Reliability
The EcoHopper 450 shows an innovative design. The biggest changes with respect to general aviation will be the high aspect ratio, high wing and the strutted design. Besides this is a new landing gear design present as well. These concepts have not yet been proven in practice like the conventional passenger aircraft. To check the reliability of this design extensive testing is required after the design phase, after which redesigns should be made to improve on reliability.

12.4.2 Availability
The goal of the EcoHopper 450 is to be available for 10 flying hours each day, this excludes turnaround and time on ground. Using effective loading. The total turnaround time from landing to take-off is around 75 minutes. The mean flight time for a mission is set at 2 hours. Depending on regulations for night flights the EcoHopper 450 is able to operate on 2 to 3 rounds trips per day ranging between 12.5 to 19 operational hours per day, with 8 to 12 flying hours. Another important factor in availability is the maintenance time. The maintenance strategy is focused on checking the aircraft on a regular basis, this way maintenance can be done in early stages keeping the maintenance time to a minimum.

12.4.3 Maintainability
For time effective maintenance and operation the maintainability of the aircraft is important; if the aircraft is easy to service and accessible for maintenance the maintenance time will improve and therefore the availability. One of the differences with general aviation is the high wing, this will make accessing the wing and engines slightly harder. This should be taken into account in the maintenance time for the aircraft. The strut also adds an extra component to be checked and maintained on a regular basis. The rest of the airframe may be serviced in the same way as the current state of the art. This will make the EcoHopper 450 slightly worse considering the maintainability with respect to general aviation but still be within an acceptable range.

12.4.4 Safety
Safety is arguably the most important aspect of an aircraft. The aircraft will be equipped with standard safety equipment like oxygen masks and LED lights lighting up the aisles in case of an emergency. Based on CS25, the emergency exits per compartment were sized. The exit limit of one side of the aircraft is above the amount of passengers in each compartment. When comparing the safety of the EcoHopper 450 with the current market no significant changes are present, so this will have no impact on the operational aspect of the aircraft.

12.5 Data handling
In this section the components involved in the data handling process are discussed. The processor data bus is found centrally located and can be described as the main hub for data flow between various components. The CPU (central processing unit) processes tasks and is monitored by a watchdog unit. This component observes the CPU's performance. When it notices faults in the way the CPU is operating (for example in the case of so-called hangups), it will reset the system. The CPU is assisted by other processors, referred to as co-processors in Figure 12.2. These can carry out specific tasks assigned to by the central processing unit. Next are the different types of memory incorporated in the data handling system: random access memory (RAM) and read only memory (ROM). The former is short-term memory that stays just as long as the computer is operative. The latter refers to long-term memory that is retained even if the system is shut down. Another component connected to the processor data bus is mass storage that stores accumulated data that needs to be preserved. Two very common forms of mass storage are the magnetic disk drives and the solid state drives. It was opted to implement solid state drives as they are more reliable, durable and come with a higher storage density . Input/Output ports are connected to the processor data bus to ensure communication with external devices. [3]

The processor data bus is connected to the bus interface, which essentially acts as a bridge between the processor data bus and primary flight computer [3]. The primary flight computer sends data to and receives data from the subsystems. The major systems being monitored by the primary computer are the electrical system, flight control system, engine control system, environmental control system and the avionics. The avionics consist of the flight deck and at least five flat panel displays. Furthermore, the avionics feature a head-up display for both the pilot and co-pilot and include the overhead panel [42].

[3] Starshipengineer. Command and Data Handling System. Retrieved June 15, 2019, http://starshipengineer.blogspot.com/2013/07/command-and-data-handling-system.html

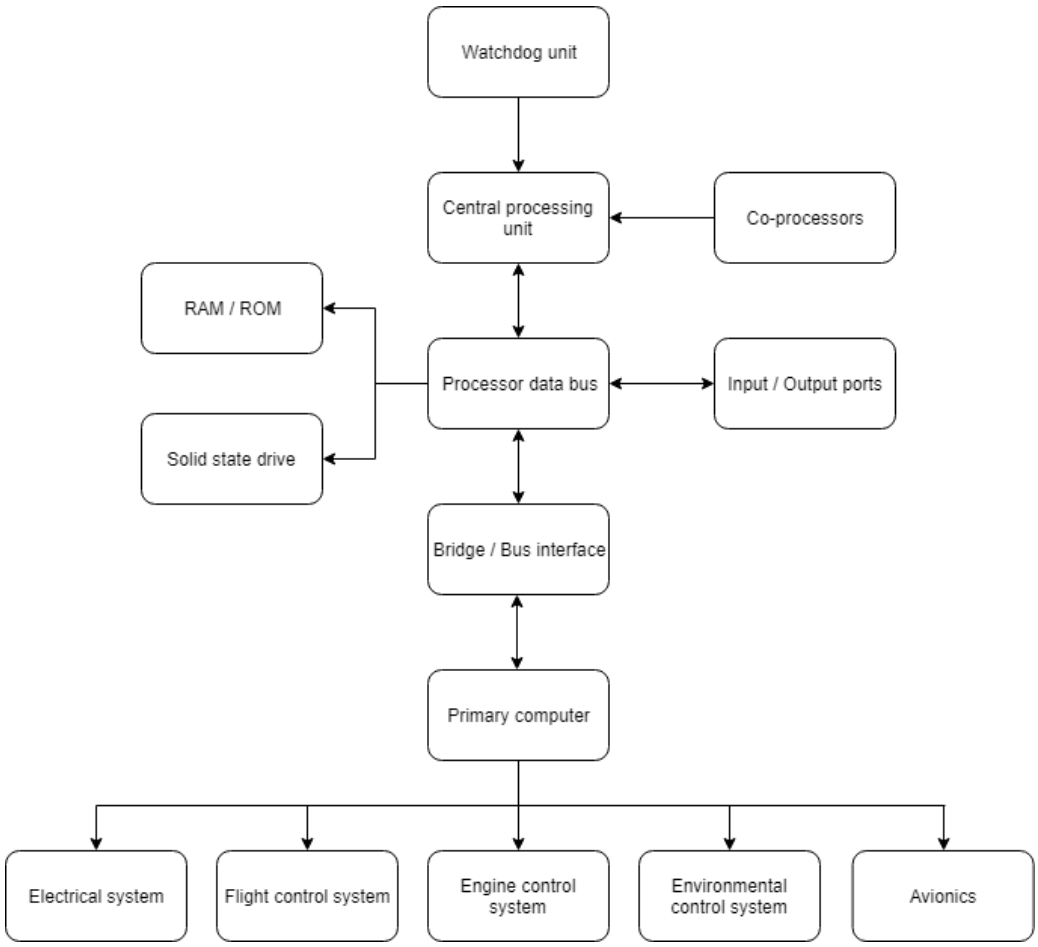

Figure 12.2: Block diagram of data flow within the EcoHopper 450.

12.6 Operational risks

Since the operations of the EcoHopper 450 differ from current state of the art aircraft, risks considering the operations of the aircraft occur. These risks will be listed below.

- **Parking space difficulties occur:** larger aircraft require larger parking spots, which might incur more costs due to more advanced infrastructure requirements. This risk is classified as improbable and marginal.
- **Only one boarding bridge is available:** as the Ecohopper 450 is a double decker aircraft, multiple boarding bridge could be used at the same time. This procedure was taken into account when the turnaround time was estimated. If an airport or the specific terminal only has one boarding bridge, the turnaround time will be delayed. This negatively affect the costs and the schedule of the aircraft.
- **Loading vehicles do not fit in the near vicinity of the strut:** as the strut is a unconventional design feature, it may be that loading vehicles of certain airports are designed such that the vehicles do not fit near the strut. This may result in a turn-around time delay or it may result in an airport not being able to operate the aircraft.

13 Performance analysis

Once the design was analysed and sized, the performance of the entire aircraft could be assessed. Several parameters were chosen to be investigated using tools that were developed. The first parameter under consideration was the payload range characteristic of the aircraft, this is explained in section 13.1. Next, the climb performance is discussed in section 13.2, to assess the aircraft against the CS-25 regulations. Furthermore, the runway performance is addressed in section 13.3 to verify that the aircraft can operate from all major hubs.

13.1 Payload range characteristics

The payload range characteristics of an aircraft can be represented in a diagram which shows the relation between the weight and the range of the aircraft. It essentially shows the trade-off relation between the payload and fuel weight, and the range.

Requirements

The requirements for the payload range diagram and characteristics of the aircraft are listed below.

- **BIB-SYS-MKO-01:** The range of the aircraft shall be between 1,000 - 2,000 km.
- **BIB-SYS-TEC-02:** The cruise profile of the aircraft shall be optimised for climate optimised flights.

Methodology

The payload range characteristics can be represented in the payload range diagram. This diagram is constructed using the Brequet's range equation shown in Equation 13.1 [19].

$$R = \frac{V}{c_T g}\frac{L}{D} ln\left(\frac{W_{TO}}{W_{TO} - W_F}\right) \tag{13.1}$$

The trade-off between fuel and payload weight, and range is found by adjusting the weight fraction in the equation. This resulted in different combinations for payload to fuel weight ratios and ranges. Loading the aircraft with the maximum payload weight (MPW) and loading it with fuel up to the maximum take-off weight (MTOW) resulted in the harmonic range [19]. This is essentially the range which should be closest to the design range as it means that the aircraft can fulfil the design mission with full payload, which is economically attractive. The next range was found from decreasing the payload and increasing the fuel to reach the maximum fuel weight (MFW), this is the maximum range [19]. This range is not economically attractive as the aircraft cannot carry the MPW. Finally, the ferry range was found by removing all payload and loading it with fuel until MFW. The overall take-off weight is less compared to the maximum range as there is no payload present at all.

Results

The results for the EcoHopper 450 are shown in Figure 13.1. Next to this diagram the payload range diagram for the reference aircraft, the B737-MAX 8, is shown (Figure 13.2). This aircraft essentially completes the same type of missions as the EcoHopper 450, namely short range intra-continental flights. However, as can be seen from its payload range characteristics, it means that it is operated well below its design point. In this sense, the EcoHopper 450 performs better than the B737-MAX 8 as it is not over-designed. The numerical results for the ranges are shown in Table 13.1. As can be seen, the EcoHopper 450 meets the design range of 1,400 km under harmonic range conditions, thus with full payload which is economically attractive.

Verification & validation

The tool to create the payload range diagram also had to be verified and validated. This was done by checking some of the calculations by hand, and finally using the reference aircraft and manufacturer's data to estimate the predictive power of the tool. However, aircraft manufacturers do not share information about the conditions under which the specified range is met. Therefore, it was assumed that the range provided by Boeing [1] was valid for a maximum payload case; so all seats occupied and with a full cargo hold. This assumption was further supported by another source which provided technical data on the B737-MAX 8 [2]. The diagram and numerical results are shown in Figure 13.2 and Table 13.1 as aforementioned. The harmonic range was evaluated at 6,415 km. As it was found that the design range under these conditions is 6,570 km,

[1] About the Boeing 737 MAX. Retrieved May, 21 2019, from https://www.boeing.com/commercial/737max
[2] Detailed Technical Datasheet. Retrieved May, 21 2019, from http://www.b737.org.uk/techspecsdetailed.htm

it could be said that the offset is 2.4%. This offset was deemed acceptable as the small difference could arise from the fact that detailed information about the reference aircraft was not available. For example the thrust specific fuel consumption c_T found could not be fully verified as it is mostly classified information.

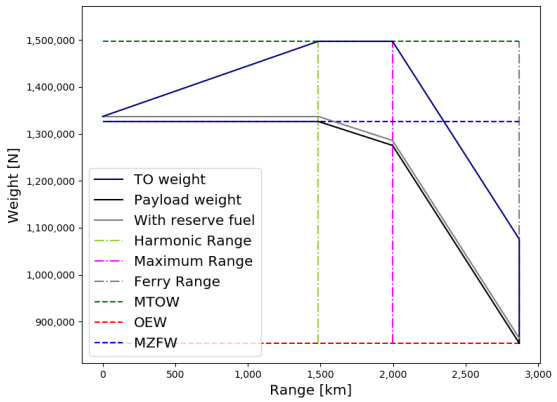

Figure 13.1: Payload range diagram for the EcoHopper 450.

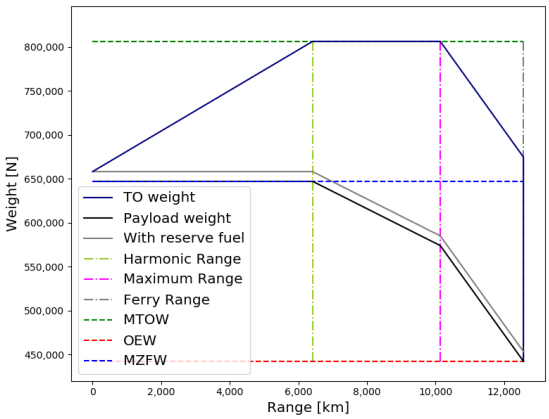

Figure 13.2: Payload range diagram for the B737-MAX 8.

Table 13.1: Harmonic, maximum and ferry range for EcoHopper 450 and the reference aircraft B737-MAX 8.

Parameter	Equation	EcoHopper 450	B737-MAX 8
Harmonic range [km]	Equation 13.1	1,484	6,415
Maximum range [km]	Equation 13.1	1,996	10,135
Ferry range [km]	Equation 13.1	2,868	12,560

13.2 Climb performance

In order to show compliance with the CS-25 regulations, the climb performance was analysed. The climb performance consists of the (maximum) rate of climb and the climb gradient. From this data, the absolute and service ceilings could also be found. These matters are discussed in subsection 13.2.1, subsection 13.2.2 and subsection 13.2.3 respectively. Finally, a special type of climb performance, a gliding flight, is discussed in subsection 13.2.4 to show the feasibility of a continuous descent approach. Again the B737-MAX 8 was chosen as reference aircraft to assess the climb performance of the EcoHopper 450[3] [2].

Requirements

Multiple requirements were imposed on the climb performance of the aircraft. They stem from the CS-25 regulations, the corresponding requirements are shown below.

- **BIB-SBS-FLP-12:** The flight performance subsystem shall comply with CS25.20 - CS25.125, CS25.201 - CS25.255 and CS25.1501 - CS25.1593.
- **BIB-SBS-FLP-12A:** The steady climb gradient of the aircraft in landing configuration shall not be less than 3.2%.
- **BIB-SBS-FLP-12B:** The steady climb gradient of the aircraft in take-off configuration shall be at least positive with the gear extended and at least 2.4% with the gear retracted.
- **BIB-SBS-FLP-12C:** The steady climb gradient of the aircraft in approach configuration shall not be less than 2.1%.

13.2.1 Rate of climb

The rate of climb (RC) is indicated by the vertical velocity of the aircraft under a certain angle (θ). It can be shown to be $RC = V_\infty sin\theta$. Using the equilibrium equations for a steady un-accelerated climb and assumptions regarding the state of the aircraft, the steady RC was found to be Equation 13.2, with $k = 1/\pi Ae$ [6]. The assumptions were that the thrust is in line with the direction of flight, and that the climb angle is small such that the small angle approximation could be used. The latter assumption was found to be valid for angles below 25 degrees as the error would then be a maximum of 3% [6]. Equation 13.2 provides the rate of climb for any flight condition which can be indicated by the T/W ratio, free stream velocity and density (thus altitude). The T/W ratio not only depends on the thrust setting and weight but also on the altitude as the thrust of a turbofan engine varies with altitude. According to Anderson, this thrust variation could be modelled as shown in Equation 13.3 [6], where the subscript 0 indicates sea level conditions and subscript h indicates the conditions at altitude h. The constant m depends on the type of turbofan and the amount of thrust it can deliver. In this

[3] B737-MAX 8. Retrieved June 15, 2019, from https://doc8643.com/aircraft/B738

case, the value of m was assumed to be 1.3 [6].

$$RC = V_\infty [\frac{T}{W} - \frac{1}{2}\rho_\infty V_\infty^2 (\frac{W}{S})^{-1} C_{D_0} - \frac{W}{S}\frac{2k}{\rho_\infty V_\infty^2}] \tag{13.2}$$

$$T_h = T_0 (\frac{\rho_h}{\rho_0})^m \tag{13.3}$$

Next to the steady RC, there is also the unsteady RC which essentially means that the aircraft accelerates as it climbs. This is the case when the aircraft is required to maintain a constant equivalent airspeed (EAS). According to Torenbeek, the unsteady rate of climb can be modelled as Equation 13.4 [3], where the factor $\frac{v}{g}\frac{dv}{dh}$ depends on the Mach number and the atmospheric layer the climb is performed in [3]. This relation is shown in Equation 13.5 [3]. The same type of relationship with altitude holds for the unsteady RC as for the steady RC. The main differences between the steady and unsteady RC is that the unsteady RC has a lower value since the excess power used to climb decreases due to increasing drag with respect to the steady case.

$$RC_{unsteady} = \frac{(T-D)V}{W(1 - \frac{v}{g}\frac{dv}{dh})} \tag{13.4}$$

$$\frac{v}{g}\frac{dv}{dh} = 0.5668M^2 \tag{13.5}$$

Sensitivity analysis

In order to assess how the (steady) RC varies with altitude, a plot could be made showing the free stream Mach number against the RC for multiple altitudes. In addition, a plot of the maximum rates of climb at different altitudes was made. These results can be seen in Figure 13.3 and Figure 13.4 respectively. As can be seen, the highest rate of climb can be attained at the lowest altitude, this is because the density is the highest there as well as the thrust the engines can deliver. From Figure 13.3 it can be seen that the RC becomes negative at certain altitudes and speed combinations. For the higher altitudes it means that the absolute ceiling of the aircraft is exceeded, this is explained in subsection 13.2.3. For the negative RC at lower altitudes it should first be noted that the RC depends on the excess power, which is the difference between the power required to overcome drag and the power available from the engines [6]. At the lower altitudes and velocities the aircraft has too little excess power to execute a climb, while it flies too fast creating too much drag (thus increasing the power required) at higher Mach numbers [6]. This can lead to negative RC values in both cases.

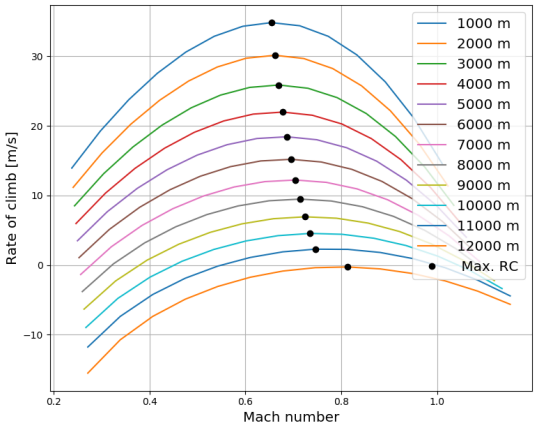

Figure 13.3: Steady rate of climb for different altitudes for the EcoHopper 450.

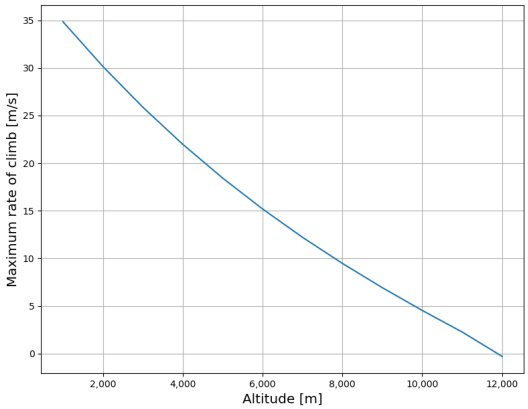

Figure 13.4: Maximum steady rate of climb as function of altitude for the EcoHopper 450.

Results

Table 13.2 presents the results of the model for the RC at FL200 for both the reference aircraft as well as for the EcoHopper 450. The latter was included to be able to assess the performance against existing aircraft. Note that the rates of climb were evaluated at MTOW as this represents the state of the aircraft during climb the best. Lastly, it can be noted that the EcoHopper 450 has lower rate of climb at 6,096 m with a similar speed as the B737-MAX 8. In essence, this means that the EcoHopper 450 has a lower service ceiling as its rate of climb is less, and the rate of climb decreases with altitude, see Figure 13.3. The service ceiling is discussed in subsection 13.2.3.

Table 13.2: Maximum (un)steady rate of climb of the EcoHopper 450 and the B737-MAX 8.

Parameter	Equation	EcoHopper 450	B737-MAX 8
Steady RC [m/s]	Equation 13.2	14.89	16.67
Unsteady RC [m/s]	Equation 13.4	11.66	13.16
Altitude [m]	-	6,096	6,096
Velocity cruise [m/s]	-	221.2	221.2

Verification & validation

In order to verify and validate the model, a comparison was made between the model's output and data retrieved for the reference aircraft B737-MAX 8. As the climb performance data is mostly withheld by the aircraft manufacturer, only the maximum steady RC at a certain altitude could be found [3]. Therefore it was harder to validate the rate of climb tool. However, verification could be done by hand calculations and by checking the magnitude of the computed RC, as well as checking the shapes of the graphs. These values and graphs could be compared to graphs provided by Anderson [6]. Although the graphs provided represented different aircraft, the order of magnitude and trend of the graphs should be similar. Then validation was done based on the value for the RC of the B737-MAX 8 found. The maximum RC at FL200 (6,096 m) with an airspeed of 221.2 m/s was found to equal 3,000 ft/min (or 15.24 m/s) [3]. From Table 13.2 it be seen that the computed RC for the B737-MAX 8 at FL200 was 16.67 m/s, which resulted in an offset of 9.38%. This was deemed acceptable as it was not know how trustworthy the data for the reference aircraft was, and since the tool was completely verified.

13.2.2 Climb gradient

The CS-25 regulations do not stipulate exact required rates of climb, however they do indicate the minimum climb gradient required during different flight phases. These requirements are listed in the beginning of this section (see BIB-SBS-FLP-12A, BIB-SBS-FLP-12B and BIB-SBS-FLP-12C). The climb gradient could be found from the ratio between the vertical speed (RC) and the horizontal speed (V_h). The flight phases considered were landing, take-off and approach. The corresponding free stream velocities could be found from relationships with the stall speed: $V_{td} = 1.15V_{s,land}$, $V_{LOF} = 1.2V_{s,TO}$ and $V_a = 1.3V_{s,land}$ respectively [3]. The stall speeds were determined in landing and take-off configuration, meaning that the weight would be the maximum landing weight and maximum take-off weight respectively. In addition, the $C_{L,max}$ during these phases was obtained from the analysis performed in chapter 8.

The maximum climb angle which can be achieved throughout the flight could also be computed. This angle depends on the T/W ratio and the zero lift drag. As the thrust depends on the altitude the maximum angle does too. The maximum climb angle could be found from Equation 13.6, while the required speed at the maximum angle was found from Equation 13.7 [6].

$$sin\theta_{max} = \frac{T}{W} - \sqrt{4C_{D_0}k} \qquad (13.6)$$

$$V_{\theta_{max}} = \sqrt{\frac{2}{\rho_\infty}\left(\frac{k}{C_{D_0}}\right)^{0.5}\frac{W}{S}cos\theta_{max}} \qquad (13.7)$$

Results

The results for the different flight phases and climb gradients are shown in Table 13.3. As can be seen, the aircraft meets all regulations with a similar margin. On average the aircraft has a climb gradient which is 14% larger than the regulations. This was deemed acceptable as it can serve as a contingency value for the further design stages, e.g. if the aircraft gets heavier. It can thus be said that the requirements BIB-SBS-FLP-12(A-C) are met.

Table 13.3: Climb gradient for the EcoHopper 450 with respect to the regulations.

Parameter	Equation	EcoHopper 450	Regulations
Landing climb gradient	gradient = $\frac{RC}{V_h}$	3.8%	3.2%
Take-off climb gradient	gradient = $\frac{RC}{V_h}$	2.8%	>0; 2.4%
Approach climb gradient	gradient = $\frac{RC}{V_h}$	2.4%	2.1%

The results for the maximum climb angle and the corresponding conditions are shown in Figure 13.5, Figure 13.6 and Figure 13.7. Which indicate the maximum climb angle that can be achieved at different altitudes, the required airspeed, and the RC at maximum climb angle respectively. The stall speed was included in Figure 13.6 to check whether the theoretical maximum climb angle could be achieved in real life. As can be seen, there is a significant margin between the required and the stall speed, indicating that the angle can be achieved. It can immediately be noted that the RC at maximum climb angle is lower than the maximum attainable RC. This is because the maximum RC indicates the quickest way of reaching a certain altitude, regardless of the distance covered while doing it. While the maximum climb angle indicates the climb

condition in which the aircraft gains the most altitude in a given horizontal distance. Thus in the latter case, the horizontal speed should be limited while for the first case the vertical speed should be maximised. These two optimums both happen at different conditions, leading to different horizontal and vertical speeds.

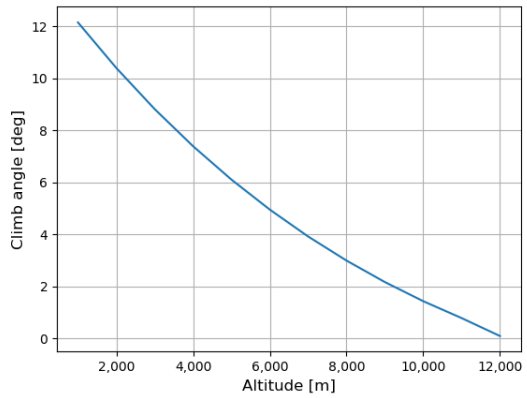

Figure 13.5: Maximum climb angle for EcoHopper 450 at different altitudes.

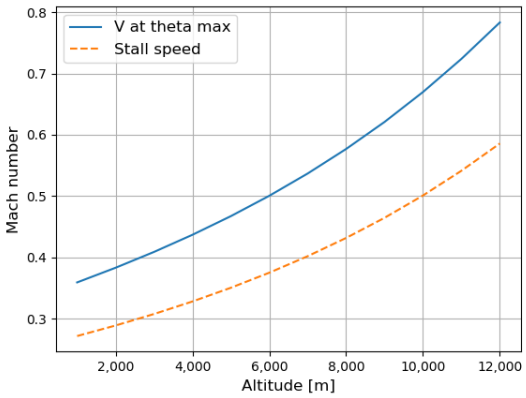

Figure 13.6: Required airspeed at maximum climb angle for the EcoHopper 450.

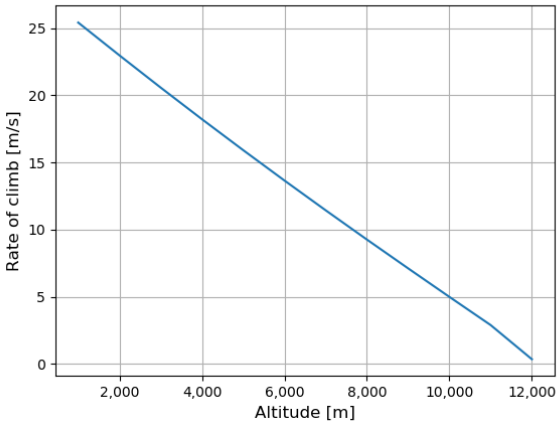

Figure 13.7: Rate of climb at maximum climb angle for the EcoHopper 450.

Verification & validation

As no data regarding the maximum achievable climb angle for reference aircraft was available, this tool could not be fully validated. However, the tool could be verified using reasoning logic and hand calculations. Looking at the plots, it can be seen that the maximum angle decreases with increasing altitude this is due to the decreasing available thrust. However, the required speed does increase with increasing altitude. This is because the density decreases and the maximum angle decreases, which increases the cosine function of that angle (see Equation 13.7). However, as the effect of a decreasing angle usually dominates over the increase in velocity, the RC decreases with altitude as well [6]. Finally, the shape of the graphs and magnitude of the values could be verified by comparing them to graphs given by Anderson [6].

13.2.3 Operating ceilings

Another aspect that could be derived from the (steady) rate of climb obtained in subsection 13.2.1 were the absolute and service ceilings of the aircraft. The absolute ceiling is the altitude at which the maximum steady rate of climb is equal to zero, while the service ceiling it the altitude at which the maximum steady rate of climb is equal to 100 ft/min (0.508 m/s) [6].

Results

The absolute and service ceilings for the EcoHopper 450 and the reference aicraft, the B737-MAX 8, are shown in Figure 13.8 and Figure 13.9 respectively. The numerical values are shown in Table 13.4. As can be seen, the margin between the two ceilings is fairly small. Therefore, airlines tend to only use the service ceiling of an aircraft to plan the routes. Otherwise dangerous situations can occur when the absolute ceiling of the aircraft is met, e.g. in the case of an emergency

climb to avoid oncoming traffic. In addition, it can be noted that the ceilings of the EcoHopper 450 are lower than for the B737-MAX 8. This was also concluded from subsection 13.2.1 as the aircraft had a lower RC compared to the reference aircraft. This also follows from the chosen design point as the EcoHopper 450 is designed and thus optimised for a lower altitude, meaning that the ceilings also go down as the chosen point is suitable for lower altitudes only.

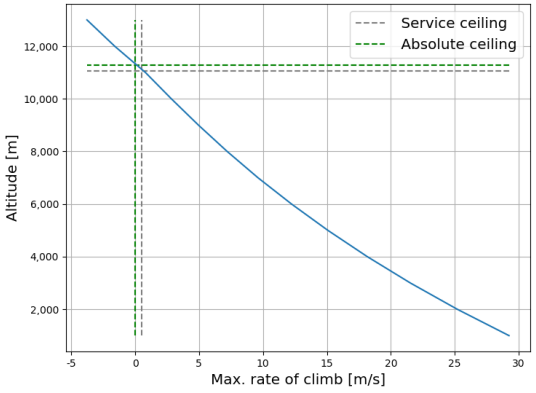

Figure 13.8: Absolute and service ceilings for EcoHopper 450.

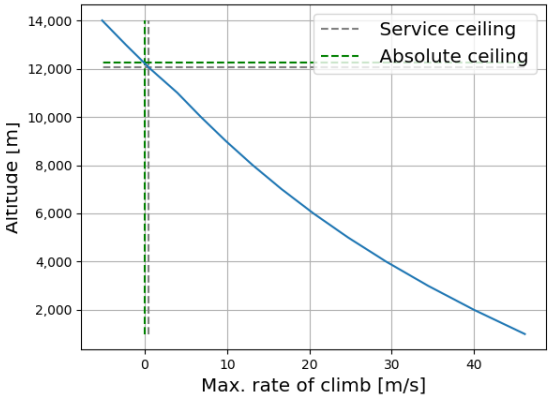

Figure 13.9: Absolute and service ceilings for the reference aircraft B737-MAX 8.

Verification & validation

The tool was essentially verified and validated in subsection 13.2.1 as it uses the data obtained from the rate of climb tool. However, the service ceiling found for the reference aircraft could still be compared to the actual service ceiling obtained from the FAA data sheet on the B737-MAX 8 [51] as this data is more accessible than rate of climb data. The service ceiling was found to be 41,000 ft (or 12,497 m), while the computed ceiling was 12,074 m. This yielded an offset of 3.38%, which was deemed acceptable as the offset of the rate of climb tool was carried on in the interpolation to find the service ceiling.

Table 13.4: Absolute and service ceilings for the EcoHopper 450 and the B737-MAX 8.

Parameter	Equation	EcoHopper 450	B737-MAX 8
Absolute ceiling [m]	Equation 13.2	11,280	12,240
Service ceiling [m]	Equation 13.2	11,050	12,074

13.2.4 Gliding flight

A special type of climb performance is the gliding flight, which essentially results in negative rates of climb, or positive rates of descent (RD). During a gliding flight all engines are shut down. This can happen in case of an emergency, or it can represent the case when a continuous descent approach is conducted. In the first case, the minimum rate of descent should be found, this value can be computed using Equation 13.8 according to Anderson [6]. This rate highly depends on the wing loading and the fraction C_L^3/C_D^2. The fraction has to be maximised to obtain the minimum rate of descent [6]. In the case of an optimal continuous descent approach the aircraft glides from its cruise altitude down do to the ground. In this case it is necessary to know the horizontal distance that can be covered by the aircraft when starting at a certain altitude. This horizontal distance highly depends on the lift to drag ratio (L/D). The horizontal distance can simply be found by multiplying L/D with the altitude at which the glide is started.

$$RD = \sqrt{\frac{W}{S}\frac{2}{\rho_\infty (C_L^3/C_D^2)}} \tag{13.8}$$

Sensitivity analysis

Next to the ratio C_L^3/C_D^2, the wing loading W/S also influences the rate of descent significantly. When decreasing the wing loading by 50% it decreases the overall rate of descent by almost 30%. Thus, for a low rate of descent which is desirable for an engine flame-out, it is desired to aim for a low wing loading. Nevertheless this is not desirable for the overall design as it makes the wings less efficient.

Results

The rate of descent could be plotted against the altitude, this is shown in Figure 13.10. From the plot it can be deduced that the rate of descent increases with increasing altitude, this is due to the decreasing density. To have the overall minimum

rate of descent it is thus desired to have an engine flame-out at a low altitude. However, a low rate of descent does not immediately indicate that the horizontal distance covered is the lowest as this also depends on the starting altitude. This is visualised in Figure 13.11 for the EcoHopper 450. The glide angle which should be maintained to reach the maximum range is 3.1 degrees, which is a typical value according to Anderson [6]. In the optimal case the aircraft can start its continuous descent approach from its cruise altitude of 9 km, 157 km before the airport such that it can glide down towards the runway. This procedure can save fuel as well as (noise) emissions. The reduction in fuel and emissions is discussed in chapter 15.

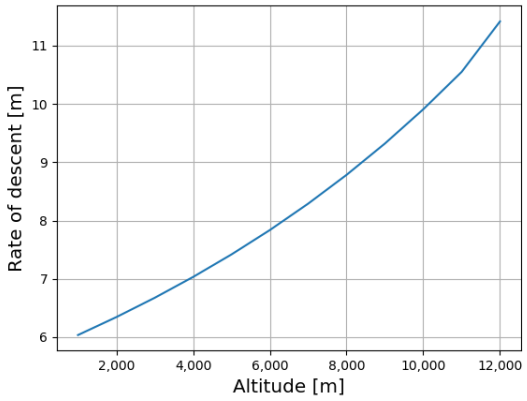

Figure 13.10: Minimum rate of descent as a function of altitude for the EcoHopper 450.

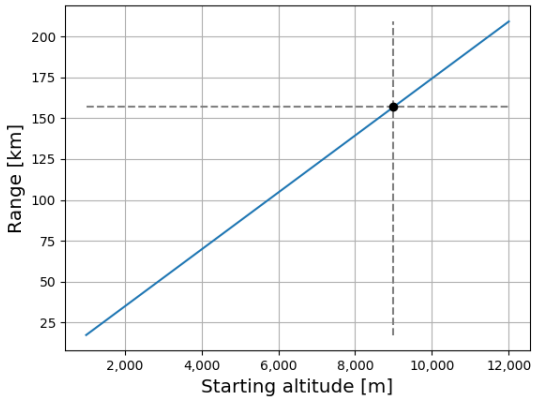

Figure 13.11: Horizontal gliding distance as a function of starting altitude for the EcoHopper 450.

Verification & validation

As aircraft manufacturers do not provide information on the descent rate of the aircraft in either a powered or unpowered descent the tool could not be fully validated. However, it could be verified in the same way as the climb gradient tool (subsection 13.2.2). The graphs and values were compared to results provided by Anderson for different aircraft [6]. In addition, the calculations were verified by hand to check whether no implementation errors were made.

13.3 Runway performance

In order to determine whether the EcoHopper 450 meets the requirements regarding runway performance, the take-off distance, landing distance and balanced field length were evaluated. This is described in subsection 13.3.1, subsection 13.3.2 and subsection 13.3.3 respectively.

Requirements

The runway performance is linked to multiple requirements. Some requirements were set by the client while other requirements were found from the analyses performed in the Baseline report [8].

- **BIB-SYS-TEC-06:** The aircraft shall be able to operate from all major European airports.
- **BIB-SBS-FLP-01:** The aircraft shall be able to take-off from a runway of 2,700 m at sea-level at MTOW.
- **BIB-SBS-FLP-02:** The aircraft shall be able to land on a runway of 2,700 m at sea-level at MLW.

13.3.1 Take-off distance

The take-off distance indicates the distance needed for an aircraft to accelerate from standstill to the lift-off speed (the ground run), and from lift off to passing the screen height h_s (the airborne phase) [3]. The screen height indicates the altitude the aircraft needs to have before it is cleared of any obstacles around the airport. This height was set at 35 ft (or 10.7 m) according to regulations [3, 5]. The ground run could be computed using Equation 13.9 [3]. The lift-off speed V_{LOF} was assumed to be $1.2V_{S,TO}$ (stall speed during take-off) [3]. Next, the mean thrust $\bar{T}$ was given by Equation 13.10 [3], where λ is the bypass ratio of the engines. Finally, the parameter μ' was given by $\mu' = 0.02 + 0.01C_{L_{max}}$ [3]. The distance covered in the airborne phase could then be computed using Equation 13.11 [3], where γ_{LOF} could be found from Equation 13.12 [3]. The result for the take-off distance and verification of this tool are presented in subsection 13.3.2.

$$s_{ground} = \frac{V_{LOF}^2/2g}{\bar{T}/W_{TO} - \mu'} \tag{13.9}$$

$$\bar{T} = 0.75\frac{5+\lambda}{4+\lambda}T_{TO} \tag{13.10}$$

$$s_{air} = \frac{V_{LOF}^2}{g\sqrt{2}} + \frac{h_s}{\gamma_{LOF}} \quad (13.11)$$

$$\gamma_{LOF} = 0.9\frac{\bar{T}}{W_{TO}} - \frac{0.3}{\sqrt{A}} \quad (13.12)$$

13.3.2 Landing distance

The landing distance also consists of two phases: the airborne phase followed by the ground run. The airborne phase indicates the horizontal distance covered by the aircraft from the obstacle height h_{land} until the wheels touch the ground. The obstacle height indicates the altitude the aircraft needs to pass in order to clear all obstacles in front of the runway, this height was found to be 35 ft (or 15.3 m) [3, 5]. The second phase, the ground run, includes the distance covered from touch down until the aircraft comes to a complete standstill. The distance covered during the airborne phase could be found using Equation 13.13 [3]. The approach speed, V_a, was assumed to be equal to $1.3V_{s,land}$ [3]. The touchdown speed V_{td} was then found from Equation 13.14 [3], where the constant $\bar{\gamma}$ was assumed to equal 0.1, as well as the change in load factor Δn.

$$s_{air} = \frac{1}{\bar{\gamma}}\left(\frac{V_a^2 - V_{td}^2}{2g} + h_{land}\right) \quad (13.13)$$

$$\frac{V_{td}^2}{V_a^2} = 1 - \frac{\bar{\gamma}^2}{\Delta n} \quad (13.14)$$

Next, the ground run was found using Equation 13.15 [3], where $\bar{a}_{break}$ indicates the mean deceleration during landing. Torenbeek stated that this value usually ranges between 0.35g and 0.45g depending on the braking systems used [3].

$$s_{ground} = \frac{V_{td}^2}{2\bar{a}_{break}} \quad (13.15)$$

Sensitivity analysis

As the approach, landing and take-off speed have a clear influence on the landing and take-off distances according to their relations, another parameter was further investigated. Namely, the elevation of the airport as it has a significant effect on the landing and take-off distances due to the varying density. Increasing the elevation of the airport to 1,000 m leads to a take-off distance of 2,302 m and a landing distance of 1,554 m for the B737-MAX 8. With respect to the model outputs at zero elevation, the increase in distance is 9.4% for take-off and 8.9% for landing. The model could then also be used to determine the maximum airport elevation the aircraft can take-off from to meet the 2,700 m distance specified in the requirement. For the B737-MAX 8 this turned out to be 2,700 m while it is 2,000 m for the EcoHopper 450.

Results

Combining both phases resulted in the total landing distance required. The results can be seen in Table 13.5. The results for both the take-off, discussed in subsection 13.3.1, and landing distances for the EcoHopper 450 and the B737-MAX 8 are shown. The B737-MAX 8 was chosen again as reference aircraft as the EcoHopper 450 needs to be able to operate from all airports the B737-MAX 8 also operates from. From the results it can be seen that the EcoHopper 450 has a similar take-off and landing distance compared to the B737-MAX 8. Comparing the computed distances with the ones specified in the requirements, it can be seen that the aircraft meets these requirements.

Table 13.5: Take-off and landing distanced for the EcoHopper 450 and the B737-MAX 8.

Parameter	Equation	EcoHopper 450	B737-MAX 8
Take-off distance [m]	Equation 13.9 & Equation 13.11	2,216	2,104
Landing distance [m]	Equation 13.13 & Equation 13.15	1,594	1,427

Verification & validation

In order to verify the tools, hand calculations were done to check the implementation of the equations. In addition, the order of magnitudes were checked to ensure that the equations yielded realistic values. To validate the tools, the take-off and lading distances for the reference aircraft were compared to the computed distances. From the certification data sheet of the FAA, the take-off and landing distances of the B737-MAX 8 were found to be roughly 2,042 m and 1,372 m respectively [51]. Comparing these values to the computed values shown in Table 13.5 resulted in an offset for the take-off distance of 3.0%, and for the landing distance of 4.0%. These offsets were deemed acceptable as no exact data was provided on the atmospheric conditions and the airport elevation at which the take-off and landing distances were provided. These conditions can heavily impact the runway performance as explained before.

13.3.3 Balanced field length

In the case of an engine failure the aircraft is still required to safely operate from all major hubs. Considering that the engine failure occurs at V_x, there are two types of situations that needed to be investigated: a continued and an aborted take-off. For both cases the distance covered before the engine failure is the same. This distance could be estimated using Equation 13.16 [3], where the subscript 0-1 indicates the first stage of take-off. The mean acceleration ($\bar{a}/g$) of the aircraft during take-off was found to be approximately 0.25g [3].

$$s_{0-1} = \frac{V_x^2}{2\bar{a}_{0-1}} \tag{13.16}$$

After the engine failure, the distances covered begin to differ. In the case of a continued take-off, the distance required could be found using Equation 13.17. In the case of an aborted take-off the distance covered could be found from Equation 13.18 [3]. The average deceleration ($\bar{a}_{stop}$) with one engine inoperative was found to be 0.37g [3]. Finally combining the distances lead to the total required distance for a continued take-off ($s_{0-1}+s_{1-2}$) and an aborted take-off ($s_{0-1}+s_{stop}$).

$$s_{1-2} = \frac{1}{\bar{\gamma}}\left(\frac{V_2^2 - V_x^2}{2g} + h_s\right) \tag{13.17}$$

$$s_{stop} = \frac{V_x^2}{2\bar{a}_{stop}} + V_x \Delta t \tag{13.18}$$

Results

The balanced field length, or BFL, is the distance at which the continued and aborted take-off require the same amount of runway. The BFL could be found by varying the engine failure speed V_x and computing the required runway distance for both cases. This could subsequently be plotted which is shown in Figure 13.12. For the EcoHopper 450 it can be seen that the balanced field length is 1,774 m, which happens when V_x is equal to 65.7 m/s. In order to measure the performance against a reference aircraft the BFL for the B737-MAX 8 was also computed. This can be seen in Figure 13.13. The BFL turned out to be 1,614 m at an engine failure speed of 61.9 m/s. The BFL is shorter for the reference aircraft as its thrust to weight ratio is higher, thus being able to take-off faster.

Also the minimum required runway length for a safe take-off and landing could be computed from the previous results. According to regulations the required landing runway length is 10/6 times the landing distance, while the required take-off runway length may depend on the BFL [7]. If the BFL is larger than the take-off distance, the required runway length is equal to the BFL, while if the take-off distance is larger, the required runway length is 1.15 times the take-off distance. This yielded a required runway length for landing of 2,657 m and for take-off of 2,548 m for the EcoHopper 450. It could thus be said that it meets the requirements for the 2,700 m long runway, BIB-SBS-FLP-01 and BIB-SBS-FLP-02.

Verification & validation

In order to verify the tool, some hand calculations were performed and the order of magnitude was checked. Once it was determined that no errors were present in the code, it was time to investigate the predictive power of the tool. However, aircraft manufacturers do not provide any data on the aircraft's performance in case of an engine failure during take-off. Therefore the exact predictive power could not be determined. Nevertheless, the order of magnitude and shape of the curves were further investigated by comparing them to graphs provided by Torenbeek [3]. The tool was therefore verified to the best extent based on the available data.

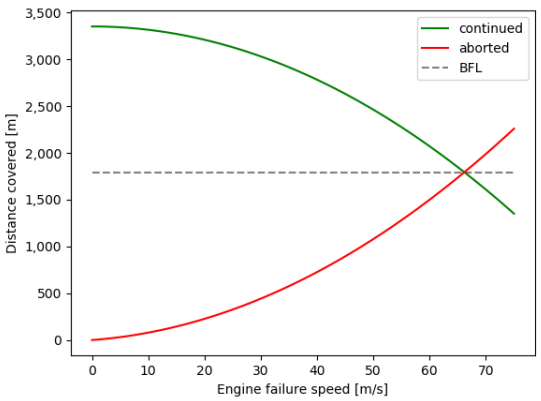

Figure 13.12: Balanced field length for the EcoHopper 450.

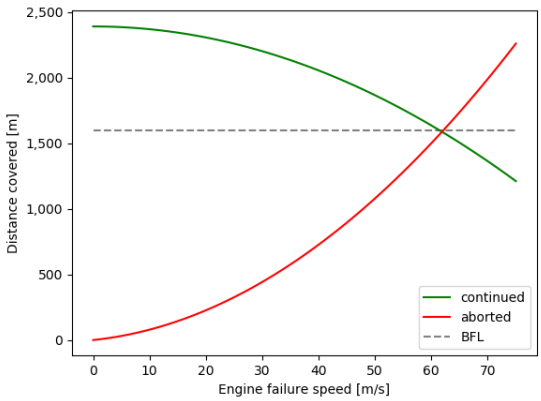

Figure 13.13: Balanced field length for the B737-MAX 8.

14 Fuel consumption

As a requirement was imposed on the fuel consumption this parameter had to be investigated. The requirement was given with respect to the current state of the art aircraft, e.g. B737-MAX 8. Therefore, this aircraft was used as reference aircraft. To determine the fuel consumption of the entire flight, it was divided into multiple phases: the LTO cycle (all operations below 3,000 ft), second climbing phase, cruise and initial descent phase. The fuel consumption during cruise and the second climbing and descent phase (above 3,000 ft) are discussed in this chapter. The fuel consumption for the LTO cycle is determined in chapter 15. The EcoHopper 450 and reference aircraft, B737-MAX 8, were evaluated as if they were performing the same mission: a mission range of 1,400 km while cruising at 9,000 m. This allowed one to compare the results objectively as they have to climb to and descent from the same altitude.

Requirements

There was only one requirement given/found for the fuel consumption, however it is a highly driving requirement for the design:

- **BIB-SYS-TEC-08:** The aircraft shall have 10% reduced fuel consumption per passenger-kilometre with respect to current state of the art aircraft.

14.1 Cruise fuel consumption

In order to compute the cruise fuel consumption the Specific Air Range, or SAR, was used [9]. Which is essentially the amount of kilometres the aircraft can fly with 1 kg of fuel. The goal is to maximise this number in order to have the lowest fuel consumption. The SAR could be computed using Equation 14.1 [9]. In order to link the SAR to the fuel consumption requirement, it was decided to use 1/SAR to obtain the amount of fuel consumed per kilometre flown. Finally, this value was divided by the number of passengers to obtain the kg/km-pax value.

$$SAR = \frac{V_{cr}}{[C_{D_0} + k(\frac{W_{cr}}{q_{cr}S})^2]q_{cr}SC_T} \tag{14.1}$$

Equation 14.1 essentially states that the SAR is equal to the ratio of cruise speed over fuel flow. Where the fuel flow in a steady flight condition is found by multiplying the drag with the Thrust Specific Fuel Consumption C_T (TSFC). The TSFC highly depends on the engine of the aircraft. Next, the factor k in Equation 14.1 is the factor $\frac{1}{\pi Ae}$ from the drag polar.

Sensitivity analysis

As can be seen from the variables involved, the fuel consumption changes with changing airspeed and altitude. The direct influence can be seen in parameter V_{cr} while the indirect influence can be seen in the dynamic pressure $q_{cr} = \frac{1}{2}\rho V_{cr}^2$. In addition, the aircraft configuration, such as the surface area and aspect ratio also influence the fuel consumption. To determine the effects of all parameters involved a thorough sensitivity study was carried out in the Midterm report [1]. The sensitivity analysis concluded that the cruise conditions highly influence the fuel consumption; for low Mach numbers the minimum fuel consumption is obtained at lower altitudes, while for higher Mach numbers flying at a higher altitude is more beneficial. This trend can also be observed in the diagram shown in Figure 14.1, which indicates the fuel consumption of the B737-MAX 8 at different cruise conditions. The dot represents the actual fuel consumption of the B733-MAX 8. The interested reader is referred to the Midterm report for more details on the sensitivity analysis [1].

Results

The fuel consumption was computed at cruise weight, which was assumed to be MTOW minus 40% of the trip fuel weight [36]. It resulted in a cruise fuel consumption of 0.00969 kg/km-pax for the EcoHopper 450, and 0.0108 kg/km-pax for the B737-MAX 8. It can be noted that the fuel consumption during cruise is 10.3% lower for the EcoHopper 450 than for the B737-MAX 8. This is due to the aerodynamic efficiency of the design as well as due to the selection of highly efficient engines.

Verification & Validation

In order to verify the code, the fuel consumption of the Boeing 737-MAX 8 was found and plotted against the lines obtained from Equation 14.1. The fuel consumption found for the reference aircraft was valid at an altitude of 12,000 m and a cruise speed of 0.79 Mach, and with 200 passengers [52]. The fuel consumption per passenger estimated by the tool was obtained using data of the reference aircraft and an educated guess for the zero lift drag coefficient [1] [19]. The results can be seen in Figure 14.1 in which the fuel consumption of the reference aircraft is represented as a dot. As can be seen in the plot, the fuel consumption of the reference aircraft lies on the estimated fuel consumption line at 12,000 m. This implies that the

[1] Detailed Technical Datasheet. Retrieved May, 21 2019, from http://www.b737.org.uk/techspecsdetailed.htm

tool is capable of predicting the fuel consumption per passenger-km with a high precision in the first stage of the detailed design phase.

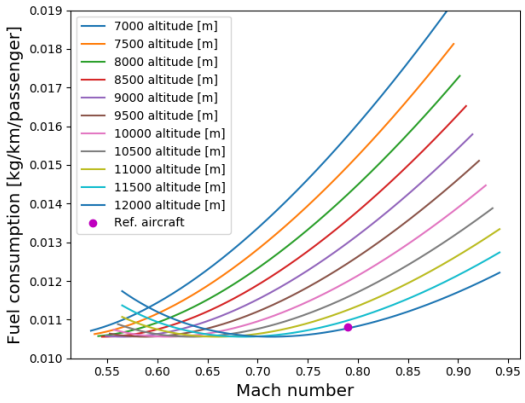

Figure 14.1: Fuel consumption of the B737-MAX 8 for different cruise conditions.

14.2 Climb fuel consumption

The next step was to assess the fuel consumption during the second climbing phase. This phase starts at an altitude of 3,000 ft and assumes a steady climb rate until the cruise altitude is reached. The fuel consumption during climb can be found from an integration of the time to climb and the reduction in weight: $t = \frac{\Delta h}{RC}$ and $\Delta W = \dot{F}t$, in which RC is the rate of climb computed in chapter 13. The starting weight of this climbing phase was found by subtracting the fuel used during the LTO cycle from the MTOW. The fuel burnt during the LTO cycle of the EcoHopper 450 was found to be 288 kg, while it was 365 kg for the B737-MAX 8 (see chapter 15). The Δh considered in this computation was from 3,000 ft until cruise altitude. The cruise altitude for both aircraft was set at 9 km as explained in the beginning of this chapter.

The climb was assumed to be a full thrust climb as it offers the best fuel economy for an unrestricted climb according to Boeing [2]. However, as the engines can only deliver the maximum thrust for a limited amount of time, the climb cannot be executed at a thrust setting of 100% like the take-off. Therefore, the thrust setting during the climb was assumed to be 90% as this is usually the maximum continuous thrust the engine can deliver [10]. The RC was then computed using the tool explained in chapter 13. Note that the thrust still varies with altitude as discussed in chapter 7. This means that the thrust setting remains constant but the available thrust for climb decreases as the altitude increases. The velocity at which the climb was executed was assumed to be 60% of the cruise velocity as obtained from aircraft data from Filippone [11]. Finally, as the take-off fuel flow was found in chapter 7 and the fuel flow varies linearly with the thrust output, the fuel flow during the climb phase could be found.

Results

Following the methodology set out above resulted in an initial estimation for the climb phase fuel consumption. However, it must be noted that the computed fuel consumption is only valid for the specified climb conditions. As the climb profile differs from flight to flight it cannot be considered as the only true fuel consumption. The results for this climb profile are shown in Table 14.1 for both the EcoHopper 450 as well as for the B737-MAX 8. As can be seen, the EcoHopper 450 consumes more fuel during the climb than the B737-MAX 8. This was expected as the aircraft is heavier and the engines need to produce more thrust. However, when looking at the fuel consumption per passenger, it can be noted that the EcoHopper 450 is more efficient with respect to the fuel consumption over payload weight ratio. Moreover, the EcoHopper 450 takes more time to reach the cruise altitude, and thus covers a larger horizontal distance while performing the climb. This is because the aircraft has a lower rate of climb compared to the B737-MAX 8, which was also concluded from the rate of climb analysis performed in chapter 13.

Table 14.1: Fuel consumption for the climb to cruise altitude.

Parameter	Time to climb [min]	Average RC [m/s]	Fuel consumed [kg]	Fuel consumed [kg/pax]	Distance [km]
EcoHopper 450	25.6	5.6	1,643.5	3.7	201.6
B737-MAX 8	23.5	6.1	1,213.6	6.1	187.4

[2]Fuel conservation strategies: take-off and climb. Retrieved June, 25 2019, from `https://www.boeing.com/commercial/aeromagazine/articles/qtr_4_08/article_05_3.html`

Verification & validation

In order to verify the implementation of the code, the code was checked using unit tests. This way the intermediate results were checked for their sign and magnitude. Then the validation could be done using data provided by Filippone on the A320-200 [11][pg. 280]. It provided the calibrated airspeed (CAS) at which the climb is executed, the fuel flow during the climb and the results for the time to climb and the fuel consumption. The data on the aircraft specifications and dimensions were obtained from Elsevier [3]. This finally resulted in the modelled fuel consumption and time to climb shown in Table 14.2. The values obtained from Filippone are also shown next to the offset. As can be seen, the average offset for the parameters considered is 5.7%. The offset for the model was deemed acceptable, however it should be noted that the fuel consumed is underestimated. This means that the climb fuel consumption computed earlier is underestimating the amount of fuel used during the climb leading to a lower trip fuel weight than expected. This should be kept in mind when drawing conclusions on the total fuel consumption. The average RC was included to check the order of magnitude, whether the gradient and the vertical speed are within reasonable limits.

Table 14.2: Validation data for the climb fuel consumption tool.

Parameter	Climb altitude [m]	Time to climb [min]	Average RC [m/s]	Fuel consumed [kg]	Horizontal distance [km]
Model A320-200	3,098-10,058	26.7	4.3	1,158.7	251.3
Data A320-200	3,098-10,058	25.4	4.6	1,220.3	268.3
Offset	-	5.12%	6.52%	5.05%	6.3%

14.3 Descent fuel consumption

The last phase considered was the descent phase. As this also highly depends on ATC, a specific profile was chosen to be investigated. According to Filippone one of the possible descent trajectories is essentially gliding down from cruise altitude to the airport with the engines in idle [11]. As the fuel consumption in idle is negligible compared to the fuel consumption in the other phases, it was assumed that the engines were completely switched off. Meaning that a continuous descent is executed up to an altitude of 3,000 ft. From there on the engines are switched on and put in the approach mode as the final approach is usually conducted with the engines operating [11]. As the engines are switched off from cruise altitude to 3,000 ft no fuel is consumed. However the aircraft still covers quite come horizontal distance gliding down from cruise. This could be investigated using the glide tool explained in chapter 13.

As found in chapter 13, the EcoHopper can start its descent approximately 157 km before the airport if the aircraft glides down from cruise (9 km) to the beginning of the runway. However, the aircraft must now glide down to the LTO cycle, leading to a horizontal distance of 137 km. As no data on the L/D ratio for the B737-MAX 8 could be found, data for the A320-200 from [11] was used as a reference. It was found that a distance of approximately 180 km is acceptable.

14.4 Flight fuel consumption

Now that the fuel consumption during the different phases was computed, the total trip fuel could be found by summarising the results. The nominal LTO cycle fuel consumption from Table 15.5 was used as the fuel consumption during this phase. This finally resulted in Table 14.3, which is only valid for the climb and descent trajectories discussed previously. The cruise distance was computed using the horizontal distances covered during climb and descent. This resulted in a cruise distance of 1,041 km for the EcoHopper 450 and 1,032 km for the B737-MAX 8. Note that the descent does not contribute to the fuel consumption as it was assumed that a continuous descent was conducted from cruise until the LTO cycle. If ATC allows to conduct a continuous descent approach down to the runway, 84 kg extra fuel could be saved (see Table 15.3). From Table 14.3 it can be concluded that the EcoHopper 450 consumes more fuel during the mission, however it carries more than twice the amount of passengers of a B737-MAX 8. When taking this into account, the fuel efficiency per passenger for the flight considered here is a better metric to compare the aircraft. This lead to a fuel efficiency of 14.4 kg/pax for the EcoHopper 450 and 19.1 kg/pax for the B737-MAX 8, meaning that the fuel consumption per passenger is 24.6% less for the EcoHopper 450. This large reduction in fuel consumption is caused by the highly efficient engines, aerodynamic design and novel technologies such as electric taxiing.

Table 14.3: Resulting trip fuel consumption for the EcoHopper 450 and the B737-MAX 8.

Parameter	LTO cycle [kg]	Climb [kg]	Cruise [kg]	Total [kg]	Total [kg/pax]
EcoHopper 450	288.2	1,643.5	4,539.3	6,471.0	14.4
B737-MAX 8	365.9	1,213.6	2,230.5	3,810.0	19.1

[3] Aicraft data file: Airbus aircraft. Retrieved June, 25 2019, from https://booksite.elsevier.com/9780340741528/appendices/data-a/table-1/table.htm

15 Emission analysis

Aircraft emissions are the most well-known sustainability aspects of aviation. These emissions do not only contribute to the global warming, but they also affect the air quality at ground level. The different aircraft emissions and their impacts were thoroughly discussed in the Baseline and Midterm report [1, 8]. All in all it could be concluded that the emissions at ground level can cause health issues and reduce the air quality, while emissions at cruise altitude can contribute to the global warming problem. In order to assess how sustainable the EcoHopper 450 actually is, it was investigated how much the aircraft emits. This highly depends on the flight phase, therefore the investigation was divided into the landing and take-off cycle (LTO cycle) and cruise phase. These are discussed in section 15.1 and section 15.2 respectively. Finally, the impact of the emissions on the global warming was evaluated using the Radiative Forcing (RF), which is explained in section 15.3. First, the requirements related to the emissions of the aircraft were identified.

Requirements

- **BIB-SYS-TEC-02:** The cruise profile of the aircraft shall be optimised for climate optimised flights.
- **BIB-SYS-TEC-08:** The aircraft shall have 10% reduced fuel consumption per passenger with respect to current state of the art.
- **BIB-SBS-FLP-04:** The aircraft shall have a NO_x emission at least lower than current state of the art.
- **BIB-SBS-FLP-09:** The aircraft shall have a CO_2 emission at least lower than current state of the art.

15.1 LTO cycle emissions

According to TNO, the LTO cycle consists of all aircraft operations under the 3,000 ft (or 1,000 m) [53]. This includes taxiing out, take-off, initial climb out, approach, landing and taxiing in. Each of these modes have different aircraft settings which changes the amount of particles emitted. The emissions during such a mode depend on the number of engines, the time in mode, the fuel flow (thus thrust setting) and the emission factor. Their relation can be seen in Equation 15.1 [53]. E_{mode_i} indicates the amount of particles of emission i, in kg, emitted during the specified LTO mode. The number of engines and the time in each mode are represented by N_{eng} and t in seconds respectively. Then the fuel flow is indicated by $\dot{F}$, which depends on the thrust setting of the engines. Lastly, the emission factor of emission i, EF_i, indicates the mass emitted of i per kilogram of fuel burnt [53].

$$E_{mode_i} = N_{eng} * t * \dot{F} * EF_i \tag{15.1}$$

Data regarding the typical times in mode and the thrust settings was obtained from similar research projects, such as the research conducted by TNO [53] and the research conducted by ENEA C.R.E. Casaccia in Italy [54]. In addition, these are the thrust settings and times the International Civil Aviation Organisation (ICAO) uses to measure engine emissions [1]. Therefore it was decided to adopt these thrust settings and times as this made it possible to compare the the ICAO data and the model. This resulted in the times in mode and thrust settings shown in Table 15.1. It should be noted that the time in idle, or taxiing, highly depends on the airport size. It was assumed that the major hub average taxiing times were valid to use as the EcoHopper 450 operates from these major hubs. In order to obtain the fuel flow during each mode, the cycle calculation explained in chapter 7 was used. As the fuel flow during take-off was found to be 0.583 kg/s per engine, the fuel flow during the other modes could be found by multiplying it with the thrust setting, as it was found that it is a linear relations. The cycle calculation for the take-off condition was also performed for the reference aircraft, B737-MAX 8, to obtain the fuel flow. This resulted in a take-off fuel flow of 0.456 kg/s for one engine.

Table 15.1: Thrust setting and time in mode for the LTO cycle phases [53, 54].

Mode	Take-off	Climb out	Approach	Taxiing/idle	Idle/electric taxiing
Thrust setting	100%	85%	30%	7%	7%
Time in mode [min]	0.7	2.2	4.0	26.0	5.0

Finally, the emission factors had to be found. The emissions considered were H_2O, CO_2, SO_2, N_2O, NO_x, non methane volatile organic compounds (NMVOC), CO, and hydrocarbons HC. As aforementioned, the emission factor indicates the amount of emission emitted per kilogram of fuel burnt during the LTO cylce. As every research and government uses different emission factors for the LTO cycle, multiple sources were combine to end up at the emission factors shown in

[1] ICAO Aircraft Engine Emissions Databank. Retrieved June, 17 2019, from https://www.easa.europa.eu/easa-and-you/environment/icao-aircraft-engine-emissions-databank

Table 15.2: Emission factors for the LTO cycle [55][2] [3].

Emission	H_2O	CO_2	SO_2	N_2O	NO_x	NMVOC	CO	HC
EF [kg/kg]	1.237	3.15	1.0x10^{-3}	1.0x10^{-4}	$\frac{1}{10{,}000} 10^{1+0.0032(T_{in,cc}-581.25)} \sqrt{\frac{p}{p_0}}$ [55]	7.43x10^{-3}	6.39x10^{-3}	4.0x10^{-5}

Table 15.2[2] [3]. It should be noted that the emission factor of NO_x depends on altitude, via pressure, as well as the inlet temperature of the combustion ($T_{inlet,cc}$) chamber, which in turn varies with thrust (or thrust setting TS) [55][pg. 103]. In the case of the LTO emissions, the altitude was assumed to equal zero. The combustor inlet temperature was obtained from the engine cycle calculations performed in chapter 7 (985 K for take-off). The same calculation was performed for the engine of the B737-MAX 8 using data obtained from EASA [4]. This resulted in a combustor inlet temperature $T_{inlet,cc}$ of 1,055 K. How the emission factor of NO_x varies with $T_{inlet,cc}$ and altitude is shown in Figure 15.1 and Figure 15.2 respectively. To obtain the lowest emission factor for NO_x the aircraft must fly at a high altitude while maintaining a low inlet

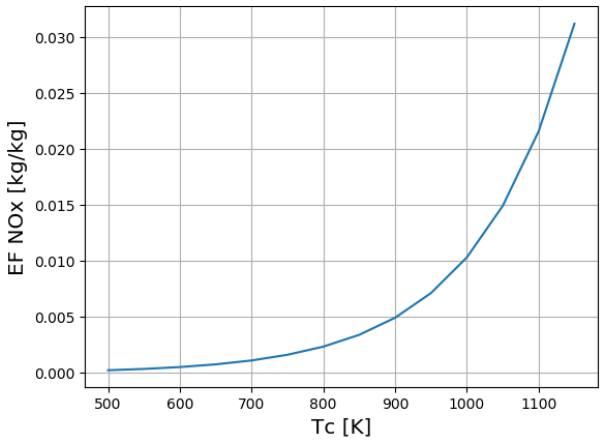

Figure 15.1: The emission factor for NO_x at constant altitude.

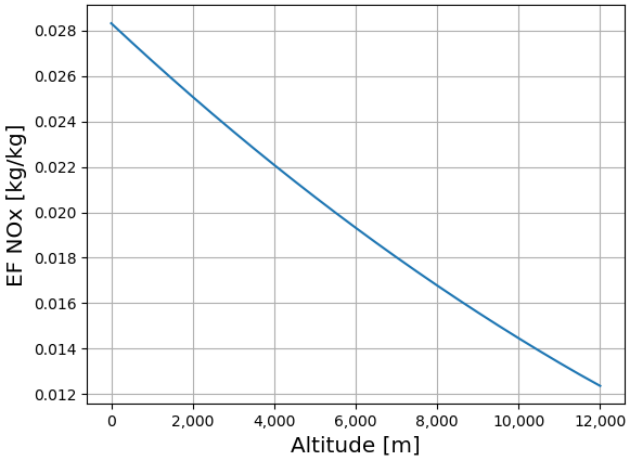

Figure 15.2: The emission factor for NO_x at constant combustor inlet temperature.

An additional source of emissions during the LTO cycle is the APU. As discussed in chapter 11, the EcoHopper 450 does not possess an APU. In order to assess how the absence of the APU reduces the emissions from the aircraft, the APU emissions were also modelled. The emissions could be found using Equation 15.2 [53]. The typical fuel flow and running time for the APU were found from an article presented at the 5th CEAS Air & Space Conference Challenges in European Aerospace[5]. It showed that the average fuel consumption for an APU is 2 kg of fuel per minute, while the average running time of the APU was estimated to be 30 minutes[4] [53]. The running time of the APU used to be around 45 minutes, however as more airports make use of ground based power this time is expected to decrease linearly until 2025 [53]. But not all gates at airports equipped with ground based power have access to this power grid, therefore the time was taken slightly higher than the International Civil Aviation Organisation (ICAO) estimated time for 2020 [53].

$$E_{APU_i} = \dot{F}_{APU} * t_{APU} * EF_i \tag{15.2}$$

Results

Combining the calculations explained above the emissions during the LTO cycle could be estimated. The results are shown for the EcoHopper 450 as well as for the B737-MAX 8, which still possess an APU, see Table 15.3 and Table 15.4. Note that both aircraft were assessed with and without an APU to investigate the effect of the APU emissions. It was found that the average reduction in the amount of particles emitted, excluding NO_x, is 13.3% when the aircraft is not equipped with an APU. The reduction in NO_x is only 2.1% as the APU does not emit much NO_x compared with the other LTO modes. By comparing the EcoHopper 450 without an APU, as designed, and the B737-MAX 8 with APU, as is the case in real life, it

[2]Emission Factors for Greenhouse Gas Inventories. Retrieved June, 17 2019, from https://www.epa.gov/sites/production/files/2018-03/documents/emission-factors_mar_2018_0.pdf

[3]Emission factors used in the estimations of emissions from combustion. Retrieved June, 17 2019, from https://www.ssb.no/_attachment/291696/binary/95503?_version=547186

[4]Type certificate data sheet LEAB-1B. Retrieved June, 20 2019, from https://www.easa.europa.eu/sites/default/files/dfu/EASA%20E115%20TCDS%20Issue%205%20LEAP-1B.pdf

[5]An optional APU for passenger aircraft. Retrieved June, 18 2019, from https://www.fzt.haw-hamburg.de/pers/Scholz/Airport2030/Airport2030_PUB_CEAS_15-09-07_Scholz.pdf

can be noted that the EcoHopper 450 produces overall more emissions as it also consumes more fuel. This was as expected since the aircraft is bigger and thus heavier. However, it can be noted that the NO_x for the EcoHopper 450 is less than for the B737-MAX 8. This was due to the engine design, as it has a low combustion chamber inlet temperature (see chapter 7).

However, as the real EcoHopper 450 is equipped with electric taxiing, the emissions can be further reduced as the time in idle/taxiing is less and the aircraft does not need an APU anymore. A time of 5 minutes was now used for the idle mode, this should give the pilots enough time to start up the engines, getting them to the desired temperature and extending all flaps and other devices. This resulted in a total fuel use of 288.22 kg which is a reduction of 21.2% with respect to the B737-MAX 8 (with APU). This in turn reduces the amount of emitted particles by 21.2% on average. The reduction in emissions and fuel are summarised in Table 15.5, the actual EcoHopper 450 with electric taxiing and thus no APU was compared to the actual B737-MAX 8, thus with APU. The NO_x is reduced by the most amount, this is mainly due to the combustor inlet temperature setting as explained before.

The emissions could be further reduced by a continuous descent approach, or gliding flight, this case was also analysed. The results are shown in Table 15.3. Note that the aircraft includes electric taxiing and does not posses and APU. This demonstrates the lowest possible emissions during the LTO cycle for the EcoHopper 450. As the continuous descent approach is highly dependent on Air Traffic Control (ATC) it is often not allowed. Therefore this was seen as a special case and not as the nominal operation of the aircraft. Thus these results are not shown in Table 15.5 which do represent the nominal operation. However, a continuous descent approach is a valid option to reduce the LTO emissions and fuel use even more, namely 29.1% reduction with respect to the nominal operations of the aircraft. This excludes the reduction in NO_x as this was only 13.5%. This anomaly stems from the fact that the thrust setting is low during approach and thus little NO_x is produced anyhow.

Table 15.3: Resulting emissions for the LTO cycle in kg of the EcoHopper 450.

Mode	Fuel	H_2O	CO_2	SO_2	N_2O	NO_x	NMVOC	CO	HC
Take-off [kg]	48.97	60.58	154.26	$4.89x10^{-2}$	$4.89x10^{-3}$	0.96	0.36	0.31	$1.96x10^{-3}$
Climb [kg]	130.81	161.83	412.10	0.13	$1.31x10^{-2}$	2.18	0.97	0.84	$5.23x10^{-3}$
Approach [kg]	83.95	103.85	264.45	$8.39x10^{-2}$	$8.39x10^{-3}$	0.49	0.62	0.54	$3.36x10^{-3}$
Idle/taxiing [kg]	127.32	157.50	401.08	0.13	$1.27x10^{-2}$	0.17	0.95	0.81	$5.09x10^{-3}$
Idle/ electric taxiing [kg]	24.49	30.29	77.13	$2.45x10^{-2}$	$2.45x10^{-3}$	$3.35x10^{-2}$	0.18	0.16	$9.79x10^{-4}$
APU [kg]	60.0	74.22	189.0	$6.0x10^{-2}$	$6.0x10^{-3}$	$8.23x10^{-2}$	0.45	0.28	$2.40x10^{-3}$
Total (with APU)	451.06	557.98	1,420.9	0.45	$4.51x10^{-2}$	3.89	3.35	2.88	$1.80x10^{-2}$
Total (no APU)	391.06	483.76	1,231.9	0.39	$3.91x10^{-2}$	3.81	2.91	2.49	$1.56x10^{-2}$
Total (electric taxiing + no APU)	288.22	356.55	907.94	0.29	$2.88x10^{-2}$	3.66	2.14	1.84	$1.15x10^{-2}$
Total (continuous descent)	204.27	252.69	643.49	0.20	$2.04x10^{-2}$	3.17	1.52	1.30	$8.17x10^{-3}$

Table 15.4: Resulting emissions for the LTO cycle in kg of the B737-MAX 8.

Mode	Fuel	H_2O	CO_2	SO_2	N_2O	NO_x	NMVOC	CO	HC
Take-off [kg]	38.30	47.38	120.66	$3.83x10^{-2}$	$3.83x10^{-3}$	1.26	0.28	0.24	$1.53x10^{-3}$
Climb [kg]	102.32	126.58	322.33	0.10	$1.02x10^{-2}$	2.85	0.76	0.65	$4.09x10^{-3}$
Approach [kg]	65.66	81.23	206.84	$6.57x10^{-2}$	$6.57x10^{-3}$	0.65	0.49	0.42	$2.63x10^{-3}$
Idle/taxiing [kg]	99.59	123.19	313.71	$9.96x10^{-2}$	$9.96x10^{-3}$	0.23	0.74	0.64	$3.98x10^{-6}$
APU [kg]	60.0	74.22	189.0	$6.0x10^{-2}$	$6.0x10^{-3}$	$8.23x10^{-2}$	0.45	0.28	$2.40x10^{-3}$
Total (no APU)	305.88	378.38	963.54	0.31	$3.05x10^{-2}$	4.98	2.27	1.95	$1.22x10^{-2}$
Total (with APU)	365.88	452.59	1,152.54	0.37	$3.65x10^{-2}$	5.07	2.72	2.34	$1.46x10^{-2}$

Table 15.5: Resulting emissions for the nominal LTO cylce.

Aircraft	Fuel	H_2O	CO_2	SO_2	N_2O	NO_x	NMVOC	CO	HC
EcoHopper 450 [kg]	288.22	356.55	907.94	0.29	$2.88x10^{-2}$	3.66	2.14	1.84	$1.15x10^{-2}$
B737-MAX 8 [kg]	365.88	452.59	1,152.54	0.37	$3.65x10^{-2}$	5.07	2.72	2.34	$1.46x10^{-2}$
Reduction	21.2%	21.2%	21.2%	21.2%	21.2%	27.7%	21.2%	21.2%	21.2%

Verification & validation

In order to verify the tool, some emissions were evaluated by hand using the data and equations explained before. In addition the order of magnitude was compared to the results following from the researches aforementioned [53, 54]. By comparing the results, the used emission factors could also be verified. This was done by finding the ratios between the emissions for the different substances for the model, and compare them to the ratios found by the TNO and ENEA C.R.E. Casaccia researches. Some slight inconsistencies were discovered, e.g. for the NO_x emissions it was found that the model

slightly overestimates the NO_x emissions compared to the papers. This was found to originate from the fact that TNO and ENEA C.R.E. Casaccia used either a constant emission factor or a different model to estimate EF_{NO_x}. The ratios were checked using the ICAO Emissions database of EASA [1], which showed similar ratios for some the emissions in the different LTO modes.

To investigate the predictive power of the model, results for the B737-MAX 8 were compared to the values provided by the aircraft emissions database of ICAO for the LEAP-B1 engine [1] (the engine mounted on most conventional B737-MAX 8 aircraft). The data could be compared as the same times in mode and thrust settings were used as explained earlier. However, only values for the amount of emitted NO_x, CO, and HC were provided. The other emissions were validated using the ratios between the used fuel and the content of the substance in the fuel or product [1]. This resulted in the offsets shown in Table 15.6. It can be noted that the model to predict the fuel consumption, i.e. the engine cycle calculation, is fairly accurate as the offset is only 1.67%. However, the offset for the hydrocarbon emission is significant, namely 83.41%. This can be explained by the fact that the numbers are small, such that a small difference already leads to a large offset. But also because the emission factor used for HC could not be fully verified as there is a lot of uncertainty as it depends on the combustion process in the engine [55]. It is related to the incomplete combustion of Jet-A fuel, which is hard to model. As the used emission factor consideres a complete combustion, the content of HC is low. However this is often not the case in real life as can be seen from the measured data of ICAO. Nevertheless, the model was said to be validated as the HC emissions are only a couple of grams while the other emissions are in the order of magnitude of hundreds of kilograms.

Table 15.6: Validation data for the B737-MAX 8 aircraft for the LTO emissions [2].

Source	Fuel flow	NO_x	CO	HC
Model [kg]	365.89	5.07	2.34	0.0146
ICAO measurements [kg]	359.3	6.07	2.24	0.088
Offset	1.83%	16.47%	4.46%	83.41%

15.2 Cruise emissions

Next to the ground level emissions, the aircraft also emits particles during cruise. The same type of calculation could be performed for the cruise emissions as for the LTO emissions. However, the cruise time may vary from mission to mission. Therefore it was chosen to express the amount of emissions emitted in kg/km. However, it was also interesting to look at how many particles the EcoHopper 450 and the B737-MAX 8 emit when they are flying the same cruise range, e.g. 1,000 km (to take into account climb and descent with respect to the design range of 1,400 km). Therefore, the kg/km value was simply multiplied by 1,000 km to find the total emitted particle mass.

The amount of emitted particles was found by multiplying the cruise fuel consumption, found in chapter 13, with the emission factor and the number of passengers to end up at the kg/km value. The emission factors for cruise differed from the values found for the LTO cycle. This is due to the engine operation at a higher altitude and the changing ambient conditions. The cruise emission factors were obtained from the RIVM (Rijksinstituut voor Volksgezondheid en Milieu) [56], ENEA C.R.E. Casaccia [54] and Rypdal [57]. No exact values for the emission factors of N_2O and H_2O during cruise were available, therefore these values were assumed to equal the LTO emission factors. The other factors do not differ significantly as can be seen. Again the emission factor of NO_x varies with altitude as well as combustor inlet temperature, see Figure 15.1 and Figure 15.2, but now also with the thrust setting TS. The thrust setting for the EcoHopper 450 was found to be 70%, see chapter 7, while the thrust setting for the B737-MAX 8 was found to be 73%. The same procedure was applied to the B737-MAX 8 and EcoHopper 450 to find the thrust setting as the static total thrust of the engines at sea level was known. The thrust setting could then be found from the required thrust at the cruise altitude.

Table 15.7: Emission factors for cruise[56].

Emission	H_2O	CO_2	SO_2	N_2O	NO_x	NMVOC	CO	HC
EF [kg/kg]	1.237	3.15	$1.0x10^{-3}$	$1.0x10^{-4}$	$\frac{TS}{10{,}000} 10^{1+0.0032(T_{in,cc}-581.25)} \sqrt{\frac{p}{p_0}}$ [55]	$7.0x10^{-3}$	$5.0x10^{-3}$	$4.0x10^{-5}$

Results

Computing the emissions using the emission factors for cruise resulted in the values presented in Table 15.8. The fuel consumption used for the EcoHopper 450 was 0.00969 kg/km-pax and for the B737-MAX 8 0.0108 kg/km-pax as explained in chapter 14. As can be seen, the kg/km emissions for the EcoHopper 450 are higher compared to the B737-MAX 8, this is due to the higher overall fuel flow. Then comparing the emissions for a cruise distance of 1,000 km, expressed in kg/pax, it can be seen that the mass of the emitted particles is significantly lower for the EcoHopper 450. This is due to the reduced fuel consumption per passenger, or lower fuel consumption over payload weight ratio. This means that the aircraft is more fuel efficient when carrying the same amount as passengers as the B737-MAX 8. All emissions are reduced by

10.3% as they are linearly scaled with the fuel consumption which is also 10.3% lower. However, the reduction for NO_x is significant. The large reduction is due to the cruise altitude at which the EcoHopper 450 is flying and due to the low inlet temperature for the combustion chamber. The trends shown in Figure 15.1 and Figure 15.2 are reflected by the NO_x emission values. It can thus be concluded that the EcoHopper 450 is a more sustainable aircraft as it is more efficient in carrying passengers.

Table 15.8: Resulting emissions for cruise of the EcoHopper 450 and the B737-MAX 8.

Aircraft	H_2O	CO_2	SO_2	N_2O	NO_x	NMVOC	CO	HC
EcoHopper 450[kg/km]	5.39	13.73	$4.36x10^{-3}$	$4.36x10^{-4}$	$3.29x10^{-2}$	$3.05x10^{-3}$	$2.18x10^{-2}$	$1.74x10^{-4}$
Cruise of 1,000 km [kg/pax]	11.98	30.52	$9.69x10^{-3}$	$9.69x10^{-4}$	$7.32x10^{-2}$	$6.78x10^{-3}$	$4.84x10^{-2}$	$3.88x10^{-4}$
B737-MAX 8 [kg/km]	2.67	6.80	$2.16x10^{-3}$	$2.16x10^{-4}$	$2.34x10^{-2}$	$1.51x10^{-3}$	$1.08x10^{-2}$	$8.64x10^{-5}$
Cruise of 1,000 km [kg/pax]	13.36	34.02	$1.08x10^{-2}$	$1.08x10^{-3}$	0.12	$7.56x10^{-3}$	$5.40x10^{-2}$	$4.32x10^{-4}$
Reduction	10.3%	10.3%	10.3%	10.3%	37.5%	10.3%	10.3%	10.3%

Verification & validation

The method of calculation was already verified and validated in section 15.1. Only the emission factors differed in this case. The emission factors for cruise were found from three literature sources mentioned before [54, 56, 57]. Each of these papers provided emission factors which differed by a small amount. As the three papers overall agreed on the same emission factors, these were deemed valid. Unfortunately, validation data for the cruise emissions is unavailable as cruise emissions are not needed for certification. The ICAO only certifies for LTO emissions, therefore no data was tabulated in the database about the cruise emissions. However, as the calculation method was validated as well as the emissions factors the results were deemed sufficiently valid for the current design phase.

15.3 Radiative forcing

The impact of the different emissions discussed before can be measured using the Radiative forcing (RF). As emissions have a complex effect on the climate, the RF is used to give an indication of this effect. Furthermore, RF enables to compare the impact of the different emissions. RF is a measure for the change in energy the Earth receives from the Sun, and the energy that the Earth radiates back into space [8]. The RF is thus expressed in Watts per square meter (W/m^2). The RF not only considers the emissions discussed before, but also takes into account the phenomena which occur high in the atmosphere due to these emissions. The phenomena are contrails and cirrus clouds, the latter can occur due to the spreading of the contrails as well as due to the accumulation of particles emitted by the aircraft that may act as cloud condensation nuclei [58]. Moreover, as the emissions are emitted at higher altitudes, typically between 8-12 km, the emissions have an increased impact on the climate. This is due to their elevated effectiveness to participate in chemical reactions, e.g. cloud and ozone (O_3) formation [58]. To investigate the impact of aircraft cruise emissions, only the main contributors were analysed. These are listed below, as well as some additional notes on their effect [58]:

1. CO_2 (positive RF)
2. NO_x (positive RF), it affects the atmosphere in three ways;
   (a) It produces ozone (positive RF)
   (b) It reduces CH_4 on the long term (negative RF)
   (c) On an even longer term it reduces ozone by a small amount (negative RF)
3. H_2O (positive RF)
4. Contrails (positive RF)
5. Cirrus clouds (potentially positive RF)
6. SO_4 (negative RF), which originates from a chemical reaction of SO_2
7. Soot particles (positive RF)

It should be noted that the values for the RF of contrails and cirrus clouds are highly uncertain. The effect of the latter phenomenon is uncertain to the extent that it is not fully known whether it produces a positive or negative RF. Nowadays, the RF of cirrus clouds is mostly estimated to be positive [58]. The uncertainty arises from the lack of understanding processes in the higher atmosphere, and from the lack of data about the extent to which these un-natural cloud like structures are formed [58]. Nevertheless, since these phenomena have a significant effect on the climate and lots of time has gone into predicting these RF values, they were still included in the evaluation of the RF of the aircraft. The values for the RF were obtained from a research conducted by Lee et al. [58] into how aviation will contribute to the global climate change in upcoming century. In order to obtain the values, Lee consulted the Intergovernmental Panel on Climate Change (IPCC) database while making predictions using models for the RF values up to 2020. These values are presented in Table 15.9, they are the best estimate values for a confidence interval of 90%.

Sensitivity analysis

It should be noted that the RF values for NO_x and contrails vary with altitude. The first was found to vary with altitude steps according to a research conducted by the Imperial College London [59]. For certain altitudes, the base value of the NO_x RF shown in the table had to be multiplied with certain weighing functions to reflect the increased effect of the emitted particles. The general trend displayed that the effect of NO_x increases significantly with altitude. The latter, contrails, also exhibit a relation with the altitude, as found by Fitcher et al. [60]. They varied the cruise altitudes of aircraft and concluded that the effect of contrails reduce linearly with respect to a decreasing altitude; starting at 36,000 ft and reducing the altitude with 6,000 ft leads to a reduction of 45% in the RF caused by contrails [1, 59]. However, it must be noted that the effects of contrails also heavily depend on the latitude of the flight trajectory and the time of the year. Assuming the aircraft flies at all latitudes, the average value for the RF should be considered. The (base) value shown in Table 15.9 represents the average RF for contrails, this value was then varied according to the trend found by Fitcher et al.

Table 15.9: Radiative forcing (RF) values for the main cruise emissions [58].

Parameter	CO_2	NO_x	H_2O	Contrails	Cirrus clouds	SO_4	Soot
RF [W/m^2]	28.0	12.6	2.8	11.8	21.2	-4.8	3.4

Results

These values and varying RF relations led to the plot in which the relation between the total RF of aircraft and altitude could be observed. This diagram is shown in Figure 15.3. As can be seen, the EcoHopper 450 and reference aircraft, B737-MAX 8, are also shown in the plot. Since the cruise altitude of the EcoHopper 450 is 2 km lower than the B737-MAX 8, the RF lowered due to the varying RF of contrails and NO_x. The RF value for the EcoHopper 450 equals 69.2 W/m^2 while the RF for the B737-MAX 8 equals 87.7 W/m^2. Thus, this means that the impact of the EcoHopper 450's emissions are lowered by 21.1% due to the lower cruise altitude. Taking into account the fuel reduction discussed in chapter 13 and subsequently the reduction of emissions discussed earlier, it could be said that the EcoHopper 450 performs significantly better than the current state of the art aircraft from a sustainability point of view.

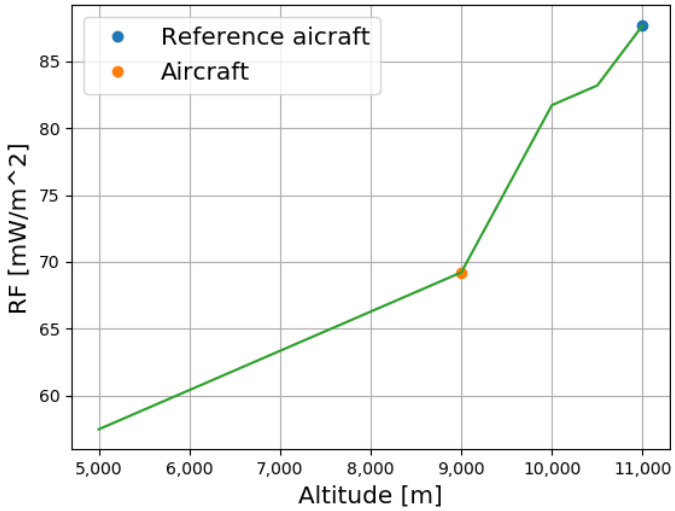

Figure 15.3: Radiative forcing (RF) with respect to altitude including the EcoHopper 450 and B737-MAX 8.

16 Noise analsyis

When thinking about sustainability, one is tempted to think about emissions. However, aircraft noise is one of the main topics in the discussion about aviation sustainability nowadays. Milions of people worldwide who live close to airports are affected by noise. A long term exposure to noise has a negative effect on the health of human beings. Exposure to noise is namely associated with multiple health issues such as sleep disturbance, annoyance, nervousness and increased blood pressure [8, 61]. However, as the cities and airports are growing bigger and bigger over the upcoming years, more people will be living close to airports. In order to reduce the impact on the society, it is important to reduce aircraft noise as much as possible. The EcoHopper 450 should be even better than current state of the art aircraft like the Boeing 737-MAX 8 and A320NEO. It was chosen to use the first aircraft as reference aircraft as more data was available for the B737-MAX 8 and the cumulative noise levels for both aircraft are similar. The noise is namely centred around 160 dB for both aircraft [1]. Therefore it was safe to say that comparing the EcoHopper 450 to the B737-MAX 8 would yield sufficient results. It was found that there are two sources of aircraft noise: the airframe and the propulsion system [13]. These noise sources are discussed in section 16.2 and section 16.3 respectively. The combined noise output is shown in section 16.4. But first the overall methodology is discussed in section 16.1.

Requirements

- **BIB-SYS-TEC-09:** The noise produced by the aircraft shall be at least one noise class better than current state of the art aircraft.
- **BIB-SBS-FLP-03:** The accumulated noise generated by the aircraft shall be below 282 dB at the ICAO measurement points.

16.1 Methodology

The noise metric used to model the aircraft noise was the Sound Pressure Level (SPL). The sound pressure level depends on the effective sound pressure of a spherical sound wave due to a point source. Their relation is shown in Equation 16.1, where p_e and p_{e0} represent the effective sound pressure and the reference sound pressure ($2x10^{-5}$ Pa) respectively [12]. The models for both sources express the noise in SPL (dB).

$$SPL = 10^{10} log(\frac{p_e^2}{p_{e0}^2}) \tag{16.1}$$

However, these modelled SPLs assume a homogeneous atmosphere and an observer who is free of any obstacles. In reality this is not the case as the atmosphere absorbs some of the noise and the ground on which the observer is standing generates the ground effect noise [12]. Ground effect means that the noise of some of the frequencies are amplified by reflecting their sound waves back from the ground to the observer. This ground effect can be modelled as shown in Equation 16.2, where the ratio r_1/r_2 indicates the length of the sound wave to the observer over the length of the wave to the ground [12]. In most cases, it could be assumed that this ratio equals one. Next, the factor Q indicates the reflectivity of the ground, as it was assumed that the observer is standing on a hard surface this value was found to equal one as well [12]. Lastly, the observer, or microphone, is placed at a certain height h_m and the emission angle of the noise θ indicates the angle between the observer and the aircraft's direction.

$$\Delta SPL_g = 10^{10} log[1 + (\frac{r_1}{r_2})^2 Q^2 + 2\frac{r_1}{r_2} Q cos(\frac{4\pi f}{a} h_m sin\theta)] \tag{16.2}$$

Finally, the noise absorption of the atmosphere could be modelled as $-\alpha_{aa} r$. Where α_{aa} indicates the the atmospheric absorption in dB/m which is depending on the temperature and relative humidity, and r is the distance the sound has to travel from the source to the observer [12]. The temperature was assumed to be 20 °C with a relative humidity of 50%. Then the value for α_{aa} could be obtained from Simons [12][pg. 40] for different frequencies. Using a regression line through these data points, the value for α_{aa} could be obtained for every frequency. The final corrected SPL could then be found according to Equation 16.3 [12].

$$SPL_{cor} = SPL_{model} + \Delta SPL_g - \alpha_{aa} r \tag{16.3}$$

[1] EASA Certification noise levels. Retrieved Jul1, 1 2019, from https://www.easa.europa.eu/easa-and-you/environment/easa-certification-noise-levels

16.2 Airframe noise

The general public might think that the main source for aircraft noise are the engines, however this is far from realistic. The airframe itself contributes significantly to the total noise output. The noise originates from a turbulent airflow over the outer surface of the aircraft [12]. Especially geometries which disturb the airflow, like flaps and the landing gear, produce a significant amount of noise. Noise in general consists of broadband and tonal noise, where broadband noise has a continuous spectrum, i.e. it has energy over a wide range of frequencies [13]. While tonal noise has a discontinuous spectrum, i.e. there are certain frequencies where the energy is concentrated. Airframe noise mostly consists of broadband noise, therefore the model used here only assessed this spectrum for the airframe noise [13]. The broadband noise behaves like V^5 or V^6 depending on the so-called compactness of the source. For example, the gear can be considered compact as it is a point source such that the noise behaves like V^6. While the flaps are not compact and thus the noise behaves like V^5 [12].

The model chosen to compute the airframe noise is NASA's Aircraft Noise Prediction Program (ANOPP). It is a semi-empirical method based on databases containing measured acoustic data [12]. Only the components which contribute the most to the airframe noise were modelled [12][pg. 189]:

- The clean wing due to the convection of the turbulent boundary layer past the trailing edge.
- The horizontal tail according to the same principle as the wing.
- The leading edge slats due to the increment of the wing noise and due to the noise generation of the slat itself.
- The trailing edge flaps due to lift fluctuations produced by turbulent flow on the flap.
- The landing gear, i.e. the nose and main gear, due to vortex generation around the gear and the subsequent force exerted on the gear.

Each noise component could be modelled as Equation 16.4 [12][pg. 187]. Which could be transformed into the SPL by Equation 16.1. The definitions of the angles θ and ϕ can be seen in Figure 16.1. $D(\theta, \phi)$ represents the directivity function while P is the power function in Watts. The function $F(S)$ is the empirical spectral function which is dependent on the Strouhal number S [12]. These functions will be discussed below. The factors in the denominator, $1/4\pi r^2$ and $1/(1 - Mcos\theta)^4$, represent the spherical spreading factor and the Doppler effect respectively [12]. The Doppler effect is caused by the forward motion of the aircraft while the noise is being emitted [13].

$$p_e^2(f, \theta, \phi) = \frac{\rho_\infty c P D(\theta, \phi) D F(S)}{4\pi r^2 (1 - Mcos\theta)^4} \tag{16.4}$$

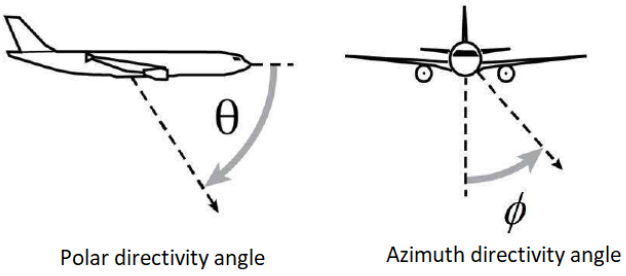

Figure 16.1: Definition of the polar and azimuth angle [12].

The power function can be described by Equation 16.5, where k and a are dimensionless constants based on empirical data, and G is geometry function. The values for the constants and equation for the geometry function for every component are given in Table 16.1. Next, the Strouhal number can be computed by Equation 16.6, where L is the length scale characteristic of the component under consideration. The equations for L can be found in Table 16.1 as well. The variable n in the equations for the landing gear represent the number of wheels in either the nose or main gear. Finally, the empirical spectral functions, for which the strouhal number is the input, and the directivity functions for each component are shown in Table 16.2.

$$P = kM^a G(\rho_\infty c^3 b_w^3) \tag{16.5}$$

$$S = \frac{fL(1 - Mcos\theta)}{Mc} \tag{16.6}$$

Table 16.1: The geometry function, length scale and empirical constants for the airframe noise sources [12][pg. 189]

Source	G [-]	L [m]	K	a
Clean wing	$0.37\frac{S_w}{b_w^2}(\frac{\rho_\infty McS_w}{\mu_\infty b_w})^{-0.2}$	Gb_w	$4.464\text{x}10^{-5}$	5
Horizontal tail	$0.37\frac{S_h}{b_h^2}(\frac{\rho_\infty McS_h}{\mu_\infty b_h})^{-0.2}$	Gb_h	$4.464\text{x}10^{-5}$	5
Slats	$0.37\frac{S_w}{b_w^2}(\frac{\rho_\infty McS_w}{\mu_\infty b_w})^{-0.2}$	Gb_w	$4.464\text{x}10^{-5}$	5
Flaps	$\frac{A_f}{b_w^2}sin^2\theta_f$	$\frac{A_f}{b_f}$	$2.787\text{x}10^{-4}$	6
Landing gear	$n(\frac{d_{wheel}}{b_w})^2$	d_{wheel}	$4.349\text{x}10^{-4}$ for 1-2 wheels $3.414\text{x}10^{-4}$ for 4 wheels	6

Table 16.2: The empirical spectral and directivity functions for each noise source [12][pg. 190-191]

Source	F(S)	D(θ, ϕ)
Clean wing	$0.613(10S)^4[(10S)^{1.5}+0.5]^{-4}$	$4cos^2\phi cos^2(\theta/2)$
Horizontal tail	$0.613(10S)^4[(10S)^{1.5}+0.5]^{-4}$	$4cos^2\phi cos^2(\theta/2)$
Slats	$0.613(10S)^4[(10S)^{1.5}+0.5]^{-4}$ $+ 0.613(2.19S)^4[(2.19S)^{1.5}+0.5]^{-4}$	$4cos^2\phi cos^2(\theta/2)$
Flaps	$0.0480S$ for S<2 $0.1406S^{-0.55}$ for 2 ≤ S ≤ 20 $216.49S^{-3}$ for S > 20	$3(sin\delta_f cos\theta + cos\delta_f sin\theta cos\phi)^2$
Gear n = 2	$13.59S^2(S^2+12.5)^{-2.25}$	$\frac{3}{2}sin^2\theta$
Gear n = 4	$0.0577S^2(0.25S^2+1)^{-1.5}$	$\frac{3}{2}sin^2\theta$

Results

Once the model was set out, plots could be made for the noise generated by each component by varying the frequency. Based on the ICAO noise measurement points, the angles θ and ϕ could be determined. For example, for an overhead noise measurement θ is 90 degrees while ϕ equals 0 degrees. Noise plots were made for the three measurement points set out by ICAO [2]:

1. Approach: 6.5 km before the runway threshold, 120 m under the flight path (overhead).
2. Sideline: the highest noise measurement recorded at any point 450 m from the runway axis during take-off.
3. Fly-over: 6.5 km from the brake release point, 1,000 ft (300 m) under the take-off flight path (overhead).

The plots are shown in Figure 16.2, Figure 16.3 and Figure 16.4 for the measurement points respectively. As can be seen, the airframe noise during approach is the highest. This was expected as the aircraft is in landing configuration which means that the gear is extended and full flaps are employed. Whereas the sideline and fly-over measurements indicate the lowest airframe noise. This follows from the fact that the distance to the sideline measurement point is the largest and the velocity is low. For the fly-over, most high lift devices are retracted, creating less noise. However the velocity is much higher meaning that it creates a similar amount of noise as at the sideline measurement point. In Figure 16.5, the noise plot for the approach measurement point including the ground effect and atmospheric absorption is shown. It can be noted that mostly the highest frequencies are affected by these effects. This was expected as mostly the higher frequencies are reflected by the ground due to their short wavelength, and the higher frequencies are absorbed more by the atmosphere than the lower frequencies [12]. The latter was based on the value for α_{aa} for the higher frequencies. However, the average overall noise level is not affected significantly, therefore it was chosen to work with the pure model only as it provides sufficient precision and yields more distinct results.

Verification

In order to verify the tool, the effective sound pressure for some frequencies and noise sources were computed by hand. This ensured that no implementation errors were present in the code. In addition, Simons provided graphs with model results as well as noise measurements for the Fokker 70, and the required inputs for the model [12]. This way the Fokker 70 could be modelled using the developed tool in order to assess the implementation of the equations. It was found that the tool outputted the exact same graph as the one provided, meaning that the tool was verified. In addition, the model outputs could be compared to the given noise measurements. It could be noted that the model closely represents reality, especially when turning on the correction factors for the ground effect and the atmospheric absorption.

[2]Aircraft noise technology and international noise standards. Retrieved June, 13 2019, from https://www.icao.int/Meetings/EnvironmentalWorkshops/Documents/2015-Warsaw/3_2_Aircraft-Noise-Technology-and-International-Noise-Standards.pdf

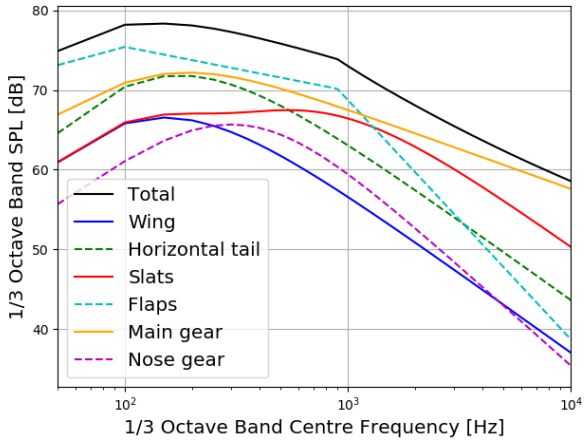

Figure 16.2: Airframe noise at the approach measurement point for the EcoHopper 450.

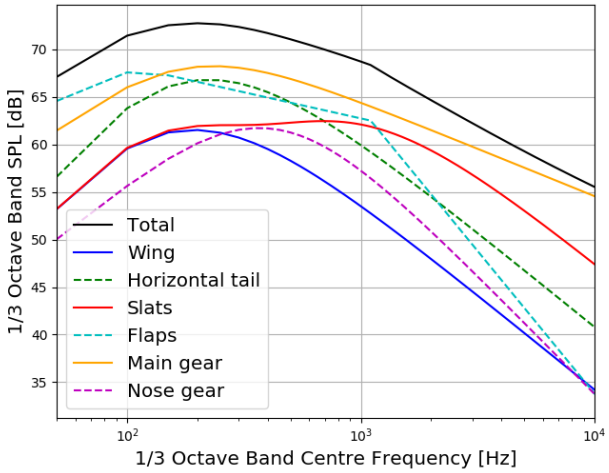

Figure 16.3: Airframe noise at the sideline measurement point for the EcoHopper 450.

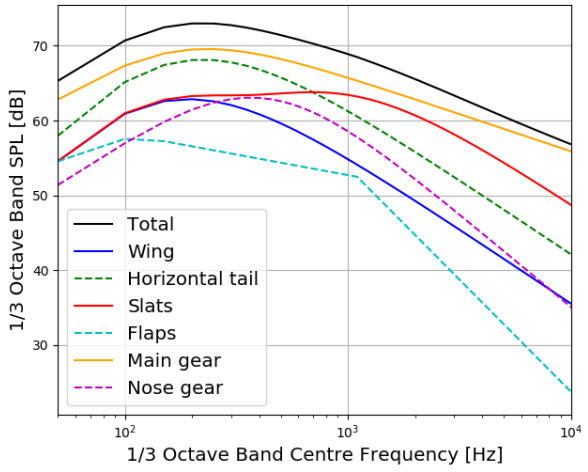

Figure 16.4: Airframe noise at the fly-over measurement point for the EcoHopper 450.

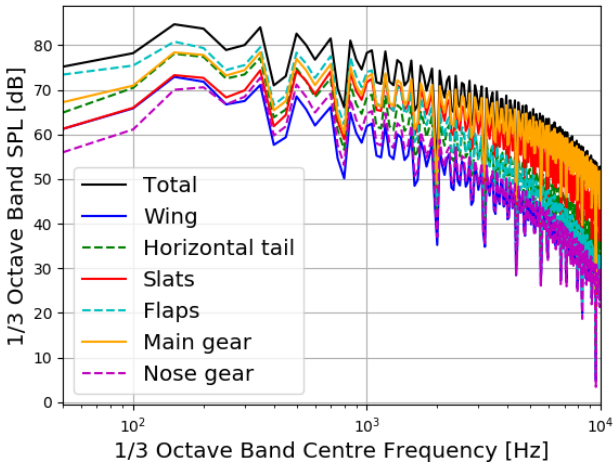

Figure 16.5: Airframe noise at the approach measurement point including atmospheric absorption and ground effect.

16.3 Propulsive noise

Next to the airframe, the most well known noise source is the engines. The noise generated by the engines originates from multiple components; the fan, compressor, combustor, turbine and exhaust jet. However, the fan and the jet exhaust dominate the noise spectrum of a turbofan engine in both tonal as well as broadband noise [13]. This is because the noise from the other sources is shielded by the engine cowling as well as by the noise of the fan and jet (some frequencies cancel out). Fan noise originates from turbulent flow passing through the blades [11]. The noise can radiate forward through the air as well as aft through the fan discharge duct [13]. Jet noise originates from the turbulent mixing of hot gas with ambient air outside the aircraft. However, as more air passes through the fan (higher bypass ratio), less air with a lower velocity will end up in the jet. This results in a fan with an increased noise output while the jet has a decreased noise output [13]. From Ruijgrok it was found that the jet noise is completely overruled by the fan noise once the bypass ratio passes four [13]. It should be noted that the noise of the different components expressed in dB cannot be simply summed due to the logarithmic scale, therefore it is safe to say that the fan noise overrules the jet noise. The relationship between the bypass ratio and noise can be seen in Figure 16.6 and is expected to exhibit the same trend past the bypass ratio of eight [13]. Therefore, it was deemed acceptable to only compute the fan noise to model the propulsive noise as the bypass ratio of the EcoHopper 450's engines is 15.

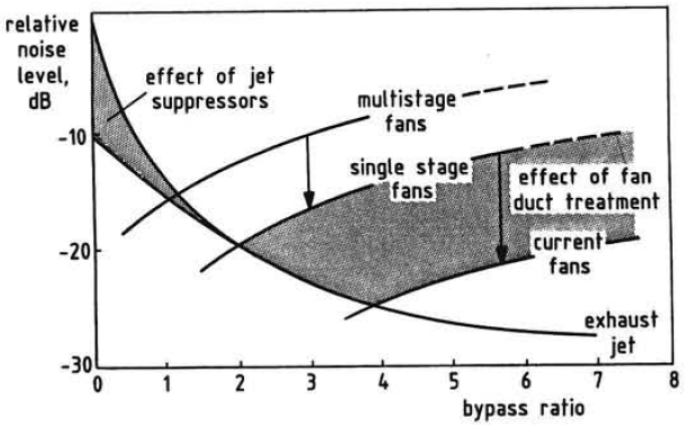

Figure 16.6: The effect of bypass ratio on the relative jet and fan noise [13][pg. 271].

To model the fan noise, it was chosen to use NASA's ANOPP method as well [11]. In this model, the SPL was directly computed as opposed to the airframe noise model in which the effective sound pressure was first computed. The relation for the SPL for the fan is shown in Equation 16.7 [11]. The first term on the right hand side represents the noise generated by the mass flow that passes through the engine. It is scaled by the reference mass flow rate $\dot{m}_0$ of 1 lbs/s or 0.453 kg/s [62]. The second term represents the noise generated by the temperature difference across the fan, indicated by ΔT, scaled by the reference temperature, ΔT_0, of 1 Rankine or 0.555 Kelvin [62]. These parameters were obtained from the cycle calculation performed on the engine, which is described in chapter 7. The latter parameters are constants depending on the engine functionality. These are described below:

- F_1 is a function of the Mach number of the fan blade tips (M_{TR}).
- F_2 is a function of the ratio of the stator spacing over the fan blade chord (RSS).
- F_3 is a function of the emission angle (θ).
- F_4 is a function of the ratio of the frequency analysed over the blade passing frequency (f_b).

$$SPL(f) = 10^{10} log(\frac{\dot{m}}{\dot{m}_0}) + 20^{10} log(\frac{\Delta T}{\Delta T_0}) + F_1(M_{TR}) + F_2(RSS) + F_3(\theta) + F_4(f/f_b) \tag{16.7}$$

The aforementioned constants had different values for the different noise spectra and noise propagation paths. The different situations considered were the inlet broadband noise, inlet tonal noise, aft broadband noise, aft tonal noise and combination tones. The combination tones spectra peak at 1/2, 1/4, and 1/8 of the blade passing frequency, each peak having its own values for the constants. The values for the constants for all situations discussed were obtained from NASA [62][pg. 9]. Some assumptions had to be made in order to be able to evaluate the constants. To be able to compute F_1, the angular velocity, or RPM, of the fan had to be estimated. This could then be converted to the velocity of the tips, and thus Mach number, using the diameter of the fan obtained in chapter 7. The maximum RPM for the geared fan was estimated to be 2,000, as it was found that regular high bypass turbofan engines spin at a nominal rate of 2,500 RPM [63]. In addition, to take into account the gearbox, which has a 3:1 ratio for geared turbofans nowadays [3], it was deemed feasible that the maximum RPM, which produces the highest noise, is 2,000.

Next, to be able to compute F_2 the ratio of the stator spacing over the fan blade chord was estimated to be larger than 100, based on the number of blades and fan diameter found in chapter 7. The emission angle for F_3 depends on the measurement point as explained in section 16.2. Finally, to determine F_4 the blade passing frequency f_b had to be determined. This could be found using $f_b = NB$ [11], where N is the angular velocity of the fan and B is the number of fan blades. As the SPL given by Equation 16.1 is only valid for an observer 1 m away from the source (r_1), the actual distance of the observer (r_2) was accounted for using Equation 16.8.

$$SPL_2 = SPL_1 + 20^{10} log(\frac{r_1}{r_2}) \tag{16.8}$$

Results

This finally resulted in the fan noise plots shown in Figure 16.7, Figure 16.8 and Figure 16.9 for the measurement points explained in section 16.2 respectively. The difference arises from the thrust setting of the engine, thus mass flow rate and

[3]GTF Engine family. Retrieved June, 14 2019, from https://www.mtu.de/engines/commercial-aircraft-engines/narrowbody-and-regional-jets/gtf-engine-family/

temperature rise, during the different phases. The thrust settings were derived for the different flight phases discussed in chapter 15. As expected, the engine produces the highest noise during the sideline measurement as the thrust setting is the highest. The fan noise during approach is significantly lower as can be seen from Figure 16.7, as the thrust setting is much lower which reduces the mass flow rate. The same goes for the fly-over point, which has a similar noise output as the approach point. This is because the thrust setting is lower than during the sideline measurement and the distance is large.
However, it should be noted that some question marks were placed on the accuracy of the model for frequencies lower than 1 kHz since the model has a cut-off. This is due to the uncertainty of the empirical data at lower frequencies [11]. Therefore, in order to compute the cumulative noise, the fan noise below 1 kHz was assumed to be equal to the airframe noise instead of the modelled noise. When looking at the noise spectrum starting at 1 kHz, it can be seen that the high frequency noise has a higher SPL than the lower frequency noise. This is because of the fast spinning fan blade tips which create high frequency noise [12]. Again, a corrected noise plot is shown in Figure 16.10 this time for the fly-over measurement point. Also for the fan noise, mostly the higher frequencies are affected, in the sense that the dB level is higher than for the pure model due to the ground effect.

Verification

In order to verify the tool, hand calculations were performed for selected frequencies, ranging from the low frequencies to the high frequencies. In addition, the code was unit tested by checking intermediate outputs for their sign and magnitude. After determining that the equations and constants were implemented correctly, the shape of the graphs was verified. This was done by looking at similar research projects which modelled the engine noise and compared it to noise measurements, for example an investigation performed by Filipone for the University of Manchester [64]. Hard numbers could not be verified as the access to databases for engine noise is highly restricted and engine manufacturers do not provide noise performance data.

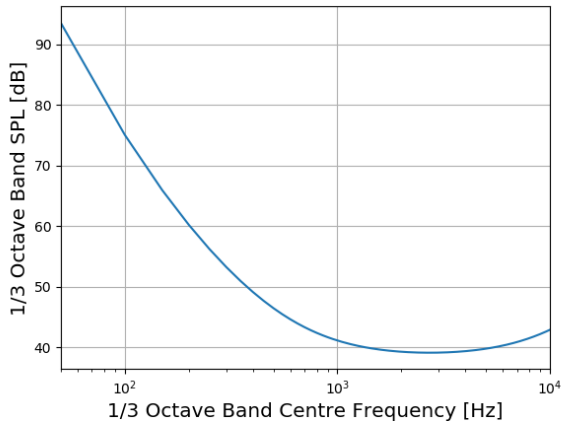

Figure 16.7: Fan noise at the approach measurement point for the EcoHopper 450.

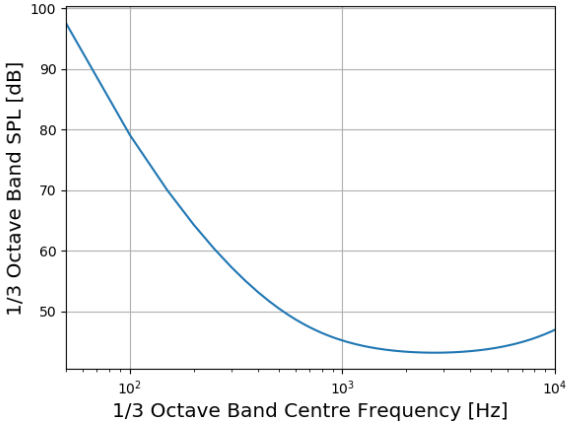

Figure 16.8: Fan noise at the sideline measurement point for the EcoHopper 450.

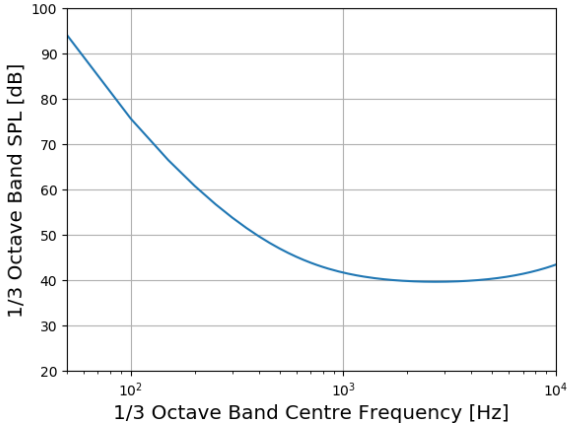

Figure 16.9: Fan noise at the fly-over measurement point for the EcoHopper 450.

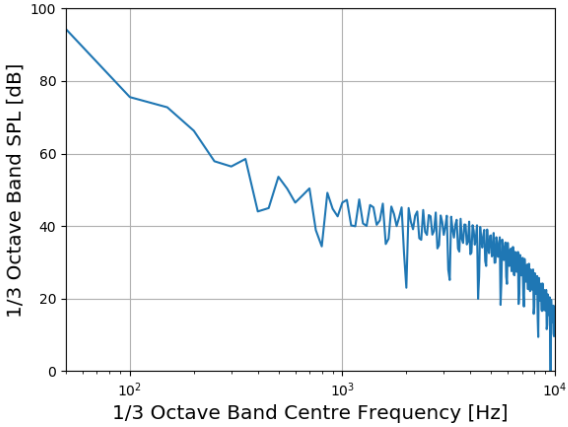

Figure 16.10: Fan noise at the fly-over measurement point including atmospheric absorption and ground effect.

16.4 Cumulative noise

Once the aircraft noise sources were modelled, it was time to compute the cumulative noise level of the aircraft to show compliance with the noise requirements. The SPL is a good metric to get an overview of the intensity of the sound at different frequencies, however it does not indicate anything about how the noise is perceived. For this reason, it was decided to look at A-weighted SPL. A-weighing means that an A filter is run over the SPL to correct them for the perceived loudness of the different frequencies [12]. The filter has much more effect on the lower frequencies as high frequencies are more annoying. The filter was found to be Equation 16.9 [12]. Then the overall A-weighted SPL [dBA] could be found using Equation 16.10.

$$\Delta L_A = -145.528 + 98.262(logf) - 19.509(logf)^2 + 0.975(logf)^3 \tag{16.9}$$

$$L_A = 10^{10} log \sum_{i=1}^{n} 10^{\frac{SPL(f_i)+\Delta L_A(f_i)}{10}} \tag{16.10}$$

Sensitivity analysis

In order to investigate the total effect of the corrections for the ground effect and the atmospheric absorption, the Overall Sound Pressure Level (OASPL) could be computed using Equation 16.11 [12]. It was found that the corrected OASPL was 3 dB higher than the OASPL of the pure model. This means that the noise is essentially doubled when taking into account environmental effects.

$$OASPL = 10^{10} log \sum_{i=1}^{n} 10^{\frac{SPL(f_i)}{10}} \tag{16.11}$$

Results

The cumulative SPL level could be plotted for the three measurement points, this resulted in Figure 16.11, Figure 16.12 and Figure 16.13 which show the cumulative SPL for the entire aircraft for the three different measurement points. As can be seen, the medium frequencies posses the highest SPL, while the higher frequencies posses the lowest SPL. This is because the airframe noise, specifically the flaps and main gear noise, dominate at medium frequencies. In addition, only the airframe noise was considered below the 1 kHz mark for the aircraft noise model. At the 1 kHz mark, a small kink can be observed which indicates the addition of the engine noise. In Figure 16.14 the corrected SPL, including the ground effect and atmospheric absorption for the approach measurement point is shown. As can be seen, the peak has a higher value for the corrected SPL compared to the model itself.

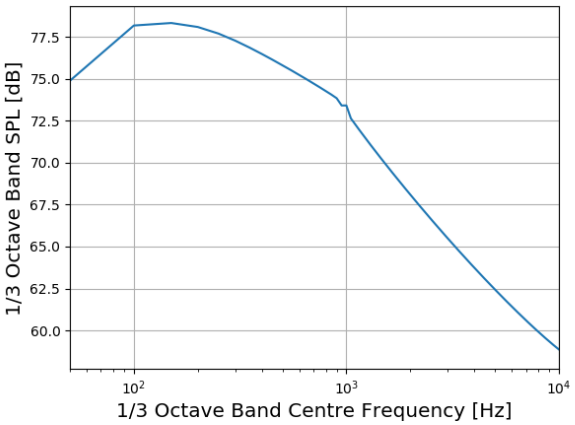

Figure 16.11: Cumulative SPL for the entire aircraft at the approach measurement point.

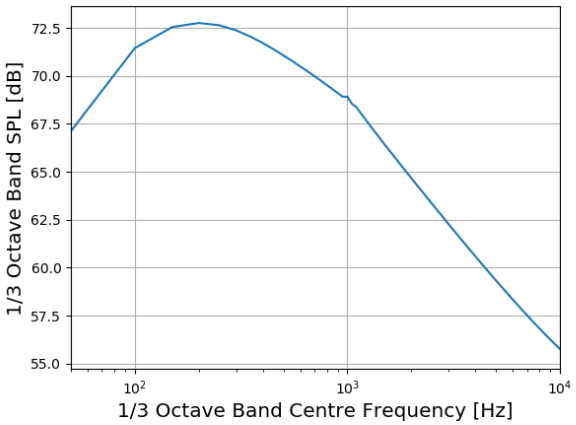

Figure 16.12: Cumulative SPL for the entire aircraft at the sideline measurement point.

Finally, using the A-weighted SPL, the compliance with the requirements could be shown. The results can be seen in Table 16.3 in combination with the total A-weighted SPL. As can be seen, the aircraft produces significant less noise than the B737-MAX 8 during take-off. This is because the engine is a geared turbofan, the gearbox ensures that the fan spins slower and thus creates less noise. In combination with the acoustic liners in the fan inlet duct, the overall noise reduction was estimated to be 5-7 dB [14]. This all resulted in a total noise lower than 282 dB specified by BIB-SYS-FLP-03, and 5.4 dB lower than the B737-MAX 8. Per passenger the resulting noise output is also reduced significantly, it is namely less than half of the noise the reference aircraft generates per passenger. When looking at the noise chapters specified by

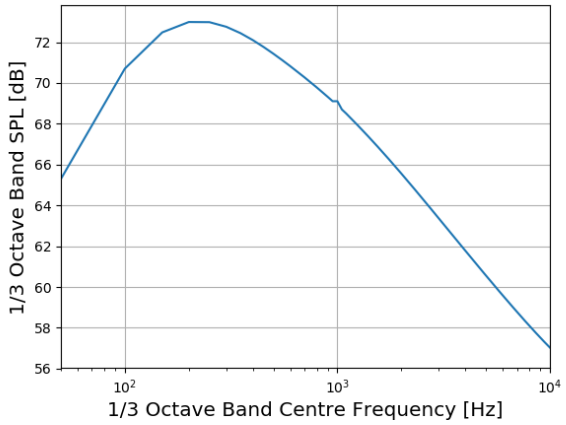

Figure 16.13: Cumulative SPL for the entire aircraft at the fly-over measurement point.

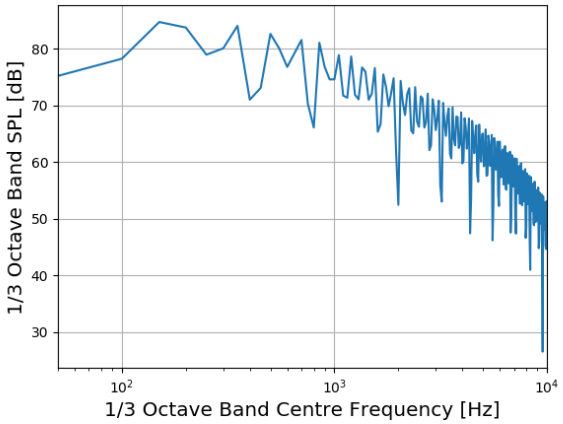

Figure 16.14: Cumulative SPL including atmospheric absorption and ground effect for the aircraft at approach measurement point.

ICAO [2], it can be seen that the B737-MAX 8 complies with the chapter 14 requirements. However, as EcoHopper 450 has a larger MTOW, it means that it is allowed to produce more noise while still meeting chapter 14. As the overall noise is estimated to be lower, and as noise Chapter 16 is still under development [2], it can be said that the aircraft is at least better than the B737-MAX 8. Therefore, (partially) meeting requirement BIB-SYS-TEC-09.

Table 16.3: Final modelled A-weighted SPL for the EcoHopper 450 and B737-MAX 8 at the measurement points.

Parameter	Approach	Sideline	Fly-over	Total	Total per pax
EcoHopper 450 A-weighted SPL [dBA]	89.6	81.8	85.4	256.8	0.57
B737-MAX 8 A-weighted SPL [dBA]	88.1	87.9	86.2	262.2	1.3

Verification & validation

Using the A-weighted SPL metric, the overall tool could be validated as the FAA provided a list of estimated maximum A-weighted SPL for many different types of aircraft and engine combinations [4]. The data sheet contained information on the type of aircraft and engine, weights, and the A-weighted noise levels during take-off and approach. Using the engine cycle calculation tool explained in chapter 7, estimations were made for the engine inputs needed for the engine noise tool, as no data by the engine manufacturers was provided. This introduced some uncertainty in the results. Multiple aircraft were examined, however to keep an overview only the validation results for the B737-800 and the A320 are shown in Table 16.4 [5], where TO represents take-off and App. represents the approach. It was chosen to show these aircraft as they are the predecessors of the aircraft (B737-MAX and A320NEO) the EcoHopper 450 has to beat. Unfortunately no noise data was available for these newer aircraft.

The average offset for the model was found to be 2.1% , which is quite accurate considering some assumptions had to be made. From a sensitivity analysis it was found that the exact engine parameters did not influence the engine noise linearly. For example, the mass flow had to be estimated using data from the engine manufacturers and the cycle calculation tool set out in chapter 7. However, a change in the mass flow rate of 100 kg/s only influenced the A-weighted SPL by 0.2 dBA. This is because it is not a linear scale and the airframe noise is almost equally as loud, which covers the extra noise from the engine. Considering the offsets, the model was deemed valid and could be used to assess the noise performance of the EcoHopper 450.

Table 16.4: Validation results for the overall noise estimation tool.

Parameter	B737-800 TO	B737-800 App.	A320 TO	A320 App.
FAA A-weighted SPL [dBA]	72.7	86.8	70.6	84.4
Model A-weighted SPL [dBA]	70.3	84.5	69.6	85.5
Offset model %	3.2%	2.6%	1.4%	1.3%

[4] Noise Levels for U.S. Certificated and Foreign Aircraft. Retrieved June, 17 2019, from `https://www.faa.gov/about/office_org/headquarters_offices/apl/noise_emissions/aircraft_noise_levels/`

[5] Elsevier Aircraft Data File. Retrieved June, 21 2019, from https://booksite.elsevier.com/9780340741528/appendices/data-a/default.htm

17 Financial Analysis

Since the EcoHopper 450 is intended to be sold to airlines, it has to be competitive with other existing aircraft. From the market analysis performed in chapter 5 the total amount of aircraft to be sold was determined. Once this amount is known, the production costs were estimated in section 17.1. In this section, the return of investment potential will be analysed as well. Finally, the direct operating costs and the return on investment of the operating phase will be analysed in section 17.2

17.1 Aircraft costs

Once the number of aircraft that has to be produced has been set, the costs of the aircraft may be estimated. The costs of the EcoHopper 450 have an influence on the profit of investors and is directly linked to the direct operational costs (DOC) as will be described in section 17.2. No requirement has been set on the aircraft cost, however, when the costs are too high, the DOC requirement would not be met. Aircraft costs are dependent on both recurring costs: the costs for actually building the aircraft, and non-recurring costs: the costs of the design phase, the engineering and the testing. In this section the production costs will be discussed first, subsequently the non-recurring costs will be presented, and finally they will be combined to estimate the return on investment.

17.1.1 Production Costs

The production costs represent the costs made for producing each individual aircraft. The actual costs being made per individual aircraft differ. This is due to the learning curve of the production staff, decreasing the costs of aircraft built in a later time period. However, for this analysis, the costs of each aircraft are assumed to be equal for simplicity. The costs of the aircraft depend on both the components that are being bought from other companies, such as the engines, and on components being produced by the aircraft manufacturer.

Various methods of estimating the production costs are investigated in order to determine the best method to be used for the EcoHopper 450. In general there are two types of estimations, a top-down method, using top-level mission parameters, and the bottom-up method, using an estimation for every subsystem. The top-down method is an estimation based on a regression on statistical data. The formulae used, described by Sforza [65] is shown in Equation 17.1. The costs are purely based on the OEW of the aircraft and no other parameters are used. This causes the estimation to be quite uncertain for unusual aircraft. Even though the estimation will be uncertain, the estimation may be used to get an estimation of the actual costs.

$$C_{AC} = -0.002695 \cdot m_{oe}^2 + 1967 \cdot m_{oe} - 2158000 \tag{17.1}$$

A second method, called the DAPCA IV or RAND method [66] made by the company RAND, uses slightly more inputs to estimate the costs. This method is also used by Raymer [4]. The method first uses formulae based on the OEW and maximum speed of the aircraft to estimate engineering, tooling, manufacturing and quality control hours needed to produce the aircraft. The hours needed are multiplied by the salary per hour and the inflation factor to get a cost estimation. Besides the salaries, costs of the materials are also included. The method also includes non-recurring costs, however, these will be discussed later in subsection 17.1.2. The RAND method also includes a so-called 80% learning curve, meaning that every time the batch size of the aircraft doubles, the costs increase by only 80%. This method is relatively precise compared to a statistical approach, however, when batch sizes increases to a large amount, the accuracy is rather limited. The RAND method is also called a top-down method, since it uses mission data and total weight to estimate the costs. A benefit is that relatively few input data is needed. The estimation excludes the costs of the engine and the avionics.

A third method considered is a so-called bottom-up method. The estimation of such methods first analyses the costs of each subsystem independently, then combine these costs and finally, add 25% for extra assembly costs. This method is described by Science Applications INC and NASA [67] and it is based on statistical data of all of the subsystems. The formulae used to calculate the costs of each system use the weight of the corresponding subsystem as input, rarely combined with another parameter. An estimation of the weight of each subsystem is again provided by the report, however, since some weights are already determined using another approach mentioned elsewhere in the report, different weights may be filled in. This document is rather old though, and so, for determining modern production costs, formulae of certain subsystems may and should be changed, as is stated in the document. The formulae stated in the report already take the learning curve into account. The influence of the learning curve varies within the subsystems. Some subsystems, in general the larger ones such as the wing and the fuselage, endure a 80% learning curve. Most systems, however, endure a 91% learning curve and some systems endure a 82% learning curve according to NASA [67]. A benefit of this approach is that the costs of each subsystem may be compared with each other, and subsystem specific adjustments may be done. The method excludes the costs of the engine.

In order to get an overview of the costs of the aircraft and compare it to reference aircraft, the bottom-up method will be used and so, all of the subsystem costs are analysed independently. At the end, assembly costs will be added. An engine costs estimation by Ali and Al-Shammah [65] will also be used. The subsystems and their percentage of the entire production costs are shown in Figure 17.1 and Figure 17.2 for both the Ecohopper 450 and the B737 MAX-8. The subsystems analysed together with their respective costs and weight are shown in Table 13.1. An extra 10% profit is given to the manufacturer, which is already included in the subsystem costs in the table. Most of the subsystem costs are determined using formulae from the NASA report without changes. However, some of the formulae are adjusted by multiplying the costs with a factor, as suggested in the NASA report. All the changes that were made are listed below.

- The costs of the wing have been multiplied with a factor 1.5. Since composite materials will be used for the strut of the wing of the EcoHopper 450, the costs of the wing per kg will be higher. When composites are used, the costs should be multiplied by a factor 1.2-2 according to Raymer [4]. Only the strut is made from composite, so a relatively low value may be chosen since the wing itself is made from aluminium. The costs of the wing will also increase due to production difficulties of the strut. Struts have not been used in aircraft production often, so production difficulties may be encountered. The total costs of the wing will thus be 50% higher than the costs estimated using the NASA report.
- The costs of the fuselage have been multiplied by a factor of 1.2. Using a novel double decker design, which is not used before, might lead to engineering difficulties. The fuselage costs will thus be estimated 20% higher.
- The costs of the hydraulics have been multiplied by a factor of 1.1. As stated in section 11.4, some designed components differ from older aircraft. The system uses a higher hydraulic pressure, which leads to a reduction of fluid needed. The hydraulic fluid has a significant effect on the total weight of the system. However, the reservoirs of the system have to be built from titanium, which in return increases the costs. Whether the total weight decreases or increases could not be stated with certainty. What can be said though, is that the production of titanium and more complex pumps increases the costs. It is concluded that the costs of the hydraulic system are estimated to be 10% higher than those estimated by NASA.
- The costs of the flight control system have been multiplied by a factor of 0.9. Because a fly by wire system is used, less weight is needed for the connections. This reduction in weight, and thus costs of the system, is estimated to be 10% less than estimated by NASA.
- The costs of furnishing have been multiplied by a factor of 0.8. Using the formulae provided by NASA, the furnishing costs scale with the number of passengers in the aircraft. The costs consist of costs being made the produce: crew seats, cockpit instruments, passenger seats, interior, galleys, oxygen masks, insulation, ceiling structure, lavatory, luggage stowage and even more. The costs of the galley is relatively high (20% of total furnishing costs) for large aircraft. However, since the EcoHopper 450 is large but flies short range, the galleys are not needed to be as large. The weight of the insulation is also decreased due to the double decker design. So, to conclude, the weight and so the costs of the furniture have been reduced by 20%.
- The costs of the electrical, air-conditioning and anti-icing systems are multiplied by a factor of 1.2. Since the EcoHopper 450 uses no pneumatic system and no APU, the performance of the other systems has to be increased which causes an increase in weight and costs. Extra generators, extra compressors, and relatively heavy heat blankets are used. The increase in costs of these systems is estimated to be 20%. Obviously, since the weight of the pneumatic system and APU are zero, the costs of these systems will be zero too.

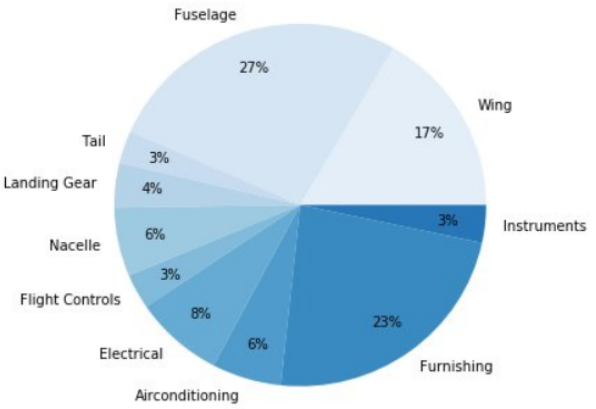

Figure 17.1: Distribution of the production costs of the EcoHopper 450.

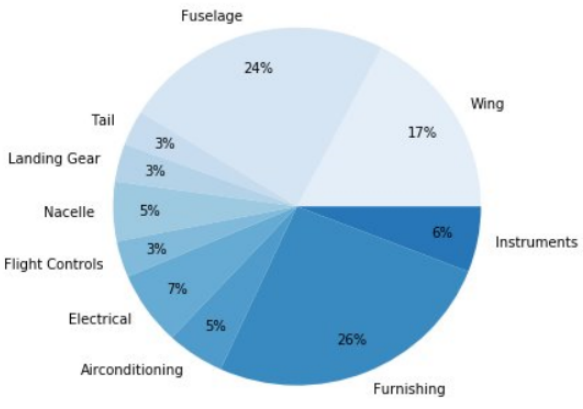

Figure 17.2: Distribution of the production costs of the B737 MAX-8.

17.1.2 Non-recurring Costs

During the design process various costs will be made before actually building aircraft which are intended to be sold. Engineering and preparing tooling require a lot of man hours and so, cost. Flight aircraft also have to be built and development support has to be paid. These costs have to be paid before the aircraft will actually be built. To make up for these costs, the costs will be split over each planned aircraft to be built in the future. The previously used bottom-up method does not estimate the non-recurring costs, so another estimation has to be used. The RAND method calculates the previously described non-recurring costs and was used. The manufacturing and quality control costs are left out to calculate. The engineering and tooling hours are calculated as described in the RAND report [66] and the results are shown in Table 17.1. The final estimated non-recurring, or program, costs of the EcoHopper were estimated to be 5.39 billion dollars. The estimated cost of the B737 MAX-8 is also presented. However, the actual costs of the 737 are lower, since the B737 MAX-8 is based on earlier 737 series. The final estimated program cost of the 737 results is five billion dollars, which is considerably higher than the 1 billion dollar actual program costs. It is noticeable that the non-recurring costs of the 737 MAX and the EcoHopper 450 are roughly the same. The batch size of the 737 MAX is larger, which increases the total costs, while the OEW of the EcoHopper 450 is higher, which also increases the total costs. So, the program costs of the EcoHopper 450 are significantly higher than for a Boeing aircraft, which was based on a previous aircraft. However, every newly designed aircraft will have higher program costs since at some point in the future aircraft will have to be redesigned to improve performance.

17.1.3 Aircraft Price

The total price of the aircraft consists of the recurring costs, non-recurring costs and profit. The resulting production costs, including the above listed changes and an inflation factor of 4.76 for 1975 to 2019 [1], resulted a relatively low cost. The engine costs, non-recurring costs and profit of the manufacturer already have been taken into account. Using input data of the Boeing 737 MAX, a cost estimation of this aircraft was also made. Again, the production costs resulting from the estimation were too low. A reason could be that the equations are out-dated, or that the batch size (5000) of the 737 MAX is too high to use for the equations. Even when the batch size would be lowered, the costs are too low. Other cost estimation tools have been used to estimate the costs too. However, when they were used, the total costs were estimated too low as well. So, in order to get a proper estimation, the production costs of the subsystems have been multiplied with a factor of 2.0 in order to reach realistic results. When it is applied on the B737 MAX-8, the total cost resulted in 121.6 million dollars, which is close to the actual value of 120 million dollars [2]. The factor two is also used when calculating the EcoHopper 450 costs.

The final costs of each subsystem is shown in Table 17.1. The assembly costs have been estimated to be 25% of the combined subsystem costs, as stated in [67]. The costs of the Boeing 737 are also shown as reference, using the same formulae from [67]. However, the listed changes in the formula are not used for the 737.

[1] Inflation Calculator. Retrieved June, 18 2019 from https://www.usinflationcalculator.com/

[2] Prices of Boeing aircraft. Retrieved June, 18 2019 from https://www.statista.com/statistics/273941/prices-of-boeing-aircraft-by-type/

Table 17.1: Costs estimation of the EcoHopper 450 per subsystem in 2019 million dollars.

Aircraft Component	Weight / Costs Estimation Method	Cost Estimation	B737 MAX-8 Cost Estimation
Wing	Class II, NASA	19.14	7.88
Fuselage	Class II, NASA	28.40	10.77
Tail	Class II, NASA	3.05	1.44
Landing Gear	Class II, NASA	4.26	1.55
Nacelle	Class II, NASA	6.45	2.44
Flight Control	NASA, NASA	2.81	1.30
Hydraulics	NASA, NASA	0.45	0.19
Electrical System	NASA, NASA	8.25	3.02
Air-conditioning	NASA, NASA	6.37	2.30
Anti-ice System	NASA, NASA	0.78	0.33
Furniture + Interior	NASA, NASA	24.59	11.74
Engine + fuel Systems	NASA, NASA	1.10	1.45
Avionics	NASA, NASA	1.67	0.90
APU	-, NASA	0	1.42
Pneumatic system	-, NASA	0	0.81
Assembly	NASA, NASA	28.81	13.41
Engine	Class II, Kroo	59.92	34.85
Recurring Costs	-	201.0	100.3
Engineering	RAND	5.37	0.19
Tooling	RAND	3.79	0.01
Flight test	RAND	0.33	0.19
Development Support	RAND	1.28	0.03
Non-Recurring Costs	RAND	10.78	0.42
Profit	-	42.53	20.27
Total	-	254.2	121.6
Total per pax	-	0.565	0.608

The table shows that the cost per passenger of the EcoHopper 450 is quite similar to that of the B737 Max8, with the actual costs being only 7% lower per passenger for the EcoHopper 450. The EcoHopper 450 has room for 450 passengers and the B737 Max-8 has room for a maximum of 200 passengers. The production costs of the airframe of the EcoHopper 450 is relatively high due the complexity of it, while the engine costs are considerably lower due to a lower maximum thrust. Furthermore, the EcoHopper 450 has a lower design range than the 737, but the costs are increased due to complexity of certain subsystems. All of the values are expressed in 2019 dollars.

17.1.4 Return on Investment

As explained in subsection 17.1.2, there are costs that have to be made before the aircraft intended to be sold can be built. These non-recurring costs have to be paid by one or multiple investors, and only once the aircraft starts to be sold, the investors earn their invested money back. In order to see if the investment is worth the risk, an estimated return on investment has to be analysed. The price of the aircraft has been set at 254.2 mln 2019 dollars in subsection 17.1.1. This price already includes a 10% profit for the manufacturer and on top of that, an extra 20% profit is included, being 42.53 mln dollars. The profit will be paid out after an aircraft has been sold. The aircraft production will start in 2028, at a rate of 50 aircraft each year. The 500 aircraft will thus be built in 2038. Starting investors to invest in 2019, the return on investment per year is calculated as shown in Equation 17.2. With N_{ac} being the number of aircraft built, C_p, the profit per aircraft, NC, the non-recurring costs and y being the amount of year until the last aircraft is build.

$$RoI_y = \frac{N_{ac}C_p + NC}{NC}^{1/y} \tag{17.2}$$

The total return return on investment is 21.18 bln dollars above the re-earned program costs, which results in a rate of 8.8% year. This number is above an estimated interest rate of 5-7%. Usually, investments pay out more when the risk of the investment increases. Since there are quite some risks coming with the production of the EcoHopper 450, an interest rate of roughly 9% is reasonable. The net present value (NPV) of the investment is calculated according to Equation 17.3, using an discount rate (R_d) of 1.07 (7%). The resulting NPV of the program is 7.35 bln dollars, while the actual program cost is 5.39 bln dollars. When a less optimistic discount rate of 1.05 (5%) is used, the resulting NPV is 10.55 bln dollars.

$$NPV = \frac{RoI + NC}{R_d^y} \tag{17.3}$$

The batch size of 500 aircraft being built is just an estimation, meaning that over 18 years, this value might change. When the number of aircraft built increases, the return on investment will also increase. When it drops, the profit will decrease. In order to get an estimate the minimal number of aircraft that needs to be built, a break-even point needs to be determined. When this point is reached, all of the costs made are repaid. The break-even point is calculated by dividing the non-recurring costs by the profit gained from one aircraft. The break-even point has found to be at 126 aircraft. This number does not include a discount rate, so the number of aircraft that has to be built to break-even compared to the current discount rate is actually higher. The cost of the 126 aircraft will also be slightly higher due the lower batch size. This phenomena is also not taken in consideration.

The assumption that the first aircraft will be produced in 2028 is rather optimistic, a delay in the design process, testing phase or production phase may occur rather likely. The production phase of 10 years may be delayed easily as well. So, in order to measure the consequences, the return on investment will be checked when the last delivered aircraft will be delayed two, five and ten years. Equation 17.2 will be used again, the only difference will be the years until the end of the project. When the project is delayed two, five and ten years, the new return on investment will be 7.9%, 6.9% and 5.7% respectively. The actual return on investments are actually higher, since some of the profit is cashed out during the project. Still, a delay of two years results in a profit above the estimated 7% interest rate. A delay of five and ten years results in a slightly lower profit than the current estimated interest rate, but it is still in the 5-7% range. So, even though a delay in the design or production process results in a loss in profit, a slight delay still results in an above average profit. When the process is delayed a lot, the actual profit of the EcoHopper 450 program becomes comparable to the profit gained from other investments.

17.1.5 Verification

A combination of methods has been used to compute the price of the EcoHopper 450. These methods are based on statistical data and so, they provide a rough estimate. When the method is used to calculate the price of the B737 MAX-8, the total price was estimated very accurately, this verifies the method. When the price of the engines is compared to the estimated one, a difference is seen. The estimated price is 35 million dollars, while the actual value is 29 million dollars [3]. The result is that the engine costs estimation and also the production cost estimation are not the same as reality. The entire cost perdition method is slightly off, as expected. Comparing a large and small aircraft to each other using the same method probably leads to errors in the result.

17.2 Direct Operating Costs

The costs made during flight determine the profit an airliner makes. The costs of an airliner may be split up in Direct Operating Costs (DOC), Indirect Operating Costs (IOC), and Overhead Costs (OHC). The DOC is approximately 55% of the total costs [68]. The IOC and OHC heavily depend on the airliner that uses the aircraft. The costs do have an influence on the DOC. However the exact influence is neglected since it varies a lot and it may change over time. The following requirement has been set on the DOC:

- **BIB-SYS-COS-01**: The operating costs of the aircraft shall be at least 10% less than current state of the art

To calculate the DOC a different approach from the approach of the midterm report is used [1]. According to Ali and Al-Shammah [65], three main approaches on calculating the DOC exist, the Air Transport Association of America (ATA), the NASA and the American Economic Association (AEA) method. In the report, the DOC estimated by each model is compared to each other for multiple existing aircraft from both Boeing and Airbus. The methods estimate different values for the DOC. This is because manufactures calculate the estimated DOC by various ways. The article states that the AEA method estimates the DOC the highest, the ATA thereafter and the NASA the lowest. A downside of the AEA method is that the method estimates the maintenance costs below 1%, which is not the case for existing aircraft according to the article. A downside of the NASA method is that the ranges are only divided between 'short', 'medium', and 'large'. The NASA method estimates the DOC quite low too. This is why the ATA method has been used to calculate the DOC of the EcoHopper 450. The only downside of the method is that the maintenance costs are estimated quite high.

The ATA method calculates the total DOC by calculating the different components of the DOC. The inputs required by the method are the aircraft costs, block time, and so the flight speed, the range, the MTOW and OEW, the thrust, mach number, number of engines, fuel weight and more. The aircraft costs calculated in section 17.1 is used as aircraft price. The other parameters were already calculated. The DOC consists of the depreciation, insurance, fuel, both airframe and engine maintenance, flight crew and cabin crew. The exact stated are written in [65]. Optionally, the interest costs and navigation and landing fees could be added. The results of the costs of the EcoHopper 450 are shown in Table 17.2. The distribution of the DOC of both the aircraft are shown in Figure 17.3 and Figure 17.4

[3] CFM-Leap-1B Order, Retrieved June 23 2019 from: https://www.cfmaeroengines.com/press-articles/alc-finalizes-348-million-cfm-leap-1b-engine-order/

Table 17.2: Cost estimation of every component of the direct operating costs per flight, presented in 2019 dollars.

Component	EcoHopper 450 [$]	B737 MAX-8 [$]
Depreciation	5,777	2,288
Insurance	348	133
Interest	3745	1,617
Flight Crew	1855	1,605
Cabin Crew	2321	919
Navigation and Landing Fees	1,556	1,080
Maintenance	8,445	4522
Fuel	9,425	5247
Total	33,473	17,410
Total per Block Hour	14,463	8447
Total per pax	74.4	87.1
Total per pax per Block Hour	32.1	42.2

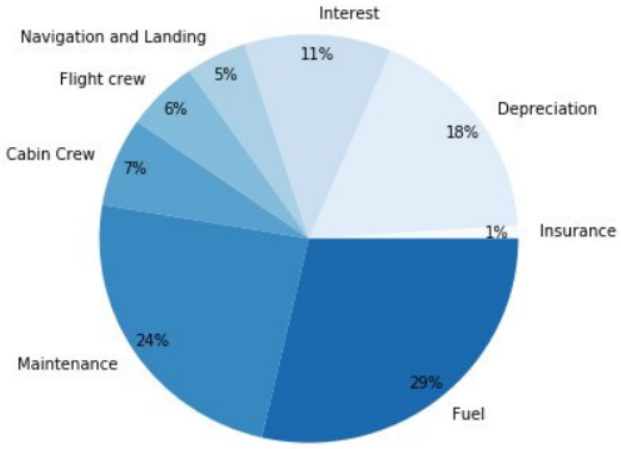

Figure 17.3: Distribution of the direct operating cost of the EcoHopper 450

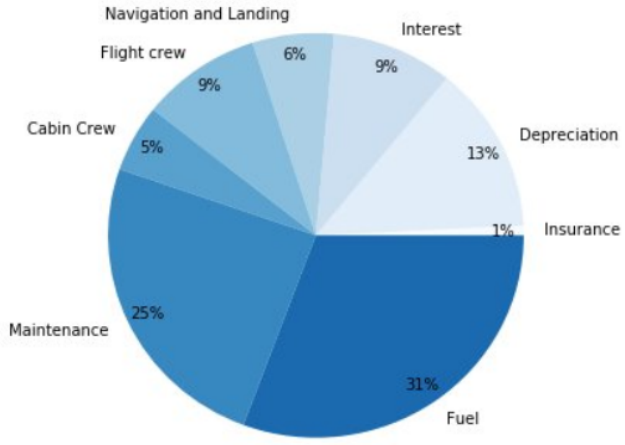

Figure 17.4: Distribution of the direct operating costs of the B737 Max-8

Resulting from the calculations made, the BIB-SYS-COS-01 requirement, a reduction of DOC of at least 10% is met. The actual reduction of the DOC per passenger is 14%. As is noticeable in the table, some of the DOC components of the EcoHopper 450 actually cost more than that of reference aircraft. The depreciation, insurance and interest cost all depend on both the aircraft costs as the flight time. As both the aircraft cost is higher as the flight time being lower, the costs for these components rise for the EcoHopper 450. The life time of both the aircraft have been estimated to be 27 years. The flight time is included by first calculating the annual utilisation of the aircraft using Equation 17.4 from ATA [65]. The block time is calculated by adding the cruise time using a 1,400 km range, take-off and landing time, taxi time and turnaround time with each other. The utilisation factor is then used in the calculation of the depreciation, insurance and interest cost. The costs of the cabin crew is also higher for the EcoHopper 450 due to a longer flight time. The costs of the flight crew is relatively low, since the same amount of pilots is used for more passengers. The navigation and landing fees are relatively low too. Although it is dependent on the MTOW of the aircraft, a larger aircraft has a relative benefit considering this component.

$$U = 6100 - 3100 \cdot t_B^{-0.3342} \tag{17.4}$$

The two DOC components in which the EcoHopper 450 is significantly cheaper at are the maintenance and the fuel costs. The fuel costs are this low since the EcoHopper is very fuel efficient and actually uses 24% less fuel. The maintenance costs is this low due to multiple reasons. The maintenance costs estimated by ATA consists of 5 components, the airframe labour and material costs, the engine labour and material costs and the overhead costs. The airframe costs are lower since the mach number in cruise is lower, which lowers the maintenance labour needed. The airframe material costs is almost the same for reference aircraft. The engine maintenance labour cost is dependend on the engine thrust, and the engine maintenance material cost is dependent on the engine cost. The engine costs again estimated using the engine thrust. Both the engine cost as engine thrust per passenger are significantly lower for the EcoHopper 450, which causes the maintenance costs to be lower. The overhead costs is a factor of the airframe and engine maintenance costs and so it is also lower. So to conclude, the requirement BIB-SYS-COS-01 is mainly met due to a decrease in fuel consumption and relatively small

engines. A change one of those two components should be critically looked up on considering the DOC. A sensitivity analysis will be performed to check the influences.

17.2.1 Sensitivity Analysis

As the DOC is purely based on parameters of the aircraft which might change later in the project, a sensitivity analysis has to be performed to see what the influences will be. As explained in the section above, are the aircraft cost, block time, fuel consumption and engine thrust are the four components that influence the DOC the most and whose values might change later during the project. These parameters will be investigated to measure the sensitivity. The block time is not checked for sensitivity since taxi, take-off and landing times are usually set by airports and the cruise speed influences the entire desing. In order to meet requirement BIB-SYS-COS-01, the DOC has to be 10% less. For every parameter, the value is checked to see what the limit is to still meet the requirement. The limit of the DOC of the entire aircraft is 35,256 dollars. All relations are linear, so the graphs are not shown as they don't provide extra information. However, the limits of the parameters are interesting to measure. The limits heavily depend on other parameters and even eachother, but an estimation of the maximum bounds could still be given.

To start with, are the aircraft costs estimated in section 17.1 still relatively uncertain. An increase in costs leads to an increase in depreciation, insurance interest and airframe maintenance costs. The aircraft costs may only increase by 9%, which is 23 mln dollars, in order to still meet the requirement. Secondly, the fuel consumption of the EcoHopper 450 also might change during the design process. The cruise, take-off and landing may consume more fuel or the electric systems may require more energy from the engines. In order to determine the limit of the fuel consumption, a sensitivity analysis is made. The fuel consumption may increase by 12%, to 20,484 kg, in order to still meet the requirement. At last, the thrust of the engine heavily influences the DOC due to the maintenance costs of the engine. In order to determine the limit of the thrust, a sensitivity analysis is made. The engine thrust may increase by 18%, to 470 kN, in order to still meet the requirement.

17.2.2 Return on Investment

The airliners that will use the EcoHopper 450 in the future invest in the aircraft and intend to make profit using the aircraft by means of passenger tickets. A part of the profit has to compensate the costs being made, and the rest will be the left over profit. In section 17.2 the DOC of the EcoHopper 450 has been made. However, besides the DOC, airliners also make other costs. The indirect operating costs (IOC) and overhead costs (OHC) are approximately 45% of the total costs as is explained in the midterm report [1]. So, the total costs of a flight will actually be approximately 60,860 dollars in total, or 135 dollars per passenger. When a load factor of 0.8 is assumed, the costs per passenger will be approximately 169 dollar per passenger. The actual costs will differ, since different missions result in for example different fuel or crew costs. However, the costs are estimated to remain constant. The profit of each flight will also differ heavily on the mission. Whether a flight route is long, crowded, or time/season dependend will all influence the ticket price. To get an estimation of ticket prices, Google flights is used [4]. A few typical intra asian flights are analysed at different times of the day and of the year. The flight prices heavily depend per airliner. For some routes the ticket prices may even vary between 80 dollars to 500 dollars on the same day. However, after analysing the flight routes between Shanghai, Beijing, Seoul and Tokio with ranges of 800-1300 km, an estimation of the ticket price have been set to 190 dollars. The ticket prices below 150 dollars have been assumed to be plane-fill prices, or ticket prices from price fighting airliners which use less costs. The ticket prices from the airliner Asiana vary from 170-260 dollars, the ticket prices from Air China from 150-220 dollars, while the ticket prices from Korean Air vary from 280-400 dollars. The reason for the ticket prices of Korean Air are being this high is uncertain, but it probably results from their customer services.

When the cost of a flight is approximately 169 dollars for 80% of the passengers and the ticket prices are 200 dollars, 11,140 dollars is earned by the airliner during each flight. The interest costs of the aircraft are already included in these costs. So, all of the profit is profit on top of the interest rate. To calculate the profit on a yearly basis, there will be assumed that the aircraft flies 6 times a day and flies roughly 350 days a year. The other days will the aircraft be held down for maintenance reasons. An airliner will make 23.4 million dollar profit each year on the EcoHopper 450. This would be only the case is every flight will be filled for 80%, the actual value might be lower, or some flights might just be necessary to replace the aircraft. The resulting profit will thus be slightly lower than estimated. When the average load factor of the EcoHopper 450 is 68%, the costs of a flight equals the profit. This break-even point already includes interest costs. The limit of the break-even point is relatively high and so, the risk of a low load factor is critical. However, since assumptions has been made, especially regarding the profit, the value for the break-even point might actually differ later during the design.

[4] Flights, Retrieved June 21, 2019 from: https://www.google.com/flights?

17.3 Costs related risks

Both the production costs as the direct operating costs are crucial for the operational life of the aircraft. When the costs increases, customers are less likely to use the aircraft. Cost related risks of the EcoHopper 450 are listed below.

- **Low number of orders:** 500 order of the EcoHopper 450 are estimated. When the number of order drops, either due to market shrinkage or due to a new competitor, the production cost per aircraft will be more expensive. In subsection 17.1.4 has been stated that 126 aircraft have to build in order to reach the break-even point. As this value is well below the 500 mark, the probability of the risk is considered improbable.
- **Low load factor:** filling smaller aircraft is easier than filling a large aircraft. As a larger aircraft has less flights a day, passengers may choose to go with smaller aircraft which has more departures a day. Season dependent flight routes affect a larger aircraft relatively more too since the aircraft won't be filled out season. The average load factor should be above 68% as described in subsection 17.2.2 in order to make profit, which is relatively high. So the risk of a low load factor occurring is considered probable and critical.
- **Costs exceed projections:** the aircraft could become too expensive due to unforeseen circumstances in the design or production phase of the project. This makes the aircraft less attractive for airlines. The maximum extra costs may only be 9% of the estimated costs as described in subsection 17.2.2 in order to meet the DOC requirement, BIB-SYS-COS-01. The profit of investors will simply increase if the costs increase, so the investors are not affected. Extra costs for unconventional design features such as the strut or the one-of-a-kind fuselage is already included in the production costs so the probability is not frequent. An increase of 9% is relatively low meaning the probability of the risk occurring is determined to be probable. If the DOC requirement is not met, the aircraft will be less competitive to other aircraft, but is still able to fly and the risk is classified as critical.
- **Maintenance costs are too high:** As the maintenance costs of the aircraft is equal to 28% of the direct operating costs, a change in the costs does have a large effect on the total costs. New design features such as a composite strut for the wing might increase the costs of the maintenance. When this increase is too high, the DOC requirement, BIB-SYS-COS-01, may not be fulfilled.

18 Sustainability strategy

As the goal of the project was to develop a highly sustainable aircraft, it was necessary to investigate the impact of the EcoHopper 450 on aviation sustainability. Therefore, a strategy was developed to discuss the sustainability of the design as well as how the aircraft contributes to the sustainability of aviation. The sustainability approach used throughout the project is discussed in section 18.1. Next, the manufacturing process of the aircraft is analysed in section 18.2. Once the aircraft is taken out of operation its impact on sustainability does not end, therefore, some end of life solutions must be investigated, see section 18.3.

18.1 Sustainability approach

The goal of the project was to design a highly sustainable aircraft in costs, noise, fuel and emissions. Hard requirements were imposed on the costs, fuel consumption and noise output (see requirements BIB-SYS-COS-01, BIB-SYS-TEC-02, BIB-SYS-TEC-08, BIB-SYS-TEC-09 and BIB-SBS-FLP-03). In order to ensure that these requirements were met, a design approach focused on sustainability had to be used. The first step of this approach was to analyse requirement BIB-SYS-TEC-02 which specifies that the aircraft's cruise conditions had to be climate optimised. As the cruise conditions highly influence the possible design points in the $T/W - W/S$ diagram, this was the first step to be taken. A thorough analysis was performed on the influence of the altitude and speed on the fuel consumption during cruise, the radiative forcing and the costs. This was presented in the midterm report [1]. It resulted in diagrams and numbers showing which cruise conditions could meet the fuel and cost requirements. Several cruise conditions were then analysed per design concept to find the optimum conditions per concept. This was subsequently used to assess the different design concepts.

During the trade-off for the different design concepts, trade-off criteria looked at the fuel consumption, radiative forcing and costs to ensure that the sustainability aspect of each concept was also considered. The noise requirements were taken into account through the selection of the engine for each concept. The sustainability criteria were given high weights as these drive the design and were considered to be important for the client. It finally resulted in the current design with cruise altitude of 9,000 m and a cruise Mach number of 0.72. Once the design was established, further analysis into the configuration and details of the design had to be done. Design choices were based on their effect on the sustainability of the aircraft. It was chosen to opt for design choices and systems which would have a technological readiness level (TRL) of a minimum of 6 as the aircraft's design has to be finished by 2025 (BIB-SYS-SDL-03). A literature study was conducted to investigate the possible options to further improve the aircraft's sustainability. This finally resulted in the implemented technologies and design choices listed in Table 18.1. The first column indicates the sector to which the technology or design choice is related, the second column indicates the technology or design choices which were implemented, and finally the last column indicates the impact on the sustainability.

The EcoHopper 450 contributes to sustainable aviation in the sense that it reduces the fuel consumption, costs, emissions and noise with respect to current state of the art aircraft. The compliance with all (other) requirements is further discussed in chapter 20. The aircraft poses as a short term solution for the sustainable aviation problem as it still uses kerosene but introduces some novel solutions to improve the sustainability of the aircraft.

18.2 Production plan

As the aircraft also needs to be manufactured and assembled, a production plan was established from a sustainability point of view. The aircraft itself might be highly sustainable, however the entire process from paper to operations needs to be sustainable as well. Therefore, the different aspects of manufacturing, assembly and integration (MAI) of the aircraft are discussed in this section. A flow diagram of the general process was made, which is shown in Appendix D. The light coloured blocks represent the smaller components of the aircraft which will be produced at work stations separated from the assembly line, while the dark coloured blocks represent the work stations part of the assembly line. The parts needed to produce the components like the side panel of the fuselage will be obtained from warehouses. These warehouses will be stocked by workshops which produce common products in batches, like rivets and other fasteners. The flow of parts and components can be seen in Figure 18.1.

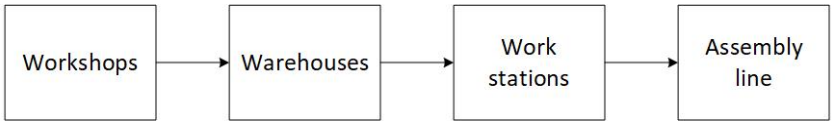

Figure 18.1: Flow of parts and components during the manufacturing and assembly process.

Table 18.1: Measures taken to improve the sustainability aspect of the EcoHopper 450.

Sector	Technology or design choice	Impact
Operations	Cruise conditions: 9,000 m and a Mach number of 0.72	- Reduced radiative forcing due to the altitude - Reduced fuel consumption due to the Mach number which is lower than for conventional aircraft. - Reduced emissions due to lower fuel consumption
	Continuous descent approach	- Reduced emissions during LTO cycle - Reduced fuel consumption during LTO cycle - Reduced noise output at the ICAO measurement points
Propulsion	Ultra high bypass geared turbofan engine (15:1)	- Improved engine efficiency - Reduced fuel consumption - Reduced emissions - Reduced fan RPM thus reduced fan noise - Reduced jet velocity thus reduced jet noise
	Low combustion chamber inlet temperature	- Reduced NO_x emissions
	Acoustic liners in fan inlet duct	- Reduced engine noise
Systems	No auxiliary power unit (APU)	- Reduced (LTO cycle) fuel consumption - Reduced (LTO cycle) emissions - Reduced noise output during ground operations - Reduced direct and maintenance costs
	Bleedless systems	- Improved engine efficiency - Reduced fuel consumption - Reduced emissions - Reduced operational empty weight - Reduced maintenance costs
	Electric taxiing	- Reduced (LTO cycle) fuel consumption - Reduced (LTO cycle) emissions - Reduced noise output during ground operations - Reduced push back time - Reduced operating costs
Aerodynamics/ structures	Unswept wings	- Improved wing efficiency - Reduced drag, and thus thrust required at low speeds - Reduced structural weight
	Material selection: composites	- Reduced operational empty weight, thus; improved fuel efficiency
	Strutted wing	- Reduced wing weight/operational empty weight, thus: reduced fuel consumption

It was chosen to opt for a lean manufacturing philosophy. This means that there is manufacturing where waste is minised. Waste is defined as anything that uses resources but that does not add any value to the final product for its customers. All forms of waste should ideally be eliminated from a lean manufacturing process. The actions in a production stream can be divided into [69]:

- Actions which create value as perceived by the customer.
- Actions that create no value but are required and cannot be eliminated, e.g. the transportation of the engines from the manufacturer to the aircraft assembly line.
- Actions which do not create any value and can be eliminated.

The latter two are forms of waste. One should start by eliminating waste from category three before moving on to eliminate waste from category two. There are many different forms of waste, however the processing waste and transportation of goods are the ones which should be eliminated from a sustainability point of view. Other types of waste like waiting time and under utilising people are associated with economical drawbacks [69]. To eliminate the processing waste, one should opt for novel manufacturing processes like lay-up processes and casting which produce as little waste as possible. In the optimal case, parts that can be 3D printed should be as it produces no waste. Manufacturing processes like milling should be avoided as they lead to the waste of a lot of raw material. Finally, transportation can be limited by placing all of the work stations and assembly lines in the same place. Companies tend to distribute their production over multiple locations and sometimes even countries. This introduces the need for transportation of the various components to the final assembly line. This leads to expensive transportation operations and a lot of emissions during the process. As the emissions during a manufacturing process are already significant due to the forming of raw materials and production of components, the emissions due to transportation by e.g. aircraft or trucks, should be limited as much as possible. This can help to decrease the carbon footprint of aviation manufacturing.

18.3 End of life solutions

Nowadays, most aircraft which are retired are not used to their full extent as they are being stored at abandoned places like the aircraft graveyards in the desert of the United States. Other solutions must be sought in order to maintain a sustainable operation after its operational life. Therefore, the aircraft has to be recycled as much as possible. Recycling contributes to the reduction of parking costs, minimises the environmental impacts, produces economical benefits and it contributes to the market for aircraft parts [1]. The market consists of airlines and other customers who are interested in still functioning aircraft parts or interested in raw materials. Therefore a recycling strategy was developed to indicate the EcoHopper's end of life operations.

Once the aicraft is taken out of operation, it should be transported to a dismantling site where it is washed to remove all contaminants like salt. Next, all fluids like fuel are drained from the aircraft. Normally the toxic de-icing fluid also has to be removed, however as the EcoHopper 450 does not use de-icing fluid it can move on to the next phase. The de-icing system without de-icing fluid is explained in chapter 11. It can already be said that this improves the recycling process as the toxic fluid cannot be re-used. Then the explosive devices for the emergency slides are removed before the real scrapping process begins which can take up to twelve weeks.

As the engines contribute a significant part to the aircraft's total cost they are the first components to be salvaged from the retired aircraft. Once they are recovered from the aircraft, they are tested and certified again such that they can be used on other aircraft. Or, if they do not pass the tests, the engines can be stripped further down for parts or returned to the engine manufacturer to be repaired. The still working components of the engine can be sold. The next phase consists of unbolting and salvaging other valuable systems. These systems include the flight deck instruments, black boxes, air conditioning, flight controls, landing gears including the hydraulic system, aerodynamic devices (e.g. flaps, slats and spoilers), the fuel system and the cabin interior (e.g. seats, galleys, doors and windows) [2]. All these components are then subjected to extensive testing to obtain a certificate of airworthiness from the FAA before they can return to service.

The last part to be taken off of the aircraft is the landing gear, after which only the frame is left. The composite parts should be separated from the metal parts as they cannot be recycled in the same way. The metal parts are crunched and the aluminium can be melted down. This ensures that the aluminium can be re-used as raw material for other processes [2]. The process to recycle composites, in this case mainly the carbon fibre strut, is more difficult as the resin used is often toxic. However, nowadays there are numerous companies that offer composite recycling services. The fibres resulting from these processes are almost always discontinuous, meaning that they cannot be used to produce new aircraft composite components as they use continuous fibres mostly. Therefore, the difficulty in recycling composites mostly lies in the application of the recycled composites [3]. Boeing is investigating a way to integrate the recycled carbon fibre of their B787 into the interior of the aircraft. This application could make the aircraft even more lightweight from inside out [3]. As Boeing is already in the demonstration phase it is expected that it will be employed widely by the time this aircraft is in operation, meaning that even the composites can be fully recycled.

The Aircraft Fleet Recycling Association (AFRA) can help to better recycle the aircraft as they are the leading global trade association regarding aircraft recycling. They maintain collaboration between companies worldwide such that they can return aircraft parts to the market. AFRA itself is a non-profit organisation, however it connects the recycling companies with the airlines and other stakeholders. The companies and AFRA together focus on the end of life solutions for commercial aircraft [4].

[1] AiMeRe project. Retrieved June, 22 2019, from https://www.icao.int/Meetings/EnvironmentalWorkshops/Documents/2014-GreenTechnology/3_Elliff_Envisa.pdf

[2] How do you recycle a jumbo jet? Retrieved June, 22 2019, from http://news.bbc.co.uk/2/hi/8542482.stm

[3] Composites recycling becomes a necessity. Retrieved June, 22 2019, from https://www.compositesworld.com/articles/composites-recycling-becomes-a-necessity

[4] Airplane recycling and value extraction. Retrieved June, 22 2019, from https://www.thebalancesmb.com/airplane-recycling-and-value-extraction-2877922

19 Resource Allocation

Throughout large engineering projects it is generally the case that certain technical parameters tend to grow without bounds when this is not explicitly prevented. These technical parameters are needed to design certain subsystems and therefore, they need to be set at a certain value. A contingency on this value ensures that the designed subsystems still perform well even when the technical parameters have changed during the design phase. During the baseline report [8] budgets were shown and values for technical parameters were set. These values have changed throughout the project since the design concept has changed drastically from that point, since design changes were made after the midterm report, the technical parameters also have changed since then. All of the subsystems have been designed using the most up to date technical parameters. A contingency value also has been used on top of these parameters. In this chapter, values of technical parameters of the baseline and midterm phase are shown in order to see their behaviour throughout the project. These values will be compared to the values at the current stage. When technical parameters have grown out of bounds, all influences have to be critically investigated. Current contingencies for parameters are also presented is this chapter. The technical parameters that have the largest influence on the design of subsystems were determined to be the maximum take-off weight (MTOW) and the engine thrust (T). Due to large differences in one of these parameters, the performance of subsystems may be questioned. Although requirements of the project are also influenced by other factors, these were identified as the primary drivers. Other budgets presented in the baseline report are not analysed since they will not affect the design of the EcoHopper 450 as much or are mainly influenced by the already analysed mass and thrust.

19.1 Weight

The MTOW determines the size of many other subsystem and has a large influence on the performance and costs of the aircraft. The snowball effect when one of the systems weight increases is already included in the estimated MTOW. The MTOW of the EcoHopper 450 was estimated to be 1623 kN in the baseline report, which was based on a class I weigth estimation, without an iteration. Since the estimation was premature, a contingency value of 25% has been set for the MTOW. During the midterm report, the mass estimation has been elaborated by combining class I and class II weight estimations. The resulting MTOW was 1475 kN. A 10% contingency was determined to be sufficient for this stage. The MTOW of the current, more detailed design was determined to be 1497 kN. This small increase was already included as safety margin, and so the increase won't have a large influence on the design. The updated MTOW always has been within the contingency bounds. Based on statistics the weight generally increases by around 5% at this point in the design [3, 4], this value will be used as contingency value at the current phase. The estimated mass of the EcoHopper 450 throughout the project is shown in Figure 19.1.

19.2 Thrust

The thrust of the engines was sized for every flight condition during the mission of the EcoHopper 450. The thrust was mainly dependent on the mass of the aircraft, the zero lift drag and the high lift devices used. The thrust of of the EcoHopper 450 was estimated to be in the order of 445 kN. This value was based on the estimated take-off mass, an estimated surface area and found by analysing all critical flight conditions. A contingency value of 25% has been used at the baseline phase. The engine has been chosen based on this value, and so, the validity of this choise should be refelected upon. Since the thrust is still within bounds, the choice of the engine might be considered valid. During the midterm phase a thrust of 427 kN was estimated with a contingency of 15%. The current estimated thrust is 392 kN, the thrust has been between the contingency bounds. Since the thrust is dependent on a lot of different parameters, the actual value still might change during the future design phases. So a contingency of 10% will be used for the future design. The estimated thrust of the EcoHopper 450 throughout the project is shown in Figure 19.2.

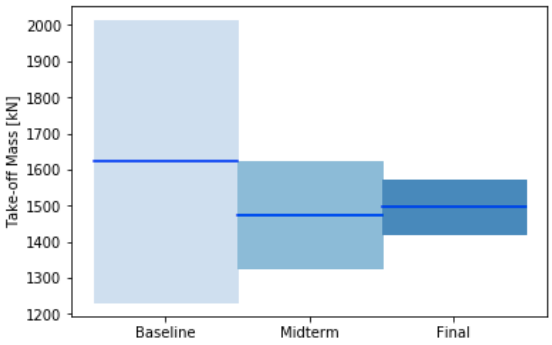

Figure 19.1: Mass development including contingency.

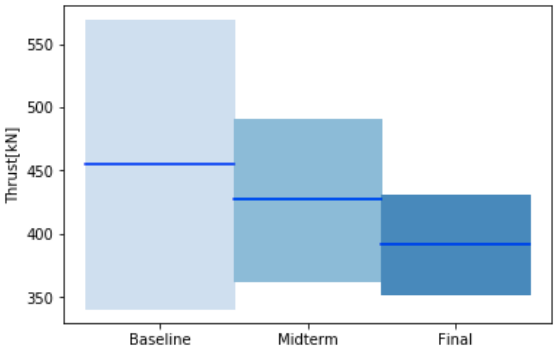

Figure 19.2: Thrust development including contingency.

20 Requirement compliance

This chapter covers the verification of the requirements as well as the compliance of the design with the requirements analysed in the baseline report [8]. The verification of a requirement describes how it is proven that the imposed requirements are met [15]. The methods to obtain proof are testing, analysis, simulation, review of design or documentation, and similarity. The latter means that a comparable design is already in operation. The compliance with the main requirements and the method to verify the requirements is shown in Table 20.1. As can be seen BIB-SYS-TEC-05 is not fully met as the turnaround time using two boarding bridges is 48 minutes while it should be 45 minutes. However, increasing the number of boarding bridges led to the required 45 minutes turnaround time. Nevertheless, using three boarding bridges is usually not feasible at major airports. Therefore the requirement is only partially met, modifications to the design could be applied, like increasing the number of doors to fully meet the requirement. Furthermore, BIB-SBS-OPS-01 is not met as well as the aircraft relies on ground based power to start its engines. It was chosen to not equip the EcoHopper 450 with an APU as it makes the aircraft more sustainable, however it does mean that this requirements is not met. Nevertheless, no modifications are needed as the sustainability of the aircraft is more important and all major hubs possess gates with ground based power.

Table 20.1: Compliance matrix of the project requirements including the verification method.

Code	Requirement	Compliance	Verification method
BIB-SYS-SDL-01	The operational costs of the aircraft shall be 10% less than current state of the art aircraft.	Reduced by 14%	Analysis and documentation
BIB-SYS-SDL-03	The aircraft design phase shall be finished by 2025.	Finished in 2025	Documentation
BIB-SYS-MKO-01	The range of the aircraft shall be between 1,000-2,500 km.	Design range of 1,400 km	Analysis and documentation
BIB-SYS-MKO-02	The aircraft shall be operational at least 10 hrs a day.	2-3 Round trips a day (10-12 hrs)	Analysis and test
BIB-SYS-TEC-01	The aircraft shall be propelled by either jet or propeller driven propulsion.	UHBP geared turbofan	Documentation
BIB-SYS-TEC-02	The cruise profile of the aircraft shall be optimised for climate optimised flights.	Altitude of 9 km and Mach number of 0.72	Documentation
BIB-SYS-TEC-03	The aircraft shall accommodate 450 passengers in a single class configuration.	450 passengers, 15 crew members	Documentation
BIB-SYS-TEC-04	The aircraft MTOW shall not exceed that of the mass budget.	MTOW of 152,615 kg, budget of 162312 kg [6]	Documentation
BIB-SYS-TEC-05	The aircraft shall have a turnaround time of at most 45 minutes.	With 2 boarding bridges: 48 min., with 3 boarding bridges: 45 min.	Analysis and simulation
BIB-SYS-TEC-06	The aircraft shall be able to operate from all major European airports.	Wingspan of 52 m, required runway length of 2,657 m	Documentation and analysis/simulation
BIB-SYS-TEC-07	The aircraft shall have a wide body fuselage.	8 seats abreast (twin aisle)	Documentation
BIB-SYS-TEC-08	The aircraft shall have 10% reduced fuel consumption per passenger with respect to current state of the art.	24% reduction for entire flight fuel consumption per passenger	Analysis
BIB-SYS-TEC-09	The noise produced by the aircraft shall be at least one noise class better than current state of the art aircraft.	Cumulative noise of 257 dBA, Chapter 14 noise 282 EPNdB	Test and simulation
BIB-SBS-FLP-01	The aircraft shall be able to take-off from a runway of 2,700 m at sea level at MTOW.	Required take-off runway length is 2,548 m	Analysis and simulation
BIB-SBS-FLP-02	The aircraft shall be able to land on a runway of 2,700 m at sea level at MTOW.	Required landing runway 2,657 m	Analysis and simulation
BIB-SBS-FLP-03	The accumulated noise generated by the aircraft shall be below 282 dB at the ICAO measurement points.	Cumulative noise is 257 dB	Test and simulation
BIB-SBS-FLP-04	The aircraft shall have a NO_x emission at least lower than current state of the art.	28% reduction in LTO, 38% in cruise (for the design range)	Analysis and simulation
BIB-SBS-FLP-09	The aircraft shall have a CO_2 emission at least lower than current state of the art.	21% reduction in LTO, 10% in cruise (for the design range)	Analysis and simulation

Code	Requirement	Compliance	Verification method
BIB-SBS-FLP-12	The flight performance subsystem shall comply with CS25.20-CS25.125, CS25.201-CS25.255 and CS25.1501-CS25.1593.	Meets climb gradient requirement with a margin of 14% on average	Simulation
BIB-SBS-STR-01	Passengers shall be able to board the aircraft.	4 doors on lower and 4 on upper decks	Documentation
BIB-SBS-STR-02	The aircraft shall contain windows for passengers to view the outside world.	Windows on both floors	Documentation
BIB-SBS-STR-03	The wings of the aircraft shall be able to carry all limit loads in the flight envelope.	n = 2.56; V = 201 m/s n = 2.5; V = 272.5 m/s n = -1; V = 218 m/s	Analysis and simulation
BIB-SBS-STR-04	The structure shall withstand the maximum loads in the flight envelope.	n = 2.56; V = 201 m/s n = 2.5; V = 272.5 m/s n = -1; V = 218 m/s	Analysis and simulation
BIB-SBS-STR-05	The structure shall not fail below ultimate load level.	It does not fail below n = 3.84	Analysis and simulation
BIB-SBS-STR-06	The structure shall withstand fatigue life during its whole operational life.	Designed for 27 yrs: 4,730,040 cycles (6 flights a day)	Analysis and documentation
BIB-SBS-STR-07	The structure shall not fail due to thermal expansion.	Use of carbon fibre, 2024 and 7075 aluminium alloy	Test and simulation
BIB-SBS-STR-08	The structure shall not corrode due to changing humidity levels.	Use of carbon fibre, 2024 and 7075 aluminium alloy	Test and simulation
BIB-SBS-STR-09	The structure subsystem shall comply with CS25.300-CS25.899.	See all of the above	Documentation
BIB-SBS-PRO-01	The aircraft engines shall operate with a fuel efficiency of at least $12x10^{-6}$ kg/Ns.	$C_{T0} = 11.6x10^{-6}$ kg/Ns	Documentation and analysis
BIB-SBS-PRO-02	The propulsion subsystem shall comply with CS25.901-CS25.1207.	FAA certification engine manufacturer	Documentation
BIB-SBS-STC-01	The neutral point of the aircraft shall always remain behind its centre of gravity.	Elevator control	Analysis
BIB-SBS-STC-02	The aircraft shall be stable during all flight phases.	Control surfaces	Analysis
BIB-SBS-STC-03	The aircraft shall possess static stability all flight phases.	Neutral point behind cg	Analysis
BIB-SBS-STC-04	The aircraft shall be controllable during all flight phases.	Control surfaces	Analysis and documentation
BIB-SBS-STC-05	The stability and control subsystem shall comply with CS25.143-CS25.255.	See all of the above	Documentation
BIB-SBS-OPS-01	The aircraft shall be able to start on its own.	Ground based power needed	Documentation and analysis
BIB-SBS-OPS-02	The aircraft shall be able to stop on its own.	Landing distance of 1,594 m	Simulation and test
BIB-SBS-OPS-03	The aircraft wingspan and length shall be less than 80 metres.	Span of 52 m + length of 49.3 m	Documentation
BIB-SBS-OPS-04	The cargo hold of the aircraft shall accommodate cargo containers of standard dimensions.	Designed for LD1 containers	Documentation and test
BIB-SBS-OPS-05	The aircraft shall not tip-over during loading on the ground.	Tip back angle of 15 degrees	Analysis
BIB-SBS-OPS-06	The aircraft shall be refuelled from empty to maximum within 45 min.	Pressure refuelling, flow rate of 6.4 kg/s	Simulation
BIB-SBS-AED-01	The whole operational envelope of the aircraft shall be evaluated.	See aerodynamic analysis: take-off, landing and cruise	Documentation

21 Conclusions and Recommendations

The goal of this project was to design a state of the art, dedicated fixed wing aircraft capable of carrying 450 passengers on a typical intra-continental flight. As a result, the EcoHopper 450 was designed, an double decker with a strutted high aspect ratio wing and ultra high bypass engines. The purpose of this aircraft is to form the first step in the direction of more sustainable aviation.

In order to be more sustainable, several novel systems were introduced in the aircraft. First of all, the EcoHopper 450 uses a self-powered brake system, which is an innovative feature and will be available by 2025. Furthermore, an electric taxi system is used, which leads to a fuel consumption reduction of 1.55%. The EcoHopper 450 will also be equipped with a no-bleed system which reduces fuel consumption even more, while also reducing the weight and maintenance costs. As all these novel systems require energy, a battery pack was used which will be recharged both during flight and while docked at the gate. This made it possible to leave the APU out. Furthermore, an ultra high bypass engine is used such that the fuel efficiency is optimised and noise is reduced.

The strut is an innovative feature for large commercial aircraft. Placing a strut allowed for a high aspect ratio, aerodynamically efficient wing. Generally, high aspect ratio wings are heavy, however, the strut allowed to reduce the structural weight of the wing due to bending relief. Although 11% of the zero lift drag was due to the strut, the overall aerodynamic performance still increased due to the high aspect ratio wing.

Reflecting on the requirements that were determined at the start of this project, it can be concluded that all requirements have been met. Due to the innovations, the total fuel consumption per passenger was reduced with 24.6%, of which 10.3% of the reduction was reached during cruise. As all emissions, except NO_x, are linearly scaled with the fuel consumption, these were reduced with a similar amount. Looking at just NO_x, the reduction is more significant, being 37.5% during cruise. The large reduction is the result of the cruise altitude at which the EcoHopper 450 is flying combined with the low inlet temperature for the combustion chamber. During ground operations, the NO_x emissions was reduced with 27.7%, significantly improving the air quality on the ground.

The accumulative noise of the aircraft and total noise per passenger were reduced with 5.4 dB and 57% respectively. Besides, due to the high capacity of the aircraft the number of flights could be reduced. As currently noise plays an important role around airports, limiting the airports in the number of flights that can be flown, the EcoHopper 450 is an attractive option.

Finally, 500 future orders of the aircraft were estimated from the market analysis. Close monitoring of the market is required as the orders are highly dependent on the future market. The total production cost of each aircraft was estimated to be 254 million dollars. Most importantly, the direct operating cost of the EcoHopper 450 were found to be 14% lower than current state of the art aircraft.

Summarising, the EcoHopper 450 will be significantly more sustainable than current aircraft, while consuming 24.6% less fuel, producing 5.4 dB less cumulative noise and improving the direct operating cost with 14%. Nevertheless, some additional investigations can be performed in order to further improve the aircraft design. First of all, boundary layer ingestion on the strut would be an option in reducing the drag penalty induced by the strut.

Also, in this design phase, the centre of gravity range was estimated in a conservative way, assuming a safety margin of 10%. When moving into more detailed design, this safety margin could be reduced such that this range becomes more narrow. This would in turn result in a decrease in required control surface dimensions.

Finally, some additional structural analyses could be performed. The 3D effects on the strut should be investigated using an FEM analysis in combination with an aeroelasticity analysis. In addition, the winglets and the landing gear retraction system should be researched more in depth.

Bibliography

[1] Jansen H. Knoop M.W. Lampe R.P.N. Terleth M. van Luijk N.L.M. van Paasen S.M.N. van Steen F.A. Wittenberg M.L. Asselman B., Brus D. Midterm report: Bigger is better group 12. 2019.

[2] A. Melkert J.A. & Cervone. *AE2230-II Propulsion & Power*. Delft University of Technology, 2019.

[3] E. Torenbeek. *Synthesis of subsonic airplane design*. Kluwer Academic Publishers, 1982.

[4] Daniel P. Raymer. *Aircraft Design: A Conceptual Approach*. American Institute of Aeronautics and Astronautics, 1999.

[5] Cs-25 large aircraft. Technical report, European Union Aviation Safety Agency (EASA).

[6] J.D. Anderson. *Aircraft performance and design*. McGraw-Hill, 1999.

[7] P.C. Roling. *Flight & Orbital Mechanics AE2230-I*. Delft University of Technology, 2019.

[8] Jansen H. Knoop M.W. Lampe R. Terleth M. van Luijk N.L.M. van Paasen S.M.N. van Steen F.A. Wittenberg M.L. Asselman B., Brus D. Baseline report: Bigger is better group 12. 2019.

[9] Hansman R.J. Lovegren J.A. Estimation of potential aircraft fuel burn reduction in cruise via speed and altitude optimisation strategies. Technical report, MIT International Centre for Air Transportation (ICAT), 2011.

[10] Airbus training. A320 power plant. *Flight crew operating manual*.

[11] A. Filippone. *Advanced aircraft flight performance*. Cambridge University Press, 2012.

[12] Prof. Dr. D.G. Simons. *AE4431: Introduction to Aircraft Noise*. Delft University of Technology, 2018.

[13] G.J.J. Ruijgrok. *Elements of Aviation Acoustics*. Delft University Press, 2600 MG Delft, 2004.

[14] Simons D. Snellen M. Bertsch, L. Aicraft noise: the major sources, modelling capabilities and reduction possibilities. Technical report, University of Technology Delft, 2015.

[15] Melkert J.A. *Project Guide Design Synthesis Excercise*. Delft University of Technology, 2019.

[16] Jansen H. Knoop M.W. Lampe R. Terleth M. van Luijk N.L.M. van Paasen S.M.N. van Steen F.A. Wittenberg M.L. Asselman B., Brus D. Project plan: Bigger is better group 12. 2019.

[17] Dr. Roskam J. *Airplane Design Part V: Component Weight Estimation*. Design, Analysis and Research Corporation (DAR corporation), Lawrence, Kanses 66049, 2003.

[18] G.J.J. Ruijgrok. *Elements of Airplane Performance*. Delft University Press, 2600 MG Delft, 2009.

[19] Melkert J.A. & Zandbergen B.T.C. Vos R. *Aerospace Design and Systems Engineering Elements I – AE1222-II*. Delft University of Technology, 2019.

[20] M.F. Basher. Optimum turbofan engine performance through variation of bypass ratio. *Journal of Engineering and Development*, (1), 2013.

[21] Fonod R. & Oliviero F. Cervone A. *Aerospace Design and Systems Engineering Elements II – AE2111-II*. Delft University of Technology, 2019.

[22] S.F. Hoerner. *Fluid-Dynamic Drag: Theoretical, experimental and statistical information*. Hoerner Fluid Dynamics, 1965.

[23] Charles D. Harris. Nasa supercritical airfoils :a matrix of family-related airfoil. Technical report, NASA, 1990.

[24] Robert J. McGhee Charles D. Hrrris and Dennis 0. Allison. Low-speed aerodynamic characteristics of a 14-percent-thick nasa phase 2 supercritical airfoil designed for a lift coefficient of 0.7. Technical report, NASA, 1980.

[25] Dr. Roskam J. *Airplane Design Part VII: Layout Design of Cockpit, Fuselage, Wing and Empennage: Cutaways and Inboard Profiles*. Design, Analysis and Research Corporation (DAR corporation), Lawrence, Kanses 66049, 1989.

[26] Scholz D. Nita, M. Estimating the oswald factor from basic aircraft geometrical parameters. *Deutscher Luft- und Raumfahrtkongress*, 2012.

[27] Hoekstra J.M. Ellerbroek J. Sun, J. Aircraft drag polar estimation based on a stochastic hierarchical model. Technical report, University of Technology Delft, 2018.

[28] P.K.C. Rudolph. High-lift systems on commercial subsonic airliners. Technical report, National Aeronautics and Space Administration, 1996.

[29] P.K.C. Rudolph. Mechanical design of high lift system for high aspect ratio wings. Technical report, National Aeronautics and Space Administration, 1998.

[30] G.F. Bartley. Boeing b-777: Fly-bywire flight controls. Technical report, Boeing, 2001.

[31] Airbus. A320 aircraft characteristics, aiport and maintenance planning. Technical report, Airbus, 2019.

[32] Sadraey M. H. *Aircrafat Design: A Systems Engineering Approach*. John Wiley & Sons, Ltd, 2013.

[33] Hasan H.S. Al-Shamma O., Ali R. An instructive algorithm for aircraft elevator sizing to be used in preliminary aircraft design software. *Journal of Applied Engineering Science*, 2017.

[34] Hasan H.S. Al-Shamma O., Ali R. An educational rudder sizing algorithm for utilization in aircraft design software. *International Journal of Applied Engineering Research*, 2018.

[35] Granta Design Limited. Ces edupack 2018.

[36] Dr. Roskam J. *Airplane Design Part II: Preliminary Configuration Design and Integration of the Propulsion System*. Design, Analysis and Research Corporation (DAR corporation), Lawrence, Kanses 66049, 1985.

[37] Juliette Ran. Aeroelastic tailoring of strut-braced wings. Technical report, Delft University of Technology, 2017.
[38] Duan L. & Chen W.F. ". *Effective Length Factors of Compression Members*. Boca Raton: CRC Press LLC, 1999.
[39] W.C. Young. *Roark's formulas for Stress & Strain*. McGraw-Hill, 1989.
[40] Melkert J. & Rans C. *Biaxial & Unsymmetrical Bending, AE2135-I Structural Analysis & Design*. Delft University of Technology, 2018.
[41] M. Sinnett. 787 no-bleed systems: Saving fuel and enhancing operational efficiencies. *Boeing Aeromagazine*, (4), 2007.
[42] Seabridge A. Moir, I. *Aircraft systems*. Wiley, 2008.
[43] Ruf C. Fleuti, E. Aircraft ground energy systems at zurich airport. Technical report, Zurich Airport, 2018.
[44] Liu X. Jiao Z. Wu S. Shang, Y. A novel integrated self-powered brake system for more electric aircraft. Technical report, Chinese Society of Aeronautics and Astronautics & Beihang University, 2017.
[45] Li Y. Bo, L. Research on simulation of aircraft electric braking system. *LNEE*, (126), 2012.
[46] Martin Hewitt Roy Langton, Chuck Clark and Lonnie Richards. *Aircraft fuel systems*. Aerospace series. Wiley and Sons, Ltd, 2009.
[47] B. Riecken. *Airbus A320: An Advanced Systems Guide*. Commercial aviation. Fluge, 2015.
[48] T. Jomier. More open electric technical project. Technical report, European Commission, Airbus Operations, 2009.
[49] Hebala A. Giangrande P. Klumpner C. Nuzzo S. Chen G. Gerada C. Eastwick C. Galea M. Lukic, M. State of the art of electric taxiing systems. Technical report, University of Nottingham, Nottingham, United Kingdom, 2018.
[50] *Electric Taxiing by Safran*. Safran Landing Systems, 2017.
[51] FAA. Type certificate data sheet a16we. Technical report, Department of transportation federal aviation administration, 2017.
[52] Lucintel. Global commercial aero turbofan engine market, supply chain and opportunities: 2012 -2017. Technical report, 2012.
[53] Hulskotte J.H.J. Dellaert, S.N.C. Emissions of air poullutants from civil aviation in the netherlands. Technical report, The Netherlands Organisation for applied scientific research TNO, 2017.
[54] Gaudioso D. De Lauretis R. Romano, D. Aircraft emissions: a comparison of methodologies based on different data available. Technical report, ENEA C.R.E. Casaccia, Environment department, 1999.
[55] Paassen D.M. Ruijgrok G.J.J. *Elements of Aircraft Pollution*. Delft University Press, 2600 MG Delft, 2005.
[56] Olivier et al. Inventory of aircraft emissions; a review of recent literature. Technical report, Rijksinstituut voor Volksgezondheid en Milieu (RIVM), 1991.
[57] K. Rypdal. Aircraft emissions. Technical report, Intergovernmental Panel on Climate Change (IPCC), 2000.
[58] Fahey D.W. Forster P.M. Newton P.J. Wit R.C.N. Lim L.L. Owen B. Sausen R. Lee, D.S. Aviation and global climate change in the 21st century. Technical report, 2009.
[59] Dynamic cost indexing: Including climate impacts of nox in a dynamic cost indexing tool. Technical report, 2009.
[60] Sausen R. Lee D.S. Fitcher C., Marquart S. The impact of cruise altitude on contrails and related radiative forcing. *Meteorologische Zeitschrif*, 14, 2005.
[61] European Environment Agency. Aviation and shipping — impacts on europe's environment. Technical report, European Environment Agency, 2017.
[62] Stone J.R.. Krejsa, E.A. Enhanced fan noise modeling for turbofan engines. *NASA/CR—2014-218421*, 2014.
[63] US Department of Transportation FAA. Type certificate data sheet e00049en. 2016.
[64] A. Filipone. Aircraft noise prediction. 2016.
[65] Al-Shamma O. Ali, R. A comparative study of cost estimation models used for preliminary aircraft design. *Global Journal of Researches in Engineering: B Automotive Engineering*, 14, 2014.
[66] Romanoff-H.P. Hess, R.W. Aircraft airframe cost estimating relationships: All mission types. Technical report, RAND, 1987.
[67] Trapp D. L. Beltramo, M. N. Parametric study of transport aircraft systems cost and weight. Technical report, Science Applications, INC., 1977.
[68] *Airline Operating Costs and Productivity*. International Civil Aviation Organisation, Teheran, 2017.
[69] J. Sinke. Production of aerospace systems ae3211-ii. Technical report, University of Technology Delft, 2019.

A Task division

- Executive overview: Everybody
- Introduction: Nikki
- Design overview: Max, Nikki
  - Design Process: Nikki
  - Weight breakdown, Fuselage Design: Max
- Systems: Nikki, Bram, Daniel, Reinoud
  - Electrical System, Electric Taxiing: Bram, Daniel
  - Pneumatic System, Hydraulic System: Bram
  - Hydraulic System, Flight Control System, Environmental Control System: Reinoud
  - Fuel system: Nikki
- Aerodynamic design and analysis: Floyd, Max, Reinoud
  - 3D wing, Lift Analysis, Drag Analysis, Drag Polars: Max, Floyd
  - High Lift Devices: Reinoud
  - AVL Analysis, Verification: Floyd
- Structural analysis: Mels, Sebastiaan, Mathilde
- Stability and control: Daniël, Hidde
- Performance analysis: Nikki
- Propulsion: Bram and Nikki
  - Propulsion system selection, mass estimation: Bram
  - Cycle calculation, outer dimensions: Nikki
- Operations: Max, Bram, Mels, Hidde
  - Turnaround time: Hidde
  - Maintenance: Mels
  - Ground handling: Bram
  - RAMS: Max
  - Data handling: Bram
- Emission analysis: Nikki
- Fuel consumption: Nikki
- Noise analysis: Nikki
- Resource Allocation: Reinoud
- Financial analysis: Daniël and Reinoud
  - Market analysis: Daniël
  - Aircraft costs, direct operational costs: Reinoud
- Sustainability strategy: Nikki
- Requirement analysis: Nikki
- Project Design: Reinoud
- Gantt Chart: Hidde
- Conclusions and Recommendations : Max and Mathilde
- CATIA: Floyd

B Functional Flow Diagram

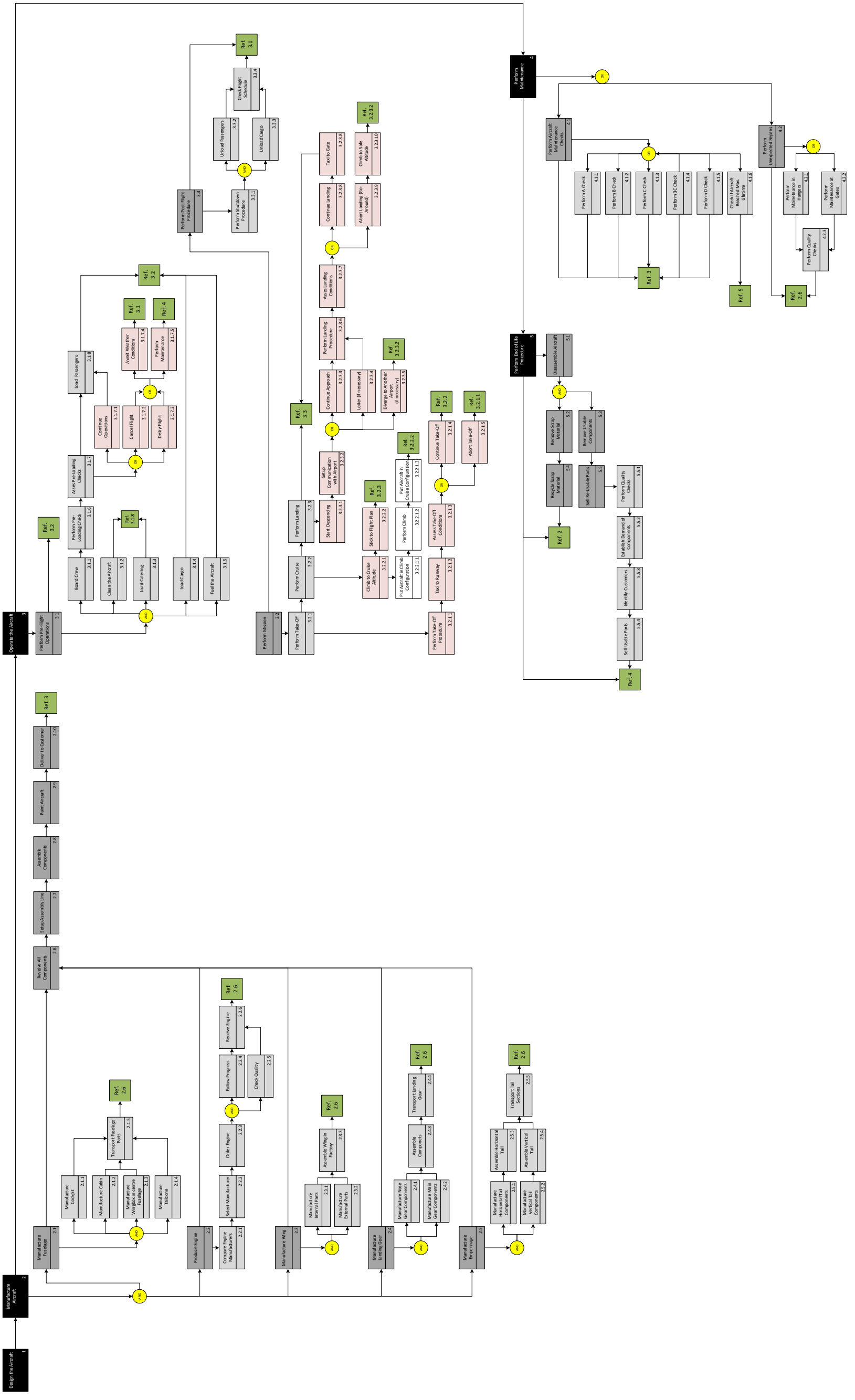

C Functional Breakdown Structure

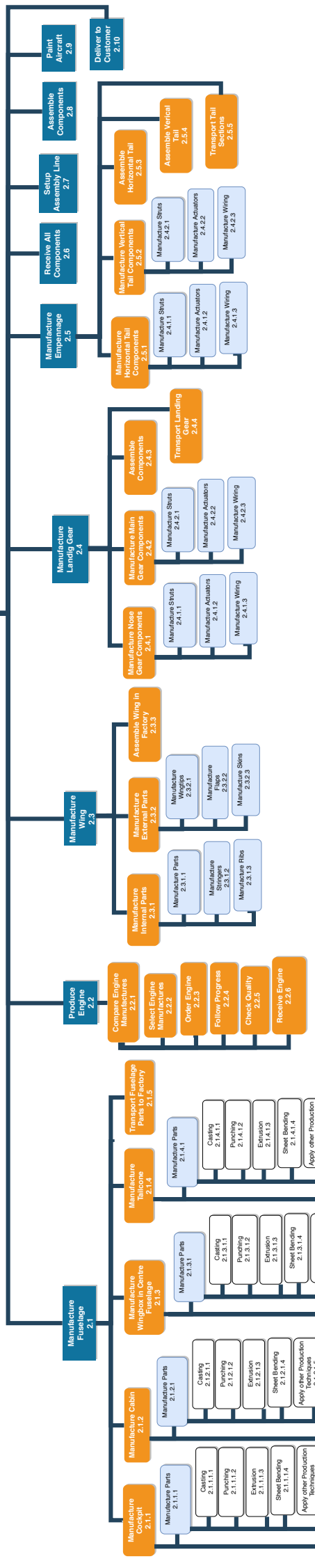

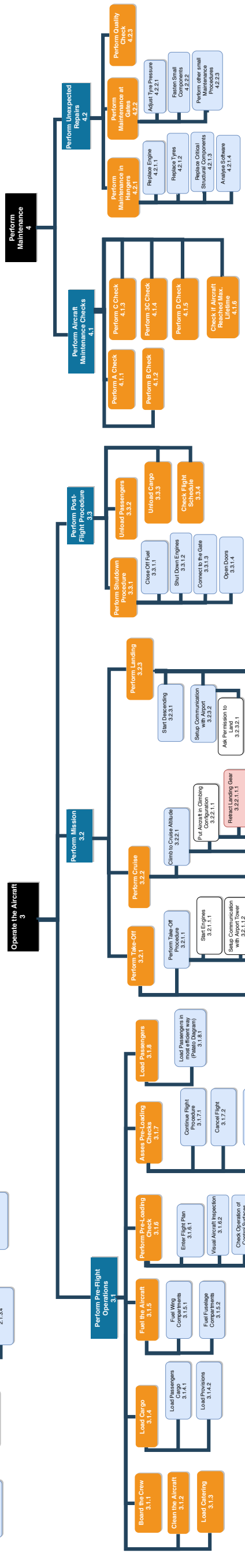

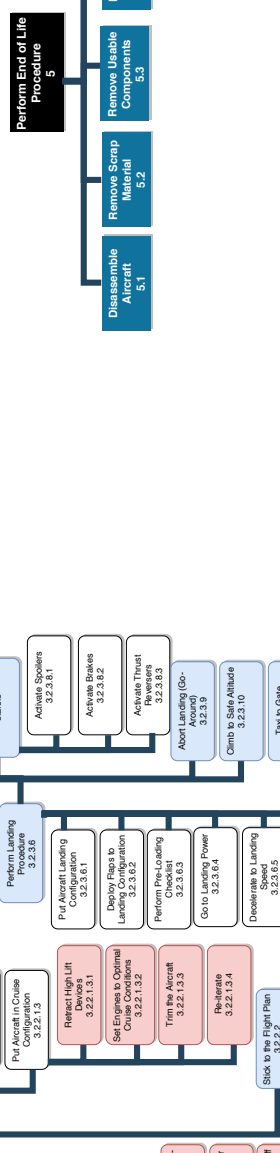

D MAI plan

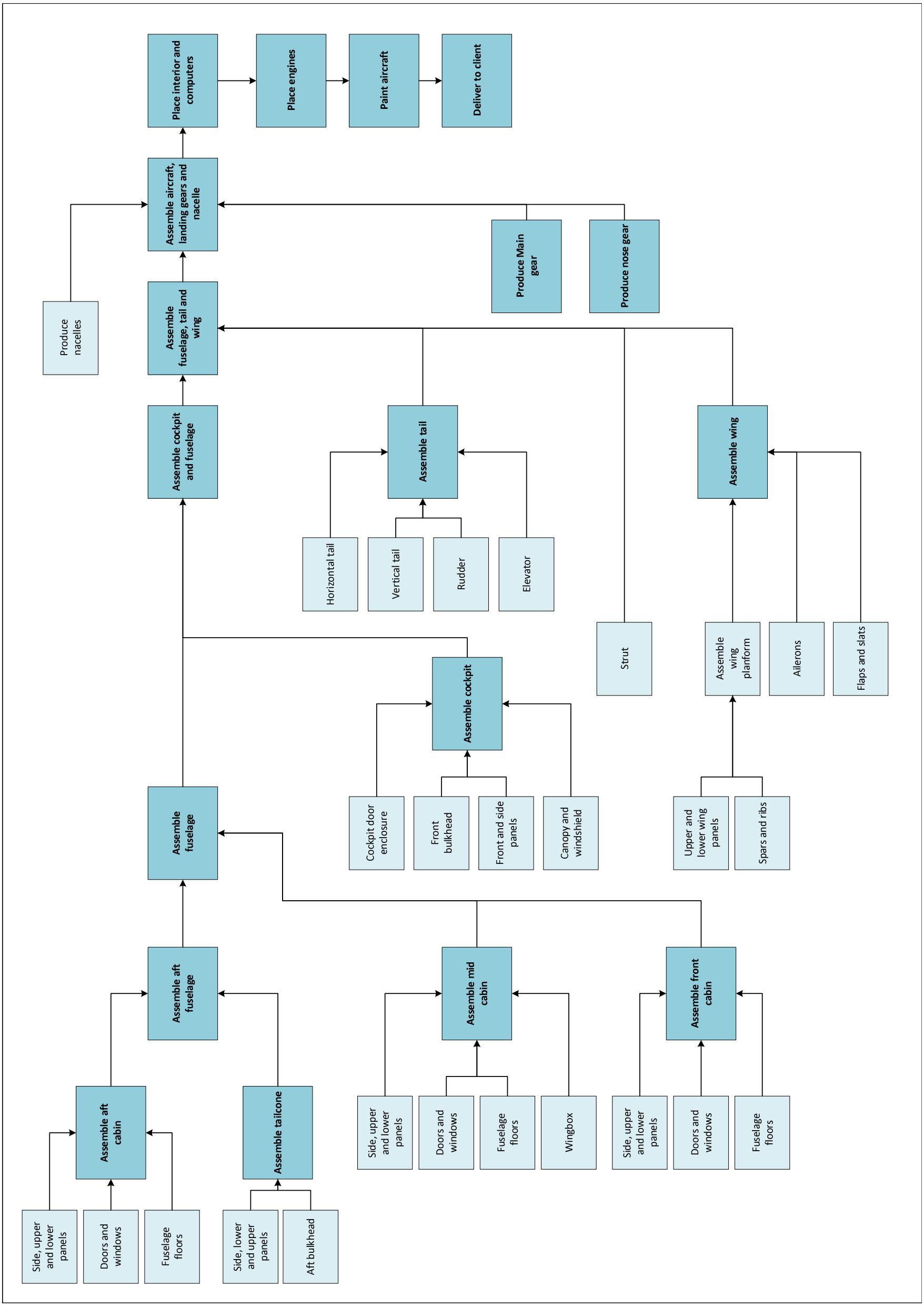
Place interior and computers
Place engines
Paint aircraft
Deliver to client
Assemble aircraft, landing gears and nacelle
Produce Main gear
Produce nose gear
Produce nacelles
Assemble fuselage, tail and wing
Assemble cockpit and fuselage
Assemble tail
Horizontal tail
Vertical tail
Rudder
Elevator
Strut
Assemble wing
Assemble wing planform
Ailerons
Flaps and slats
Assemble cockpit
Cockpit door enclosure
Front bulkhead
Front and side panels
Canopy and windshield
Upper and lower wing panels
Spars and ribs
Assemble fuselage
Assemble aft fuselage
Assemble aft cabin
Side, upper and lower panels
Doors and windows
Fuselage floors
Assemble tailcone
Side, lower and upper panels
Aft bulkhead
Assemble mid cabin
Side, upper and lower panels
Doors and windows
Fuselage floors
Wingbox
Assemble front cabin
Side, upper and lower panels
Doors and windows
Fuselage floors

E Project Gant Chart

Gantt chart post-DSE

ID	Task Mode	Task Name	Duration	Start	Finish	WBS
1		**Finalise preliminary design**	**4090 days**	**Mon 24-6-19**	**Fri 23-2-35**	**1**
2		**Finalise technical analysis per department**	**800 days**	**Mon 24-6-19**	**Fri 15-7-22**	**1.1**
3		Perform FEM	800 days	Mon 24-6-19	Fri 15-7-22	1.1.1
4		Perform CFD	800 days	Mon 24-6-19	Fri 15-7-22	1.1.2
5		Perform windtunnel tests	800 days	Mon 24-6-19	Fri 15-7-22	1.1.3
6		Analyse detailed flight performance characteristics	800 days	Mon 24-6-19	Fri 15-7-22	1.1.4
7		Size systems in detail	800 days	Mon 24-6-19	Fri 15-7-22	1.1.5
8		Research licensing of the aircraft	800 days	Mon 24-6-19	Fri 15-7-22	1.2
9		Finalise operational analysis	800 days	Mon 24-6-19	Fri 15-7-22	1.3
10		**Finalise financial analysis**	**800 days**	**Mon 24-6-19**	**Fri 15-7-22**	**1.4**
11		Investigate possible customers	300 days	Mon 24-6-19	Fri 14-8-20	1.4.1
12		Contact customers	500 days	Mon 17-8-20	Fri 15-7-22	1.4.2
13		**Perform detailed design**	**800 days**	**Mon 18-7-22**	**Fri 8-8-25**	**1.5**
14		**Perform construction analysis**	**350 days**	**Mon 18-7-22**	**Fri 17-11-23**	**1.5.1**
15		Select rivets	100 days	Mon 18-7-22	Fri 2-12-22	1.5.1.1
16		Analyse rivet spacing	250 days	Mon 5-12-22	Fri 17-11-23	1.5.1.2
17		Make production plan	300 days	Mon 20-11-23	Fri 10-1-25	1.5.2
18		Select manufacturing tools	150 days	Mon 13-1-25	Fri 8-8-25	1.5.3
19		Perform flight simulations of the aircraft	800 days	Mon 18-7-22	Fri 8-8-25	1.5.4
20		Lobby customers	800 days	Mon 18-7-22	Fri 8-8-25	1.5.5
21		**Perform aircraft testing**	**640 days**	**Mon 11-8-25**	**Fri 21-1-28**	**1.6**
22		Build test aircraft	400 days	Mon 11-8-25	Fri 19-2-27	1.6.1
23		Test performance and all relevant parameters	80 days	Mon 22-2-27	Fri 11-6-27	1.6.2
24		Apply possible design changes	80 days	Mon 14-6-27	Fri 1-10-27	1.6.3
25		Obtain license from airworthiness organisations	80 days	Mon 4-10-27	Fri 21-1-28	1.6.4
26		Safety margin	250 days	Mon 24-1-28	Fri 5-1-29	1.7
27		Start producing aircraft	800 days	Mon 8-1-29	Fri 30-1-32	1.8
28		Deliver aircraft to customer	800 days	Mon 2-2-32	Fri 23-2-35	1.9